

PREDICTION OF
TRANSFORMATION TEXTURES
IN STEELS

by



Philippe Chapellier

A Thesis Submitted to the Faculty of Graduate Studies
and Research in Partial Fulfillment of the Requirements
for the Degree of Master of Engineering

Department of Mining and Metallurgical Engineering
McGill University
Montreal, Canada

June 1989

ABSTRACT

The prediction of transformation textures is studied from a theoretical and analytical point of view, and some of the resulting models are applied to the austenite-to-ferrite transition in steels. Both discrete and continuous mathematical formalisms are presented to simulate texture evolution in the course of the phase change. In the discrete description, the texture is represented by means of ideal orientations and the transformation law by various strict crystallographic relationships. In the continuous description, the texture and transformation laws are described by statistical ODF and MODF functions, respectively. Some important aspects related to the existence of several variants of the transformation laws are dealt with. The different kinds of transformation textures observed experimentally in controlled rolled steels are also reviewed and the dependence of their development on certain compositional and processing parameters is discussed.

Five fcc Ni-Co alloys with different stacking fault energies (SFE's) were previously cold rolled to four reductions (40%, 70%, 90% and 95%) and their textures characterized by the orientation distribution function (ODF) method. The corresponding bcc transformation textures were calculated from these experimental textures according to three different orientation relationships for the $\gamma \rightarrow \alpha$ transition. The transformed ODF's derived from the Bain relationship are much sharper than the ones deduced from the Kurdjumov-Sachs (KS) or the Nishiyama-Wassermann (NW) relations, although the general trends of the three families of textures are similar. Ferrite textures determined on controlled rolled steels, heavily deformed in the unrecrystallized γ region, agree reasonably well with the bcc textures calculated, according to the KS relationship, from the Ni-Co alloy with similar SFE. The two major ferrite components, namely the $\{332\} \langle 113 \rangle$ and $\{113\} \langle 110 \rangle$, are found to originate from the three main orientations of cold rolled fcc materials, i.e. the $\{112\} \langle 111 \rangle$ (Cu), $\{110\} \langle 112 \rangle$ (Bs) and $\{123\} \langle 634 \rangle$ (S). Such ferrite transformation from heavily deformed austenite appears to follow the KS relationship without any variant selection. By contrast, the texture of martensite produced from deformed austenite seems to involve significant amounts of such selection. Finally, although similar ϕ_1 -section ODF's are observed, comparison between the simulated textures and those determined in cold rolled steels leads only to partial correspondence, since no fibre type components are actually predicted.

RÉSUMÉ

Les textures de transformation sont étudiées d'un point de vue théorique et analytique, et quelques uns des modèles proposés sont appliqués au cas de la transition austénite-ferrite dans les aciers. L'évolution de la texture au cours d'un changement de phase est présentée à l'aide de formalismes discret et continu. Décrite de façon discrète, la texture est représentée par des orientations idéales et la loi de transformation par diverses relations cristallographiques. De façon continue, les descriptions sont basées sur les fonctions statistiques de distribution des orientations (FDO) et des transformations (FTO), respectivement. Les principaux problèmes liés à l'existence de plusieurs variants de transformation sont traités avec soin. Les différentes textures de transformation observées pour des aciers obtenus par laminage contrôlé sont revues ainsi que l'influence de certains paramètres de composition et de traitement.

Cinq alliages cfc Ni-Co possédant différentes énergies d'empilement ont été préalablement laminés de 40 à 95% et leurs textures déterminées par la méthode des FDO. Les textures de transformation correspondantes (cc) ont été calculées à partir de ces textures expérimentales à l'aide de trois relations de transformation. Les FDO obtenues avec la relation de Bain sont toujours plus sévères que celles déduites des relations de Kurdjumov-Sachs (KS) et Nishiyama-Wassermann (NW), bien que l'aspect général des trois familles de cartes soit très semblable. Les textures ferritiques, déterminées sur des aciers obtenus par une réduction élevée en laminage contrôlé dans la zone de non recristallisation, sont en accord satisfaisant avec les FDO simulées par la relation KS à partir de l'alliage Ni-Co d'énergie d'empilement voisine. On montre que les deux composantes de la ferrite, voisines de $\{332\}\langle 113 \rangle$ et $\{113\}\langle 110 \rangle$, ont leur origine dans trois orientations prépondérantes pour les matériaux cfc laminés à froid, i.e. $\{112\}\langle 111 \rangle$ (Cu), $\{110\}\langle 112 \rangle$ (laiton) et $\{123\}\langle 634 \rangle$ (S). Il apparaît donc que les transformations ferritiques suivent la loi KS, sans aucune évidence de sélection des variants. Au contraire, les textures martensitiques produites à partir de l'austénite déformée semble impliquer une telle sélection. Enfin, bien que l'on observe des sections ϕ_1 de FDO similaires, les textures simulées et celles mesurées pour les aciers laminés à froid ne montrent qu'une ressemblance partielle puisqu'aucune fibre n'est en fait prédite.

ACKNOWLEDGEMENTS

I would like to express my sincere appreciation for his guidance, support and constant encouragement to my thesis supervisor Professor John J. Jonas, who introduced me to the exciting field of textures and acquainted me with the subject of this thesis. I am also indebted to Professor Ranjit K Ray (Dept of Metallurgical Engineering, Indian Institute of Technology, Kanpur, India) who contributed significantly to the success of the study and always lent me an attentive ear.

I also want to express my sincere thanks to my fellow graduate students and to the post doctoral fellows and visiting scientists with whom I had the pleasure to work during my stay at McGill. Here special mention must be made of Dominique Daniel and Kei Sakata, who kindly shared their room, time and good humor with me.

I am also deeply grateful to Lorraine Mello, Carole Rousseau and Joanne Guimond, who participated in the excellent memories I will always retain from these two years.

Le plus important et le plus précieux soutien m'est venu de ma femme qui a su, jour après jour, m'apporter toute la joie et toute la volonté nécessaire à la réalisation de ce projet. C'est à elle et à Amandine, notre petite fille, que je souhaite dédier ce travail.

TABLE OF CONTENTS

	page
ABSTRACT	i
RÉSUMÉ	ii
ACKNOWLEDGEMENTS	iii
TABLE OF CONTENTS	iv
LIST OF FIGURES	vi
LIST OF TABLES	xxi
 CHAPTER I INTRODUCTION	 1
 CHAPTER II TEXTURE REPRESENTATION	 3
II.1 ORIENTATION OF INDIVIDUAL CRYSTALS	5
II.2 THE ORIENTATION DISTRIBUTION FUNCTION	15
 CHAPTER III PRINCIPLES OF TEXTURE TRANSFORMATION	 24
III.1 REPRESENTATION OF THE TRANSFORMATION	27
III.2 TRANSFORMATION LAWS	33
III.3 SYMMETRY CONSIDERATIONS	41
III.4 METHODS OF SIMULATION	53

	page
CHAPTER IV TRANSFORMATION TEXTURES IN STEELS	63
- LITERATURE REVIEW -	
IV.1 INTRODUCTION	65
IV.2 GENERAL FEATURES	66
IV.3 FACTORS AFFECTING TRANSFORMATION TEXTURES	69
IV.4 CORRESPONDENCE BETWEEN ANALYTICALLY PREDICTED AND EXPERIMENTAL TEXTURES	84
CHAPTER V PREDICTIONS OF TRANSFORMATION TEXTURES	99
V.1 EXPERIMENTAL METHOD AND SIMULATIONS	101
V.2 RESULTS	108
V.3 DISCUSSION	151
CHAPTER VI CONCLUSIONS	181
REFERENCES	187
APPENDICES	194

LIST OF FIGURES

	<u>page</u>
<u>Figure 2-1:</u> Mirror planes of a rolled sheet.	5
<u>Figure 2-2:</u> Orientation of a given cubic crystal with respect to the reference frame of the rolled specimen.	6
<u>Figure 2-3:</u> Definition of the Euler angles.	8
<u>Figure 2-4:</u> The two sets of polar coordinates : (a) in the sample, (b) in the crystal.	10
<u>Figure 2-5:</u> Equivalent choices of the crystal reference axes for a cubic system.	13
<u>Figure 2-6:</u> Equivalent orientations due to the crystal symmetry.	14
<u>Figure 2-7:</u> Equivalent orientations due to the sample symmetry.	14
<u>Figure 2-8:</u> Equivalent orientations due to the combined crystal and sample symmetries	15
<u>Figure 2-9:</u> ϕ_2 -section ODF of a Ni-30Co alloy 95% cold rolled.	16
<u>Figure 2-10:</u> Stereographic projection.	18
<u>Figure 2-11:</u> Projection in the rolling plane of the three (100) poles of a cubic crystal.	19
<u>Figure 2-12:</u> (a) : 200 pole figure (b) . ND inverse pole figure of a Ni-30Co alloy 95% cold rolled.	20
<u>Figure 2-13:</u> Standard triangle for the cubic system.	20

<u>Figure 2-14a :</u>	Representation of Euler angles on a pole figure, after [2]	21
<u>Figure 2-14b :</u>	Representation of Euler angles on an inverse pole figure, after [2]	21
<u>Figure 3-1 :</u>	Definition of the transformation	27
<u>Figure 3-2 :</u>	Definition of the symmetrically equivalent transformation rotations.	29
<u>Figure 3-3 :</u>	Schematic illustration of the progressive modeling approach : (a) a unique relationship, (b) a unique family of equivalent variants, (c) several families of equivalent variants, (d) non-strict relationships	31
<u>Figure 3-4 :</u>	Illustration of the Nishiyama-Wassermann relationship and its deviation from the Bain and Kurdjumow-Sachs relationships.	36
<u>Figure 3-5 :</u>	Relative positions of the different orientation relations in Euler space.	37
<u>Figure 3-6 :</u>	ϕ_2 -section misorientation distribution function for the KS relationship.	39
<u>Figure 3-7 :</u>	Densities of (a) : the (111) γ -poles in the α -crystal, (b) : the (110) α -poles in the γ -crystal.	40
<u>Figure 3-8 :</u>	Graphical illustration of the definition of variants.	42
<u>Figure 3-9 :</u>	Variants of the B, KS and NW relationships in the ϕ_2 - sections.	48

<u>Figure 3-10:</u>	Variants of the B, KS and NW relationships in the ϕ_1 -sections.	48
<u>Figure 4-1:</u>	Effect of Mn on the textures of Nb-free steels (100 pole figures).	69
<u>Figure 4-2:</u>	Effect of T_f on the textures of Nb-free steels ($\phi = 45^\circ$ sections): (a) $T_f = 900^\circ\text{C}$ (b) $T_f = 760^\circ\text{C}$ (c) $T_f = 600^\circ\text{C}$.	70
<u>Figure 4-3:</u>	Effect of Mn on the textures of Nb-containing steels ($\phi = 45^\circ$ sections).	70
<u>Figure 4-4:</u>	Skeleton lines of Nb steels.	71
<u>Figure 4-5:</u>	Skeleton lines of Fe-Ni alloys.	71
<u>Figure 4-6:</u>	Partial ODF's of 2.48% Mn steel, Fe-22.5Ni and Fe-30.8Ni (ψ sections).	72
<u>Figure 4-7:</u>	Effect of Ni on the textures of C-Mn-Nb steels (100 pole figures).	72
<u>Figure 4-8:</u>	(a) C-Mn-Nb steel (b) C-Mn-Nb steel with 0.3% Mo and 0.7% Cr. (100 pole figures)	73
<u>Figure 4-9:</u>	ODF of a C-Mn-Nb steel quenched after 80% reduction at 1000°C .	74
<u>Figure 4-10:</u>	$\phi = 45^\circ$ sections of a C-Mn-Nb steel finished at: (a) 850°C , (b) 800°C , (c) 750°C , (d) 710°C , (e) 650°C , and (f) skeleton lines.	75
<u>Figure 4-11:</u>	Density along $\langle 110 \rangle // \text{TD}$ of a C-Mn-Nb steel.	76

<u>Figure 4-12:</u>	Density along $\langle 110 \rangle$ RD of a C-Mn-Nb steel.	76
<u>Figure 4-13:</u>	Skeleton lines of a C-Mn steel.	77
<u>Figure 4-14:</u>	Density along $\langle 110 \rangle$ TD of a C-Mn steel.	77
<u>Figure 4-15:</u>	Density along $\langle 110 \rangle$ RD of a C-Mn steel.	77
<u>Figure 4-16:</u>	$\phi = 45^\circ$ sections of a C-Mn steel finished at (a) 750°C and (b) 650°C.	77
<u>Figure 4-17:</u>	C-Mn-Nb steel rolled in the $(\gamma + \alpha)$ region (a) 0%, (b) 10% and (c) 60% ($\phi = 45^\circ$ sections).	79
<u>Figure 4-18:</u>	Surface texture of a Nb-V steel finished at (a) 750°C, (b) 700°C, (c) 650°C.	79
<u>Figure 4-19:</u>	Principle of formation of a texture gradient in hot rolled sheets.	80
<u>Figure 4-20:</u>	Effect of soaking temperature on the texture of C-Mn-Nb steels.	81
<u>Figure 4-21:</u>	Effect of cooling rate on the texture of controlled rolled C-Mn-Nb steels.	81
<u>Figure 4-22:</u>	$\phi = 45^\circ$ sections for a C-Mn-Nb steel after rolling at (a) 810°C, (b) 710°C.	82
<u>Figure 4-23:</u>	ODF of a C-Mn-Nb steel quenched after 80% reduction at 815°C.	82
<u>Figure 4-24:</u>	Effect of heat treatment on a C-Mn-Nb steel ($\phi = 45^\circ$ sections).	83

<u>Figure 4-25 :</u>	ODF of a C-Mn-Nb steel (ψ sections) and ideal orientations derived from $\{110\}\langle 112 \rangle$ (■) and $\{112\}\langle 111 \rangle$ (●) with the KS relationship.	85
<u>Figure 4-26 :</u>	NW-predicted ODF of an Fe-30Ni alloy cold rolled 67% in the bcc structure and transformed into fcc.	86
<u>Figure 4-27 :</u>	Experimental ODF of the alloy of Figure 4-26.	86
<u>Figure 4-28 :</u>	Parent austenite ODF untransformed from Figure 4-9.	87
<u>Figure 4-29 :</u>	ODF of 60% cold rolled high purity aluminum.	87
<u>Figure 4-30 :</u>	Ferrite ODF predicted from Figure 4-29 with the KS relationship	88
<u>Figure 4-31 :</u>	Component A : (a) experimental, (b) NW predicted, component B : (c) experimental, (d) NW predicted.	89
<u>Figure 4-32 :</u>	$\phi = 45^\circ$ sections of observed and calculated ODF's.	90
<u>Figure 4-33 :</u>	Austenite ODF untransformed from Figure 4-23.	90
<u>Figure 4-34 :</u>	MODF ($\phi = 0^\circ$) relating the two phases of an annealed Fe-30Ni alloy.	91
<u>Figure 4-35 :</u>	MODF's ($\phi = 0^\circ$) relating the two phases of an Fe-30Ni alloy for prior reductions of (a) 50%, (b) 60%, (c) 70%, (d) 75%, (e) 80%, and (f) 90%.	91
<u>Figure 4-36 :</u>	Variant selection functions after 10% rolling along (a) $\langle 100 \rangle$, (b) $\langle 110 \rangle$.	91

	<u>page</u>
<u>Figure 4-37 :</u> Fe-30Ni textures (a) without load, (b) with load along RD (● :NW poles).	92
<u>Figure 4-38 :</u> Experimental and KS-predicted ODF's of Fe-30Ni rolled 80%.	93
<u>Figure 4-39 :</u> (a) $\phi = 0^\circ$ and 45° ODF sections assuming a grain shape equivalent to 95% reduction, (b) associated $\phi = 0^\circ$ MODF section.	93
<u>Figure 4-40 :</u> (100) pole figure of the α orientations KS-derived from (110)[2-25] _γ .	94
<u>Figure 4-41 :</u> (a) $\phi = 0^\circ$ and 45° ODF sections assuming the transformation to take place on the most favored habit plane, (b) associated $\phi = 0^\circ$ MODF.	94
<u>Figure 4-42 :</u> (a) $\phi = 0^\circ$ and 45° ODF sections assuming the transformation to take place on the two most favored habit planes, (b) associated $\phi = 0^\circ$ MODF.	94
<u>Figure 4-43 :</u> (a) $\phi = 0^\circ$ and 45° ODF sections assuming the transformation to take place on the four most favored habit planes, (b) associated $\phi = 0^\circ$ MODF.	95
<u>Figure 4-44 :</u> (a) $\phi = 0^\circ$ and 45° ODF sections assuming the transformation to take place on all weighted habit planes, (b) associated $\phi = 0^\circ$ MODF.	95
<u>Figure 4-45 :</u> (100) pole figure of the α orientations derived from {110}<112>(■), {123}<856>(►), {112}<111>(●) by the variants associated with the slip systems upon which the largest shear stresses acted.	95

<u>Figure 4-46:</u>	(100) pole figure of Fe-25.7Ni derived with all 24 GT variants.	95
<u>Figure 4-47:</u>	Experimental (100) pole figure of martensite in Fe-25.7Ni.	96
<u>Figure 4-48:</u>	Experimental (100) pole figure of martensite in Fe-30.2Ni.	96
<u>Figure 4-49:</u>	Observed and calculated textures for (a) ferrite/pearlite, (b) martensite.	96
<u>Figure 4-50:</u>	$\phi = 0^\circ$, $\phi = 45^\circ$ ODF and $\phi = 0^\circ$ MODF sections predicted from 90% cold rolled austenite by means of the slip system/variant coincidence criterion assuming a rotation of the principal axes of the strain tensor about TD (shear) by (a) 0° , (b) 5.6° , (c) 13.2° , (d) 22.5° , (e) 45° .	97
<u>Figure 4-51:</u>	(a)Experimental, (b)simulated (100) pole figure for martensitic Fe-25.7Ni.	98
<u>Figure 4-52:</u>	Simulated Fe-30Ni ODF's assuming (a) maximal deformation along ND, (b) minimal deformation in the sheet plane.	98
<u>Figure 5-1:</u>	Extract of the 'Periodic Table of the Elements'.	103
<u>Figure 5-2:</u>	Partial ϕ_2 -section ODF's after 95% cold reduction for pure Ni and five of its alloys containing 10, 20, 30, 40 and 60 percent cobalt (levels 3,6,9...).	109
<u>Figure 5-3:</u>	Partial ϕ_2 -section ODF's for Ni-30Co cold rolled 40, 70, 90 and 95% (levels 3,6,9...).	111

<u>Figure 5-4 :</u>	Partial ϕ_2 -section ODF's for Ni-40Co cold rolled 40, 70, 90 and 95% (levels 3,6,9...).	112
<u>Figure 5-5 :</u>	Partial ϕ_2 -section ODF's for Ni-60Co cold rolled 40, 70, 90 and 95% (levels 3,6,9...).	113
<u>Figure 5-6 :</u>	(a) Some classical bcc texture components; (b) KS-related orientations transformed from some fcc recrystallization components.	115
	KS-related orientations transformed from (c) the three main fcc rolling components, and (d) some other fcc rolling components.	116
<u>Figure 5-7 :</u>	Transformation of the fcc cube component (100 pole figures); comparison of the (a) Bain and KS orientations, and (b) Bain and NW orientations.	119
<u>Figure 5-8 :</u>	(a) Some classical bcc texture components; (b) transformation of the three most important fcc rolling components with the KS relationship.	120
	Transformation of the three most important fcc rolling components with the (c) Bain and (d) NW orientation relationships.	121
<u>Figure 5-9 :</u>	Transformation of the fcc S rolling component (100 pole figures) with the (a) KS, (b) Bain, and (c) NW orientation relationships.	122
<u>Figure 5-10 :</u>	(a) Some classical fcc texture components; (b) KS-related orientations untransformed from the Cube, Goss and associated rotated orientations.	123
	KS-related orientations untransformed from bcc rolling components (c) near the $\alpha = \langle 110 \rangle // \text{RD}$ fibre and (d) near the $\gamma = \langle 111 \rangle // \text{ND}$ fibre.	124

<u>Figure 5-11 :</u>	ϕ_1 -section ODF's obtained by transforming the texture of Ni-10Co according to the KS relationship after (a) 40%, (b) 70%, (c) 90%, and (d) 95% reduction prior to transformation (levels 1,2,3...).	127
<u>Figure 5-12 :</u>	ϕ_1 -section ODF's obtained by transforming the texture of Ni-20Co according to the KS relationship after (a) 40%, (b) 70%, (c) 90%, and (d) 95% reduction prior to transformation (levels 1,2,3...).	128
<u>Figure 5-13 :</u>	ϕ_1 -section ODF's obtained by transforming the texture of Ni-30Co according to the KS relationship after (a) 40%, (b) 70%, (c) 90%, and (d) 95% reduction prior to transformation (levels 1,2,3...).	129
<u>Figure 5-14 :</u>	Ferrite α fibres deduced from the ODF's obtained by transforming the texture of the five Ni-Co alloys according to the KS relationship after (a) 40%, (b) 70%, (c) 90%, and (d) 95% reduction prior to transformation.	130
<u>Figure 5-15 :</u>	Ferrite γ fibres deduced from the ODF's obtained by transforming the texture of the five Ni-Co alloys according to the KS relationship after (a) 40%, (b) 70%, (c) 90%, and (d) 95% reduction prior to transformation.	131
<u>Figure 5-16 :</u>	Ferrite α fibres of the ODF's obtained by transforming the texture of (a)Ni-10Co, (b)Ni-20Co, (c)Ni-30Co (d)Ni-40Co, (e)Ni-60Co with the KS relationship.	132
<u>Figure 5-17 :</u>	Ferrite γ fibres of the ODF's obtained by transforming the texture of (a)Ni-10Co, (b)Ni-20Co, (c)Ni-30Co (d)Ni-40Co, (e)Ni-60Co with the KS relationship.	133

	<u>page</u>
<u>Figure 5-18 :</u> ϕ_1 -section ODF's obtained by transforming the texture of Ni-40Co according to the KS relationship after (a) 40%, (b) 70%, (c) 90%, and (d) 95% reduction prior to transformation (levels 1,2,3...).	136
<u>Figure 5-19 :</u> ϕ_1 -section ODF's obtained by transforming the texture of Ni-60Co according to the KS relationship after (a) 40%, (b) 70%, (c) 90%, and (d) 95% reduction prior to transformation (levels 1,2,3...).	138
<u>Figure 5-20 :</u> ϕ_1 -section ODF's obtained by transforming the texture of (a) Ni-10Co, (b) Ni-20Co, (c) Ni-40Co, (d) Ni-60Co after 95% prior reduction with the Bain orientation relationship (levels 2,4,6...).	140
<u>Figure 5-21 :</u> ϕ_1 -section ODF's obtained by transforming the texture of Ni-30Co according to the Bain orientation relationship after (a) 40%, (b) 70%, (c) 90%, and (d) 95% reduction prior to transformation (levels 2,4,6...).	141
<u>Figure 5-22 :</u> Ferrite α fibres deduced from the ODF's obtained by transforming the texture of the five Ni-Co alloys according to the Bain relationship after (a) 40%, (b) 70%, (c) 90%, and (d) 95% reduction prior to transformation.	143
<u>Figure 5-23 :</u> Ferrite γ fibres deduced from the ODF's obtained by transforming the texture of the five Ni-Co alloys according to the Bain relationship after (a) 40%, (b) 70%, (c) 90%, and (d) 95% reduction prior to transformation.	144

<u>Figure 5-24 :</u>	Ferrite α fibres of the ODF's obtained by transforming the texture of (a)Ni-10Co,(b)Ni-20Co,(c)Ni-30Co(d)Ni-40Co,(e)Ni-60Co with the Bain relationship.	145
<u>Figure 5-25 :</u>	Ferrite γ fibres of the ODF's obtained by transforming the texture of (a)Ni-10Co,(b)Ni-20Co,(c)Ni-30Co(d)Ni-40Co,(e) Ni-60Co with the Bain relationship.	146
<u>Figure 5-26 :</u>	ϕ_1 -section ODF's obtained by transforming the texture of (a) Ni-10Co, (b) Ni-20Co, (c) Ni-40Co, (d) Ni-60Co after 95% prior reduction with the NW orientation relationship (levels 1,2,3...).	148
<u>Figure 5-27 :</u>	ϕ_1 -section ODF's obtained by transforming the texture of Ni-30Co according to the NW orientation relationship after (a) 40%, (b) 70%, (c) 90%, and (d) 95% reduction prior to transformation (levels 1,2,3...).	149
<u>Figure 5-28 :</u>	(a) Experimental ψ -section ODF (Roe notation) for a controlled rolled Nb steel containing 1.24% Mn; (b), (c), and (d) : ψ -section ODF's (Roe notation) obtained by transforming the texture of the 95% cold rolled Ni-30Co alloy according to the KS (levels 1,2,3..), Bain (levels 2,4,6..) and NW (levels 1,2,3..) relationships, respectively.	152
<u>Figure 5-29 :</u>	(a) Experimental ϕ -section ODF (Roe notation) for a hot rolled Nb steel containing 1.47% Mn; (b), (c), and (d) ϕ -section ODF's (Roe notation) obtained by transforming the texture of the 95% cold rolled Ni-30Co alloy according to the KS (levels 1,2,3..), Bain (levels 2,4,6..) and NW (levels 1,2,3..) relationships, respectively.	154

- Figure 5-30: (a) Experimental ψ -section ODF (Roe notation) for a controlled rolled Nb steel containing 1.24% Mn; (b), (c), and (d) ψ -section ODF's (Roe notation) obtained by transforming the texture of the 40% cold rolled Ni-30Co alloy according to the KS (levels 1,2,3..), Bain (levels 2,4,6..) and NW (levels 1,2,3..) relationships, respectively. 155
- Figure 5-31: (a) Experimental ψ -section ODF (Roe notation) for a controlled rolled Nb steel containing 1.24% Mn; (b), (c), and (d) ψ -section ODF's (Roe notation) obtained by transforming the texture of the 70% cold rolled Ni-30Co alloy according to the KS (levels 1,2,3..), Bain (levels 2,4,6..) and NW (levels 1,2,3..) relationships, respectively. 156
- Figure 5-32: (a) Experimental ψ -section ODF (Roe notation) for a controlled rolled Nb steel containing 1.24% Mn; (b), (c), and (d) ψ -section ODF's (Roe notation) obtained by transforming the texture of the 90% cold rolled Ni-30Co alloy according to the KS (levels 1,2,3..), Bain (levels 2,4,6..) and NW (levels 1,2,3..) relationships, respectively. 157
- Figure 5-33: (a) Experimental ψ -section ODF (Roe notation) for a controlled rolled Nb steel containing 2.48% Mn; (b), (c), and (d) ψ -section ODF's (Roe notation) obtained by transforming the texture of the 95% cold rolled Ni-30Co alloy according to the KS (levels 1,2,3..), Bain (levels 2,4,6..) and NW (levels 1,2,3..) relationships, respectively. 159

<u>Figure 5-34:</u>	(a) Experimental ϕ_2 -section ODF for the martensite formed from an 80% γ rolled Fe-30Ni alloy; (b), (c), and (d) ϕ_2 -section ODF's obtained by transforming the texture of the 95% cold rolled Ni-40Co alloy according to the KS (levels 1,2,3..), Bain (levels 2,4,6..) and NW (levels 1,2,3..) relationships, respectively.	161
<u>Figure 5-35:</u>	$\phi_2=0^\circ$ and $\phi_2=45^\circ$ sections from (a) the experimental ODF for the martensite formed from a 70% γ rolled Fe-30Ni alloy; (b) and (c) the textures obtained by transforming the ODF of the 95% cold rolled Ni-40Co alloy according to the KS (levels 1,2,3..) and Bain (levels 2,4,6..) relationships, respectively.	162
<u>Figure 5-36:</u>	ϕ_1 -section ODF's of (a) an Armco iron, rolled 90% at room temperature; (b) a 70% cold rolled low carbon steel; (c) and (d) the textures obtained by transforming the ODF of the 95% cold rolled Ni-30Co alloy according to the KS (levels 1,2,3..) and Bain (levels 2,4,6..) relationships, respectively.	164
<u>Figure 5-37:</u>	ϕ -section ODF's (Roe notation) of (a) an 80% cold rolled low carbon steel, and (b) the texture obtained by transforming the ODF of the 95% cold rolled Ni-30Co alloy according to the KS relationship (levels 1,2,3..).	165
<u>Figure 5-38:</u>	$\phi_2=45^\circ$ section of (a) a 72% cold rolled Nb steel, and (b) the texture obtained by transforming the ODF of the 95% cold rolled Ni-30Co alloy according to the KS relationship.	165
<u>Figure 5-39:</u>	Orientation density along the (a) α fibre and (b) γ fibre of the textures shown in Figure 5-36.	166

- Figure 5-40 : Orientation density along the α fibre for : (a) four 80% cold rolled steels; (b) the textures KS-related to 95% cold rolled Ni-Co alloys with various Co contents; (c) a vacuum degassed steel with various cold rolling reductions; and (d) the textures KS-derived from the Ni-30Co alloy with various cold rolling reductions. 167
- Figure 5-41 : Orientations derived from the three principal fcc rolling texture components (Cu, Bs and S) according to the KS relationship. These are superimposed on the ODF obtained with the same transformation law from the texture of the 95% cold rolled Ni-30Co alloy (levels 1,2,3..). 169
- Figure 5-42 : ϕ_1 -section ODF's obtained by transforming the texture of the 95% cold rolled Ni-30Co alloy according to the KS relationship : (a) without ghost correction; (b) corrected with a gaussian peak method; and corrected with an iterative positivity method (c) before and (d) after transformation (levels 1,2,3..). 172
- Figure 5-43 : ϕ_1 -section ODF's obtained by transforming the texture of the 95% cold rolled Ni-30Co alloy according to the NW relationship : (a) without ghost correction; (b) corrected with a gaussian peak method; and corrected with an iterative positivity method (c) before and (d) after transformation (levels 1,2,3..). 173
- Figure 5-44 : ϕ_1 -section ODF's obtained by transforming the texture of the 95% cold rolled Ni-30Co alloy according to the Bain relationship : (a) without ghost correction; (b) corrected with a gaussian peak method; and corrected with an iterative positivity method (c) before and (d) after transformation (levels 2,4,6..). 174

<u>Figure 5-45 :</u>	Orientation density along the α and γ fibres of the textures shown in Figures 5-42 to 5-44 pertaining to the : (a) KS, (b) NW, and (c) Bain relationships.	176
<u>Figure 5-46 :</u>	ϕ_1 -section ODF's obtained by transforming the texture of the 95% cold rolled Ni-30Co alloy according to the KS relationship with different orders of truncation : (a) $l_{\max}=22$, (b) $l_{\max}=18$, (c) $l_{\max}=12$, and (d) $l_{\max}=6$ (levels 1,2,3..).	177
<u>Figure 5-47 :</u>	Orientation density along the (a) α fibre and (b) γ fibre of the textures shown in Figure 5-46.	178
<u>Figure 5-48 :</u>	ϕ_1 -section ODF's obtained by transforming the texture of the 95% cold rolled Ni-30Co alloy according to the KS relationship with four angular spreads away from the exact law : (a) $\omega_0=0^\circ$, (b) $\omega_0=5^\circ$, (c) $\omega_0=10^\circ$ and (d) $\omega_0=15^\circ$ (levels 1,2,3..)	179
<u>Figure 5-49 :</u>	Orientation density along the (a) α fibre and (b) γ fibre of the textures shown in Figure 5-48.	180
<u>Figure 5-50 :</u>	ϕ_1 -section ODF's obtained by transforming the texture of the 95% cold rolled Ni-30Co alloy according to the KS relationship with four percentages of randomness : (a) $p_r=0\%$, (b) $p_r=15\%$, (c) $p_r=25\%$, and (d) $p_r=40\%$ (levels 1,2,3..).	181
<u>Figure 5-51 :</u>	Orientation density along the (a) α fibre and (b) γ fibre of the textures shown in Figure 5-50.	182
<u>Figure 5-52 :</u>	Dependence of the severity parameter of the transformation texture on the (a) percentage of randomness, and (b) degree of misorientation.	183

LIST OF TABLES

	<u>page</u>
<u>Table 2-1 :</u> Matrix representation of g	9
<u>Table 2-2 :</u> The rotation matrix as a function of the Euler angles.	11
<u>Table 2-3 :</u> $(hkl)[uvw]$ as a function of (ϕ_1, ϕ, ϕ_2) .	11
<u>Table 2-4 :</u> The rotation matrix as a function of $d = (d_x, d_y, d_z)$ and ω .	11
<u>Table 2-5 :</u> $d = (\theta, \psi)$ and ω as functions of the Euler angles ϕ_1, ϕ, ϕ_2 .	12
<u>Table 2-6 :</u> Polar coordinates of the system axes as functions of (ϕ_1, ϕ, ϕ_2) .	12
<u>Table 3-1 :</u> Characteristic data for the usual orientation relationships.	38
<u>Table 3-2 :</u> Number of variants determined from the parallelism conditions.	47
<u>Table 3-3 :</u> Number of variants determined from the rotation definition.	47
<u>Table 4-1 :</u> Main components as a function of the finishing temperature	67
<u>Table 5-1 :</u> Classification of fcc textures as a function of SFE.	102
<u>Table 5-2 :</u> Some SFE values.	102
<u>Table 5-3 :</u> Comparison of some physical data for Fe, Ni and Co.	103

<u>Table 5-4 :</u>	Chemical compositions of the Ni-Co alloys (weight percent).	104
<u>Table 5-5 :</u>	Most important fcc recrystallization and rolling orientations.	106
<u>Table 5-6 :</u>	Most important bcc texture components.	107
<u>Table 5-7 :</u>	List of bcc orientations KS-derived from fcc recrystallization components (Part 1).	114
<u>Table 5-8 :</u>	List of bcc orientations KS-derived from fcc recrystallization components (Part 2).	117
<u>Table 5-9 :</u>	List of bcc orientations KS-derived from the three main fcc rolling components.	117
<u>Table 5-10 :</u>	List of bcc orientations KS-derived from some other fcc rolling components.	118
<u>Table 5-11 :</u>	Main characteristics of the bcc textures KS-transformed from Ni-10Co.	134
<u>Table 5-12 :</u>	Main characteristics of the bcc textures KS-transformed from Ni-20Co.	134
<u>Table 5-13 :</u>	Main characteristics of the bcc textures KS-transformed from Ni-30Co.	135
<u>Table 5-14 :</u>	Main characteristics of the bcc textures KS-transformed from Ni-40Co.	137
<u>Table 5-15 :</u>	Main characteristics of the bcc textures KS-transformed from Ni-60Co.	139

<u>Table 5-16:</u>	Main characteristics of the bcc textures Bain-transformed from Ni-30Co.	142
<u>Table 5-17:</u>	Main characteristics of the bcc textures Bain-transformed from Ni-60Co.	142
<u>Table 5-18:</u>	Main characteristics of the bcc textures NW-transformed from Ni-30Co.	150
<u>Table 5-19:</u>	Main characteristics of the bcc textures NW-transformed from Ni-60Co.	150

CHAPTER I

INTRODUCTION

The common metals of industrial practice are polycrystalline aggregates in which each of the individual grains has an orientation that differs from those of its neighbors. However, it is quite unusual for the grains in such metals to have completely random orientations, and the non-random distributions that occur are called *preferred orientations* or *textures*. Texture can be described by linking together directions of the crystal with features of the specimen geometry. Thus, sheet textures are often described in terms of $\{hkl\} \langle uvw \rangle$ components, with the $\{hkl\}$ planes lying parallel to the rolling plane and the $\langle uvw \rangle$ directions oriented along the rolling direction. However, this description is usually insufficient and currently, orientation distribution function analysis has replaced such qualitative pole figure analysis.

Textures are formed at all stages of the manufacturing processes of metals, but their precise natures are complex functions of the preceding thermomechanical treatments, as well as of the material itself. The important processing factors which can contribute to the development of texture are : solidification, deformation, annealing and phase transformation. The present work is mainly concerned with the role of phase transitions on the textures of the final product, although the material deformation history is also taken into consideration. The effects of solidification and annealing on texture development will be completely ignored. A significant proportion of the shaping of steels is carried out when the structure is austenitic. The formation of a texture in the austenite is liable to influence the texture in subsequently formed martensite or ferrite due to the crystallographic nature of the transformation that takes place on cooling. Two factors are responsible for the importance of the textures formed at high temperatures : (i) the texture of the untransformed material plays a role in the development of texture on subsequent processing; and (ii) an increasing proportion of steels is used in the as-hot rolled condition, so that transformation directly influences the macroscopic final properties of the steel. Thus, an understanding of the way in which texture is inherited from austenite by ferrite or martensite is of considerable importance in understanding the properties of ferrous materials at ambient temperatures.

Experimental difficulties generally preclude the measurement of the texture of the austenite of conventional steels prior to transformation. Hence, it has been

necessary to make use of indirect methods to study texture development during the deformation of austenite. Assuming a crystallographic relation between the two phases, two types of transformation texture simulations can be differentiated : (i) the austenite ODF can be *untransformed* from the experimental texture of the room temperature structure, (ii) conversely, the austenite rolling texture can be assumed to be similar to the texture produced by cold rolling fcc metals with high stacking fault energies and the simulated ferrite ODF's can then be compared to the experimental observations. In both cases, the description of the known texture can be given by a set of ideal components or, on the contrary, can include the complete ODF. As a result, both discrete and continuous derivations can be carried out.

The present work is concerned with the simulation of transformed textures in steels from both a theoretical and a practical point of view. It is divided into the following chapters.

In Chapter II, the orientation of a monocrystal is defined by a series of sets of parameters and the continuous orientation distribution function (ODF) is introduced in the case of polycrystalline materials. In Chapter III, the theoretical basis of texture transformation studies is described in some detail. The concept of continuous transformation is introduced progressively and ultimately leads to the definition of an orientation transformation function (OTF) which can even take variant selection into account. The most commonly accepted crystallographic relations observed in steels are then presented, accompanied by some symmetry considerations regarding their variants. Finally, discrete and continuous methods are proposed for the simulation of transformation textures. In Chapter IV, a review of experimental transformation textures in steels is presented and the effects of the most influential parameters are discussed. Also, a critical assessment of previous simulations – based on both the discrete and continuous methods – is attempted. In Chapter V, textures of Ni-Co alloys, previously cold rolled to different reductions, are used to simulate austenite textures of comparable stacking fault energy levels and the corresponding bcc ODF's are derived, using the Kurdjumov-Sachs, Nishiyama-Wassermann and Bain transformation laws. The simulated textures are then compared to experimental ones in (i) ferrite in controlled rolled steels, (ii) martensite, and (iii) cold rolled ferrite. The simulation methods and their parameters are also discussed. Finally, in Chapter VI, the general conclusions of the study are drawn and the validity of the predictions is discussed.

CHAPTER II

TEXTURE REPRESENTATION

II.1	ORIENTATION OF INDIVIDUAL CRYSTALS	5
II.1.1	DEFINITION OF AN ORIENTATION	5
	- Reference frame of the specimen	
	- Reference frame of the crystal	
	- Orientation of one crystal within a specimen	
II.1.2	PARAMETERS DEFINING AN ORIENTATION	7
	- Eulerian angles in Euler space	
	- Miller indices	
	- rotation matrix	
	- rotation axis and rotation angle	
	- polar coordinates	
	- relations between the different parameters	
II.1.3	SYMMETRICALLY EQUIVALENT ORIENTATIONS	13
	- the crystal symmetry	
	- the sample symmetry	
	- the combined crystal and sample symmetries	
II.2	THE ORIENTATION DISTRIBUTION FUNCTION	15
II.2.1	DEFINITION AND PROPERTIES	15
	- the statistical function	
	- the normalization condition	
	- consequence of the symmetries	

II.2.2	TWO-DIMENSIONAL REPRESENTATIONS	17
	- the stereographic projection	
	- pole figures	
	- inverse pole figures	
	- comparison of the two types of planar representation	
	- Euler angles on pole and inverse pole figures	
II.2.3	THE FUNDAMENTAL RELATION OF TEXTURE ANALYSIS	22
II.2.4	INVERSION METHODS	22
	- the series expansion method	
	- reference to some other methods	

II.1 ORIENTATION OF INDIVIDUAL CRYSTALS

This section aims at defining an orientation and presenting some of the most commonly used parameters required for its representation.

II.1.1 DEFINITION OF AN ORIENTATION

Above all, the description of an orientation requires the choice of two reference frames -sets of three rectangular coordinates- in connection with the sample and each crystallite respectively. In principle, this choice is arbitrary, but in the particular case of rolled cubic metals, an easy handling of the data can be provided by a judicious selection of these systems.

- Reference frame of the specimen : (K_s)

When the deformation process is *rolling*, there results an external symmetry of the sample which, as shown in Figure 2-1, consists of three mirror planes perpendicular to the rolling, transverse and normal directions, or equivalently of three two-fold axes along these directions.

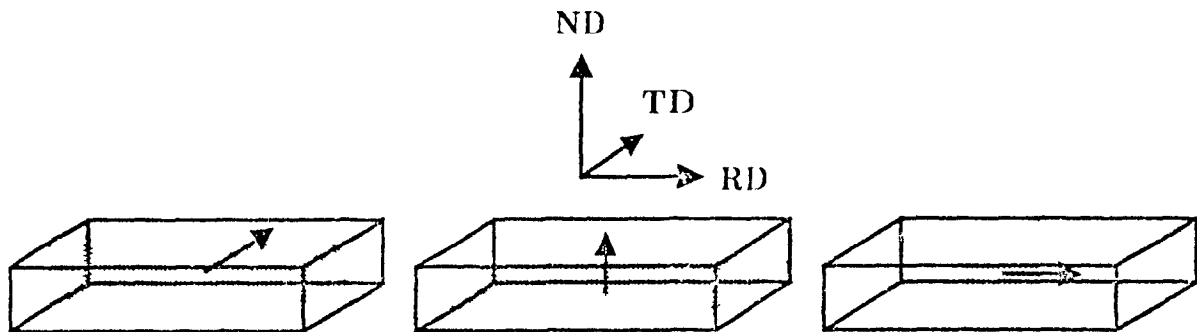


Figure 2-1 : Mirror planes of a rolled sheet.

From now on, the sample coordinate system will thus be chosen with its axes XYZ parallel to the rolling (RD), transverse (TD) and normal (ND) directions, respectively.

- Reference frame of the crystal : (K_c)

The coordinate system of a crystal is selected in agreement with the symmetry of its atomic lattice. For *cubic materials*, the choice of three rectangular cube-edge directions $[100]$, $[010]$, $[001]$ as the coordinate axes $X'Y'Z'$ is the most suitable

- Orientation of one crystal within a specimen :

As a result, the orientation of a crystal will be described by the rotation g which transforms the sample reference frame (K_s) into the crystal reference frame (K_c) as sketched below :

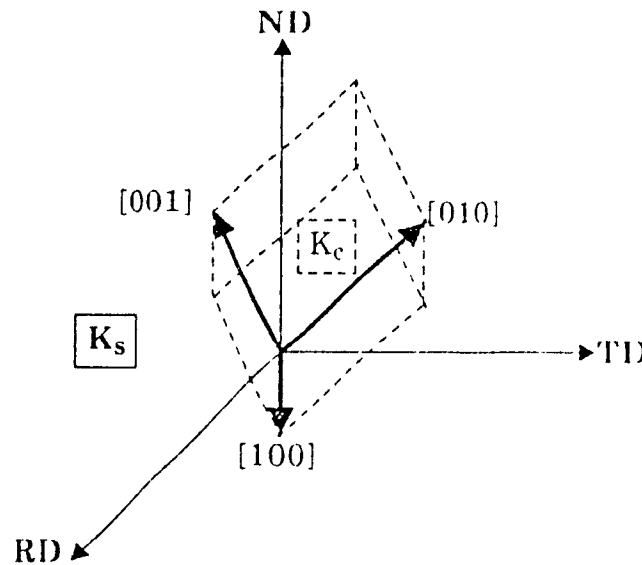


Figure 2-2: Orientation of a given cubic crystal with respect to the reference frame of the rolled specimen

This is written mathematically as

$$K_s \xrightarrow{g} K_c \quad K_c = g \cdot K_s \quad (2.1)$$

making use of the matrix formalism. The vectors of the crystal axes are obtained from the vectors of the sample axes by applying the rotation matrix g to the left hand side. From this viewpoint, the rows of g consist of the coordinates of the crystallographic axes with respect to the axes of the sample. The rotation g may also be defined with the help of different sets of parameters, reviewed in the next paragraph.

II.1.2 PARAMETERS DEFINING AN ORIENTATION

It was decided to restrict the number of representations to those that were used in the computer simulations, which have also tended to become standard [1].

- Eulerian angles in Euler space: $g = (\phi_1, \Phi, \phi_2)$

This description has proved to be especially suited to texture analysis [e.g. 2]. As illustrated for the most general case in Figure 2-3, the crystal system is first assumed to be parallel to that of the specimen (a). The following rotations are then performed successively:

- (b) ϕ_1 about the Z' crystal axis
- (c) Φ about the X' crystal axis
- (d) ϕ_2 about the Z' crystal axis

all possible orientations being obtained within the range:

$$0 \leq \phi_1 \leq 2\pi, 0 \leq \Phi \leq \pi, 0 \leq \phi_2 \leq 2\pi.$$

Although used and recommended by the best known researchers in the field, the set of Euler angles which has been chosen is not unique. Another set, known as Roe's notation [3,4] and defined by (ψ, θ, ϕ) , is also frequently found in the literature and will thus be referred to from time to time for purposes of comparison.

It is convenient to plot these three independent parameters as cartesian coordinates in a three-dimensional space, called orientation space or Euler space in the case of the Euler angles. Generally, the sections ' $\phi_2 = \text{constant}$ ' - simply called the ' ϕ_2 -sections' - are drawn because, in each section, ND remains constant when Φ is unchanged. For steels however, ' ϕ_1 -sections' are sometimes plotted and if the texture is given in terms of single orientations, each crystal orientation appears as one dot in Euler space. This space is however distorted along the Φ axis and the volume element reads

$$dg = \frac{1}{8\pi^2} \sin\Phi \, d\phi_1 \, d\Phi \, d\phi_2 \quad (2-2)$$

In the particular case of rolling, a translation along the ϕ_1 -axis in Euler space is identical to a rotation around the sample ND, while a translation along the ϕ_2 -axis corresponds to a rotation around the [001]-direction of the crystal.

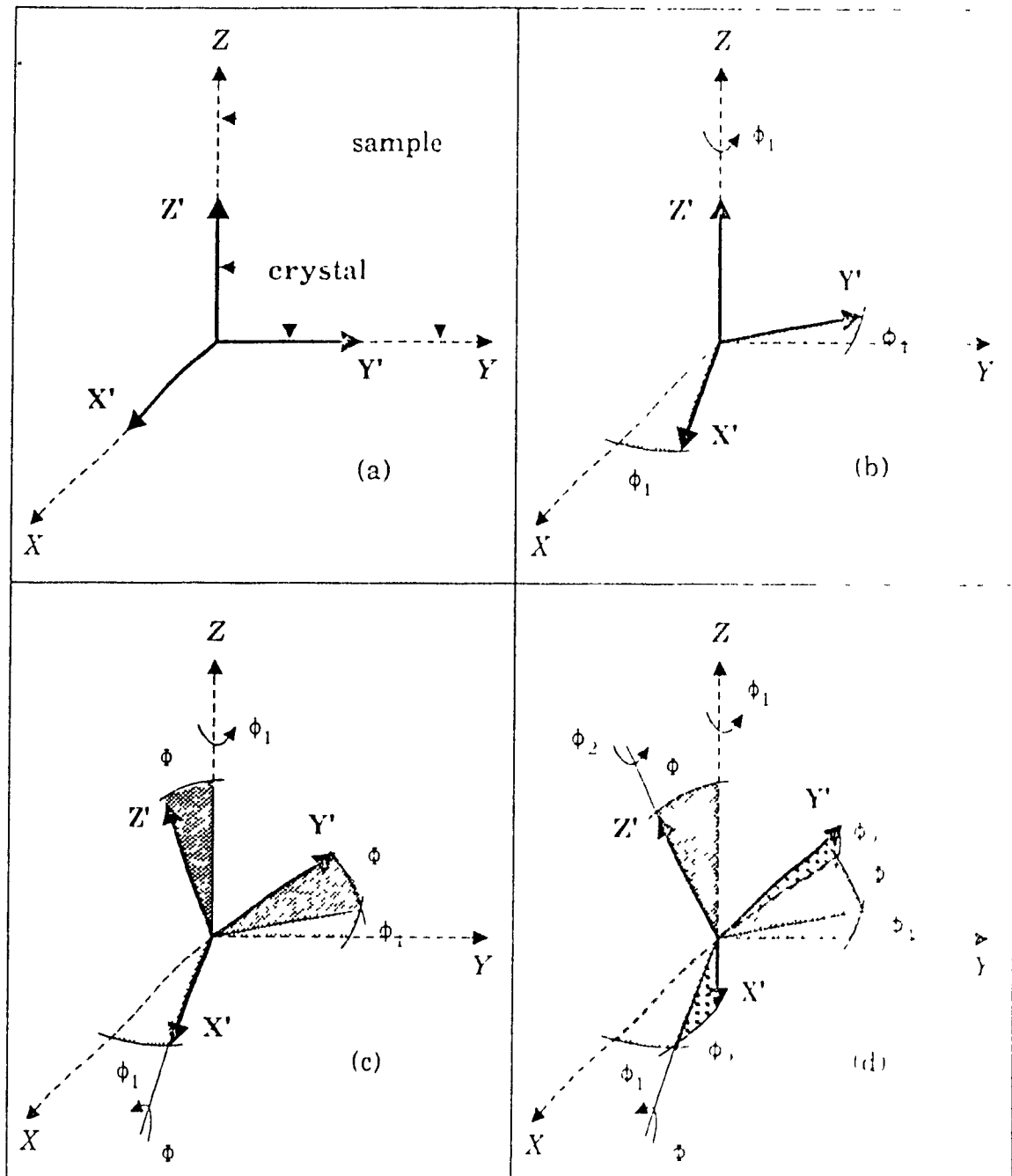


Figure 2-3 : Definition of the Euler angles

- Miller indices: $g = (hkl)[uvw]$

A representation of crystal orientations frequently used in sheets consists of the specification of the Miller indices (hkl) for the crystal plane which lies parallel to the sheet (ND), as well as the indices [uvw] of the crystal direction parallel to the rolling direction (RD).

Two particular cases are worth noting:

- in cubic materials, the indices of a lattice plane and the indices of the direction of its normal are identical (e.g. the normal to the sheet plane coincides with the normal direction),
- after rolling, the sheet plane is the rolling plane.

- rotation matrix: $g = (g_{ij})_{i,j \in \{1,2,3\}^2}$

In a three-dimensional space, a rotation can always be described by a 3×3 matrix, as sketched in Table 2-1. The columns of the matrix g are then equivalently formed from either the cosines of the axes of the initial coordinate system (K_s) with respect to the final reference frame (K_c), or conversely the cosines of the axes of the final coordinate system (K_c) with respect to the initial reference frame (K_s)

$$g = \begin{bmatrix} g_{11} & g_{12} & g_{13} \\ g_{21} & g_{22} & g_{23} \\ g_{31} & g_{32} & g_{33} \end{bmatrix} \quad \begin{array}{l} X' = (100) \\ Y' = (010) \\ Z' = (001) \end{array} \quad K_c$$

$$\begin{array}{ccc} X & Y & Z \\ \hline \text{RD} & \text{TD} & \text{ND} \end{array} \quad K_s$$

Table 2-1 : Matrix representation of g

- rotation axis and rotation angle: $g = \{d, \omega\}$

The rotation axis $d = (d_x, d_y, d_z) = (\theta, \psi)$, where θ and ψ are the polar and azimuthal angles respectively, is unchanged by the rotation, and g may be described as a rotation by an angle ω about the axis d , where ω is defined by:

$$\text{Tr}(g) = g_{11} + g_{22} + g_{33} = 2 \cos \omega + 1 \quad (2-3)$$

where $\text{Tr}(g)$ is the trace of the matrix.

- polar coordinates:

In any sample coordinate system XYZ , a crystal direction hkl can be referenced by two angles (ϕ, γ) , called polar coordinates. Identically, polar angles can be defined for a sample direction D with respect to any crystallographic coordinate system $X'Y'Z'$; these are then noted (ϕ, β) . The two sets of angles are shown in Figures 2-4 (a) and (b).

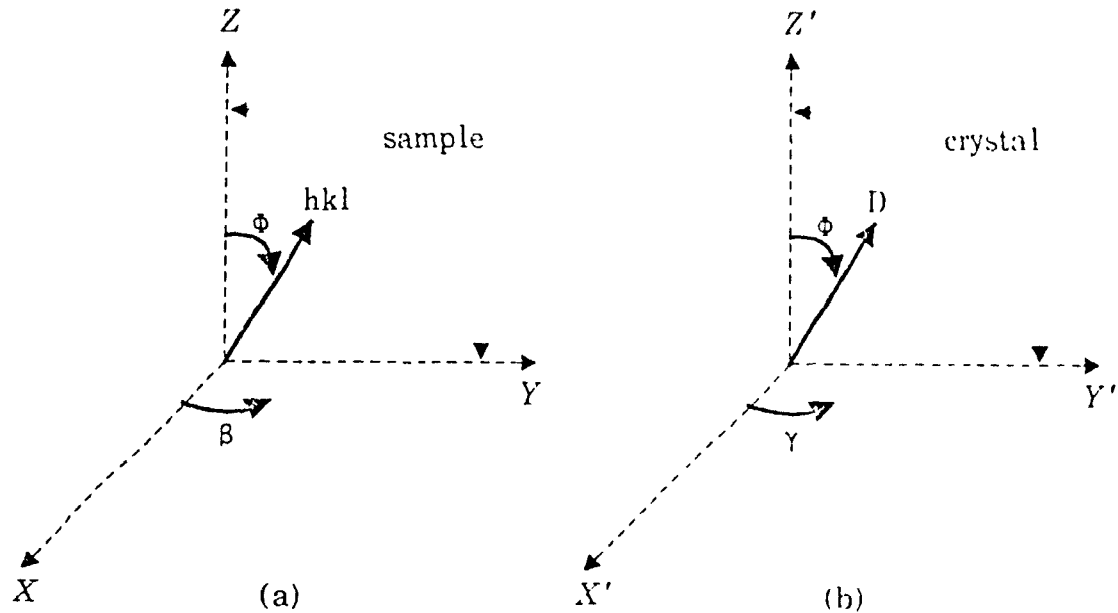


Figure 2-4 : The two sets of polar coordinates : (a) in the sample, (b) in the crystal

As a result, there are two sets of parameters for the definition of an orientation in a rolled cubic material, namely the polar coordinates $\{(\phi_{RD}, \beta_{RD}), (\phi_{TD}, \beta_{TD}), (\phi_{ND}, \beta_{ND})\}$ of RD, TD and ND in the crystal, and the polar coordinates $\{(\phi_{100}, \gamma_{100}), (\phi_{010}, \gamma_{010}), (\phi_{001}, \gamma_{001})\}$ of $[100], [010], [001]$ in the sample.

- relations between the different parameters:

The rotation g consists of three consecutive planar rotations, so that the matrix can be expressed—by simple matrix multiplication—as a function of the Euler angles (Table 2-2).

The Miller notation can easily be related to the Euler angles by setting (hkl) and $[uvw]$ equal to a multiple of the third column (ND) and of the first column (RD) of g respectively, as shown in Table 2-2. One thereby obtains the relations given in Table 2-3.

$$\begin{bmatrix} \cos\phi_1\cos\phi_2 - \sin\phi_1\sin\phi_2\cos\Phi & \sin\phi_1\cos\phi_2 + \cos\phi_1\sin\phi_2\cos\Phi & \sin\phi_2\sin\Phi \\ -\cos\phi_1\sin\phi_2 - \sin\phi_1\cos\phi_2\cos\Phi & -\sin\phi_1\sin\phi_2 + \cos\phi_1\cos\phi_2\cos\Phi & \cos\phi_2\sin\Phi \\ \sin\phi_1\sin\Phi & -\cos\phi_1\sin\Phi & \cos\Phi \end{bmatrix}$$

Table 2-2: The rotation matrix as a function of the Euler angles.

$$\begin{bmatrix} h = n_1 \cdot \sin\phi_2 \sin\Phi \\ k = n_1 \cdot \cos\phi_2 \sin\Phi \\ l = n_1 \cdot \cos\Phi \end{bmatrix} \quad \begin{bmatrix} u = n_2 \cdot (\cos\phi_1\cos\phi_2 - \sin\phi_1\sin\phi_2\cos\Phi) \\ v = n_2 \cdot (-\cos\phi_1\sin\phi_2 - \sin\phi_1\cos\phi_2\cos\Phi) \\ w = n_2 \cdot \sin\phi_1\sin\Phi \end{bmatrix}$$

$$n_1 = (h^2 + k^2 + l^2) \quad n_2 = (u^2 + v^2 + w^2)$$

Table 2-3: $(hkl)[uvw]$ as a function of (ϕ_1, ϕ_2, Φ) .

The rotation matrix can be written with the rotation axis $d = (d_x, d_y, d_z) = (\theta, \psi)$ and the rotation angle ω as orientation parameters, as can be seen in Table 2-4.

$$\begin{bmatrix} (1-d_x^2)\cos\omega + d_x^2 & d_x d_y (1-\cos\omega) + d_z \sin\omega & d_x d_z (1-\cos\omega) - d_y \sin\omega \\ d_x d_y (1-\cos\omega) - d_z \sin\omega & (1-d_y^2)\cos\omega + d_y^2 & d_y d_z (1-\cos\omega) + d_x \sin\omega \\ d_x d_z (1-\cos\omega) + d_y \sin\omega & d_y d_z (1-\cos\omega) - d_x \sin\omega & (1-d_z^2)\cos\omega + d_z^2 \end{bmatrix}$$

Table 2-4: The rotation matrix as a function of $d = (d_x, d_y, d_z)$ and ω .

If ω is chosen between 0 and π , then θ , ψ and ω can be derived from the Euler angles ϕ_1 , ϕ_2 , Φ through the conditions expressed in Table 2-5.

The cartesian coordinates of $d = (d_x, d_y, d_z)$ can be deduced either from the spherical ones (θ, ψ) or directly from the rotation matrix, as expressed in equations 2-4 and 2-5, respectively. Finally, the polar coordinates of a direction either in the crystal or in the sample are related to the three Euler angles by the relations of Table 2-6.

$$\left[\begin{array}{l} \psi = (\phi_1 - \phi_2)/2 \\ \cos(\omega/2) = \cos(\phi/2)\cos(\phi_1 + \phi_2)/2 \quad \text{and} \quad \sin\omega = 0 \\ \sin\theta = \sin(\phi/2)/\sin(\omega/2) \quad \text{and} \quad \cos\theta = \{(1 + \cos\phi)\sin(\phi_1 + \phi_2)\}/2\sin\omega \end{array} \right.$$

Table 2-5: $d = (\theta, \psi)$ and ω as functions of the Euler angles ϕ_1, ϕ, ϕ_2 .

$$d_x = \sin\theta \cos\psi, \quad d_y = \sin\theta \sin\psi, \quad d_z = \cos\theta \quad (2-4)$$

$$\cos\omega = (\text{Tr}(g) - 1)/2 \quad \text{and} \quad \sin\omega = 0 \quad (2-5)$$

$$d_x = (g_{23} - g_{32})/2\sin\omega, \quad d_y = (g_{31} - g_{13})/2\sin\omega, \quad d_z = (g_{12} - g_{21})/2\sin\omega$$

$$\left[\begin{array}{l} \phi_{001} = \phi \\ \phi_{100} = \arccos(\sin\phi_2 \sin\phi) \\ \phi_{010} = \arccos(\cos\phi \sin\phi) \end{array} \right.$$

$$\left[\begin{array}{l} \gamma_{001} = \phi_1 - \pi/2 \\ \gamma_{100} = \arccos(\cos\phi_2 \sin\phi_{100}) + \phi_1 \\ \gamma_{010} = \arccos(\sin\phi_2 \cos\phi_{100}) + \phi_1 \end{array} \right.$$

$$\left[\begin{array}{l} \phi_{ND} = \phi \\ \phi_{RD} = \arccos(\sin\phi_1 \sin\phi) \\ \phi_{1D} = \arccos(-\cos\phi_1 \sin\phi) \end{array} \right.$$

$$\left[\begin{array}{l} \beta_{ND} = \pi/2 - \phi_1 \\ \beta_{PD} = \arccos(\cos\phi_1 \sin\phi_{ND}) + \phi_1 \\ \beta_{1D} = \arccos(\sin\phi_1 \sin\phi_{1D}) + \pi - \phi_1 \end{array} \right.$$

Table 2-6: Polar coordinates of the system axes as functions of (ϕ_1, ϕ, ϕ_2) .

II.1.3 SYMMETRICALLY EQUIVALENT ORIENTATIONS

While the orientation of a crystallite within a specimen has been uniquely defined by the rotation g , the choice of both the crystal and the sample reference frames can often be achieved in many symmetrical indistinguishable ways.

- the crystal symmetry :

Depending on the lattice symmetry, the crystal reference frame can be chosen among equivalent possibilities. In a cubic system, for instance, one can select the coordinate axes through the following procedure depicted in Figure 2-5 :

X : any of the three cube edges along either of the two directions :	6
Y : any of the edges perpendicular to X along either of the two directions :	4
Z : no choice, Z is entirely determined for a right-handed system :	<u>1</u>
resulting number of equivalents :	24

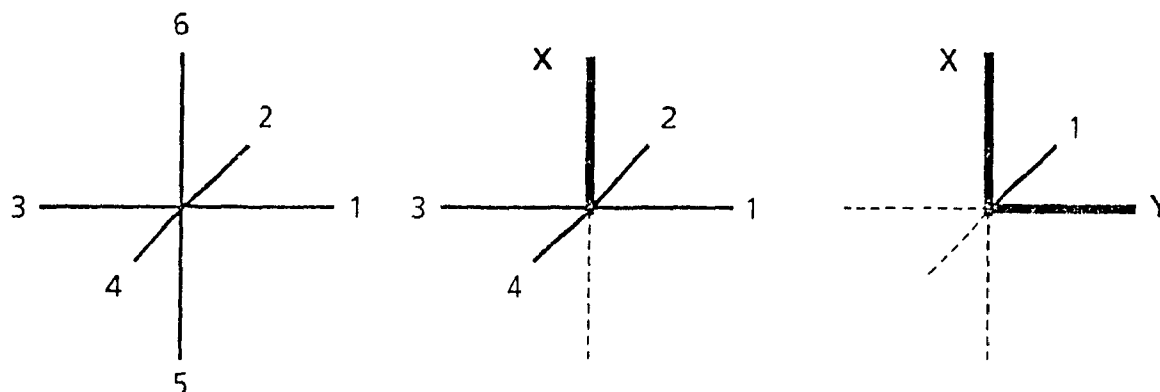


Figure 2-5: Equivalent choices of the crystal reference axes for a cubic system.

These 24 different representations of the same crystallite are related to one another by as many rotations $(S^i_1)_{i \in \{1 \dots 24\}}$ which form the rotational subgroup of the crystal symmetry. Assuming that K_{c_1} was selected to define the orientation g , any of its symmetric equivalents K_{c_i} can be written as $K_{c_i} = S^i_1 \cdot K_{c_1}$, again using the matrix formalism. The transitive theory within the rotational group thus ensures $g_i = S^i_1 \cdot g$. This is sketched in Figure 2-6, where g and g_i are different orientations, which are symmetrically equivalent for the crystal.

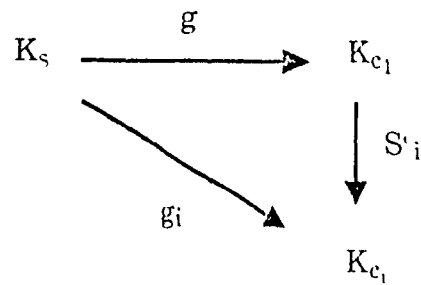


Figure 2-6: Equivalent orientations due to the crystal symmetry.

- the sample symmetry:

In addition to the crystal symmetry, the sample can also exhibit symmetry elements. This is the case in particular after rolling where the rolling, transverse and normal directions are two-fold rotation axes. It means that K_s may be chosen in four different but symmetrically equivalent ways K_{sj} , following Figure 2-7.

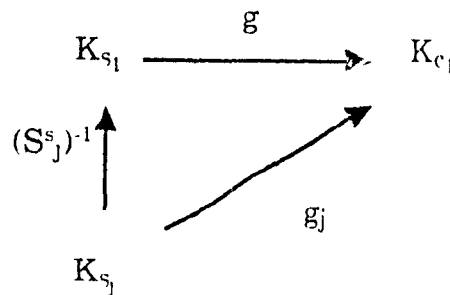


Figure 2-7: Equivalent orientations due to the sample symmetry.

In other words, the orientations $g_j = g.(S_j)^{-1}$, where the S_j 's form the rotational subgroup of the sample symmetry, are symmetrically equivalent

- the combined crystal and sample symmetries:

By simultaneously fulfilling the two kinds of symmetry conditions with respect to a given orientation g , one obtains symmetrically equivalent points in orientation space. The resulting scheme is shown in Figure 2-8 and the equivalents obey the relation

$$g_{ij} = S_i^c \cdot g \cdot (S_j)^{-1} \quad (2-6)$$

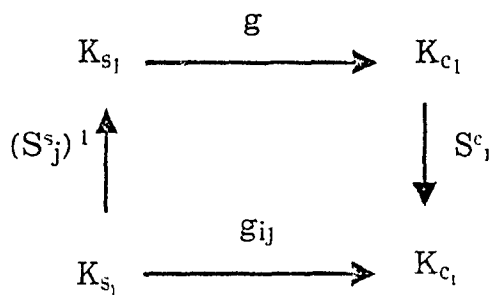


Figure 2-8: Equivalent orientations due to the combined crystal and sample symmetries.

II.2 THE ORIENTATION DISTRIBUTION FUNCTION

To describe completely the crystal orientations of a polycrystalline material with the methods reviewed in section II.1, one would have to specify the orientation g for each geometrical point (x,y,z) of the sample. Such a procedure would be very time consuming and its mathematical treatment generally not practicable. A simpler representation is obtained by considering -in a statistical manner- only the orientation, and not the position, of the volume elements in the sample.

II.2.1 DEFINITION AND PROPERTIES

- the statistical function :

If one denotes by dV the total volume of all the elements which possess the orientation g within the infinitesimal range of orientation dg defined in equation (2-2), and by V the whole sample volume, then the ratio dV/V defines the Orientation Distribution Function $f(g)$ [2] by

$$\frac{dV}{V} = f(g) dg \quad (2-7)$$

From now on, this function $f(g)$ -the ODF- will represent the quantitative definition of preferred orientation. Figure 2-9 shows the ODF representation, in $\phi_2 = \text{constant}$ sections, of a Ni-30Co alloy cold rolled to 95% reduction.

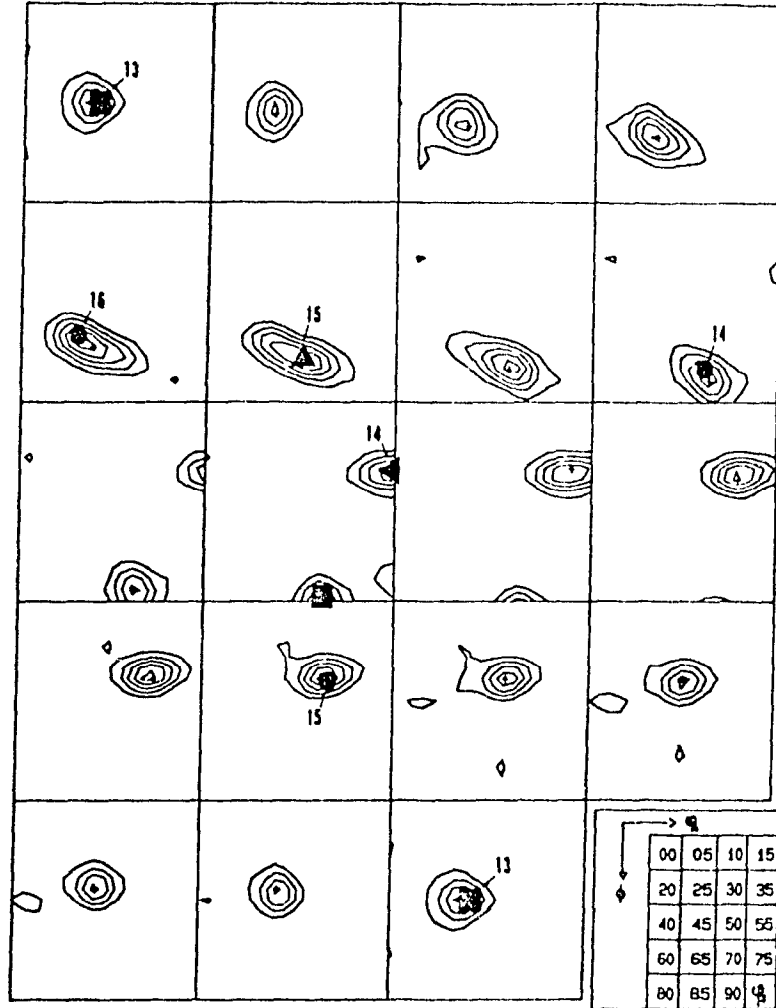


Figure 2-9 : ϕ_2 -section ODF of a Ni-30Co alloy 95% cold rolled.

▶ = {112} < 111 > (Cu) ■ = {110} < 112 > (Bs) ● = {123} < 634 > (S)

- the normalization condition :

In the case of randomly distributed crystals, the above mentioned distribution function is constant and will be assigned the value 1. Hence, the normalization condition reads

$$\int_V f(g) dg = 1 \quad (2-8)$$

- consequence of the symmetries :

The existence of equivalents to a given orientation g , resulting from the crystal and sample symmetry elements and presented in paragraph II.1.3, is translated to the distribution function by a set of conditions to be fulfilled by $f(g)$ which read

$$f(S_i^c \cdot g) = f(g) \quad f(g \cdot S_j^s) = f(g) \quad f(S_i^c \cdot g \cdot S_j^s) = f(g) \quad (2-9)$$

where S_i^c and S_j^s describe the rotational subgroups of the crystal and sample symmetries, respectively.

II.2.2 TWO-DIMENSIONAL REPRESENTATIONS

As already stated above, the ODF can be represented in Euler space—in the ϕ_2 -sections for example—by iso-density lines. It is only recently, however, that such three-dimensional graphs are widely available. Heretofore, only two-dimensional stereographic projections of $f(g)$ have been obtained experimentally, which were easy to handle but had the disadvantage of reproducing only part of the information. These are pole figures and inverse pole figures.

- the stereographic projection :

One considers a reference sphere with a unit radius and with XYZ as its coordinate axes. As illustrated in Figure 2-10, the equatorial plane $P=OXY$ is called the projection plane and $A=(0,0,-1)$ the projection point. The stereographic projection M' of any point M on the reference sphere with respect to the elements (P,A) sits at the intersection of the line AM with the projection plane P . In the next two paragraphs, this method of projection is applied to certain crystal and sample directions to obtain pole figures and inverse pole figures, respectively.

- pole figures :

These are the stereographic projections showing the distribution of particular crystallographic directions $\langle uvw \rangle$, of the assembly of grains, in the rolling plane (RD,TD).

Symmetry requirements for cubic crystals are such that a particular orientation can be described by three $\{100\}$ poles, four $\{111\}$ poles, six $\{110\}$ poles, twelve $\{hk0\}$ poles or twenty four $\{hkl\}$ poles. The simplest pole figures will be those depicting the distribution of planes with the lowest multiplicity : $\{100\}$, $\{110\}$, $\{111\}$ and sometimes

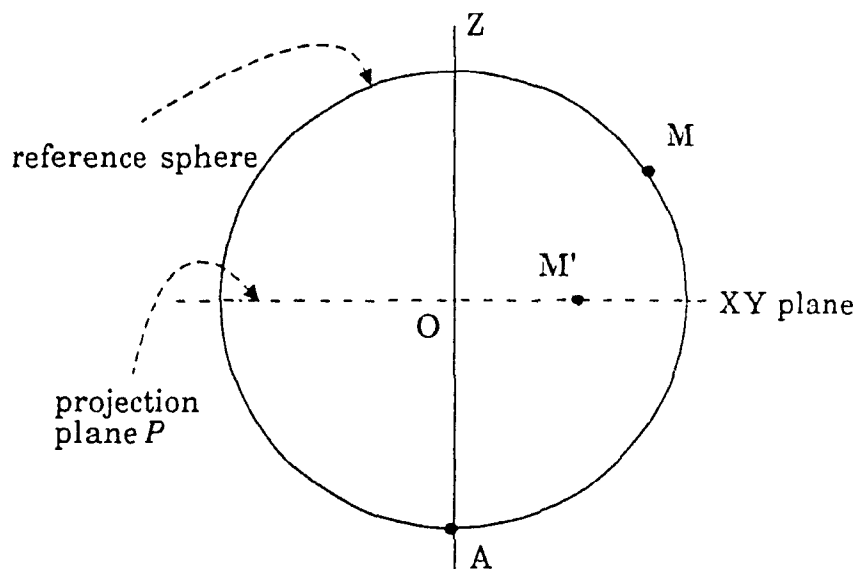


Figure 2-10 : Stereographic projection.

$\{211\}$ planes. Since it is usual to refer to the pole figure in terms of the measured reflections, bcc textures are described by (110), (200), (112), (222), etc. pole figures, while fcc textures are interpreted on the basis of (111), (200), and (220) pole figures. There is no difference between pole figures from the first and second order reflections as the poles are identical for the two cases. As an illustration, the so-called (100) pole figure is sketched for one crystal in Figure 2-11.

In a textured material, the poles tend to cluster together in certain areas of the pole figure and can be presented in the form of equal-density contours in the same manner as for CDF sections. The density values are expressed relative to that for a specimen having a random orientation. Contour levels greater than $1\times$ random imply a concentration of poles and those less than $1\times$ random a depletion of the directions concerned. If a correct average is taken over the whole pole figure, the mean density of poles must be 1 since the total number of poles in an aggregate is unchanged by the existence or the degree of texture. Finally, it is worth recalling that the pole figures of rolled materials have four equivalent quadrants, since the planes normal to RD and TD are reflection planes of symmetry. Figure 2-12 (a) shows the 200 pole figure of the Ni-Co alloy of Figure 2-9.

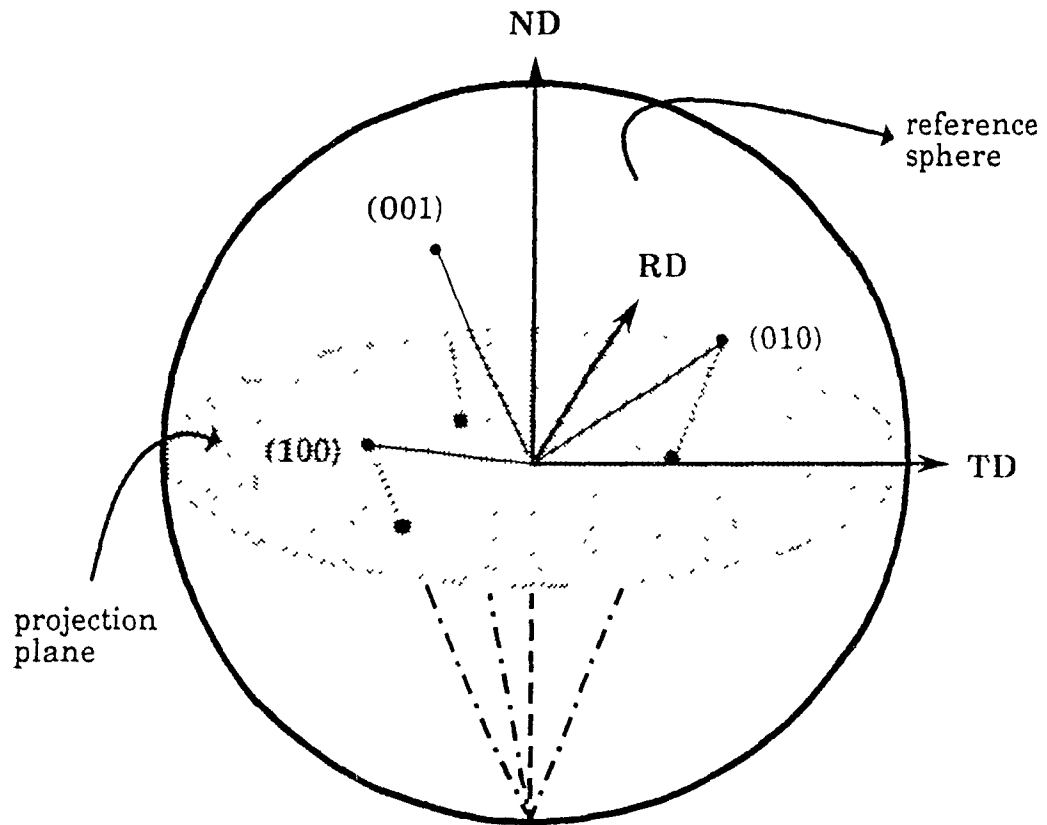


Figure 2-11 : Projection in the rolling plane of the three (100) poles of a cubic crystal.

- inverse pole figures :

These are the stereographic projections showing the distribution of any of the sample directions (ND, RD, TD...) in the crystallographic frame. The standard triangle of the cubic lattice, which contains all the information of the inverse pole figure, is shown in Figure 2-13 :

These are particularly useful for the representation of fibre textures, for which the specification of a single inverse pole figure can describe the texture in a satisfactory way. Figure 2-12 (b) shows the ND inverse pole figure of the alloy of Figure 2-9.

- comparison of the two types of planar representation :

The two kinds of figure are two-dimensional projections of the ODF $f(g)$, so that neither can be used to derive the frequency of a specific crystal orientation. The major advantage of pole figures consists of their direct measurability, by X-ray diffraction for instance; whereas that of inverse pole figures resides in their important role in the

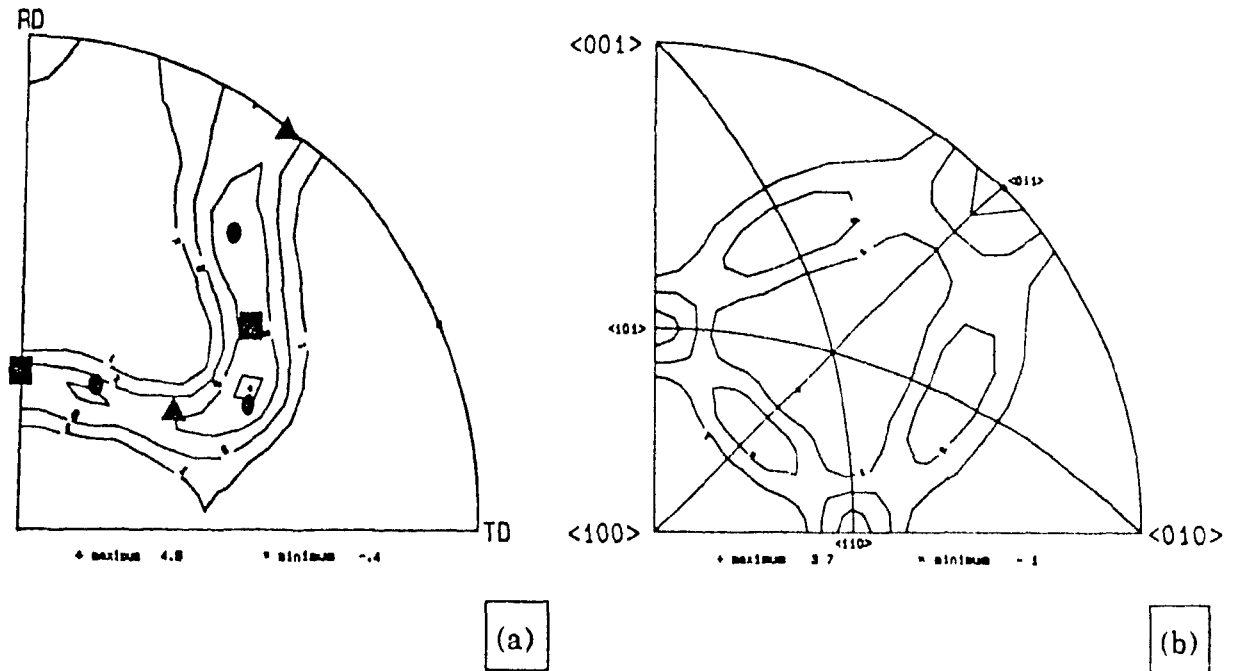


Figure 2-12: (a) : 200 pole figure (b) : ND inverse pole figure
of a Ni-30Co alloy 95% cold rolled.

▲ = {112} <111> (Cu) ■ = {110} <112> (Bs) ● = {123} <634>

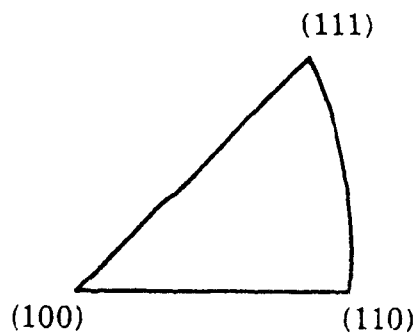


Figure 2-13: Standard triangle for the cubic system.

estimation of the physical properties of the polycrystal. A limited texture study might therefore aim at calculating inverse pole figures from pole figures.

Besides, for cubic-orthorhombic systems (e.g. rolled cubic metals), the resolving power of a representation by pole figures is higher than that by an equal number of inverse pole figures [2].

- Euler angles on pole and inverse pole figures :

The stereographic projections of an orientation, represented by its set of three Euler angles, in the sample and crystal reference frames, are found in Figures 2-14(a) and 2-14(b), respectively [2].

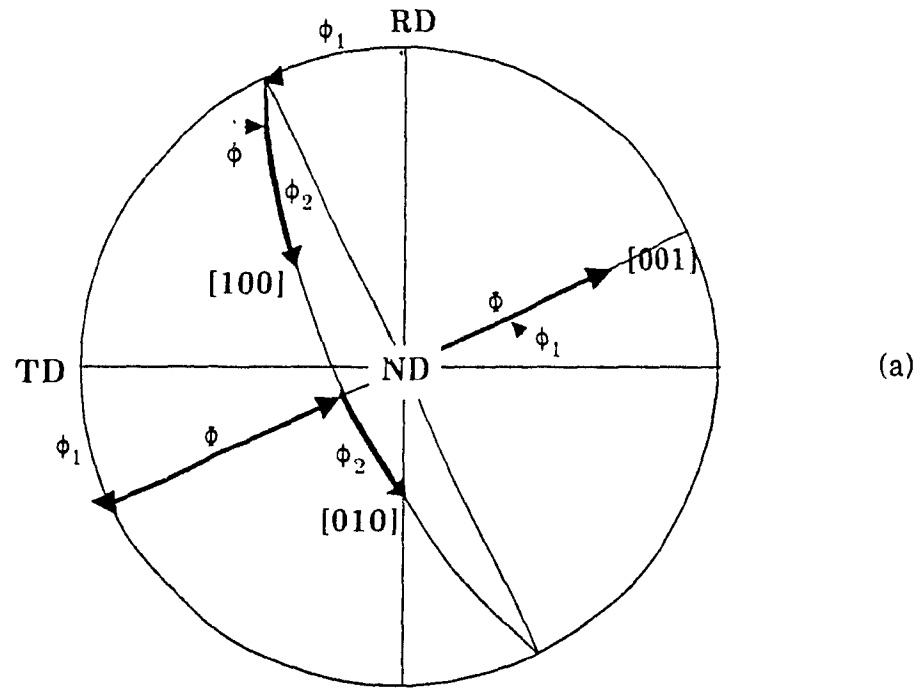


Figure 2-14 (a) : Representation of Euler angles on a pole figure, after [2].

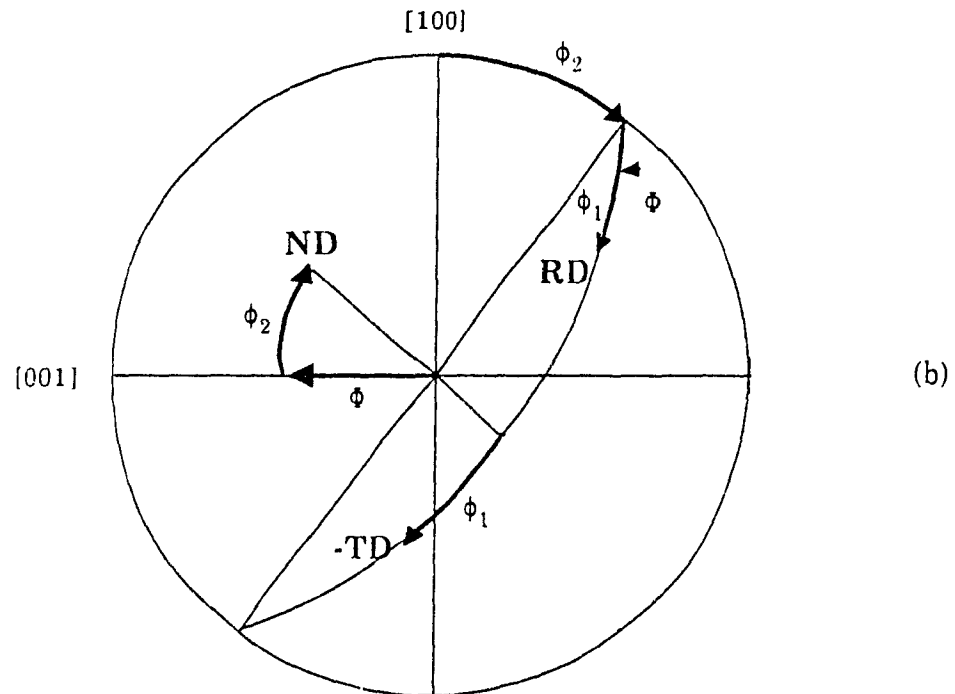


Figure 2-14 (b) : Representation of Euler angles on an inverse pole figure, after [2].

II.2.3 THE FUNDAMENTAL RELATION OF TEXTURE ANALYSIS

Since, in general, pole figures are the experimental data, it is essential to derive a relation which will enable the calculation of an ODF from these measurements. A pole figure is the angular distribution function of a chosen crystal direction h with respect to the sample reference frame K_s . It is defined by the volume fraction dV/V of crystals having their h directions parallel to the y sample direction :

$$\frac{dV}{V} = \frac{1}{4\pi} P_h(y) dy, \quad (2-10)$$

with the normalization equation :

$$P_h(y)_{random} = 1, \quad \int_V P_h(y) dy = 4\pi \quad (2-11)$$

The pole density then appears to be an integral of the ODF, $f(g)$, taken over a certain path -defined by the condition $h // y$ - in Euler space :

$$P_h(y) = \frac{1}{2\pi} \int_{h//y} f(g) dy \quad (2-12)$$

The inversion of this relation, which leads to the practical definition of the ODF, is the subject of the next paragraph.

II.2.4 INVERSION METHODS

These are the methods for the determination of the ODF from pole figure measurements by resolution of the above mentioned fundamental relation. This presentation will be restricted to the series expansion method, simultaneously developed by Roe [3] and Bunge [5] in 1965. Some other methods will also be referenced.

- the series expansion method:

Notations and formalism are those proposed by Bunge [2]. A function $f(g)$ can be developed in a series of generalized spherical harmonics $T_l^{mn}(g)$:

$$f(g) = \sum_{l=0}^{\infty} \sum_{m=-l}^{+l} \sum_{n=-l}^{+l} C_l^{mn} T_l^{mn}(g) \quad (2-13)$$

where the $T_l^{mn}(g)$ -if expressed by means of the Euler angles (ϕ_1, ϕ, ϕ_2) - are related to the generalization of the associated Legendre functions $P_l^{mn}(\phi)$ by :

$$T_l^{mn}(\phi_1, \phi, \phi_2) = e^{im\phi_2} P_l^{mn}(\phi) e^{in\phi_1} \quad (2-14)$$

where C_l^{mn} are numerical coefficients and $P_l^{mn}(\phi)$ is a mathematical function of ϕ .

In the series expansion, the symmetry conditions can be taken into account by introducing symmetric harmonics $\ddot{T}_l^{\mu\nu}(g)$, linear combinations of the classical functions $T_l^{mn}(g)$, in which the right-hand single dot "." denotes the sample symmetry and the left-hand double dot ":" the crystal symmetry, sometimes also referenced by a triple dot "::" when more than one type of crystal is at stake. The corresponding $C_l^{\mu\nu}$ coefficients completely describe the ODF and are also related to the pole density in the y direction, $P_h(y)$, in the h pole figure by :

$$P_h(y) = \sum_{l=0}^{\infty} \sum_{n=1}^{N(l)} \sum_{\mu=1}^{M(l)} \frac{4\pi}{2l+1} C_l^{\mu\nu} \dot{k}_l^{\mu}(h) \dot{k}_l^{\nu}(y) \quad (2-15)$$

where $k_l^{\mu}(h)$ and $k_l^{\nu}(y)$ are the so-called symmetric spherical surface harmonics.

The coefficients of the pole figure are proportional to those of the ODF, so that the $C_l^{\mu\nu}$ can be determined in this way. A detailed study of this derivation, its limitations and the evaluation of the errors can be found, for example, in reference [2].

- references to some other methods :

There exist five other methods for the inversion of the fundamental relation. These have not been employed as universally as the series expansion method and have not been used in the present study. The following are references to the initial work on each method :

- the vector method introduced by Ruer [6] in 1976 and improved by Vadon [7] in 1981,
- the inversion formula presented by Matthies [8] in 1979 and Muller *et al.* [9] in 1981,
- the probabilistic method developed by Imhof [10] in 1977 and Starkey [11] in 1983.
- the discretization method of Williams [12] in 1968.
- the Gaussian method [13].

CHAPTER III

PRINCIPLES OF TEXTURE TRANSFORMATION

III.1	REPRESENTATION OF THE TRANSFORMATION	27
III.1.1	THE MATRIX FORMULATION	27
III.1.2	A PROGRESSIVE APPROACH	28
	<ul style="list-style-type: none">- from the monocrystal to the polycrystal- a unique orientation relationship- a unique family of equivalent orientation relationships- several families of orientation relationships- non-strict orientation relationships- schematic evolution of the models- different probabilities for equivalent orientation relationships	
III.2	TRANSFORMATION LAWS	33
III.2.1	EXPRESSION OF THE TRANSFORMATION	33
	<ul style="list-style-type: none">- as conditions of parallelism- as a rotation	
III.2.2	THE MOST COMMONLY ACCEPTED RELATIONSHIPS	34
	<ul style="list-style-type: none">- the Bain relationship- the Kurdjumow-Sachs relationship- the Nishiyama-Wassermann relationship- the Greninger-Troiano relationship- the Pitsch relationship- their relative positions in Euler space- the limitations of crystallographic relations	

III.2.3	REPRESENTATIONS OF A TRANSFORMATION LAW	38
-	the three-dimensional orientation transformation function	
-	two-dimensional stereographic projections	
III.3	SYMMETRY CONSIDERATIONS	41
III.3.1	VARIANTS OF A TRANSFORMATION LAW	41
-	definition and vocabulary	
-	graphical illustration of the definition of variants	
-	the two practical ways of determining the variants	
-	the two ways to take the γ -symmetry into account	
-	independence from the sample reference frame	
-	B, KS and NW variants	
III.3.2	VARIANT SELECTION CRITERIA	49
-	the shape deformation model	
-	the Bokros-Parker model	
-	the active slip system models	
-	the twinning shear model	
-	the Bain strain model	
-	the GP model	
III.4	METHODS OF SIMULATION	53
III.4.1	DISCRETE METHODS	53
-	determination of the α -orientations inherited from one γ component	
-	determination of the γ -orientations leading to one α component	
-	the ideal orientation method	
-	ODF decomposition methods	

III.4.2 A CONTINUOUS METHOD: THE SERIES EXPANSION

56

- principles of the series expansion method
- a unique orientation relationship
- a unique family of equivalent orientation relationships
- several families of relationships
- non-strict orientation relationships
- different probabilities for equivalent orientation relationships
- calculation of the α texture
- calculation of the γ texture
- calculation of the transformation coefficients

III.1 REPRESENTATION OF THE TRANSFORMATION

When restricted to the study of the evolution of orientations, phase transformation essentially operates through a rotation of the original grains towards their final positions. The matrix formulation of such orientation modification will now be introduced, as well as a progressive approach to transformation modeling, applied to textured materials defined by their ODF's.

III.1.1 THE MATRIX FORMULATION

Provided that the two lattices are centro-symmetric, when a phase transition transforms one grain of the initial austenite, of orientation g^γ , into one final α -grain, of orientation g^α , the two orientations g^γ and g^α can be related to one another through a rotation Δg , named the transformation relationship, as represented schematically in Figure 3-1 :

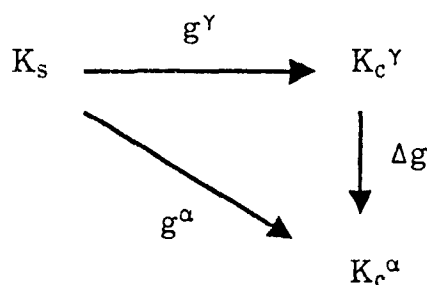


Figure 3-1 : Definition of the transformation.

The following simple relation between the three quantities can thus be derived :

$$g^\alpha = \Delta g \ g^\gamma \quad \text{or} \quad g^\gamma = \Delta g^{-1} \ g^\alpha \quad (3-1)$$

The conventional notation for matrix products will be used throughout this text so that, in the above equation, the orientation g^α is obtained by first carrying out the rotation g^γ and then the rotation Δg . It is also worth noting that, as a rotation, Δg can be represented by the same parameters as those defined in paragraph II.1.2 for a given orientation (Euler angles, rotation matrix, rotation axis and rotation angle, etc.). In particular, the rows of the rotation matrix are defined by the direction cosines of the reference axes of the α -crystal with respect to those of the γ -crystal.

III.1.2 A PROGRESSIVE APPROACH

Equation (3-1), although fundamental, only treats the ultra-simplified case of one unambiguously transformed monocrystal. Reality is much more complex and deals with polycrystals transformed through a continuous spectrum of rotations. After Esling et al. [14], the preceding formulation can be progressively extended to the most general case.

- from the monocrystal to the polycrystal :

This primary step, which has already been covered in Chapter II, results in the introduction of a continuum of orientations represented by the ODF $f(g)$. The texture of the initial polycrystal is thus described by its ODF $\check{f}^\gamma(g^\gamma)$, which satisfies the double invariance of the sample symmetry on the right-hand side and of the disappearing phase on the left-hand side, respectively denoted by "." and ":" on the function.

In the same manner, the textured final phase can also be defined by its ODF $\check{f}^\alpha(g^\alpha)$, where the crystal symmetry ":" of the product might *a priori* be different from that of the parent ":", while the sample symmetry "." is conserved.

- a unique orientation relationship :

The coordinate system K_c^γ of every pre-transformation crystal undergoes the same rotation Δg as the one presented in Figure 3-1, thus involving a modification of the coordinate system rather than a real texture change. Nevertheless, the transformed ODF is related to the initial function by

$$\check{f}^\alpha(g^\alpha) = \check{f}^\gamma(g^\gamma) \quad (3-2)$$

with

$$g^i = \Delta g^{-1} \cdot g^\alpha$$

- a unique family of equivalent orientation relationships

In paragraph II.1.3, the orientations g_{ij} , symmetrically equivalent to a given orientation g with respect to the sample and crystal symmetries, were defined. Similarly, during the phase change, the symmetries of the lattices of the two crystals are taken into account through their respective rotational subgroups $(S_{ij}^\gamma)_{i=1 \dots N^\gamma}$ and $(S_{ij}^\alpha)_{i=1 \dots N^\alpha}$, where N^γ and N^α are the number of symmetry elements in the γ and α crystals, respectively. As with the g and g_j orientations, equivalent

considerations regarding Δg lead to the definition of a family of symmetrically equivalent transformation rotations Δg_{ij} defined by $\Delta g_{ij} = S^{\alpha_i} \cdot \Delta g \cdot (S^{\gamma_j})^{-1}$. This relation is illustrated in Figure 3-2, which is based on the same principle as Figure 2-7. The Δg_{ij} are often called the variants of the transformation law.

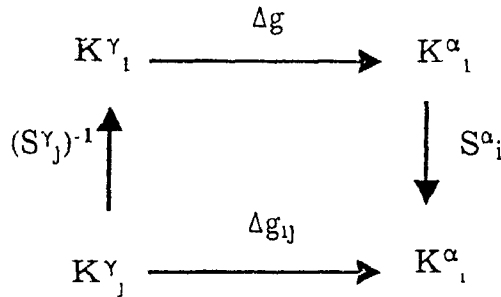


Figure 3-2 : Definition of the symmetrically equivalent transformation rotations.

Correspondingly, the relation between the two ODF's is modified as follows :

$$\dot{f}^{\alpha}(g^{\alpha}) = \frac{1}{N^{\gamma}N^{\alpha}} \sum_{j=1}^{N^{\gamma}} \sum_{i=1}^{N^{\alpha}} \dot{f}^{\gamma}(g^{\gamma}) \quad (3-3)$$

with g^{γ} taking the values

$$g^{\gamma} = \Delta g_{ij}^{-1} g^{\alpha} \quad (3-4)$$

where the different rotations occur with an equal probability $1/N^{\gamma}N^{\alpha}$.

However, the $N^{\gamma}N^{\alpha}$ rotations may not all be different and the number k of distinct rotations defines the *multiplicity* of the orientation relationship, which can be significantly lower than $N^{\gamma}N^{\alpha}$. See also paragraph III.3.1.

- several families of orientation relationships :

Two or more crystallographically distinct orientation relations may describe a given phase transformation, in general with different frequencies of occurrence W_i . For two such relations, distinguished by the suffixes (1) and (2), equations (3-3) and (3-4) are generalized as follows :

$$\dot{f}^{\alpha}(g^{\alpha}) = \frac{1}{N^{\gamma}N^{\alpha}} \sum_{j=1}^{N^{\gamma}} \sum_{i=1}^{N^{\alpha}} [W_1 \dot{f}^{\gamma}(g_1^{\gamma}) + W_2 \dot{f}^{\gamma}(g_2^{\gamma})] \quad (3-5)$$

with g_1^γ and g_2^γ running through

$$g_1^\gamma = (\Delta g_{ij}^1)^{-1} g^a \quad \text{and} \quad g_2^\gamma = (\Delta g_{ij}^2)^{-1} g^a \quad (3-6)$$

- non-strict orientation relationships:

The Δg_k 's described above correspond to ideal values which are not generally strictly respected in the polycrystal. The stresses between neighboring grains, constraints regarding the occupation of space and the plastic strain accompanying the phase change in polycrystals create slight deviations from the ideal values, thus leading to a continuous probability distribution of the Δg 's around the Δg_k 's. The stricter the orientation relationship, the smaller the peak width. This continuous function has been named the MisOrientation Distribution Function (MODF) by Bunge [15] for the study of recrystallization, or the Orientation Transformation Function (OTF) by Sargent [16], and is generally denoted as $\dot{W}(\Delta g)$. The changeover from the discrete to the continuous case leads to a new type of equation where a convolution integral replaces the summation, so that equation (3-5) is changed to .

$$\dot{f}^a(g^a) = \int_{\Delta g} \dot{W}(\Delta g) \dot{f}^\gamma(g^\gamma) d\Delta g \quad \text{with} \quad g^\gamma = \Delta g^{-1} g^a \quad (3-7)$$

While the variable Δg varies continuously within orientation space, the MODF $\dot{W}(\Delta g)$ attains significant levels only in the vicinity of certain values of Δg . As for any probability function, a normalization condition must be assumed for $\dot{W}(\Delta g)$:

$$\int_{\Delta g} \dot{W}(\Delta g) d\Delta g = 1 \quad (3-8)$$

It will be shown in paragraph III.3.1 that the symmetry of the decaying phase can be omitted on the right-hand side of the orientation transformation function, so that equation (3-7) can be rewritten in the form

$$\dot{f}^a(g^a) = \int_{\Delta g} \dot{W}(\Delta g) \dot{f}^\gamma(g^\gamma) d\Delta g \quad \text{with} \quad g^\gamma = \Delta g^{-1} g^a \quad (3-9)$$

where $\dot{W}(\Delta g)$ is no longer symmetrical with respect to the gamma phase, but still fulfills the alpha symmetry conditions on the left-hand side

- schematic evolution of the models :

A schematic illustration of the preceding approaches is given [14] in Figure 3-3, which shows the progressive improvement of the models.

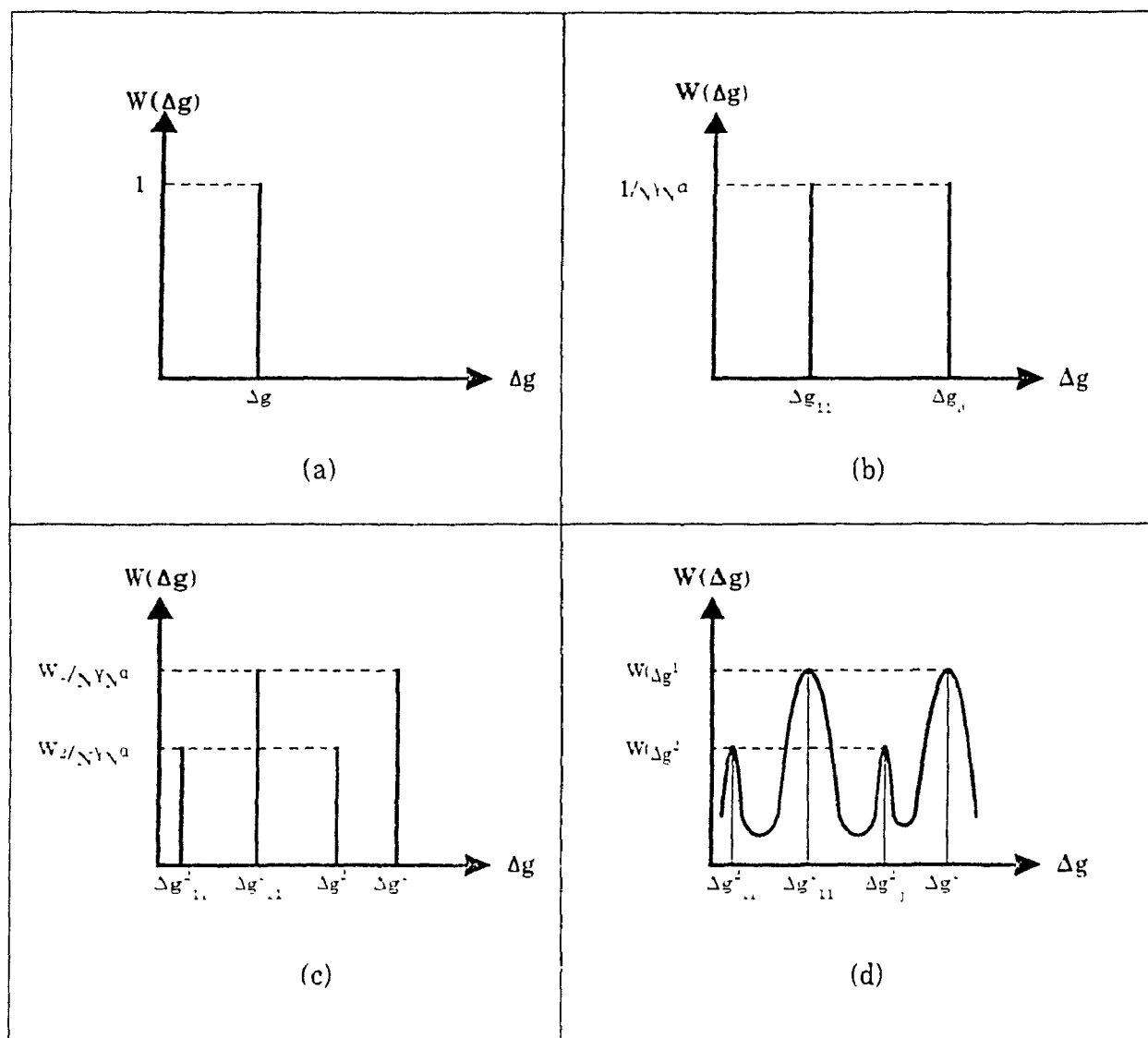


Figure 3-3: Schematic illustration of the progressive modeling approach :

- (a) a unique relationship, (b) a unique family of equivalent variants,
- (c) several families of equivalent variants, (d) non-strict relationships.

- different probabilities for equivalent orientation relationships

Although crystallographically indistinguishable, equivalent orientations g^i must be considered as distinct starting orientations for the variants of an orientation relationship. The ODF intensity of the new phase can thus be assumed to be proportional to an additional factor, termed the Variant Selection Function (VSF) and noted $\dot{v}(g^i)$ [17,18], which depends on the orientation of the disappearing phase but does not obey its symmetry. In other words, for two equivalent orientations g^i and g^j , $\dot{v}(g^i)$ and $\dot{v}(g^j)$ might have different values. The equation of the transformation then turns into its most general expression

$$\dot{f}^n(g^a) = \int_{\Delta g} \dot{W}(\Delta g) \dot{v}(g^i) \dot{f}^i(g^i) d\Delta g \quad \text{where } g^i = \Delta g^{-1} g^a \quad (3-10)$$

From the normalization conditions (2-8) and (3-8), $\dot{v}(g)$ satisfies the relation

$$\int_g \dot{v}(g) dg = 1 \quad (3-11)$$

Because the variant selection function is difficult to model and to define numerically, this step remains one of the most difficult in the interpretation and simulation of transformation textures. The experimental establishment and the consequences of variant selection will be dealt with in section IV 4. and some models and criteria presented in paragraph III.3.2.

In the course of the phase change, it appears that one crystal generally splits up into several final crystallites because various parts of the same initial crystal may transform according to different orientation relationships Δg . This dispersal leads to a decrease in the sharpness of the texture, the crystals being distributed over a greater number of orientations.

III.2 TRANSFORMATION LAWS

Solid-state phase transformations sometimes follow certain crystallographic laws, usually determined by accurate measurements of X-ray or electron diffraction spectra. Historically, several relationships as well as possible mechanisms have been proposed for the γ -to- α transformation in steels and iron-based alloys. The most commonly accepted relations are reviewed below. In addition, their two- and three-dimensional representations are introduced on the model of those defined for the orientation distribution function.

III.2.1 EXPRESSION OF THE TRANSFORMATION

A crystallographic relationship may be represented either by a rotation of the lattice or by conditions of parallelism between planes and/or directions of the two phases.

- as conditions of parallelism :

The usual way to specify an orientation relationship is to relate crystallographic planes and/or directions of the two phases by parallelism conditions, so that, for cubic lattices, it is generally expressed in terms of the Miller indices of

- either two families of planes :

$$\left| \begin{array}{l} (h_1 \ k_1 \ l_1) // (h'_1 \ k'_1 \ l'_1) \\ (h_2 \ k_2 \ l_2) // (h'_2 \ k'_2 \ l'_2) \end{array} \right. \quad (3-12)$$

- or one family of planes and one family of directions (often contained in the latter planes):

$$\left| \begin{array}{l} (h \ k \ l) // (h' \ k' \ l') \\ [u \ v \ w] // [u' \ v' \ w'] \end{array} \right. \quad (3-13)$$

which coincide in the two phases.

- as a rotation :

Practically, it is necessary to define the rotation Δg which brings the parent lattice in coincidence with that of the phase resulting from the above relations. As

already mentioned, such a rotation may be represented by -for instance- its three Euler angles $\Delta g = (\Delta\phi_1, \Delta\phi, \Delta\phi_2)$ or its axis and angle $\Delta g = (\mathbf{d}, \Delta\omega)$. Using $\Delta g = (\mathbf{d}, \Delta\omega)$, a crystal of the disappearing phase is transformed into a crystal of the product phase by a rotation of angle $\Delta\omega$ around the axis \mathbf{d} , which thus remains unchanged during the transformation. Besides, the reverse transformation Δg^{-1} can be obtained from the parameters of the direct transformation by :

$$\Delta g^{-1} = (\pi - \Delta\phi_1, \Delta\phi, \pi - \Delta\phi_2) = (\mathbf{d}, -\Delta\omega) \text{ and its matrix is the transpose of } \Delta g.$$

III.2.2 THE MOST COMMONLY ACCEPTED RELATIONSHIPS

The most commonly referenced transformations laws occurring in steels are presented below in chronological order of their appearance. Their characteristic data are gathered in Table 3-1 at the end of this section. The corresponding mechanisms will, however, not be reviewed here.

- the Bain relationship :

Introduced in 1924 by E.C. Bain [19] as a result of the mechanism he proposed for the martensitic transformation in steels, it reads :

$$\begin{vmatrix} (100)_\gamma & // & (100)_\alpha \\ (011)_\gamma & // & (001)_\alpha \end{vmatrix} \quad (3-14a)$$

or as a rotation :

$$\Delta g = (45^\circ, 0^\circ, 0^\circ) = ((100), 45^\circ) \quad (3-14b)$$

- the Kurdjumow-Sachs relationship :

By far the most "popular" is the relationship stated by G. Kurdjumow and G. Sachs [20] in 1930 for steels containing 1.4% C.

$$\begin{vmatrix} (111)_\gamma & // & (110)_\alpha \\ (1\bar{1}0)_\gamma & // & (1\bar{1}1)_\alpha \end{vmatrix} \quad \text{or equivalently} \quad \begin{vmatrix} 111_\gamma & // & 110_\alpha \\ 112_\gamma & // & 1\bar{1}2_\alpha \end{vmatrix} \quad (3-15a)$$

or as a rotation :

$$\Delta g = (84.23^\circ, 48.19^\circ, 84.23^\circ) = ((112), 0^\circ) \quad (3-15b)$$

- the Nishiyama-Wassermann relationship:

Z. Nishiyama [21,22] and G. Wassermann [23] simultaneously, but independently, introduced a slightly different crystallographic law for an iron alloy containing 30% Ni:

$$\begin{vmatrix} (111)_\gamma // (110)_\alpha \\ [1\bar{1}0]_\gamma // [001]_\alpha \end{vmatrix} \quad \text{or equivalently} \quad \begin{vmatrix} (111)_\gamma // (110)_\alpha \\ [11\bar{2}]_\gamma // [1\bar{1}0]_\alpha \end{vmatrix} \quad (3-16a)$$

or as a rotation:

$$\Delta g = (80.26^\circ, 48.19^\circ, 45^\circ) \quad (3-16b)$$

which cannot be interpreted as a rotation about an integral direction of the crystal. Analytically, it can however be expressed as a 95.27° rotation around the axis defined by $h = -1 + \sqrt{2} + \sqrt{3}$, $k = 1 + \sqrt{2} + \sqrt{3}$ and $l = \sqrt{2}$.

- the Greninger-Troiano relationship:

Studying a steel with 22% Ni and 0.8% C, A. Greninger and A. Troiano [24] concluded that the relationship could be described as about midway between those stated by Kurdjumow-Sachs and Nishiyama-Wassermann

$$\langle 110 \rangle_\gamma [11\bar{1}]_\alpha \approx 25^\circ \quad \text{and} \quad \langle 112 \rangle_\gamma [10\bar{1}]_\alpha \approx 2^\circ \quad (3-17)$$

with conditions on the high index planes and directions. They also concluded that both underlying transformation theories were untenable.

- the Pitsch relationship:

For thin films of iron-nitrogen and iron-carbon alloys, W. Pitsch [25] established the following relation

$$\begin{vmatrix} (110)_\gamma // (112)_\alpha \\ [\bar{1}10]_\gamma // [11\bar{1}]_\alpha \end{vmatrix} \quad \text{or equivalently} \quad \begin{vmatrix} (110)_\gamma // (112)_\alpha \\ [001]_\gamma // [\bar{1}10]_\alpha \end{vmatrix} \quad (3-18a)$$

or as a rotation:

$$\Delta g = (80.40^\circ, 45.82^\circ, 13.64^\circ) \quad (3-18b)$$

- their relative positions in Euler space:

If interpreted, in Euler space, in terms of a rotation with respect to the reference frame of the γ -crystal, the Bain relationship is the easiest to understand: it consists of a 45° rotation about the $[100]$ direction, so that its three angles read $(45^\circ, 0^\circ, 0^\circ)$.

Moreover, by representing some of the $[100]$, $[110]$ and $[111]$ poles of:

- a γ -crystal of orientation $\{111\}\langle 110 \rangle$, and
- an α -crystal of orientation $\{110\}\langle 001 \rangle$,

on the same pole figure, one obtains the drawing given by Bunge in [2] and reproduced below in Figure 3-4.

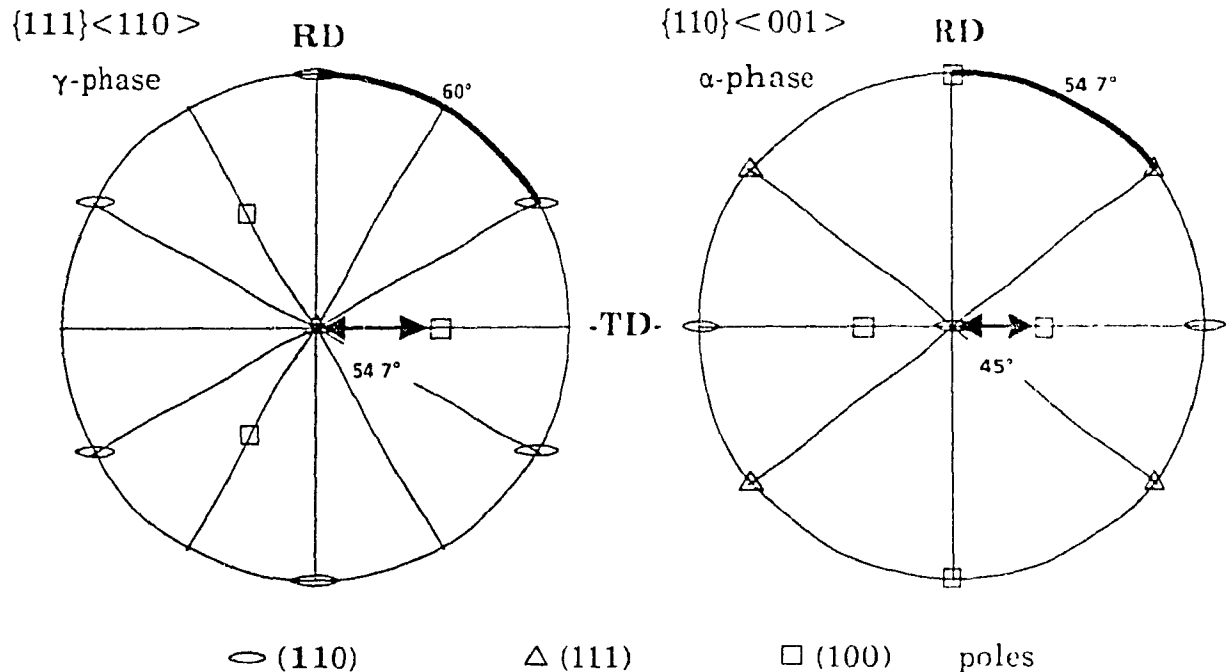


Figure 3-4: Illustration of the Nishiyama-Wassermann relationship and its deviation from the Bain and Kurdjumow-Sachs relationships.

These two diagrams thus illustrate the Nishiyama-Wassermann (NW) relationship for the $\gamma \rightarrow \alpha$ transformation, which transforms a $\{111\}\langle 110 \rangle$ γ -crystal into a $\{110\}\langle 001 \rangle$ α -crystal, and from which the relative positions of the two other laws can be assessed :

(a) the Bain relationship (B) :

It has the same parallelism condition for the directions as NW, namely $[110]_\gamma \parallel [100]_\alpha$, but a different condition for the planes : $(100)_\gamma \parallel (100)_\alpha$ instead of $(111)_\gamma \parallel (110)_\alpha$ for the NW relation. From the NW case of Figure 3-4, one can thus construct the diagram for the Bain relation by carrying out two rotations about RD (i.e. in the

equatorial plane TD-ND) to obtain Bain's condition for the planes : (arrowed bold arcs)

- one in the γ -crystal to bring $[100]_{\gamma}$ in coincidence with ND : 54.7°
 - one in the α -crystal to bring $[100]_{\alpha}$ in coincidence with ND : $\underline{45.0^{\circ}}$
- leading to a relative variation in $\Delta\beta_{RD}$ of 9.7°

(b) the Kurdjumow-Sachs relationship (KS) :

It has the same parallelism condition for the planes as NW, namely $(111)_{\gamma} // (110)_{\alpha}$, but a different condition for the directions : $[110]_{\gamma} // [111]_{\alpha}$ instead of $[110]_{\gamma} // [100]_{\alpha}$. From the NW case of Figure 3-4, one can again construct the diagram for the KS relation by carrying out two rotations about ND (i.e. in the projection plane RD-TD) to obtain the KS condition on the directions : (non-arrowed bold arcs)

- one in the γ -crystal to bring $[110]_{\gamma}$ in coincidence with RD : 60.0°
 - one in the α -crystal to bring $[111]_{\alpha}$ in coincidence with RD : $\underline{54.7^{\circ}}$
- leading to a relative variation in $\Delta\beta_{ND}$ of 5.3°

These two results are illustrated in Euler space in Figure 3-5:

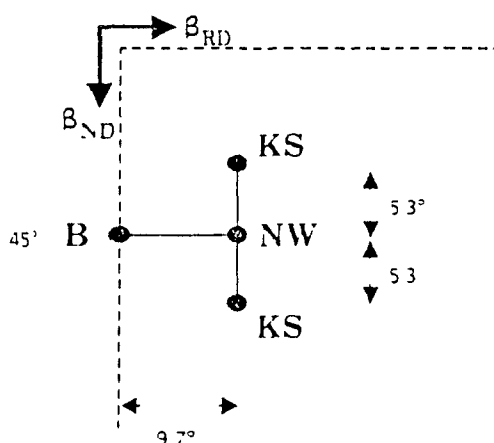


Figure 3-5 : Relative positions of the different orientation relations in Euler space.

- the limitations of crystallographic relations :

As they involve only the most compact planes and directions, whose Miller indices have low values, the above laws do not reproduce all the observations [26]. Furthermore, due to the atomic nature of the transformation mechanism, they should normally be described in terms of cooperative dislocation movements [27]. Moreover, when ferrite nucleates at a γ grain boundary, obeying a particular orientation

relation with one of the grains, the subsequent growth has been shown to occur preferentially in the grain with which no precise relation exists [28]. Lastly, because of the spread observed about the ideal values, Figure 3-5 shows that it is rather difficult to distinguish between them.

name	Euler angles	angle & axis of rotation	orientation relation
Bain	$(45^\circ, 0^\circ, 0^\circ)$	45° [100]	$(100)_\gamma$ $(100)_\alpha$ $[011]_\gamma$ $[001]_\alpha$
Kurdjumow-Sachs	$(84.23^\circ, 48.19^\circ, 84.23^\circ)$	90° [112]	$(111)_\gamma$ $(110)_\alpha$ $[1-10]_\gamma$ $[1-11]_\alpha$
Nishiyama-Wassermann	$(80.26^\circ, 48.19^\circ, 45^\circ)$	not integral	$(111)_\gamma$ $''(110)_\alpha$ $[1-10]_\gamma$ $''[001]_\alpha$
Greninger-Troiano		not integral	between KS and NW
Pitsch	$(80.40^\circ, 45.82^\circ, 13.64^\circ)$	not integral	$(110)_\gamma$ $''(112)_\alpha$ $[1-10]_\gamma$ $''[11-1]_\alpha$

Table 3-1: Characteristic data for the usual orientation relationships

III.2.3 REPRESENTATIONS OF A TRANSFORMATION LAW

Expressed as a rotation Δg , a transformation law may thus be represented in Euler space or in two-dimensional projections, in a very similar manner as ODF's

- the three-dimensional orientation transformation function

More generally, a continuous distribution of Δg rotations appearing with a probability $W(\Delta g)$ will now be considered, as proposed in paragraph III.1.2. Accordingly, the MODF is a density function of the continuous variable $\Delta g = (\phi_1, \phi, \phi_2)$, in the same manner as the ODF $\rho(g)$, and can thus be plotted in " ϕ -sections" for instance. Figure 3-6 shows the ϕ_2 -section representation of the MODF for the KS relationship. It must be remembered, however, that in this case the function

represents the distribution of orientations of the *product* crystals with respect to the reference axes of the *parent* crystal. In the case of the cubic-cubic transformation, a peak at the location $(hkl)[uvw]$ means that the (hkl) plane in the product is parallel to the (001) plane in the parent and that the $[uvw]$ direction in the product is parallel to the $[100]$ of the parent. Thus the indexing charts that have been published for ODF analysis [29] can also be used to assist in the interpretation of MODF's.

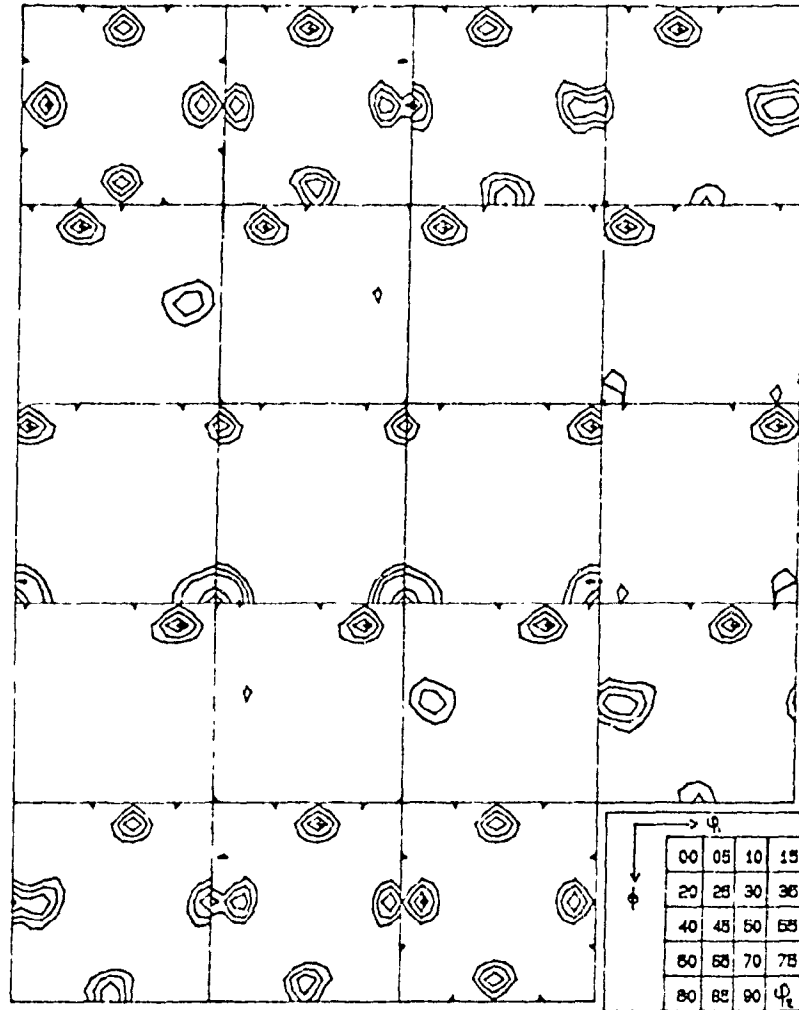


Figure 3-6: ϕ_2 -section misorientation distribution function for the KS relationship.

- two-dimensional stereographic projections:

The poles of the α -crystal in the γ reference frame or conversely the poles of the γ -crystal in the α reference frame can be represented using the stereographic projection technique described in paragraph II.2.2. The principles of their calculation from the MODF are given in APPENDIX E. Their relationships to the MODF are analogous to

those of pole figures and inverse pole figures to the ODF. As an illustration, the densities of the (111) γ -poles with respect to the α -reference frame and the densities of the (111) α -poles with respect to the γ -reference frame have been plotted for the KS relationship and are shown in Figures 3-7 (a) and 3-7 (b), respectively.

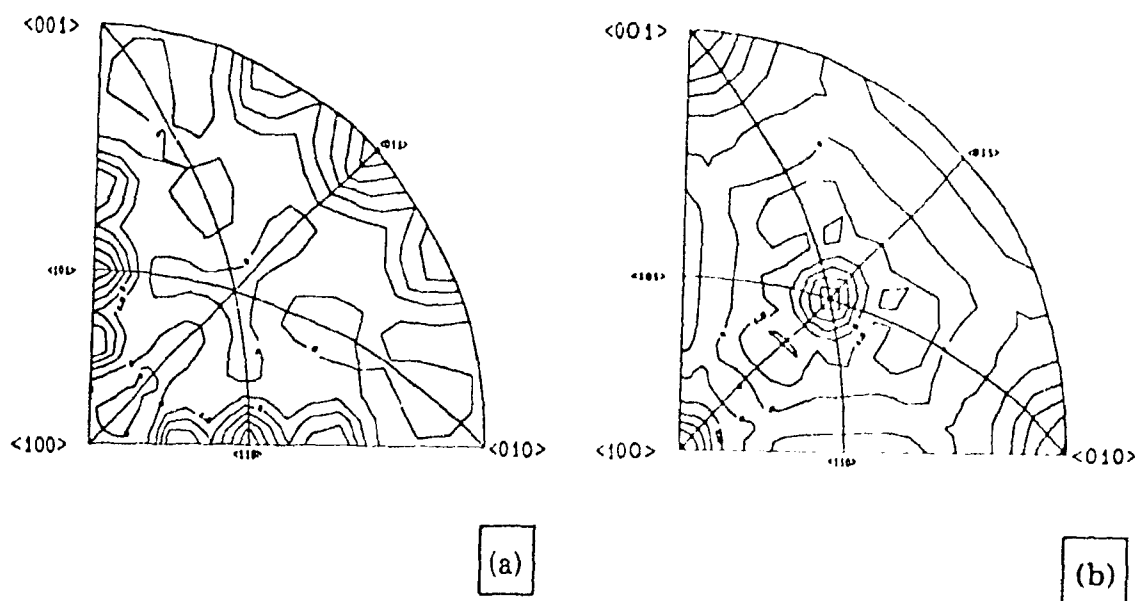


Figure 3-7: Densities of (a): the (111) γ -poles in the α -crystal,
(b): the (110) α -poles in the γ -crystal.

These representations are of practical use when the two phases are stable at room temperature, for which one can study the transformation law by comparing them with theoretical figures. In the present work, however, the orientation relationships were assumed to be known, so that MODF's and their two-dimensional projections have not been used extensively.

III.3 SYMMETRY CONSIDERATIONS

Equivalents to a given orientation, resulting from the combination of the crystal and sample symmetries, have been extensively reviewed in paragraph II.1.3. The present considerations will thus be devoted only to the presentation of some symmetry problems, introduced in II.1.2, in relation to the crystallographic laws and their impact on the study of transformation textures through the variant selection phenomenon.

III.3.1 VARIANTS OF A TRANSFORMATION LAW

- definitions and vocabulary :

As mentioned earlier in paragraph III.1.2 and illustrated in Figure 3-2, because of the symmetries of the parent and product phases, an orientation relationship between crystals of two phases can be expressed in as many as $N^\gamma N^\alpha$ crystallographically equivalent ways, named variants of the law and defined in the general equation

$$\Delta g_{ij} = S_i^\alpha \Delta g_{11} (S_j^\gamma)^{-1} \quad (3-19)$$

with S_i^α and S_j^γ running through the rotational subgroups of the α and γ symmetries, respectively. In the case of cubic-cubic transformations, however, the two subgroups coincide and consist of 24 elements denoted $(S_i^\gamma)_{i \in \{1 \dots 24\}}$. Equation (3-19) then simplifies into

$$\Delta g_{ij} = S_i^\gamma \Delta g_{11} (S_j^\gamma)^{-1} \quad (3-20)$$

Again, in equations 3-19 and 3-20, the rotations Δg_{ij} may not be all distinct, so that the multiplicity of the transformation law (number of distinct variants) can be reduced from $N^\gamma N^\alpha$ to k , where k can be drastically smaller than $N^\gamma N^\alpha$. In particular, two variants Δg_{ij} and Δg_{kl} will be said to be *equivalent* when an initial orientation leads to two equivalent final texture components, i.e. if

$$\Delta g_{ij} = S_u^\alpha \Delta g_{kl} \quad (3-21)$$

and *identical* when these two components are indeed the same. For simple relationships, e.g. Bain's, symmetry may reduce the number of distinguishable variants still further. The maximum number of distinct product orientations which can result from a single starting component is then proportionally lowered. It is

worth noting however that this number is not constant when the initial orientation is changed, but merely depends on its own multiplicity (24, 48 or 96).

- graphical illustration of the definition of variants:

Symmetry problems concerning the definition and use of the variants of a transformation law are illustrated in Figure 3-8. From this figure, relations between

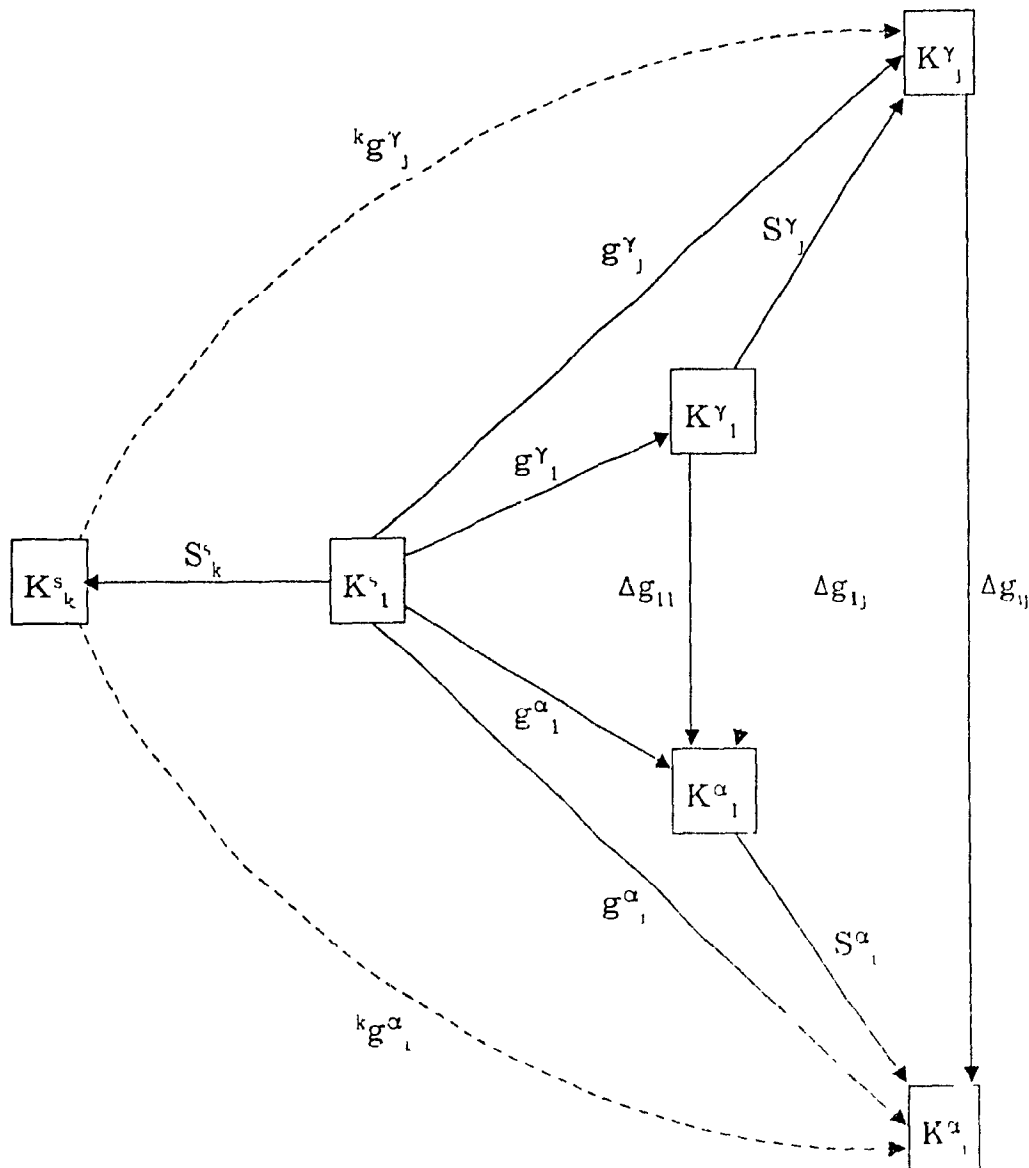


Figure 3-8: Graphical illustration of the definition of variants.

different reference frames can be readily derived; for example, K^γ_j and K^α_i can be linked in two ways, namely

$$K^\alpha_i = \Delta g_{ij} K^\gamma_j \quad \text{and} \quad K^\alpha_i = \Delta g_{ii} K^\gamma_i = \Delta g_{ii} \left((S^\gamma_i)^{-1} K^\gamma_i \right) \quad (3-22)$$

so that

$$\Delta g_{ij} = \Delta g_{ii} (S^\gamma_i)^{-1} \quad (3-23)$$

- the two practical ways of determining the variants:

Two major ways of defining an orientation relationship were introduced in paragraph III.2.1, namely a parallelism condition or a rotation. Correspondingly, the variants of the relationship can be derived using two different procedures.

(a) If the law is defined by a parallelism condition, this can be interpreted in the sense that a single γ -orientation g^γ_i is said to be transformed into a single α -orientation g^α_i . Among all the possible conditions of parallelism given by the transformation law, any one can be selected, which is then considered as the reference Δg_{ii} : e.g. the KS relationship can be seen as a $\{111\}_\gamma \langle 110 \rangle_\gamma$, say $g^\gamma_i = (111)_i [1-10]_i$, which is then changed into a $\{110\}_\alpha \langle 111 \rangle_\alpha$, say $g^\alpha_i = (110)_i [1-11]_i$. The transformation matrix can thus be obtained using equation (3-1)

$$\Delta g = \Delta g_{ii} = g^\alpha_i (g^\gamma_i)^{-1} \quad (3-24)$$

However, there are N^γ indistinguishable symmetrically equivalent ways to choose g^γ among the $g^\gamma_j = S^\gamma_{ji} g^\gamma_i$ and N^α to choose g^α among the $g^\alpha_i = S^\alpha_{ji} g^\alpha_j$. The other relations—the variants—are deduced from Δg_{ii} by taking into account the above mentioned symmetrical orientations, so that if the transformation is now expressed in terms of g^γ_j and g^α_i instead of g^γ_i and g^α_i , it appears that:

$$\Delta g = \Delta g_{ij} = g^\alpha_i (g^\gamma_j)^{-1} = \left(S^\alpha_{ij} g^\alpha_j \right) \left(S^\gamma_{ji} g^\gamma_i \right)^{-1} = \left(S^\alpha_{ij} g^\alpha_j \right) \left((g^\gamma_i)^{-1} (S^\gamma_j)^{-1} \right)$$

and

$$\Delta g_{ij} = S^\alpha_{ij} \left(g^\alpha_j (g^\gamma_i)^{-1} \right) (S^\gamma_j)^{-1} = S^\alpha_{ij} \Delta g_{ii} (S^\gamma_j)^{-1} \quad (3-25)$$

Equation (3-25) is identical to the equation proposed in paragraph III.1.1, which was derived directly from Figure 3-2.

If cubic-cubic transformations are to be dealt with, equation (3-25) can be given somewhat simpler forms, which are easier to interpret and to compare. As $(S^\gamma_i)_{i=1,2,4}$ is a group, in the mathematical sense of group theory, any of its elements S^γ_i and S^γ_j can be related by relations of the following type:

$$S^\gamma_i = S^\gamma_j S^\gamma_r \quad \text{and} \quad S^\gamma_i = S^\gamma_l S^\gamma_j \quad (3-26a)$$

or

$$S_j^c = S_l^c S_r^c \quad \text{and} \quad S_j^c = S_r^c S_l^c \quad (3-26b)$$

with

$$S_r^c = (S_l^c)^{-1} \quad \text{and} \quad S_l^c = (S_r^c)^{-1} \quad (3-26c)$$

It results therefrom that Δg_{ij} can be expressed respectively by :

$$\Delta g_{ij} = S_j^c \left(S_r^c \Delta g_{11} \right) (S_j^c)^{-1} \quad \text{and} \quad \Delta g_{ij} = S_l^c \left(S_l^c \Delta g_{11} (S_l^c)^{-1} \right) \quad (3-27a)$$

or

$$\Delta g_{ij} = S_l^c \left(\Delta g_{11} S_r^c \right) (S_l^c)^{-1} \quad \text{and} \quad \Delta g_{ij} = \left(S_l^c \Delta g_{11} (S_l^c)^{-1} \right) S_l^c \quad (3-27b)$$

It can be seen from equation (3-27a) that Δg_j is equivalent to $S_j \Delta g_{11} (S_j)^{-1}$, in the sense defined by equation (3-21), so that the multiplicity of a cubic-cubic orientation relation is reduced from $N^2 N^c = (N^c)^2 = 24^2 = 576$ in the general case to $N^c = 24$. The set of $(\Delta g_{ij})_{i,j \in \{1..N^c\}}$ is thus equivalent to $(\Delta g_{11})_{i \in \{1..N^c\}}$, which can be denoted as $(\Delta g_i)_{i \in \{1..N^c\}}$. In other words, for S_j fixed, the N^c rotations $S_l^c \Delta g_{11} (S_l^c)^{-1}$, with $l \in \{1..24\}$, are equivalent, in the sense of equation (3-21), because they give birth to the same final α -crystal. One can thus say that there exist N^c sets of N^c equivalent rotations.

(b) If the law is defined by a rotation, usually with the parameters $(d, \Delta\omega)$, the transformation matrix is given by $\Delta g = \Delta g(d, \Delta\omega)$, as shown in Table 2-4. This parametrization only applies to transformations between crystals with identical types of lattices, as in the cubic-cubic case.

The matrix product $H \Delta g(d, \Delta\omega) H^{-1}$, where H is any rotation matrix, does not change the trace of the matrix Δg which defines the angle $\Delta\omega$, it only alters the axis of rotation which is changed from d to $d' = H.d$.

In the case of cubic-cubic transformations, if H is a symmetry element of the cubic crystal, say S_l^c , $d' = S_l^c.d$ is an axis of rotation symmetrically equivalent to d , and $\Delta g(d, \Delta\omega)$ and $\Delta g(d', \Delta\omega) = S_l^c \Delta g(d, \Delta\omega) (S_l^c)^{-1}$ with $d' = S_l^c.d$ are two variants belonging to the same orientation relationship.

To obtain all the variants of the relationship, it thus suffices to have S_l^c vary within the complete rotational subgroup of the cubic crystal symmetry, so that $d' = S_l^c.d$ successively takes all the N^c positions symmetrically equivalent to d .

- independence of the sample reference frame :

From the illustration of the definition of variant, in Figure 3-8, it can be seen that the sample symmetry does not play a role in the determination of the variants of the orientation relationship. The forthcoming derivation proves this observation.

- + Δg_{ij} has been defined by ${}^1g^{\alpha_i} = {}^1\Delta g_{ij} \cdot {}^1g^{\gamma_j}$ with respect to a sample reference frame, suffixed 1, K^s_1
- + However, one could imagine defining it with respect to another reference frame, denoted K^s_k , for which ${}^kg^{\alpha_i} = {}^k\Delta g_{ij} \cdot {}^kg^{\gamma_j}$. The orientations ${}^kg^{\alpha_i}$ and ${}^kg^{\gamma_j}$ can be expressed as functions of ${}^1g^{\alpha_i}$ and ${}^1g^{\gamma_j}$, respectively, by ${}^kg^{\alpha_i} = S^s_k \cdot {}^1g^{\alpha_i}$ and ${}^kg^{\gamma_j} = S^s_k \cdot {}^1g^{\gamma_j}$, so that :

$${}^k\Delta g_{ij} = {}^kg^{\alpha_i} \left({}^kg^{\gamma_j} \right)^{-1} = S^s_k \cdot {}^1\Delta g_{ij} \cdot (S^s_k)^{-1} \quad (3-28)$$

It has been pointed out above that for a given symmetry rotation S^s_k , the transformation matrix $S^s_k \cdot {}^1\Delta g_{ij} \cdot (S^s_k)^{-1}$ is a variant of ${}^1\Delta g_{ij}$; thus there exist indices u and v such that :

$${}^1\Delta g_{uv} = S^s_k \cdot {}^1\Delta g_{ij} \cdot (S^s_k)^{-1} = {}^k\Delta g_{ij} \quad (3-29)$$

The only influence of the choice of the sample reference frame is thus to modify the order of appearance of the variants, but not their values

- the two ways to take the γ -symmetry into account :

If one now applies the transformation Δg_{11} to an initial orientation g^{γ}_1 and considers, at the same time, the equivalents of the γ -orientation

$$g^{\gamma}_j = S^{\gamma}_j \cdot g^{\gamma}_1 \quad (3-30)$$

and the right-hand side symmetry of the transformation

$$\Delta g_{1n} = \Delta g_{11} \cdot (S^{\gamma}_n)^{-1} \quad (3-31)$$

the resulting α -orientation g^{α}_{nj} is given by

$$g^{\alpha}_{nj} = \Delta g_{1n} \cdot g^{\gamma}_j = \Delta g_{11} \cdot \left((S^{\gamma}_n)^{-1} \cdot S^{\gamma}_j \right) \cdot g^{\gamma}_1 \quad (3-32)$$

As S^{γ}_n and S^{γ}_j run through the whole rotational subgroup of γ -symmetry, which is a group, $(S^{\gamma}_n)^{-1} \cdot S^{\gamma}_j$ is also an element of the subgroup and can thus be written as S^{γ}_k , so that $g^{\alpha}_{nj} = g^{\alpha}_k = \Delta g_{11} \cdot S^{\gamma}_k \cdot g^{\gamma}_1$. The result is thus globally the same if the γ -symmetry is expressed explicitly only once instead of twice.

Finally g^{α}_k can be interpreted in two different but identical ways, as far as the final results are concerned .

1st way : $g^{\alpha}_k = \Delta g_{11} \cdot (S^{\gamma}_k \cdot g^{\gamma}_1)$ the α -orientations are derived from one variant of the law and all the γ equivalents.

2nd way : $g^{\alpha}_k = (\Delta g_{11} \cdot S^{\gamma}_k) \cdot g^{\gamma}_1$ the α -orientations are derived from all the variants of the law and one γ equivalent.

The 1st solution was retained by Bunge [30] and has also been adopted in the present work, unless otherwise mentioned. This arbitrary choice enables the symmetry of the γ -crystal to be omitted in the MODF, $\dot{\tilde{W}}(\Delta g) \cdot \dot{\tilde{W}}(\Delta g)$, which is no longer symmetrical on the right-hand side, as pointed out with respect to equation (3-9). $\dot{\tilde{W}}(\Delta g)$ then takes on a maximum value at Δg_{11} and is zero at all the other Δg_{1n} 's. In terms of ideal orientation relations, it is now sufficient to choose just one of the variant Δg_{1n} 's, say Δg_{11} .

Another possibility would have been to keep the right-hand side symmetry of the MODF and to omit the crystal symmetry in the initial ODF $\dot{\tilde{F}}$, which would no longer have been symmetrical on the left-hand side, $\dot{\tilde{F}} \cdot \dot{\tilde{F}}$. It is evident that this choice would have been less suitable than the first one, as experimental and calculated ODF's do fulfill this symmetry.

- B, KS and NW variants:

The above considerations are of interest because of their application to the study of the fcc-to-bcc transformation in steels and iron-based alloys. Precise orientation relationships have been determined for this case, as reviewed in section III 2.2. It is the aim of the paragraphs that follow to define the minimum number of variants (less than or equal to $N' = 24$) for these relationships (B, KS, NW).

(a) number of variants from the parallelism conditions: Starting with one relationship defined by its parallelism condition, the other variants can be obtained by having the plane and direction of either phase vary within their sets of symmetrical positions. Only the positions that fulfill the orthogonality condition "plane \perp direction" and lead to distinct product orientation, are retained. The resulting number of variants is shown in Table 3-2 for the three transformation laws at stake. The first integer gives the number of crystallographically equivalent planes of a certain type in the phase, whereas the second integer is the number of crystallographically equivalent directions of a certain type lying in the preceding plane of the same phase.

(b) number of variants from the rotation ($d, \Delta\omega$): When the rotation definition is employed, the variants of a transformation law can be derived if d successively takes all its symmetrically equivalent positions, keeping in mind that a rotation of $\Delta\omega$ around $-d$ is not identical to a rotation of $\Delta\omega$ around d unless $\Delta\omega = \pi$ rad. (180°). The resulting number of variants is shown in Table 3-3 for the same three transformation

orientation relation	parallelism conditions	Number of alternatives		resulting number of variants
		γ phase	α phase	
Bain	$(100)_{\gamma} // (100)_{\alpha}$	3	3	3
	$[011]_{\gamma} \perp [001]_{\alpha}$	1	1	
Kurdjumow-Sachs	$(111)_{\gamma} \parallel (110)_{\alpha}$	4	6	24
	$[1-10]_{\gamma} \parallel [1-11]_{\alpha}$	3	2	
	twin-related variants	$\times 2$	$\times 2$	
Nishiyama-Wassermann	$(111)_{\gamma} \parallel (110)_{\alpha}$	4	6	12
	$[1-10]_{\gamma} \parallel [001]_{\alpha}$	3	2	

Table 3-2: Number of variants determined from the parallelism conditions.

laws. For the NW case, where hkl does not have a simple integral value, only a multiplicity of 12 distinct variants arises from the 48 possibilities, due to the fact that some of the rotations are identical [27].

orientation relation	angle of rotation	axis of rotation	number of variants
Bain	45°	(100)	3
Kurdjumow-Sachs	90°	(112)	24
Nishiyama-Wassermann	95.27°	(hkl)	48 reduced to 12

Table 3-3: Number of variants determined from the rotation definition.

The lists of the variants of the B, KS and NW relationships are given in APPENDIX A, both in terms of their Euler angles ($\Delta\phi_1$, $\Delta\phi$, $\Delta\phi_2$) and their axis d and angle ω of rotation. They are also represented in the MODF framework in ϕ_2 -sections and ϕ_1 -sections in Figures 3-9 and 3-10, respectively.

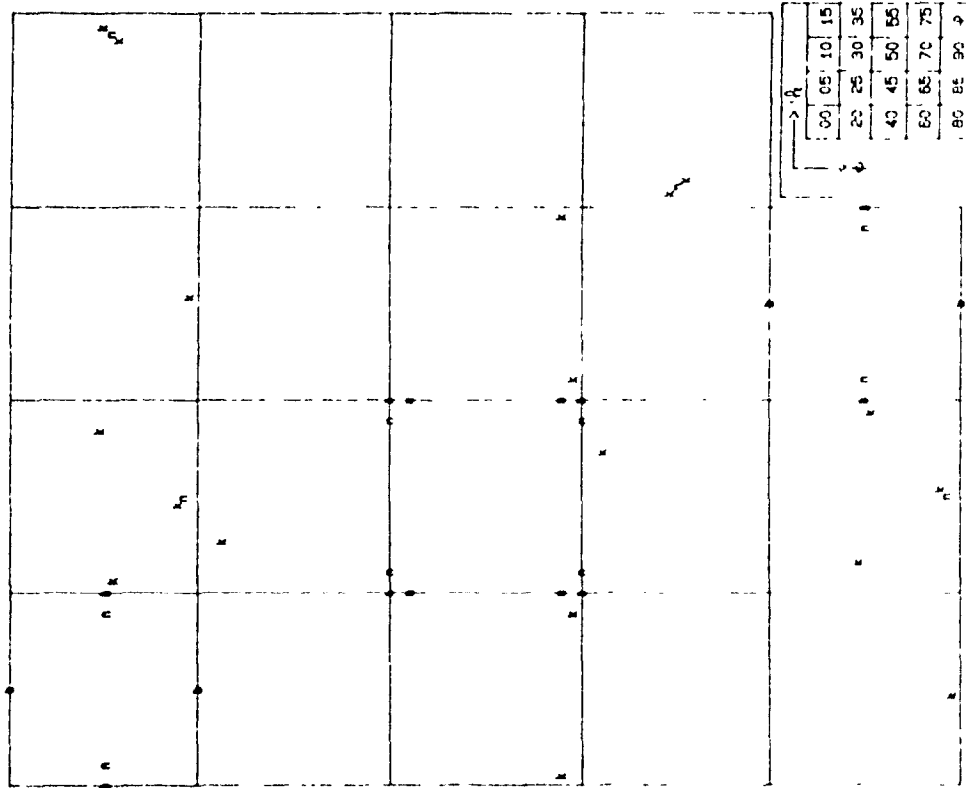


Figure 3-9. Variants of the B, KS and NW relationships in the ϕ_1 -sections.

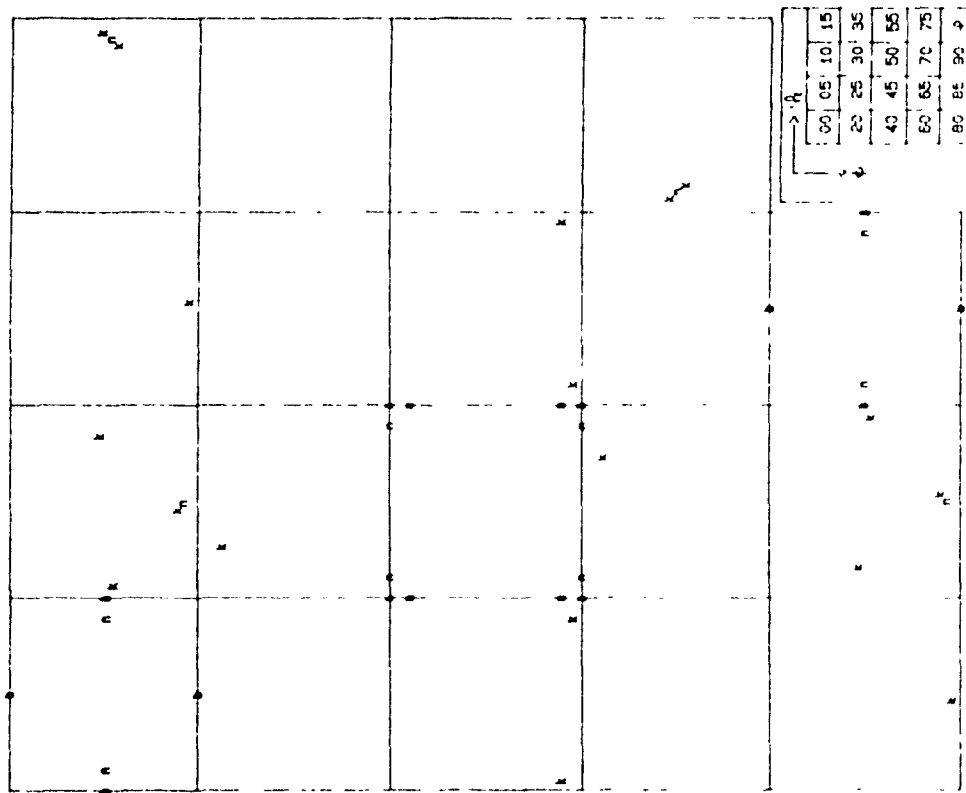


Figure 3-10. Variants of the B, KS and NW relationships in the ϕ_2 -sections.

III.3.2 VARIANT SELECTION CRITERIA

Martensite formation is generally accompanied by a change in volume and a transformation shear so that the course of the transformation is likely to be affected by the elastic and plastic deformations which result from these phenomena. Depending on the inhomogeneities in temperature, strain and initial microstructure, as well as on the physical configuration of the specimen, some variants can be favored over others during transformation [31]. Experimental evidence for such selection will be reviewed in section IV.4. Some rules or criteria for variant selection must therefore be postulated, and in order to be successful, models of texture transformation that can also take into account the relative weights of the different variants are needed. It is the aim of the present paragraphs to give brief descriptions of some of the important models proposed recently.

- the shape deformation (SD) model :

Because martensite formation involves a shear deformation, there is an external shape change in the presence of preferred orientations, and this has been regarded by Patel and Cohen [32] as an influential factor in variant selection. They considered that, when a unit volume of the parent austenite phase is transformed into martensite, the work done by the applied stress can be resolved on the habit plane and the normal to the habit plane as :

$$\frac{U}{\sigma} = \gamma_0 \cos \theta \cos \lambda + \epsilon_0 \cos^2 \theta \quad (3-33)$$

where U = work done
 σ = applied stress
 γ_0 = total transformation shear strain in the habit plane
 ϵ_0 = total transformation strain normal to the habit plane
 θ = angle between the habit plane normal and the stress axis
 λ = angle between the shear direction and the stress axis

This analysis has been extended [33-36] to estimate the effect of stress on the formation of a particular α' variant : the larger the value of U/σ , the more the stress aids the formation of a particular α' variant. However, when compared to actual martensite textures, the SD model has not been found suitable for variant selection prediction

- the Bokros-Parker (BP) model:

The model suggested by Bokros and Parker [37] is based on the interaction of slip systems and habit plane variants. In an early study of martensite burst formation in strained Fe-Ni single crystals, they noticed that the favored variants were those whose habit planes were nearly perpendicular to the active *slip plane*. Conversely, the group of variants that had habit planes which were nearly perpendicular to the active *slip direction* were suppressed. This behavior was suggested to be a consequence of the anisotropic substructure introduced during deformation. They further observed that, during martensitic transformation, there exists a mechanical stimulation (coupling) between variants of the habit plane that are geometrically oriented such that the stress induced by the transformation on one aids transformation on the others. Such a mechanical autocatalytic effect was found to be restricted to the set of four nearly parallel planes whose poles are clustered about a common $[110]_f$ direction, it rarely extends outside the group to the other 20 potential variants of the habit plane. Thus, this model automatically leads to variant selection during martensitic transformation and has been supported by other studies [38,39]. However, systematic deviations from the predictions have also been observed [40].

- the active slip system (AS) models

In a number of investigations [40-43], variant selection has been linked to the active slip systems in the γ -phase and in particular to the slip system subjected to the largest shear stresses during rolling prior to transformation. The variants produced were those which contained, in the transformation relationship, those slip systems which sustained the maximum resolved shear stress during rolling. Haslam et al. [44] proposed that the nucleation of the martensite variant took place on the active slip systems of the deformation just before transformation in proportion to the shear on each system. This defines 12 or 16 variants for any given orientation according to the theory of polycrystalline deformation due to Bishop and Hill. Predictions of the martensite texture from the parent austenite texture incorporating the above variant selection criteria have generally resulted in textures with acceptable agreement with experiment, but they are generally less intense than the experimental ones [40,45,46].

- the twinning shear (TS) model:

The twinning shear model was proposed by Higo et al. [47], who applied a directional external stress to single crystals of Fe-17.7% Cr-13.6% Ni to induce the

martensite transformation. They found that the direction and sense of the applied stress affected the relative population of the α' variants and proposed that the first shear (i.e. the twin-forming shear on the $\{111\} \langle 211 \rangle_\gamma$ system) in the double shear mechanism for fcc-to-bcc transformation is the deformation which gets affected by the applied stress. Kato and Mori [35,36] also examined the possibility that the applied stress mainly affects the Bain deformation by calculating the interaction energy between the applied stress and the Bain strain and observed that their results could be explained equally well by both methods. This, according to them, was not surprising since the Bain deformation, which may be considered as the initial stage of martensite formation, may be construed as double shear accompanied by a little expansion of the parent γ phase [36]. Thus the Bain strain and the twinning shear of the double shear mechanism both seem to have the same directionality [48].

- the Bain strain (BS) model

The Bain strain model proposed by Furubayashi et al [45,46,48,49] is based on this finding. The compression axis associated with the Bain strain was termed the 'Bain compression axis' or BCA and, for the γ -to- α transformation, the BCA for each one of the three Bain variants is parallel to the $[001]$, $[010]$ or $[100]$ axis of the austenite. If an external compressive stress is applied along the $[001]$ axis, the variant having $[001]$ as the BCA will be assisted more effectively by the applied stress than the other two. This, of course, leads directly to variant selection. The BS model thus postulates that the Bain variant that is selected is the one that will lead to the maximum work being done by the applied stress against the Bain strain [49], that is to the maximum WB with

$$WB = (\alpha \cos \theta) = \alpha \sin^2 \theta \quad (3-34)$$

where α is the axial ratio of the Bain strain $= -\epsilon_2/\epsilon_1$ and θ is the angle between the BCA and the direction of the compressive stress.

Two models were proposed by Furubayashi [48]: (a) a 'strong selection' model in which only the variant that had the maximum value of WB was selected, and (b) a 'weak selection' model, in which the variant having the minimum WB was first chosen and then one of the other two variants was selected in a random manner. Simulated pole figures, drawn assuming selection of the BS type [49], were found to correspond very well with experimental pole figures for Fe-Ni martensitic alloys inherited from annealing or rolling textures.

- the geometrical parameters (GP) model:

Recently Humbert et al. [50] reported that, irrespective of the amount of rolling reduction in the γ phase or the annealing treatment prior to transformation, variant selection was particularly strong and of the same type in a number of Fe 30%Ni sheets but that the dimensional parameters of the samples were able to influence the mechanism of variant selection during transformation. They postulated two models : model 1 : the selected variants are those which induce maximum deformation along the normal direction of the sheet, which contains few grains across the thickness ; model 2 : the selected variants are those which produce the minimum deformation in the plane of the sheet. They found the best agreement with experiment using the latter model.

III.4 METHODS OF SIMULATION

Two categories of relations were established earlier in this chapter between the textures of the two phases involved in a transformation : (i) a discrete derivation of individual orientations has led to equation (3-1), (ii) a continuous point of view, on the other hand, has resulted in a series of equations from (3-2) to (3-11) as consequences of successive steps of generalization. Two kinds of prediction methods of transformation textures can therefore be developed on the basis of these two approaches. Also, irrespective of the type of model, the above equations always relate three functions : the initial texture, the transformation law (with variant selection or not) and the final texture, so that one can hope to determine one of the preceding quantities as long as the other two are known. As a result, there are three potential axes of study.

III 4.1 DISCRETE METHODS

A method is termed discrete when the operation of transformation is applied to a finite number of individual orientations. The transformation of each such parent texture component according to a crystallographic transformation law leads to a number of product orientations related to the symmetry of the parent phase and to the number of distinct variants of the orientation relationship. The potential discrete methods differ from one another by the manner in which the simplifications are carried out to describe the initial texture by a limited number of ideal orientations.

- determination of the α -orientations inherited from one γ component :

Once the variants Δg_i of the chosen orientation relationship have been calculated, and assuming that these variants take the γ symmetry into account, any orientation of the austenite g^γ can be submitted to *transformation* according to equation (3-1). The symmetry of the sample, however, has to be introduced effectively. For rolling, one thus has to derive the α orientations for 1, 2 or 4 orthorhombic equivalents depending on the multiplicity of the initial g^γ (24, 48 or 96, respectively). The sample symmetry is then inherited by the final texture as previously stated, so that it does not have to be dealt with a second time for the α orientations. When an α orientation g^α appears, all the N^α equivalents should be obtained. In the procedure, the α crystal

subgroup S^{α}_1 intervenes at this point, and only the orientations with $(\phi_1, \phi, \phi_2) \in [0^\circ, 90^\circ]^3$ are retained. It must also be kept in mind, as pointed out by Van Houtte [51], that a given orientation might appear up to 3 times (through 3 equivalents) in the conventional ODF representation.

The procedure can thus be summarized as follows :

- a/ choose one γ orientation and define its N^γ orthorhombic equivalents,
- b/ use the N^γ variants of the transformation law,
- c/ derive $N^\gamma N^\gamma \alpha$ orientations using equation (3-1),
- d/ determine the α equivalents,
- e/ retain those in $[0^\circ, 90^\circ]^3$.

- determination of the γ -orientations leading to one α component.

This procedure, often named *untransformation*, is based on principles strictly identical to those of the *transformation* derivation presented above. But, instead of selecting a γ orientation and deriving the corresponding α 's, here the γ orientations that lead to a given α are calculated.

In the case of cubic-cubic transformations, for which the crystal symmetries are identical, the *untransformation* procedure is thus :

- a/ choose one α orientation and define its N^α orthorhombic equivalents,
- b/ use the N^α variants of the transformation law,
- c/ derive $N^\alpha N^\alpha \gamma$ orientations using equation (3-1),
- d/ determine the γ equivalents,
- e/ retain those in $[0^\circ, 90^\circ]^3$.

- the ideal orientation method :

The discrete *transformation* and *untransformation* methods are the simplest for the study of transformation textures. The starting texture is here assumed to consist of a small number of components and the resulting texture consists of the orientations obtained by applying one of the preceding procedures to each of the components. Although the main features of transformation textures can be simulated in this way, these procedures suffer from oversimplifications in the description of the starting texture.

- ODF decomposition methods :

To improve the quality of the simulations produced by the discrete methods, the description of the starting texture, which by its nature is continuous, has to be

improved. But, because of the discretization process, a systematic error will always result from the simplifications of the model. Nevertheless, such discrete methods are, up to now, the only ones which can be readily adapted to the practical study of variant selection. The error can moreover be minimized, either by increasing the number of components in the discretization and/or by choosing a small number of weighted orientations such that the improved decomposition agrees better with the continuous description. In what follows, two methods of ODF decomposition will be proposed, one for each solution : (i) a decomposition into N individual grains (N large), (ii) a gaussian decomposition. In these two methods, the continuous ODF of reference is assumed to be defined by its set of series expansion coefficients, C_l^{uv} .

(a) decomposition into N individual grains : (N large) Assuming that the decomposition of an austenite texture, given in ϕ_2 -sections, is desired, the N grains to be generated can be distributed among the 18 ϕ_2 -sections of the ODF (every 5°) according to their respective contributions to the overall integral

$$\int_{[0,90]^\circ} f(g) \cdot dg \quad (3-35)$$

The first step is thus to compute the integrals I_i of the ODF over the 18 sections, to set

$$I = \sum_{i=1}^{18} I_i \quad (3-36)$$

and then to derive

$$n_i = \frac{I_i}{I} \cdot N \quad \text{for } i=1, \dots, 18 \quad (3-37)$$

Next, instead of generating N grains from the whole ODF, one now has to generate 18 series of n_i grains. In other words, a large three-dimensional problem has been *split* into 18 two-dimensional and somewhat smaller problems. It is suggested that N should be taken equal to an integral fraction or to a multiple of 1800, so that a random texture would be defined by a rounded number of grains per section (100 for $N=1800$, 50 for $N=900$, etc.). It should also be ensured that the number of grains is large enough for statistical coherence (a random distribution of a hundred grains per section will only give about one grain per degree in a given direction !).

In each section, the position (ϕ_1^γ , ϕ_2^γ) of one grain is found as follows: two real numbers r_{ϕ_1} and r_{ϕ_2} are generated between 0 and 1, and the corresponding ϕ_1^γ and ϕ_2^γ are defined by a system that can be solved iteratively.

$$r_{\Phi} = \frac{\int_0^{\Phi^Y} f(g) d\Phi}{\int_0^{90^\circ} f(g) d\Phi} \quad \text{and} \quad r_{\Phi_1} = \frac{\int_0^{\Phi_1^Y} f(g) d\Phi_1}{\int_0^{90^\circ} f(g) d\Phi_1} \quad (3-38)$$

Detailed procedures for the splitting up of an ODF and for the generation of orientations in a specific section are given in APPENDIX B and APPENDIX C, respectively. The derivation of the transformed textures is then readily performed using, for each orientation obtained in the decomposition, the procedure described earlier. During this stage, a variant selection criterion can be introduced if desired. Of course, an identical reasoning can be applied to the simulation of austenite textures from experimental ferrite ODF's.

(b) Gaussian decomposition : This method is based on a least squares fit of the actual texture by gaussian-type components and has been demonstrated to be relatively efficient in providing simple and accurate decompositions of ODF's [13]. If g_i , M_i , ω_{0i} denote the position, weight and scatter of the i -th component, respectively, the corresponding model ODF can be defined by its coefficients :

$${}^{mod}C_l^{\mu\nu} = \sum_{i=1}^N M_i \frac{\exp(-l^2 \omega_{0i}^2/4) - \exp(-(l+1)^2 \omega_{0i}^2/4)}{1 - \exp(-\omega_{0i}^2/4)} \cdot \dot{T}_l^{\mu\nu}(g_i^0) \quad (3-39)$$

with

$$M_i = \frac{\sqrt{\pi}}{2} Z_i S_{0i} \omega_{0i} \left\{ 1 - \exp\left(-\frac{\omega_{0i}^2}{4}\right) \right\} \quad (3-40)$$

where Z_i is the symmetry multiplicity of the i -th component.

This model can be adjusted to the actual ODF, defined by ${}^{exp}C_l^{\mu\nu}$, by minimizing

$$\sum_{l,\mu,\nu} \left({}^{mod}C_l^{\mu\nu} - {}^{exp}C_l^{\mu\nu} \right)^2 \quad (3-41)$$

Again both transformation and untransformation simulations can be assessed with such types of decomposition.

III.4.2 A CONTINUOUS METHOD

It has been emphasized [52] that in order to establish a quantitative relationship between texture and mechanical properties, the precise orientation distribution must be taken into account, including even the minor components. To avoid the error

inherent in a discretization process, continuous methods should thus be developed. The series expansion method, proposed by Bunge [15] and Roe [3], has been successfully applied to the study of transformation textures. It will be presented here, step by step, on the basis of the progressive introduction of the mathematical formalism from equation (3-2) to equation (3-11). Although part of the earlier work was carried out using Roe's notation, it has been decided to restrict this presentation to Bunge's, for the sake of clarity and coherence. The main features of the mathematical treatment corresponding to the three axes of research (transformation, untransformation, study of the crystallographic law) are also described.

- principles of the series expansion method :

In section II.2.4., an orientation distribution function $\dot{f}(g)$ was expanded into a series of symmetric generalized spherical harmonics $\dot{T}_l^{\mu\nu}$ of the appropriate symmetries, using a set of coefficients $C_l^{\mu\nu}$. The indices μ and ν are related to the left- and right-hand side symmetries, i.e. the crystal and sample symmetries, respectively.

$$\dot{f}(g) = \sum_{l=0}^{\infty} \sum_{\mu=1}^{M(l)} \sum_{\nu=1}^{N(l)} C_l^{\mu\nu} \dot{T}_l^{\mu\nu}(g) \quad (3-42)$$

When the symmetries of the two crystals are to be differentiated, indices μ_1 and μ_2 are used for the parent and product, respectively, as well as different numbers of dots on the left-hand sides of the ODF's. This expansion can be carried out in the same manner on any periodic function of g or Δg , as long as the corresponding T functions introduced fulfill the required symmetries. The principles of the calculation of the cubic-orthorhombic and cubic-cubic T functions are given in APPENDIX D. In what follows, the indices 1 or α will be used for the initial texture, and the indices 2 or γ for the ODF after transformation.

- a unique orientation relationship :

During a phase transition, it has been shown [3,4] that the set of series expansion coefficients of the original phase $C_{l_1}^{\mu_1\nu_1}(1)$ can be transformed into the set of coefficients $C_{l_2}^{\mu_2\nu_2}(2)$ for the newly formed phase provided the Euler angles $\Delta\phi_1$, $\Delta\phi$, $\Delta\phi_2$ specifying the crystallographic law Δg are known.

From the series expansion of \dot{f}^α , it is possible to calculate each $C_{l_2}^{\mu_2\nu_2}(2)$ coefficient as follows :

$$C_{l_2}^{\mu_2\nu_2} = (2l_2 + 1) \int_g \dot{f}^\alpha(g) \dot{T}_{l_2}^{\mu_2\nu_2}(g) dg \quad (3-43)$$

Introducing the transformation equations (3-1) and (3-2) and the series expansion of $\dot{T}^{\mu_1 \nu_1}$, one gets

$$C_{l_2}^{\mu_2 \nu_2} = (2l_2 + 1) \sum_{l_1, \mu_1, \nu_1} C_{l_1}^{\mu_1 \nu_1} \int_g \dot{T}_{l_1}^{\mu_1 \nu_1}(\Delta g^{-1} g) \dot{T}_{l_2}^{\mu_2 \nu_2}(g) dg \quad (3-44)$$

With the addition theorem

$$\dot{T}_{l_1}^{\mu_1 \nu_1}(\Delta g^{-1} g) = \sum_{s=-l_1}^{+l_1} \dot{T}_{l_1}^{\mu_1 \nu_1}(\Delta g^{-1}) \dot{T}_{l_1}^{s \nu_1}(g) = \sum_{s=-l_1}^{-l_1} \dot{T}_{l_1}^{s \mu_1}(\Delta g) \dot{T}_{l_1}^{s \nu_1}(g) \quad (3-45)$$

the definition of the symmetric harmonics

$$\dot{T}_{l_2}^{\mu_2 \nu_2}(g) = \sum_{m_2=-l_2}^{+l_2} \dot{T}_{l_2}^{m_2 \mu_2} \dot{T}_{l_2}^{m_2 \nu_2}(g) \quad (3-46)$$

and the orthonormality condition

$$\int_g \dot{T}_{l_1}^{s \nu_1}(g) \dot{T}_{l_2}^{m_2 \nu_2}(g) = \frac{1}{2l_2 + 1} \delta_{l_1 l_2} \delta_{s m_2} \delta_{\nu_1 \nu_2} \quad (3-47)$$

equation (3-44) can be expressed as

$$C_{l_2}^{\mu_2 \nu_2}(2) = \sum_{\mu_1=1}^{M_1(l_2)} C_{l_2}^{\mu_1 \nu_2}(1) \sum_{s=-l_2}^{+l_2} \dot{T}_{l_2}^{s \mu_2} \dot{T}_{l_2}^{s \mu_1}(\Delta g^{-1}) \quad (3-48)$$

so that, finally

$$C_{l_2}^{\mu_2 \nu_2}(2) = \sum_{\mu_1=1}^{M_1(l_2)} \dot{T}_{l_2}^{\mu_2 \mu_1}(\Delta g) C_{l_2}^{\mu_1 \nu_2}(1) \quad (3-49)$$

which can be written as

$$C_l^{\mu_2 \nu_2}(2) = \sum_{\mu_1=1}^{M_1(l)} \dot{T}_l^{\mu_2 \mu_1}(\Delta g) C_l^{\mu_1 \nu_2}(1) \quad (3-50)$$

• a unique family of equivalent orientation relationships

Equation (3-3) takes the different variants of the orientation relationship into account, each with an equal probability of occurrence, so that the coefficients can be related by

$$C_l^{\mu_2 \nu_2}(2) = \sum_{\mu_1=1}^{M_1(l)} \left(\sum_{i=1}^{N^v} \frac{1}{N^v} \dot{T}_l^{\mu_2 \mu_1}(\Delta g_i) \right) C_l^{\mu_1 \nu_2}(1) \quad (3-51)$$

When some selection of variants occurs, this can be allowed for by replacing the constant term $1/N^v$ in equation (3-51) by a factor f_l which gives the relative frequency of occurrence of each variant. In that case, equation (3-51) has the form

$$C_l^{\mu_2}(2) = \sum_{\mu_1=1}^{M_1^{(1)}} \left(\sum_{i=1}^{N_1^v} f_i \ddot{T}_l^{\mu_2\mu_1}(\Delta g_i^1) \right) C_l^{\mu_1}(1) \quad (3-52)$$

- several families of relationships:

If two distinct crystallographic laws Δg_1 and Δg_2 are involved during the transformation, equation (3-52) can be replaced by

$$C_l^{\mu_2}(2) = \sum_{\mu_1=1}^{M_1^{(1)}} \left(\sum_{i=1}^{N_1^v} f_i \ddot{T}_l^{\mu_2\mu_1}(\Delta g_i^1) + \sum_{j=1}^{N_2^v} f_j \ddot{T}_l^{\mu_2\mu_1}(\Delta g_j^2) \right) C_l^{\mu_1}(1) \quad (3-53)$$

The case of 3, 4, etc. orientation relationships can easily be generalized from the case of 2 for which equation (3-53) has just been derived.

- non-strict orientation relationships:

The above procedures assume it is possible to describe the transformation in terms of a set of strict relationships. However if, as presented in equations (3-7) and (3-9), a continuous distribution of relationships Δg develops between the parent and product crystals, the corresponding misorientation distribution function $\ddot{W}(\Delta g)$ can be expanded into a series

$$\ddot{W}(\Delta g) = \sum_{l=0}^{\infty} \sum_{\mu_2=1}^{M_2^{(1)}} \sum_{\mu_1=1}^{M_1^{(1)}} W_l^{\mu_2\mu_1} \ddot{T}_l^{\mu_2\mu_1}(\Delta g) \quad (3-54)$$

where μ_1 and μ_2 are related to the symmetries of the initial and final crystals, respectively. On the basis of equation (3-7), the three sets of coefficients can then be related by

$$C_l^{\mu_2}(2) = \frac{1}{2l+1} \sum_{\mu_1=1}^{M_1^{(1)}} W_l^{\mu_2\mu_1} C_l^{\mu_1}(1) \quad (3-55)$$

- different probabilities for equivalent orientation relationships:

If some selection of variants occurs, the transformation has already been described by equation (3-10); in this case, the variant selection function $\dot{v}(g)$ is introduced, leading to:

$$\ddot{f}^{\alpha}(g^{\alpha}) = \int_{\Delta g} \ddot{W}(\Delta g) \dot{v}(g^{\gamma}) \ddot{f}^{\gamma}(g^{\gamma}) d\Delta g \quad \text{where} \quad g^{\gamma} = \Delta g^{-1} g^{\alpha} \quad (3-56)$$

where $\dot{v}(g^{\gamma})$ can also be expanded into a series

$$\dot{v}(g) = \sum_{l=0}^{\infty} \sum_{r=-l}^{-l} \sum_{s=1}^{N(l)} V_l^{rs} \dot{T}_l^{rs}(g) \quad (3-57)$$

The four sets of coefficients, $C(1), C(2), W$ and V , can be related by [30]

$$C_{l_2}^{\mu_2 \nu_2}(2) = \sum_{l_1=0}^{\infty} \sum_{\mu_1=1}^{W_1(l_1)} \sum_{s=1}^{N(l_1)} a_{l_2}^{\mu_2 \nu_2 \mu_1 \nu_1} C_{l_1}^{\mu_1 \nu_1}(1) \quad (3-58)$$

with

$$a_{l_2}^{\mu_2 \nu_2 \mu_1 \nu_1} = \frac{1}{2l_2+1} \sum_{s=-l_2}^{+l_2} \sum_{l=0}^{\infty} \sum_{s=1}^{N(l)} \sum_{m=-l_1}^{+l_1} \left(\ddot{A}_{l_1}^{\mu_1 \nu_1}(l_1 l m r | l_2 s) \right. \\ \left. l_1 \nu_1, +l_2 s \right) W_{l_2}^{\mu_2 \nu_2} V_l^r \quad (3-59)$$

where $s=m+r$

In equation (3-59), the coefficients $\ddot{A}_l^{\mu \nu}$ are the symmetry coefficients according to the definition of the symmetric harmonic functions $T_l^{\mu \nu}$, $(l_1 l m r | l_2 s)$ are the usual Clebsch-Gordan coefficients and $\{l_1 \nu_1 \nu_2 | l_2 \nu_2\}$ are the coefficients for the symmetric functions $\ddot{T}_l^{\mu \nu}$ corresponding to the sample symmetry. All these coefficients are pure mathematical quantities.

Equation (3-58) establishes a general relationship between the starting γ texture, the crystallographic transformation law, the variant selection function and the resulting α texture. The question is whether any one of these quantities can be determined if the other three are known, and this leads to three different types of study which are briefly discussed in turn below: the derivation of the final texture, the determination of the initial texture, and the study of the transformation law and selection rule.

- calculation of the α texture

Mathematically, the most straightforward problem is the calculation of the α texture if the starting γ texture is known (by its set of C coefficients), this will be called the *transformation method* as in the case of the discrete approach. This is possible if the coefficients W of the transformation function and V of the variant selection function are known. A difficulty appears, however, in equations (3-58) and (3-59) in which the summations on l_1 and l should be carried out up to infinity. These two series therefore have to be truncated at L_1 and L , respectively. Furthermore, since the final coefficients of degree l_2 depend on the coefficients of all degrees l_1 , it is

no longer possible to treat the even and odd parts of the two ODF's separately [8,53]. In the simple cases where no variant selection occurs, however, these two limitations disappear and equation (3-49) relates only the coefficients of identical degree l .

- calculation of the γ texture :

In many cases it is more important to calculate the starting ODF \hat{f}^γ when the resulting texture \hat{f}^α has been measured. This is of special interest in the case of the $\gamma \rightarrow \alpha$ transformation in steels for which it is extremely difficult under most practical conditions to measure the γ texture directly, whereas it is easy to determine the α texture. As just mentioned above for the α texture, the calculation of the γ texture, also called the *untransformation* method, requires that the coefficients a of equation (3-59) are known. The problem is then to solve equation (3-58) for the unknown $C_l^{\mu_1 \nu_1}(1)$, and this is generally possible if $M_1(l) = M_2(l)$, i.e. if the symmetry of the parent crystal is greater than that of the product crystal. In particular, when both crystal lattices have identical symmetries (e.g. cubic-cubic transformations), then $M_1(l) = M_2(l)$ and in general a solution can be found. The mathematical condition for the existence of a solution is of course that the system should not be *singular*.

- calculation of the transformation coefficients :

The calculation of a set of transformation coefficients a from the corresponding $C(1)$'s and $C(2)$'s would only be possible if as many pairs of textures were available as there are terms in the summation of equation (3-58). This shows that a direct determination of the a 's does not seem possible without additional assumptions.

If an equal probability of occurrence is assumed for the variants, equation (3-55) remains to be solved. This is generally possible if $M_1(l) = N(l)$, i.e. if the symmetry of the parent crystal is greater than that of the sample, which is true in many cases such as rolled cubic systems. When the number of equations is larger than the number of unknowns, it is possible to determine the W 's using a least-squares method to minimize

$$\sum_{\nu=1}^{N_l} \alpha_\nu \left(C_l^{\mu_2}(2) - \frac{1}{2l+1} \sum_{\mu_1=1}^{M_l} W_l^{\mu_2 \mu_1} C_l^{\mu_1}(1) \right)^2 \quad \text{for each pair of } l \text{ and } \mu_2 \quad (3-60)$$

where α_ν are weight factors, which can be given equal values if desired.

By contrast, when variant selection is involved, equation (3-55) may still be assessed if the orientation relation of the transformation is assumed to be a well-defined crystallographic relationship Δg_0 , such as the KS or NW. As already

mentioned, there may exist a certain spread about these ideal Δg_0 's, but in first approximation, this spread can be given a gaussian form defined by its angular peak width ω_0 , so that the $W_l^{\mu_1 \mu_2}$ coefficients can be calculated from

$$W_l^{\mu_2 \mu_1} = \frac{\exp(-l^2 \omega_0^2/4) - \exp(-(l-1)^2 \omega_0^2/4)}{1 - \exp(-\omega_0^2/4)} \frac{\dot{I}_l^{\mu_2 \mu_1}(\Delta g_0)}{\dot{I}_l^{\mu_2 \mu_1}(\Delta g_0)} \quad (3-61)$$

As a result, equation (3-50) can be changed to

$$C_{l_2}^{\mu_2 \nu_2}(2) = \sum_{l=0}^{\infty} \sum_{r=-l}^{-l} \sum_{s=1}^{N(l)} b_{l,l}^{\mu_2 \nu_2 r} V_l^r \quad (3-62)$$

where the coefficients

$$b_{l_2 l}^{\mu_2 \nu_2 r} = \frac{1}{2l_2 + 1} \sum_{l_1=0}^{\infty} \sum_{\mu_1=1}^{M_1(l_1)} \sum_{\nu_1=1}^{N(l_1)} \sum_{s=-l_2}^{+l_2} \left(\dot{A}_{l_1}^{m \mu_1}(l_1 l m r | l_2 s) (l_1 \nu_1, l_2 - \nu_2) \right) W_{l_2}^{\mu_2 \nu_2} C_{l_1}^{\mu_1 \nu_1}(1) \quad (3-63)$$

are available from combined calculation and experiment, with $m = s = r$

Finally, it is possible, as a rule, to solve equation (3-62) for the coefficients $V_l^{\mu \nu}$, which are generally less numerous than the number of equations ($\dot{V}(g)$ is a smooth function).

CHAPTER IV

TRANSFORMATION TEXTURES IN STEELS
- LITERATURE REVIEW -

IV.1	INTRODUCTION	65
IV.2	GENERAL FEATURES	66
IV.2.1	GENERALITIES	66
IV.2.2	EVOLUTION OF TRANSFORMATION TEXTURES	66
	- the most influential parameters	
	- influence of the thermomechanical schedule	
	- influence of composition	
IV.2.3	USUAL PROCEDURES OF SIMULATION	68
	- need for indirect methods	
	- assumptions and principles of the simulations	
IV.3	FACTORS AFFECTING TRANSFORMATION TEXTURES	69
IV.3.1	EFFECT OF COMPOSITION	69
	- influence of manganese in Nb-free steels	
	- influence of manganese in Nb-containing steels	
	- influence of niobium	
	- influence of nickel	
	- influence of some other alloying elements	
	- possible mechanism	
IV.3.2	EFFECT OF ROLLING CONDITIONS	73
	- deformation in the recrystallized γ region	
	- deformation in the unrecrystallized γ region above the A_{r3}	

	<ul style="list-style-type: none"> - deformation in the $(\gamma + \alpha)$ region - deformation in the α region - through-thickness inhomogeneities 	
IV.3.3	OTHER IMPORTANT PARAMETERS	80
	<ul style="list-style-type: none"> - initial austenite grain size - cooling rate during transformation 	
IV.3.4	STABILITY OF TRANSFORMATION TEXTURES	83
	<ul style="list-style-type: none"> - further deformation - subsequent heat treatment 	
IV.4	CORRESPONDENCE BETWEEN ANALYTICALLY PREDICTED AND EXPERIMENTAL TEXTURES	84
IV.4.1	PREDICTIONS BASED ON A DISCRETE METHOD	84
	<ul style="list-style-type: none"> - pole figure analysis - ODF analysis 	
IV.4.2	PREDICTIONS BASED ON A CONTINUOUS METHOD	85
	<ul style="list-style-type: none"> - recrystallized austenite - transformation procedure - untransformation procedure - MODF analysis - variant selection function analysis 	
IV.4.3	VARIANT SELECTION	92
	<ul style="list-style-type: none"> - practical illustration - the shape deformation model - the Bokros-Parker model - the active slip system models - the Bain strain model - the geometrical parameters model 	

IV.1 INTRODUCTION

In the upper temperature domain of conventional hot working (i.e. in the *roughing* range), conventional static recrystallization takes place. At lower hot working temperatures (i.e. in the *finishing* range), rolling is followed by static recrystallization in plain C and similar steels, or by the absence of recrystallization and pancaking in Nb steels. Pancaking or strain accumulation occurs when, as in reversing mills, the time available for carbonitride precipitation is sufficient to prevent static recrystallization. When this time is short, as in strip mills, and the presence of solutes such as Nb prevents static recrystallization, dynamic recrystallization is initiated, followed by metadynamic recrystallization in the interpass intervals.

If the austenite recrystallizes prior to transformation, only a weak texture develops and is thus transmitted to the ferrite. By contrast, much sharper textures and more marked anisotropy are encountered in the controlled rolled steels which are finished below the 'no-recrystallization' temperature, T_{nr} .

The main features of the transformation textures observed in steels and iron-based alloys are summarized below (IV.2), followed by a review of the major compositional and processing parameters that affect their development (IV.3). Finally, a critical assessment is presented of earlier results obtained by simulating the evolution of texture during phase transitions (IV.4).

IV.2 GENERAL FEATURES

A general overview of the transformation textures observed in hot rolled steels is presented below, followed by a brief presentation of their dependence on certain crucial parameters. The principles of the simulations employed are also summarized

IV.2.1 GENERALITIES

The crystallographic textures present in as-hot rolled steels are derived principally from the deformation textures in the original austenite. Depending on whether or not recrystallization occurs during the final stages of rolling, the nature and intensity of the resulting texture vary considerably : if the austenite does recrystallize, a rather weak final texture is obtained at room temperature, which consists mainly of a $\{100\} \langle 011 \rangle$ peak. On the other hand, if the γ phase is rolled in the unrecrystallized range, the inherited bcc texture is found to have two maxima located near $\{332\} \langle 113 \rangle$ and $\{113\} \langle 110 \rangle$. These orientations have been reported by many investigators [41,54-59], from both pole figure and ODF analyses, for a wide range of compositions and thermomechanical treatments, irrespective of the structure of the product phase (ferrite or martensite). However, the sharpness and relative intensities have been shown to depend on a number of such parameters. These two components can be further modified, and the overall texture sharpened, by a subsequent intercritical and/or warm rolling process. Ultimately, the α and γ fibres classically observed in cold rolled and annealed steels are formed

IV.2.2 EVOLUTION OF TRANSFORMATION TEXTURES

Much work has been devoted to the influence of composition and processing parameters on transformation textures.

- the most influential parameters :

In particular, the composition, finishing rolling temperature, amounts of reduction in the unrecrystallized γ and $(\gamma + \alpha)$ regions, initial γ grain size and cooling rate during transformation have been found to modify the final texture to a noticeable degree [31,54,57,58,60-63].

- influence of the thermomechanical schedule :

The rolling schedule can be divided into 4 regions of temperature : (i) above the T_{nr} , where recrystallization of the austenite occurs, (ii) the unrecrystallized γ range between the T_{nr} and A_{r3} , (iii) the $(\gamma + \alpha)$ region from the A_{r3} to A_{r1} , and (iv) the α range below the A_{r1} . Depending on the amount of deformation in each zone and on the finish rolling temperature T_f , different components are observed in the final ODF after transformation. These are summarized in Table 4-1.

finishing range	region	main components	sharpness
$T_f > T_{nr}$	recrystallized γ region	$\{100\} \langle 011 \rangle$	low
$T_{nr} > T_f > A_{r3}$	unrecrystallized γ region	$\{332\} \langle 113 \rangle$ and $\{113\} \langle 110 \rangle$	medium
$A_{r3} > T_f > A_{r1}$	intercritical $(\gamma + \alpha)$ region	$\{332\} \langle 113 \rangle$ and $\{113\} \langle 110 \rangle$	high
$A_{r1} > T_f$	α region	α fibre $\langle 110 \rangle$ / RD γ fibre $\langle 111 \rangle$ ND	high

Table 4-1 : Main components as a function of the finishing temperature

- influence of composition :

As described above, a first important distinction arises between the steels that recrystallize before transformation and those that do not. This can be related of course to the amount and temperature of hot deformation, but also to the effectiveness of certain alloying elements in retarding the recrystallization of austenite. The development of controlled rolled C-Mn-Nb steels may be considered here as a significant achievement, as Nb addition leads to an increase in the severity of the texture.

In addition, the initial γ grain size, which can be influenced by the soaking schedule, the cooling rate during transformation, and potential subsequent annealing also influence the texture of the ultimate product. The roles played by these parameters are described in section IV.3 and have recently been reviewed by R.K. Ray and J.J. Jonas [64].

IV.2.3 USUAL PROCEDURES OF SIMULATION

In the literature, numerous attempts to simulate transformation textures have been reported [5,14,27,29,31,39-50,54-58,60,62,63,65-73]. The general principles and assumptions employed are outlined below.

- need for indirect methods :

The evaluation of austenite textures has been handicapped by the transformation it undergoes, with the result that it cannot be preserved at room temperature in most commercial steels. This has necessitated the use of indirect methods of simulation to study the development of texture during deformation and/or recrystallization prior to transformation.

- assumptions and principles of the simulations :

As stated earlier, one approach can be to *untransform* the ferrite texture according to an appropriate orientation relation (e.g. KS). It was first used in pole figure analysis and led to the important result that *austenite rolling textures can be successfully compared to the deformation textures of other fcc metals and alloys*; these are usually characterized by high stacking fault energies, as in Al, Cu or Cu-Zn alloys.

On the basis of this finding, many researchers have tried to simulate experimental ferrite ODF's by *transforming* the cold rolled textures of the previous alloys. Such a procedure involves the choice of the initial fcc texture and a reasonable degree of success was achieved provided a sufficiently wide *library* of fcc textures was available and that criteria of choice could be defined. However, no attempt has been made to justify the choice of a particular fcc texture other than comparison with experiment. Furthermore, no qualitative parameters have been proposed in support of a given choice and no justification has ever been attempted. Nevertheless, the best agreement is found when heavily cold rolled fcc textures are assumed for the austenite rolling texture or when the cube is employed as the recrystallization texture. Moreover these characteristics happen to tally quite well with the corresponding experimental textures observed in an 18-8 austenitic stainless steel (type 304L) [31,62,102,103].

IV.3 FACTORS AFFECTING TRANSFORMATION TEXTURES

A systematic study of the transformation textures in different kinds of steels cannot neglect the effects of the above mentioned compositional and processing variables on texture formation.

IV.3.1 EFFECT OF COMPOSITION

Researchers have shown that the chemical composition of steels has a significant effect on the nature and sharpness of the final transformation texture. The effects of the most sensitive alloying elements are reviewed in turn below.

- influence of manganese in Nb-free steels:

The transformation texture of simple C-Mn steels has been discussed at great length by a number of workers [54,57,58,60,63]. It can be described as a continuous distribution of orientations from $\{100\} \langle 011 \rangle$ to near $\{111\} \langle 011 \rangle$. Figure 4-1 shows

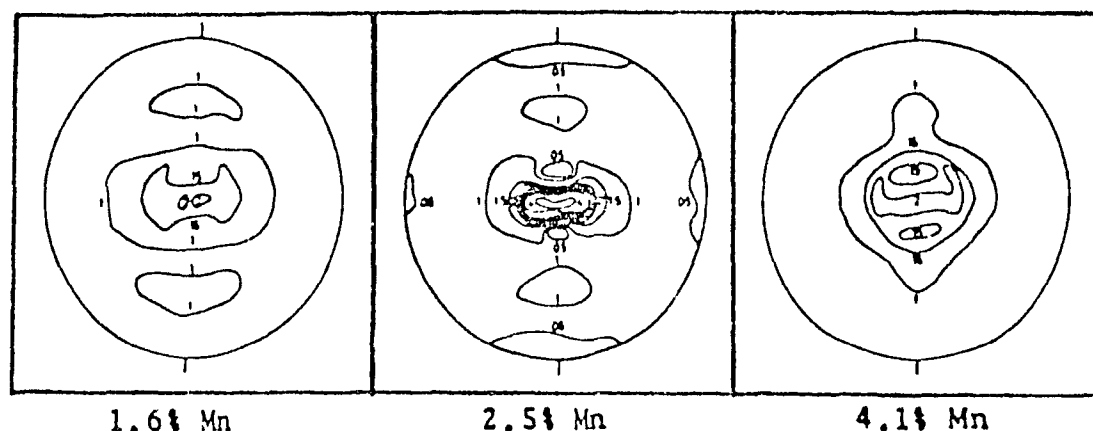


Figure 4-1: Effect of Mn on the textures of Nb-free steels (100 pole figures).

how the transformation texture of a 0.06%C steel finished at 800°C changes as a function of Mn content [54]. Modifications both in the shape and intensity can be noticed, although the 100 pole figures are all of the same $\{100\} \langle 011 \rangle$ type. The texture severity increases with decreasing finishing temperature T_f although, for these steels, the textures are far from severe (Figure 4-2) [60].

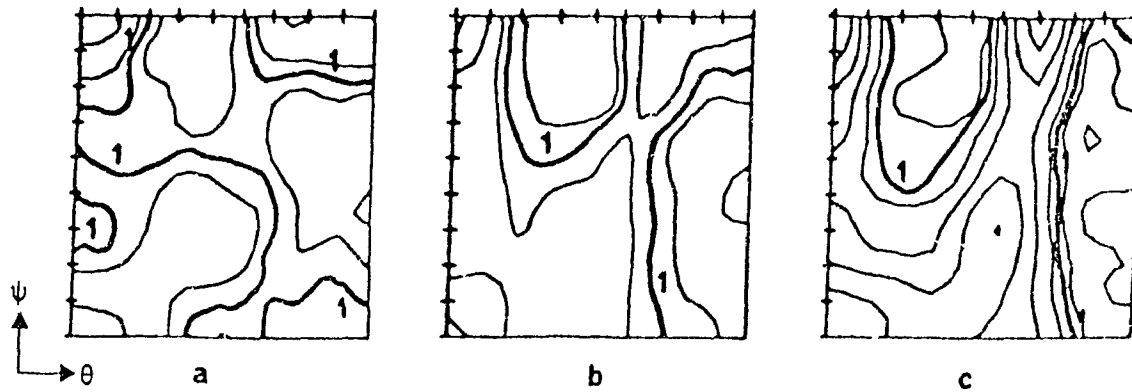


Figure 4-2. Effect of T_f on the textures of Nb-free steels ($\phi = 45^\circ$ sections):
(a) $T_f = 900^\circ\text{C}$ (b) $T_f = 760^\circ\text{C}$ (c) $T_f = 600^\circ\text{C}$.

- influence of manganese in Nb-containing steels:

Figure 4-3 shows the $\phi = 45^\circ$ sections and Figure 4-4 the skeleton lines for C-Mn-Nb steels with various Mn contents. With 1.28% Mn, $\{113\}\langle 110 \rangle$ is the main component and $\{332\}\langle 113 \rangle$ is only a minor peak. When the Mn content is increased, the microstructure is changed from polygonal ferrite/pearlite to acicular ferrite. With this change, a large increase in $\{332\}\langle 113 \rangle$ is observed, whereas the $\{113\}\langle 110 \rangle$ is rather insensitive to Mn content [54]. It is also apparent that the influence of Mn is significantly enhanced when Nb is added.

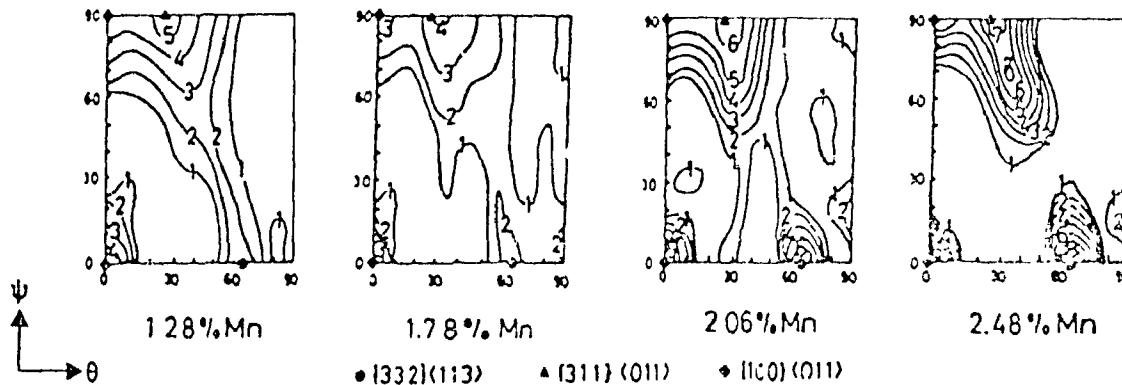


Figure 4-3: Effect of Mn on the textures of Nb-containing steels ($\phi = 45^\circ$ sections).

- influence of niobium:

From the previous paragraphs, it can be concluded that the addition of niobium increases the severity and modifies the nature of the transformation texture over a wide range of finishing temperatures, although the effect is stronger at higher T_f 's. This trend has been attributed to its effectiveness in retarding the recrystallization of austenite, which allows more deformation to accumulate before transformation.

- influence of nickel:

Transformation textures in Fe-Ni alloys are known to be strongly influenced by the Ni content [42,43,58,74]. Fe-22.5%Ni and Fe-30.8%Ni alloys were rolled 74% at 100°C and 500°C in the austenite phase and subsequently transformed to martensite [58]. Their textures are compared with that of a 2.48%Mn steel in Figures 4-5 and 4-6. The similarity with Fe-22.5%Ni is clear. Although $\{332\} \langle 113 \rangle$ was always found

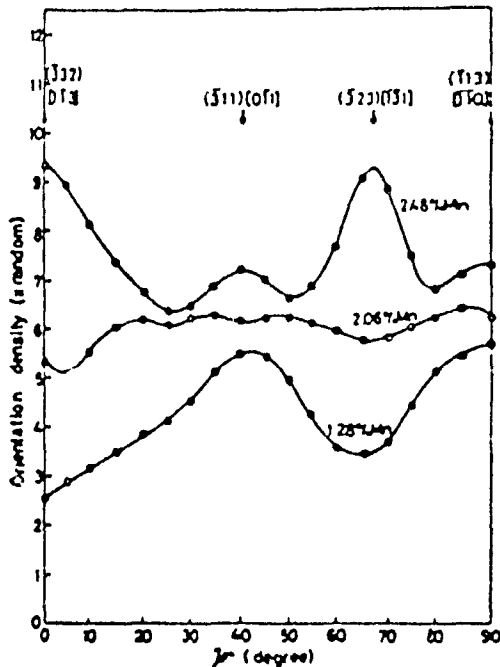


Figure 4-4 : Skeleton lines of Nb steels.

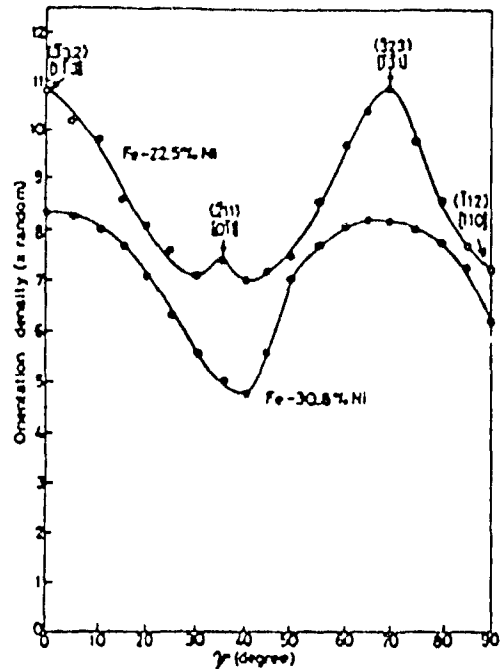


Figure 4-5 : Skeleton lines of Fe-Ni alloys.

to be the main orientation, an increase in Ni content leads to its broadening and lowering, whereas an increase in the rolling temperature generally reduces the severity of the texture. $\{113\} \langle 110 \rangle$ is also weakened by the addition of nickel. The effect of Ni on the texture of a C-Mn-Nb steel is illustrated in Figure 4-7 [54]. It is shown that $\{332\} \langle 113 \rangle$ develops remarkably as the Ni content is increased. Ni and Mn thus exhibit very similar behaviors, although larger amounts of Ni (10 times more according to reference [57]) are required to obtain an equivalent effect.

- influence of some other alloying elements:

Transformation textures are generally weakened by lowering the content of alloying elements such as C, Mn, Ni, Cr, Mo [54,57]. Comparing the (100) pole figures of a 1% Mn steel with and without Cr and Mo addition (Figure 4-8), it can be concluded that these additions enhance the formation of transformation textures[54].

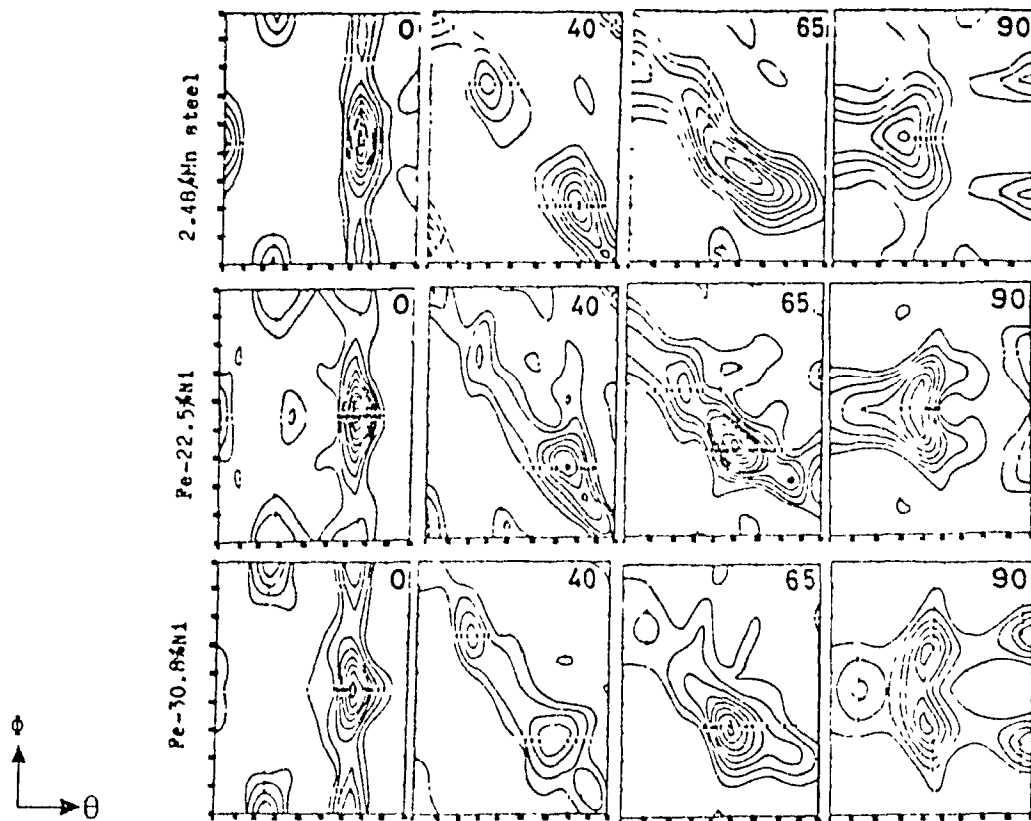


Figure 4-6 : Partial ODF's of 2.48% Mn steel, Fe-22.5Ni and Fe-30.8Ni (ψ sections).

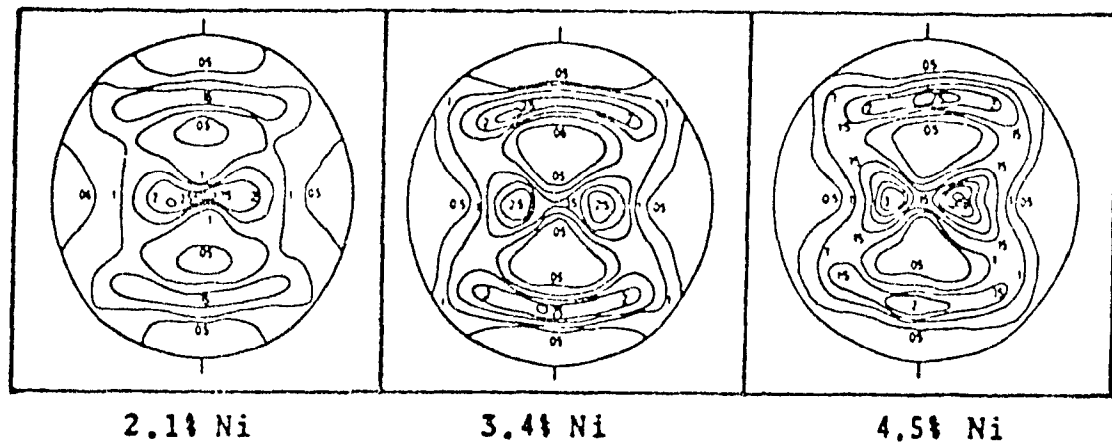


Figure 4-7 : Effect of Ni on the textures of C-Mn-Nb steels (100 pole figures).

- possible mechanism :

The fact that $\{332\}\langle 113 \rangle$ is more sensitive to the amount of alloying element and to the cooling rate (see IV.3.3) than $\{113\}\langle 110 \rangle$ suggests that the process of texture inheritance depends on the orientation of the γ grains. In fact, at high temperatures, nucleation might occur preferentially at $\{112\}\langle 111 \rangle$ than at $\{110\}\langle 112 \rangle$ austenite grain boundaries. $\{332\}\langle 113 \rangle$, which is thought to come from the $\{110\}\langle 112 \rangle$, is therefore more weakened for low alloy content or slowly

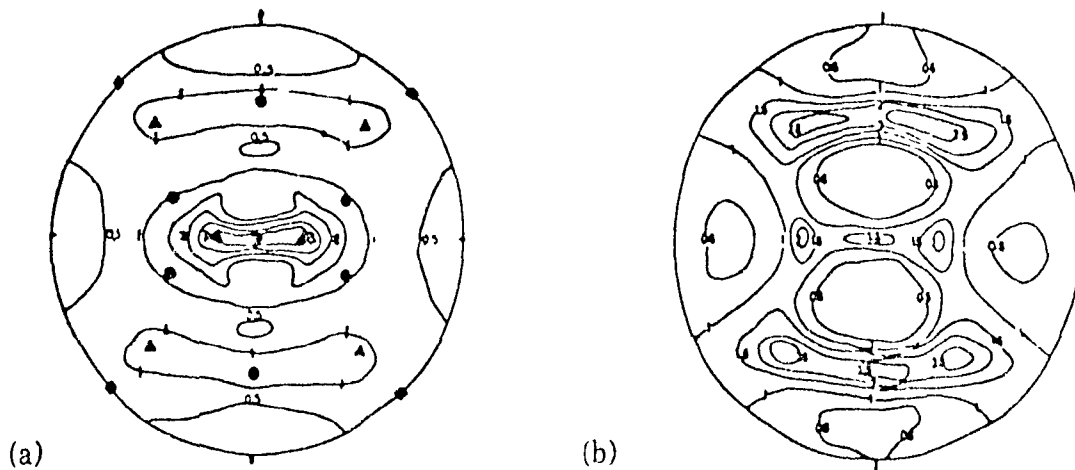


Figure 4-8: (a) C-Mn-Nb steel (b) C-Mn-Nb steel with 0.3% Mo and 0.7% Cr (100 pole figures)

cooled specimens [54]. However, the effect of alloying elements on the austenite texture is not intense enough to lead to any transition from the metal- to the alloy-type (which has never been observed). In addition, the orientation dependence of the grain growth process might differ from that of nucleation; thus the texture produced during nucleation could be weakened by the subsequent growth [57]. Experimental results support these ideas [63,75,76].

IV.3.2 EFFECT OF ROLLING CONDITIONS

The inheritance of a strong transformation texture by the α phase depends principally on the severity of the rolling texture of the parent austenite, which in turn is influenced by the temperature and accumulated amount of deformation.

- deformation in the recrystallized γ region:

Hot rolling above the no-recrystallization temperature generally results in a weak $\{100\}\langle 011 \rangle$ transformation texture [31,55,58,60-62,77-80]. The ODF of a C-Mn-Nb steel quenched after 80% reduction at 1000°C is presented in Figure 4-9 [60]. At this temperature, the austenite should be almost fully recrystallized [81]. The texture appears mostly as an extremely weak (severity parameter = 0.22) $\{100\}\langle 011 \rangle$. Figure 4-2-a shows the $\phi = 45^\circ$ section of a C-Mn steel rolled 80% in the austenite range at 900°C; here the intensity is really low and the texture consists of $\{100\}$ - $\{111\}\langle 011 \rangle$ orientations [60]. The ferrite texture is thought to be inherited from a strong cube texture $\{100\}\langle 001 \rangle$, as confirmed elsewhere [31], provided sufficient reduction (80% at least) has been applied.

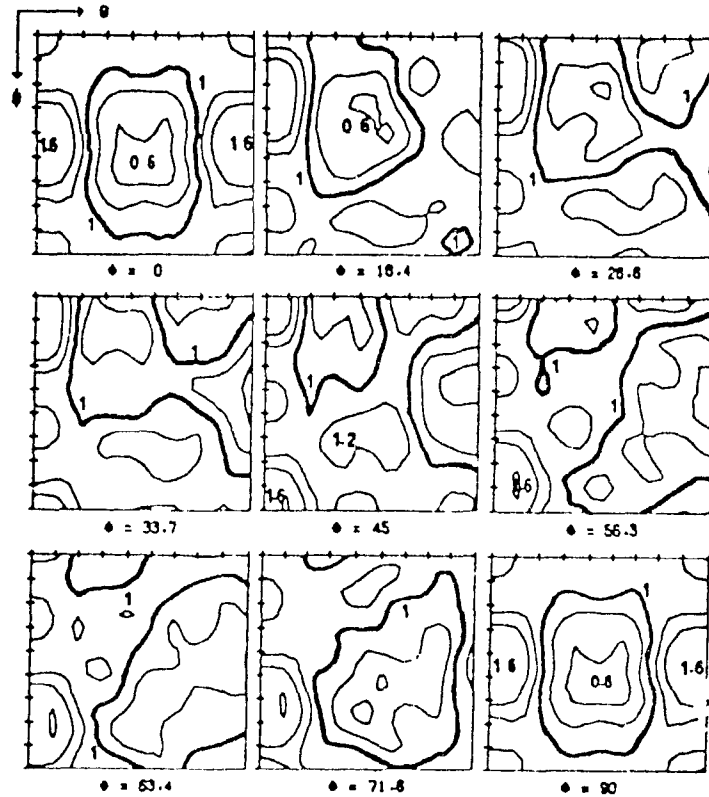


Figure 4-9 : ODF of a C-Mn-Nb steel quenched after 80% reduction at 1000°C.

- deformation in the unrecrystallized γ region above the A_{r3} :

Finishing down to near the A_{r3} in low carbon steels inhibits grain growth [82]. Further inhibition can be produced by alloying additions, such as $\sim 0.04\%$ Nb, which stop recrystallization at about 900°C and introduce a high density of deformation bands into the matrix. It is well established that the textures observed in specimens finished above the A_{r3} are inherited from the austenite through the lattice relationship existing between the two phases. The difference in texture between Nb-free and Nb-V steels finished above 800°C can be explained in terms of the difference in the austenite texture [61]. The main components were identified as $\{332\}\langle 113 \rangle$ and $\{113\}\langle 110 \rangle$, or the neighboring orientations $\{554\}\langle 225 \rangle$ and $\{112\}\langle 110 \rangle$ or $\{4\ 4\ 11\}\langle 110 \rangle$, respectively [31,54,58,60-63,67,77]. There may also remain some $\{100\}\langle 011 \rangle$ [31] after rolling in the recrystallization region.

Figures 4-10 (a) and (b) represent the $\phi = 45^\circ$ sections of a C-Mn-Nb steel finished at 850°C and 800°C, respectively [43]. $\{332\}\langle 113 \rangle$ and $\{4\ 4\ 11\}\langle 110 \rangle$ are already strong and gradually rotate with decreasing temperature towards $\{554\}\langle 225 \rangle$ and $\{223\}\langle 110 \rangle$, respectively (Figures 4-10(c),(d),(e)). This is confirmed by the skeleton lines shown in Figure 4-10(f), although $\{332\}\langle 113 \rangle$ does not appear as an

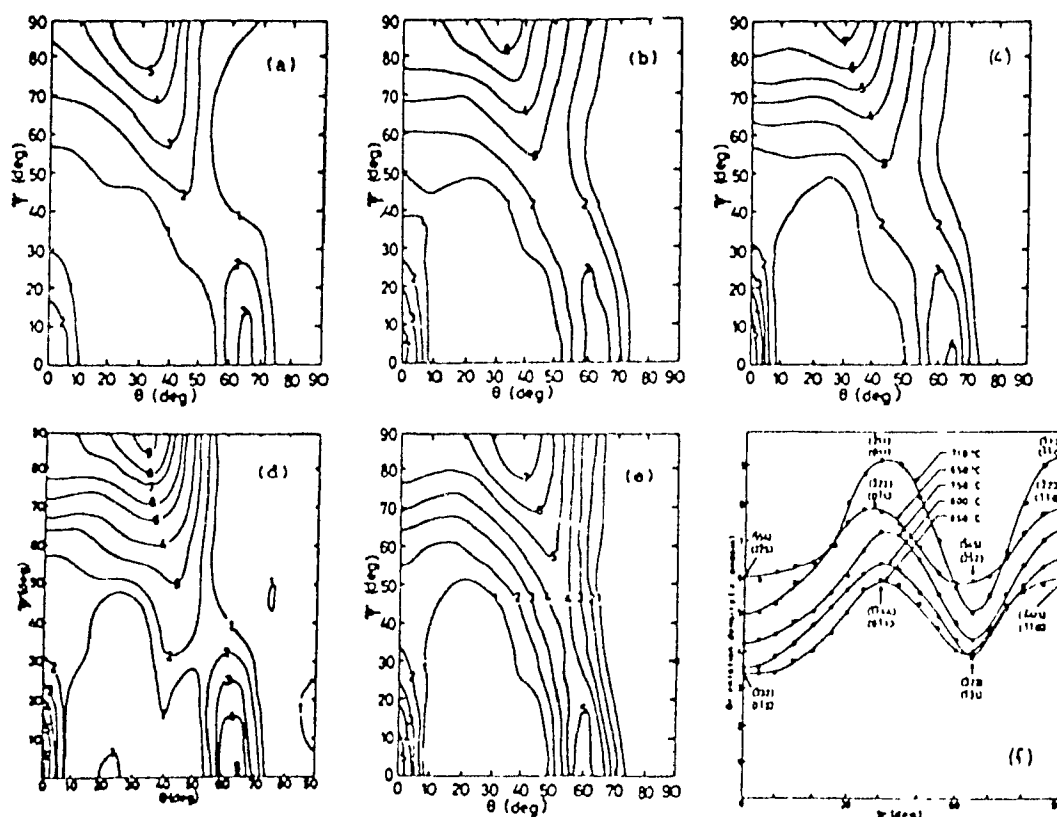


Figure 4-10: $\phi = 45^\circ$ sections of a C-Mn-Nb steel finished at:
(a) 850°C, (b) 800°C, (c) 750°C, (d) 710°C, (e) 650°C, (f) skeleton lines.

independent peak but rather in the trail of the $\{4\ 4\ 11\} \langle 110 \rangle$. As T_f is decreased, the intensity of the skeleton line gradually increases accompanied by the shifts of the peaks described above [61]. From Figures 4-11 and 4-12, which represent the $\langle 110 \rangle // \text{TD}$ and $\langle 110 \rangle // \text{RD}$ fibres, it can be concluded that the $\{4\ 4\ 11\} \langle 110 \rangle$ component is more sensitive to T_f than the $\{332\} \langle 113 \rangle$, although both are sharpened when T_f is reduced. If the amount of reduction is lowered for a given finishing temperature, the severity drops and the intensity of the $\{332\} \langle 113 \rangle$ decreases in comparison with the $\{113\} \langle 110 \rangle$ [31].

The textures of a C-Mn steel finish rolled at same temperatures were considerably weaker than those of the above Nb-V steel, and consisted of a broad $\{332\} \langle 113 \rangle$ peak and some $\{100\} \langle 011 \rangle$ [61]. Similar results have been reported by others [31,60] and the importance of the amount of rolling in the austenite emphasized [31].

- deformation in the $(\gamma + \alpha)$ region:

Below the A_{r3} , the transformation to ferrite occurs, and the microstructure consists of a mixture of ferrite and austenite, both deforming without substantial recrystallization. The textures observed in specimens finished in the $(\gamma + \alpha)$ or α

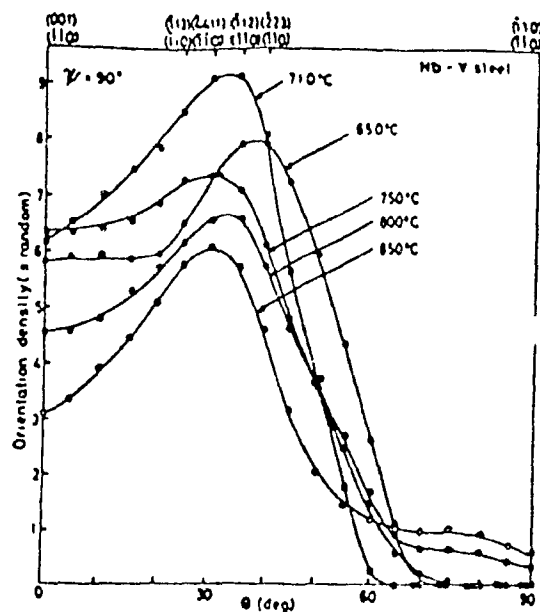
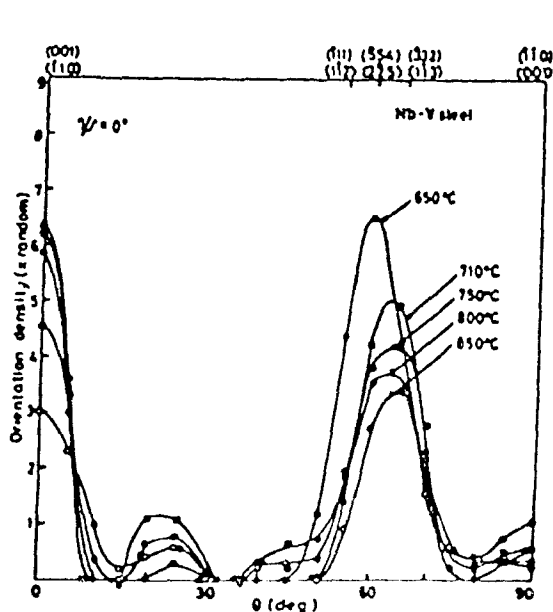


Figure 4-11: Densities along $\langle 110 \rangle // TD$ of a C-Mn-Nb steel. Figure 4-12: Densities along $\langle 110 \rangle // RD$ of a C-Mn-Nb steel.

range are far more severe than those finished above the A_{r3} [60,83-88]. In Nb-containing steels, they have been found to consist of two components, namely (i) the orientations lying in the range between $\{001\} \langle 110 \rangle$ and $\{112\} \langle 110 \rangle$ (partial fibre having the $\langle 110 \rangle$ axis parallel to RD), and (ii) a fibre texture having the $\langle 111 \rangle$ axis parallel to ND [54,58,60,83]. Figures 4-10 (c) and (d) show the $\phi = 45^\circ$ sections of a C-Mn-Nb steel finished at 750°C (upper $\gamma + \alpha$ range) and 710°C (lower $\gamma + \alpha$ range), respectively. As confirmed in Figures 4-10(f), 4-11 and 4-12, these textures mainly consist of a strong $\{112\} \langle 110 \rangle$ component, which sharpens as T_f is decreased, an increasing $\{100\} \langle 011 \rangle$, probably resulting from α recrystallization, and a second order peak near $\{554\} \langle 225 \rangle$. In the case of Nb-free steels, Figures 4-13 to 4-16 indicate the presence of a strong $\{100\} \langle 011 \rangle$ component due to γ recrystallization plus a minor peak near $\{332\} \langle 113 \rangle$ [58,61].

The latter components have been inferred to comprise the rolling texture of the α phase, which develops from the transformation texture inherited from the γ phase. During rolling in the $(\gamma + \alpha)$ region, the following three processes occur concurrently and successively: (i) deformation of the parent γ phase, (ii) the γ -to- α transformation, and (iii) deformation and recrystallization of the α phase. The relative contributions of these three processes to the final texture depend on the temperature and reduction of each pass and above all on the finishing temperature. Inagaki estimated the A_{r3} temperature of the steels he studied to be approximately 770°C [61] and made a distinction between finishing in the upper or lower $(\gamma + \alpha)$ range.

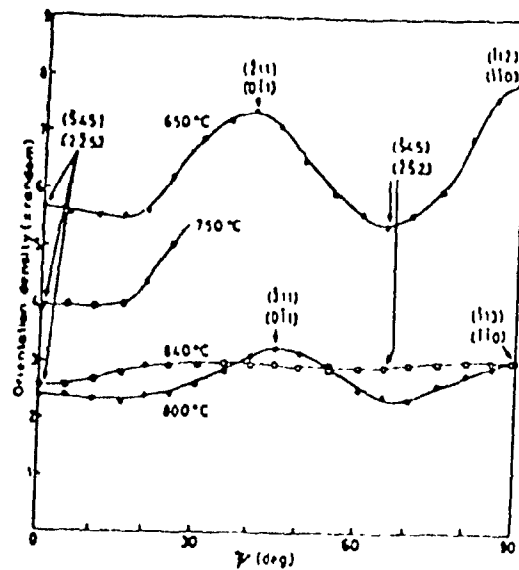


Figure 4-13: Skeleton lines of a C-Mn steel.

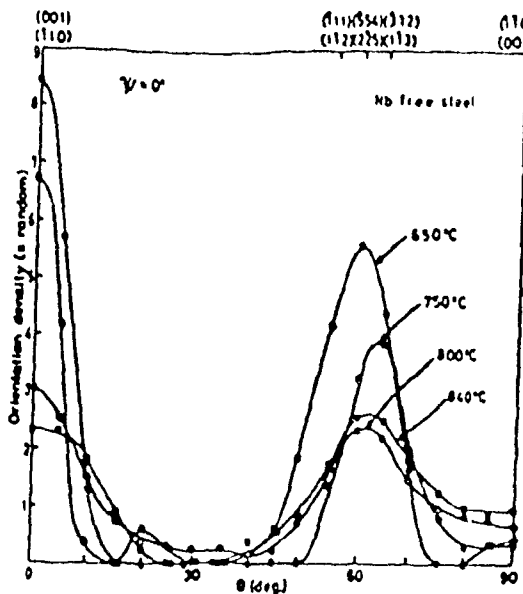


Figure 4-14: Densities along $\langle 110 \rangle // \text{TD}$ of a C-Mn steel.

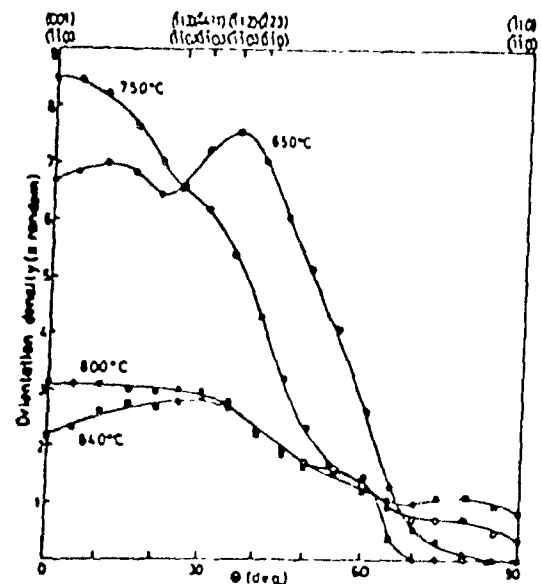
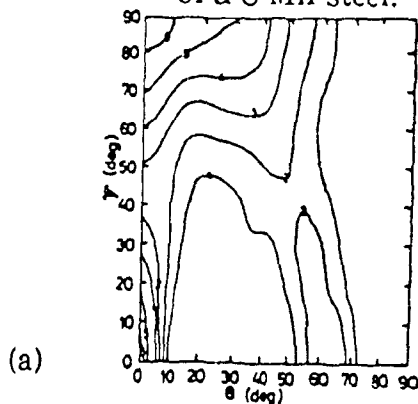
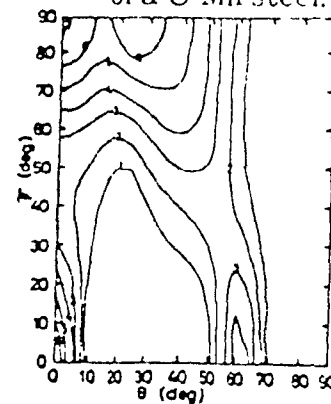


Figure 4-15: Densities along $\langle 110 \rangle // \text{RD}$ of a C-Mn steel.



(a)



(b)

Figure 4-16: $\phi = 45^\circ$ sections of a C-Mn steel finished at (a) 750°C and (b) 650°C .

In the upper ($\gamma + \alpha$) range, the amount of α phase which is formed before the final pass is relatively small. The contribution of deformation in the α phase to the overall texture is therefore not expected to be large. In the Nb-V steels finished at 750°C, most of the $\{332\} \langle 113 \rangle$ probably formed after the final pass and the remainder did not undergo any significant change during intercritical rolling, since $\{332\} \langle 113 \rangle$ is relatively stable during rolling [89]. On the contrary, orientations in the neighborhood of $\{100\} \langle 011 \rangle$, which were formed before the final pass, are quite unstable during rolling of the α phase and rotate readily at low reductions into $\{100\} \langle 011 \rangle$ [89]. For this reason, $\{100\} \langle 011 \rangle$ is expected to be increased by lowering the finishing temperature from 800°C to 750°C.

In the Nb-V free steel, on the other hand, $\{332\} \langle 113 \rangle$ in the specimen finished at 800°C is not only low in intensity but also rather broad, extending to $\{110\} \langle 001 \rangle$. Since orientations near $\{110\} \langle 001 \rangle$ are unstable and rotate readily at low reductions into $\{332\} \langle 113 \rangle$ and to $\{554\} \langle 225 \rangle$ [89], this rotation is expected to have occurred during the final pass in the two-phase region, resulting in the development of the $\{332\} \langle 113 \rangle$ to $\{554\} \langle 225 \rangle$ orientations. However, such was not the case, and the development of a strong $\{100\} \langle 011 \rangle$ component at $T_f = 750^\circ\text{C}$ can thus be related to the recrystallization of the α phase. In fact, electron microscopic observations frequently confirm the existence of large $\{100\} \langle 011 \rangle$ recrystallized α grains in Nb-free steels and seldom in Nb-containing steels.

In the lower ($\gamma + \alpha$) range, most of the remaining austenite transforms to ferrite, with strong transformation textures inherited from the sharper austenite finish rolled at lower temperatures. At the same time, the ferrite grains already transformed at the higher temperature accumulate further deformation, resulting in the sharpening of the texture of the α phase and to some modifications: orientations in the range $\{332\} \langle 113 \rangle$ to $\{554\} \langle 225 \rangle$ rotate towards $\{554\} \langle 225 \rangle$, while orientations between $\{100\} \langle 011 \rangle$ and $\{442\} \langle 110 \rangle$ rotate to $\{332\} \langle 011 \rangle$. The $\{111\}$ /ND fibre is thus enforced as a whole when T_f is reduced. These results apply both to Nb-containing and Nb-free steels, as recrystallization is not the dominant process.

For a C-Mn steel finished rolled in the intercritical range, it can also be seen (Figure 4-2-c) that, although weak, the texture has developed the $\{111\}$ fibre. Figure 4-17 shows the textures produced by deforming a C-Mn-Nb steel in the ($\gamma + \alpha$) region 0%, 10% and 60%. The sharpness increases drastically with the amount of deformation and the $\{111\}$ fibre forms gradually with rather strong $\{112\} \langle 110 \rangle$ and $\{554\} \langle 225 \rangle$ components [90].

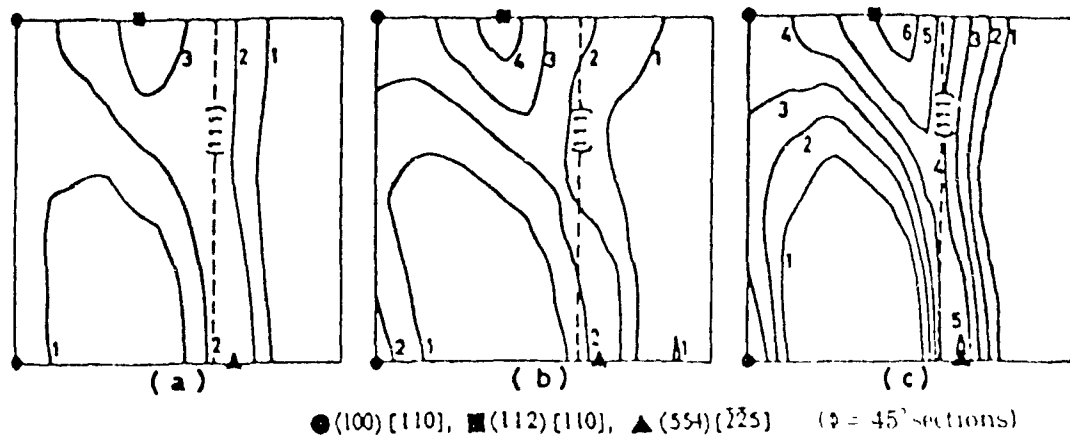


Figure 4-17: C-Mn-Nb steel rolled in the $(\gamma + \alpha)$ region (a) 0%, (b) 10% and (c) 60%.

- deformation in the α region:

The texture formed by rolling in the lower $(\gamma + \alpha)$ range is already near the stable end orientations of the α rolling texture. Therefore, orientation changes brought about by lowering the finishing temperature from 700 to around 600°C are small. For this reason, the textures of Nb-free and Nb-V steels are quite similar [61]. Figure 4-10(e) shows the $\phi = 45^\circ$ section of a C-Mn-Nb steel finished at 650°C. Combined with Figures 4-11 and 4-12, the maximum at $\{322\}\langle 011 \rangle$ is shifted from $\{211\}\langle 011 \rangle$, and a rather strong $\{554\}\langle 225 \rangle$ is seen to be shifted from $\{332\}\langle 113 \rangle$. The strong $\{100\}\langle 011 \rangle$ present in the intercritical range is reduced by further α rolling and rotates to $\{322\}\langle 011 \rangle$. The intensity of the $\{111\}$ fibre increases with the amount of deformation and when T_f is reduced.

- through-thickness inhomogeneities:

Surface textures in pure iron 90% cold rolled [91] and C-Mn-Nb steels finished at 880°C [61,62,78] were found to consist of a partial fibre having $\langle 110 \rangle$ axes parallel to ND, as suggested in Figure 4-18. These results indicate that surface textures are

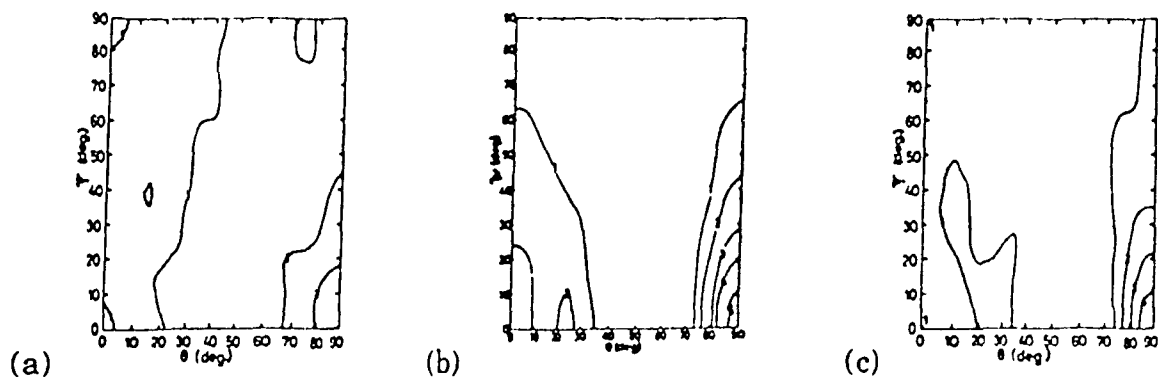


Figure 4-18: Surface texture of a Nb-V steel finished at (a) 750°C, (b) 700°C, (c) 650°C.

also greatly influenced by the finishing temperature; comparison with microstructures also indicates that they develop as a result of rolling in the α phase. In the specimens finished at 700 and 650°C by Inagaki [61], weak $\{311\} \langle 223 \rangle$ is present in addition to the fibre. These agree approximately with the main orientations of the shear texture of α iron reported by Williams [92]. It is well known that surface texture is generally related to the midsection texture by rotation about TD [62,93,94] and is not affected by recrystallization of the austenite phase. Comparison between Figures 4-10 and 4-18 indicates that this general result is satisfied in the Nb-V steels finished at 700 and 650°C with a rotation angle of 90°. The formation of a texture gradient in hot rolled steels is represented schematically in Figure 4-19 [94].

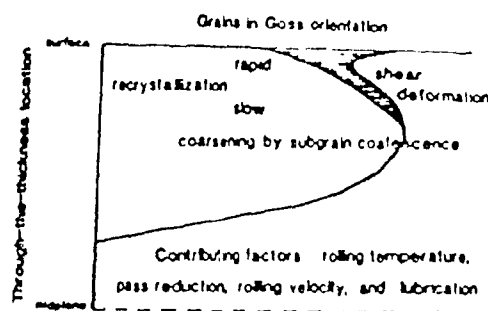


Figure 4-19: Principle of formation of a texture gradient in hot rolled sheets.

IV.3.3 OTHER IMPORTANT PARAMETERS

Two other parameters, which can be controlled in the thermomechanical schedule, are of importance in transformation textures: the austenite grain size and the cooling rate during transformation.

- the initial austenite grain size:

The austenite grain size has been reported to modify the final transformation texture [54,58,74,95]: the smaller the grain size, the sharper the texture. Figure 4-20 shows the $\phi = 45^\circ$ sections of a C-Mn-Nb steel ($T_f = 760^\circ\text{C}$) soaked at 1250 and 1050°C (large and small grains, respectively) [58]. It is clear that $\{113\} \langle 110 \rangle$ is rather insensitive to a decrease in the soaking temperature, whereas $\{332\} \langle 113 \rangle$ is strengthened remarkably. The result was the same for $T_f = 800^\circ\text{C}$, although the (100) pole figures show weaker textures [54].

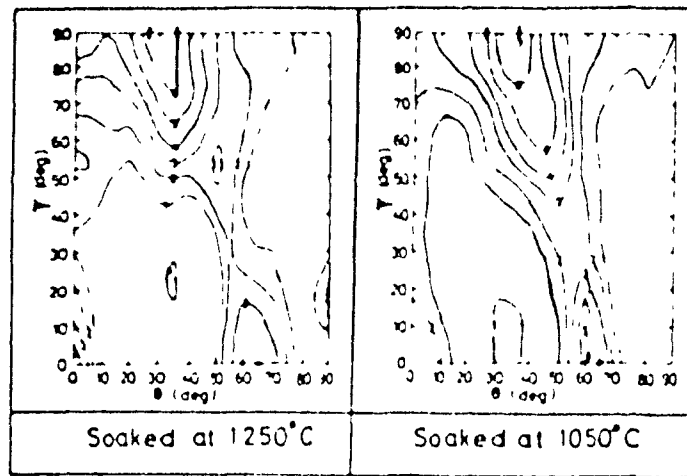


Figure 4-20 Effect of soaking temperature on the texture of C-Mn-Nb steels.

- the cooling rate during transformation.

Textures are generally weaker after slow cooling to ferrite/pearlite than after rapid cooling to martensite [44,54,58,63,95,96]. Figure 4-21 represents the $\phi = 45^\circ$ section of a C-Mn-Nb steel finished at 800 °C and cooled at different rates [58]. With decreasing cooling rate, the amount of ferrite increases and both the $\{332\} \langle 113 \rangle$ and the $\{113\} \langle 110 \rangle$ decrease remarkably. The larger contribution of growth during

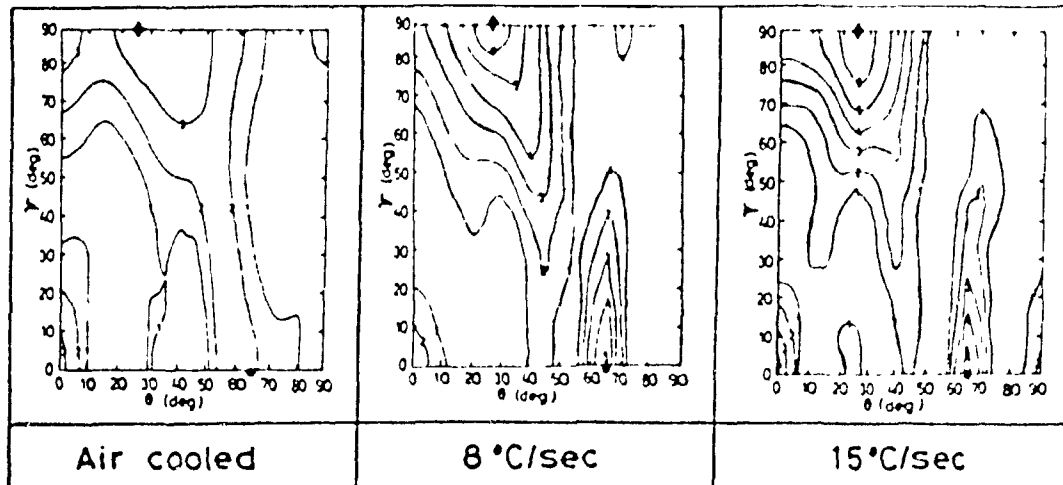


Figure 4-21 : Effect of cooling rate on the texture of controlled rolled C-Mn-Nb steels.

ferrite/pearlite formation than during the martensite transformation can explain the observed weaker ferrite textures. Also, it has been shown that the $\{332\} \langle 113 \rangle$ is weakened more than the $\{113\} \langle 110 \rangle$, probably because their nucleation rates are different. This effect was less clear in steels with lower Mn levels [58] or lower global amounts of alloying elements [63].

Figure 4-22 shows the $\phi = 45^\circ$ sections of a C-Mn-Nb steel rolled 80% in the austenite range to finish at 810 or 710°C and air cooled [60]. Comparison with the

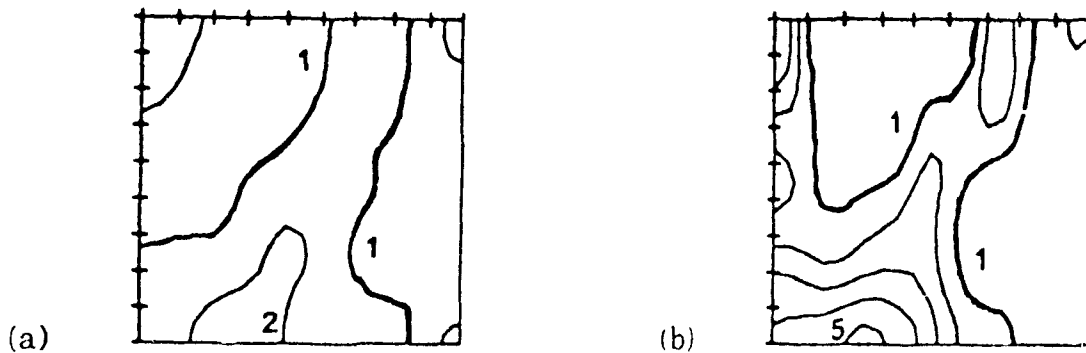


Figure 4-22: $\phi = 45^\circ$ section for a C-Mn-Nb steel after rolling at (a) 810°C, (b) 710°C

same section in Figure 4-23, in which the sample was quenched, shows that an increase in the cooling rate reduces the severity of the texture. In the two figures, the main peak is near $\{112\} \langle 110 \rangle$ and the severity increases markedly as the finishing temperature is reduced.

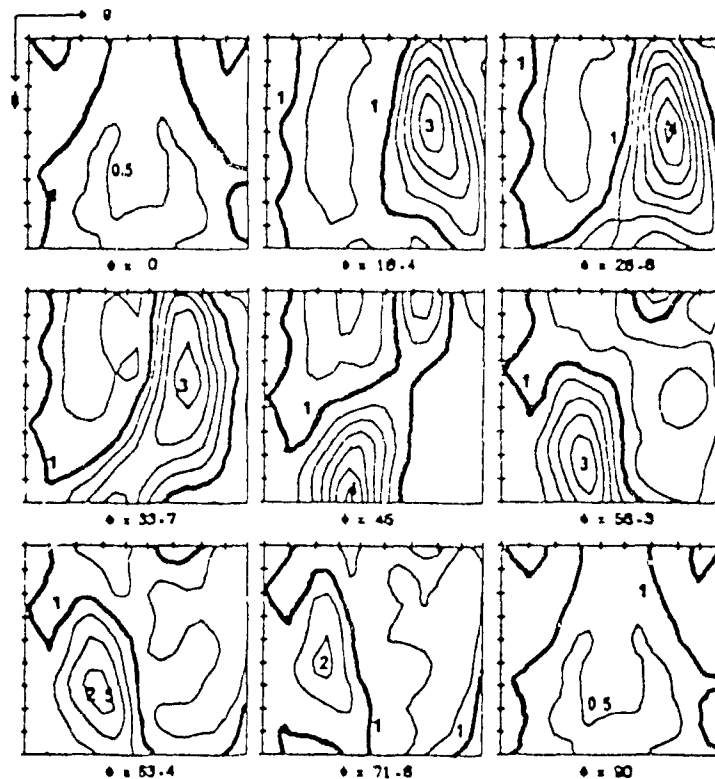


Figure 4-23: ODF of a C-Mn-Nb steel quenched after 80% reduction at 815°C.

In commercial steels, the greater weight of the slabs probably means that, in the absence of quenching, the cooling rate is lower than for experimental casts. Thus the resulting textures are expected to be less severe. Nevertheless they could still be of importance, especially in controlled rolled steels finished at lower temperatures.

IV.3.4 STABILITY OF TRANSFORMATION TEXTURES

At this point, it is worth considering the stability of the textures formed during controlled rolling, either on subsequent cold rolling or on annealing

further deformation:

As suggested by the paragraph concerning warm rolling in the α phase, further cold rolling leads to the development of the $\{111\}/ND$ fibre. For a C-Mn-Nb steel, a $\{100\}<011>$ component and a tube of orientations with $\{111\}/ND$ centered around $\{111\}<112>$ have been shown to emerge at the expense of $\{112\}<110>$ [83]. Generally, $\{112\}<110>$ has been assumed to be a stable end orientation [97,98].

- subsequent heat treatment:

It has often been reported that transformation textures formed by controlled rolling cannot be easily eliminated by simple or repeated heating into the γ range [58,74,79,99-101]. Textures of a C-Mn-Nb steel soaked at 910°C for 10 minutes and either quenched into water or air cooled are shown in Figure 4-24 [58]. Fairly strong

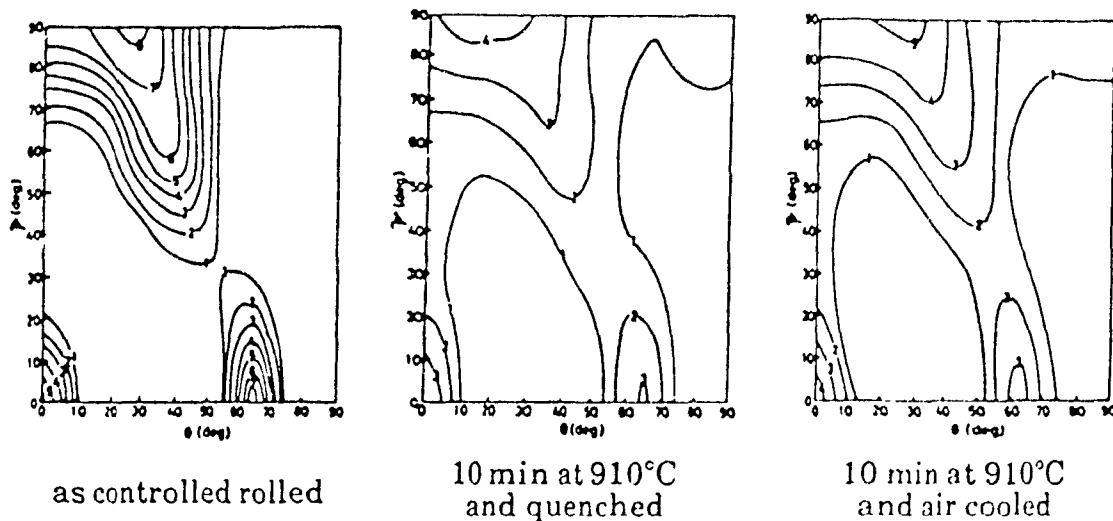


Figure 4-24 : Effect of heat treatment on a C-Mn-Nb steel ($\Phi = 45^\circ$ sections).

textures remain after these treatments, although the microstructure has changed completely. Also, variant selection appears to be absent. This can happen if, during reheating, the ferrite transforms back to the austenite texture from which it was created and if, during quenching, the austenite transforms as it did the first time.

IV.4 CORRESPONDENCE BETWEEN ANALYTICALLY PREDICTED AND EXPERIMENTAL TEXTURES

The worth of any analytical prediction should be measured by its ability to reproduce the experimental data. In the following, simulated textures will be compared to actual ODF's and pole figures.

IV.4.1 PREDICTIONS BASED ON A DISCRETE METHOD

- pole figure analysis :

In the earliest work, Jones and Walker [62] considered the major fcc rolling or recrystallization texture components [102,103] and employed the KS relationship to derive potential ferrite pole figures. They then compared them with experimental ones for a C-Mn-Nb steel rolled 50% at 950°C (as-rolled or recrystallized). The rolling texture of austenite was shown to be of the pure-metal type, and that of recrystallized austenite to be of the cube type $\{100\} \langle 001 \rangle$. No variant selection was apparent. This technique was used to ascertain whether austenite recrystallization had occurred in plain C-Mn and low alloy hot rolled steels. Using the NW relationship, a similar procedure was used to estimate the austenite texture of a martensitic 4340 steel [65]. The best agreement was found for $\{112\} \langle 111 \rangle$ plus a minor $\{110\} \langle 112 \rangle$ component, but no $\{111\}$ fibre could be assumed.

- ODF analysis :

A Cr-Ni-Mo steel rolled at 700°C and air cooled was unambiguously shown to be KS-derived from a copper (or pure-metal) type austenite texture consisting of the three classical fcc rolling components $\{112\} \langle 111 \rangle$ (Cu), $\{110\} \langle 112 \rangle$ (Bs) and $\{123\} \langle 634 \rangle$ (S) [67]. Similar conclusions were obtained in the case of Nb-containing acicular ferrite steels using $\{110\} \langle 112 \rangle$ and $\{112\} \langle 111 \rangle$ [54,57,58], as shown in Figure 4-25, where the derived orientations are plotted in the nearest sections. It should furthermore be noted that the observed maxima at $\{332\} \langle 113 \rangle$ and $\{113\} \langle 110 \rangle$ are surrounded by groups of α orientations derived mainly from $\{110\} \langle 112 \rangle$ and $\{112\} \langle 111 \rangle$, respectively. The γ rolling texture was therefore concluded to have been of the copper type. In both cases, it was not necessary to assume variant selection [57].

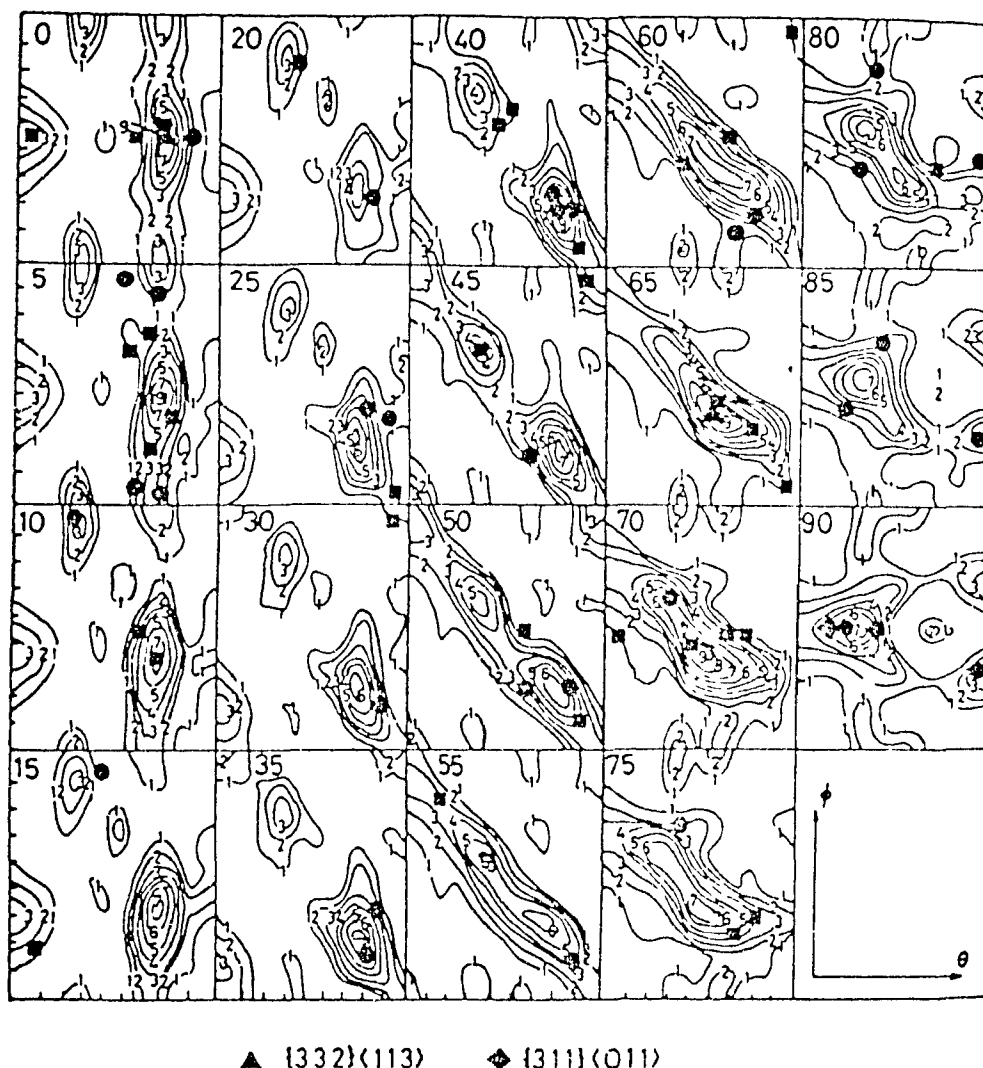


Figure 4-25: ODF of a C-Mn-Nb steel (ψ sections) and ideal orientations derived from $\{110\}\langle 112\rangle$ (■) and $\{112\}\langle 111\rangle$ (●) with the KS relationship.

An Fe-30Ni alloy was cold rolled 67% in the bcc phase and annealed to transform it into the fcc phase. The partial NW-derived and experimental ODF's are shown in Figures 4-26 and 4-27, respectively [14]. All the experimental peaks are present in the simulated ODF, although one of the predicted maxima ($\phi_2 = 45^\circ$ section) does not appear. This may result from the occurrence of some variant selection.

IV.4.2 PREDICTIONS BASED ON A CONTINUOUS METHOD

The accurate prediction of transformation textures requires a more complete description of the starting texture than the one employing ideal components. The procedures of simulation using an entire ODF have been explained in chapter III.

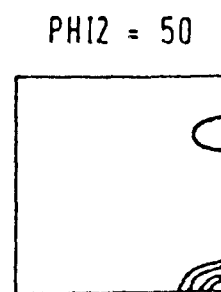
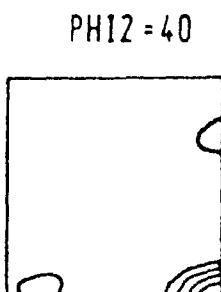
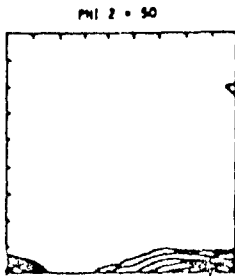
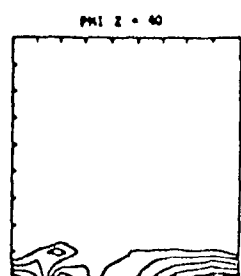
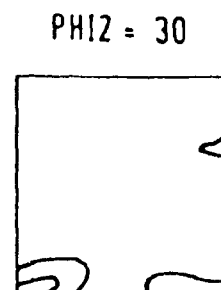
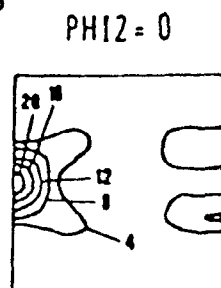
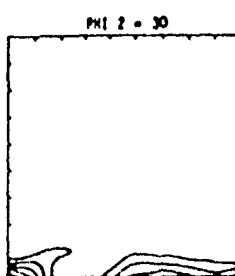
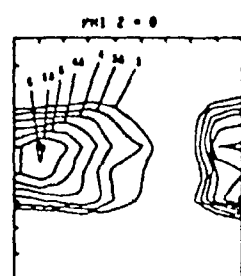


Figure 4-26 : NW-predicted ODF of an Fe-30Ni alloy cold rolled 67% in the bcc structure and transformed into fcc.

Figure 4-27 : Experimental ODF of the alloy of Figure 4-26.

- recrystallized austenite :

Figure 4-9 is the experimentally determined ODF for a C-Mn-Nb steel quenched after rolling 80% to finish at $T_f = 1000^\circ\text{C}$, where the austenite should be almost fully recrystallized. The parent austenite texture is found in Figure 4-28 [60] and consists largely of the cube component $\{100\}\langle 001 \rangle$, which is a prominent component in rolled and recrystallized fcc metals [31,60,104]. Identical results were obtained on recrystallized Fe-Ni alloys [40,41].

- transformation procedure :

Davies *et al* [60,77] used the ODF of 60% cold rolled high purity aluminum, which consists of a tube running from $\{110\}\langle 112 \rangle$ through to near $\{4\ 4\ 11\}\langle 11\ 11\ 8 \rangle$, to represent the austenite (Figure 4-29). Figure 4-30 shows the ODF predicted from Figure 4-29 with the KS relationship : there is a strong partial $\langle 110 \rangle // \text{RD}$ fibre centered around $\{112\}\langle 110 \rangle$. The ferrite texture of a C-Mn-Nb steel rolled 80% in the γ phase ($T_f = 815^\circ\text{C}$) and water quenched was shown in Figure 4-23. The correspondence between Figures 4-30 and 4-23 is most striking [60].

Depending on the amount of deformation in the fcc phase, the two texture components of an Fe-30Ni alloy (A=partial $\langle 111 \rangle // \text{ND}$ and B=partial $\langle 110 \rangle // \text{RD}$) can be separated [105]. After transformation to martensite, both fibres disappear, A giving rise to a broad peak centered on $\{110\}\langle 001 \rangle$ (Figure 4-31(a)) and B to a broad peak between $\{110\}\langle 112 \rangle$ and $\{110\}\langle 111 \rangle$ (Figure 4-31(c)).

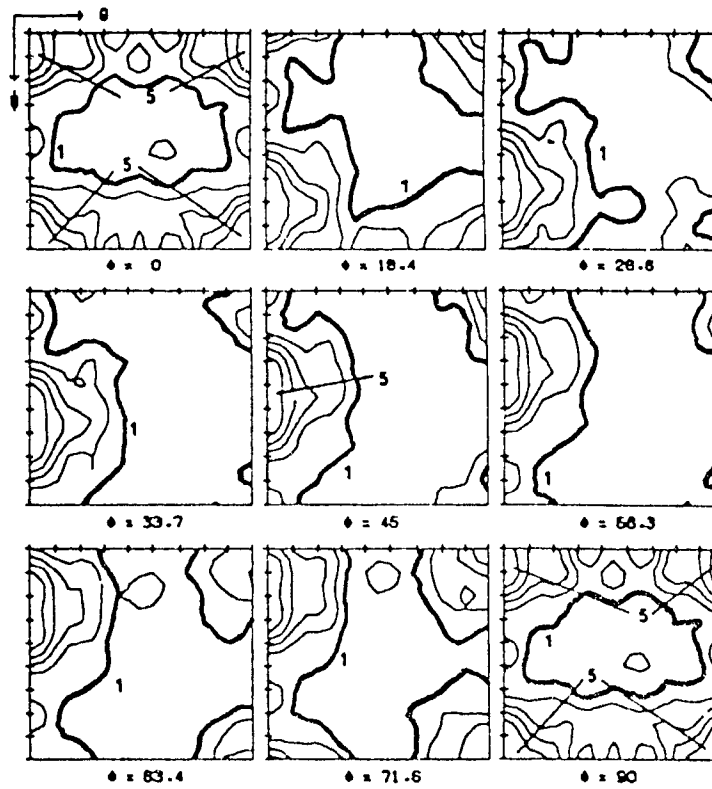


Figure 4-28 : Parent austenite ODF untransformed from Figure 4-9.

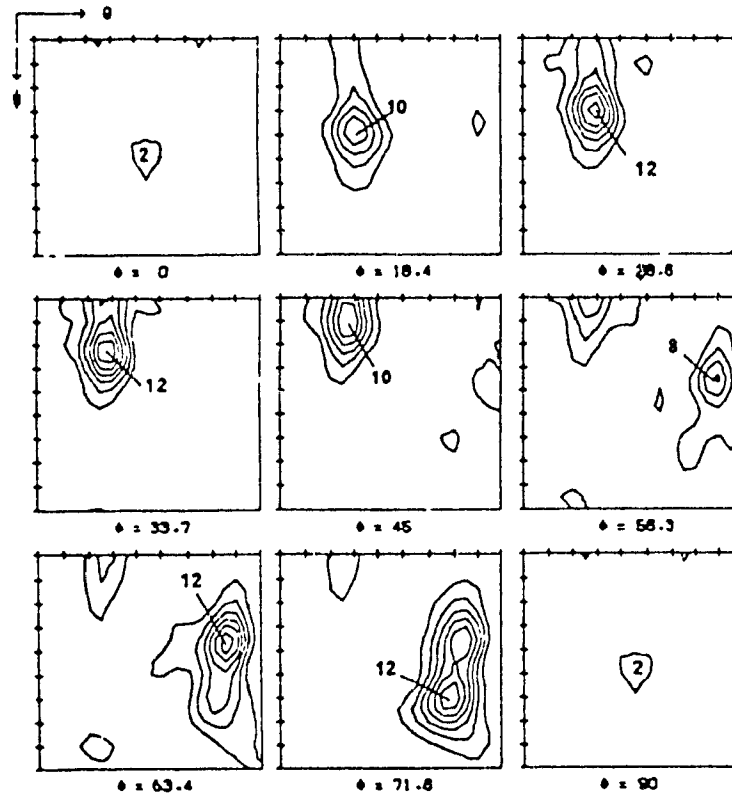


Figure 4-29 : ODF of 60% cold rolled high purity aluminum.

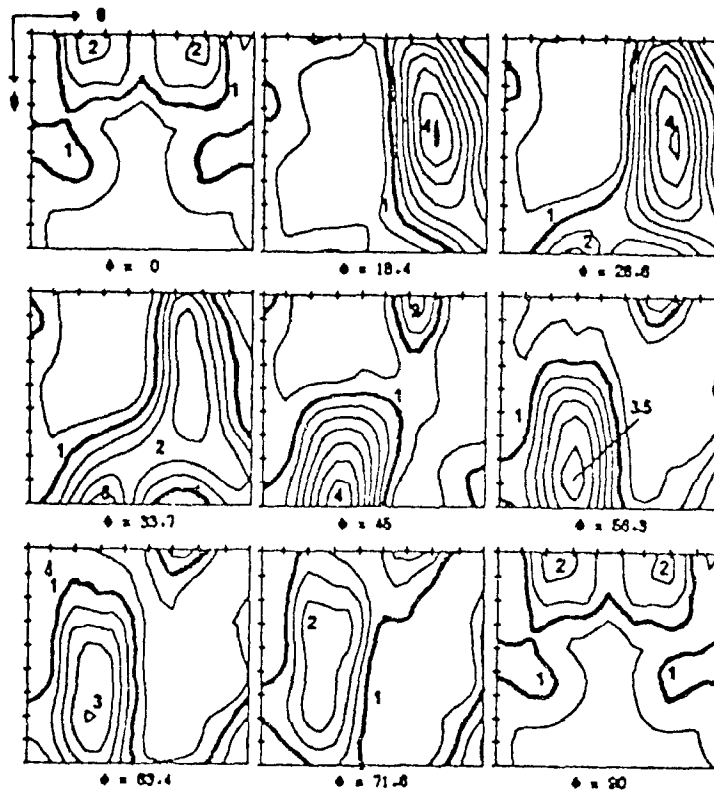


Figure 4-30 : Ferrite ODF predicted from Figure 4-29 with the KS relationship.

However, when derived analytically with the NW relationship, extra peaks not found experimentally are also predicted (Figures 4-31(b) and 4-31(d)) [27]. These calculated ODF's are less severe and no clear distinction appears between the different orientation relations.

Figure 4-32 gives the $\phi = 45^\circ$ sections of Cu and Cu-30Zn cold rolled 90%. The textures derived with the KS relationship are similar to the observed ODF's in Fe-Ni alloys rolled at 500°C [58].

- untransformation procedure :

Figure 4-33 illustrates the ODF obtained by *untransforming* Figure 4-23. It is characterized by a tube running from $\{110\}\langle 112 \rangle$ to near $\{112\}\langle 111 \rangle$ [55,60]. It is worth noting, however, that the severity is higher than for pure aluminum (used in the transformation procedure), although the main tube is recovered. Thus, the transformation and untransformation procedures are shown to predict textures correctly, although not in a strictly equivalent manner [60]. The austenite texture of a 90% rolled 5Ni steel was obtained by untransforming the martensite with the KS relationship. It consists of a $\{110\}\langle 112 \rangle$ - $\{112\}\langle 111 \rangle$ fibre plus the $\{111\}\langle 112 \rangle$ component. The latter component, which is the alloy type, has never been observed in actual austenite textures, and probably arises because the 24 variants of the KS

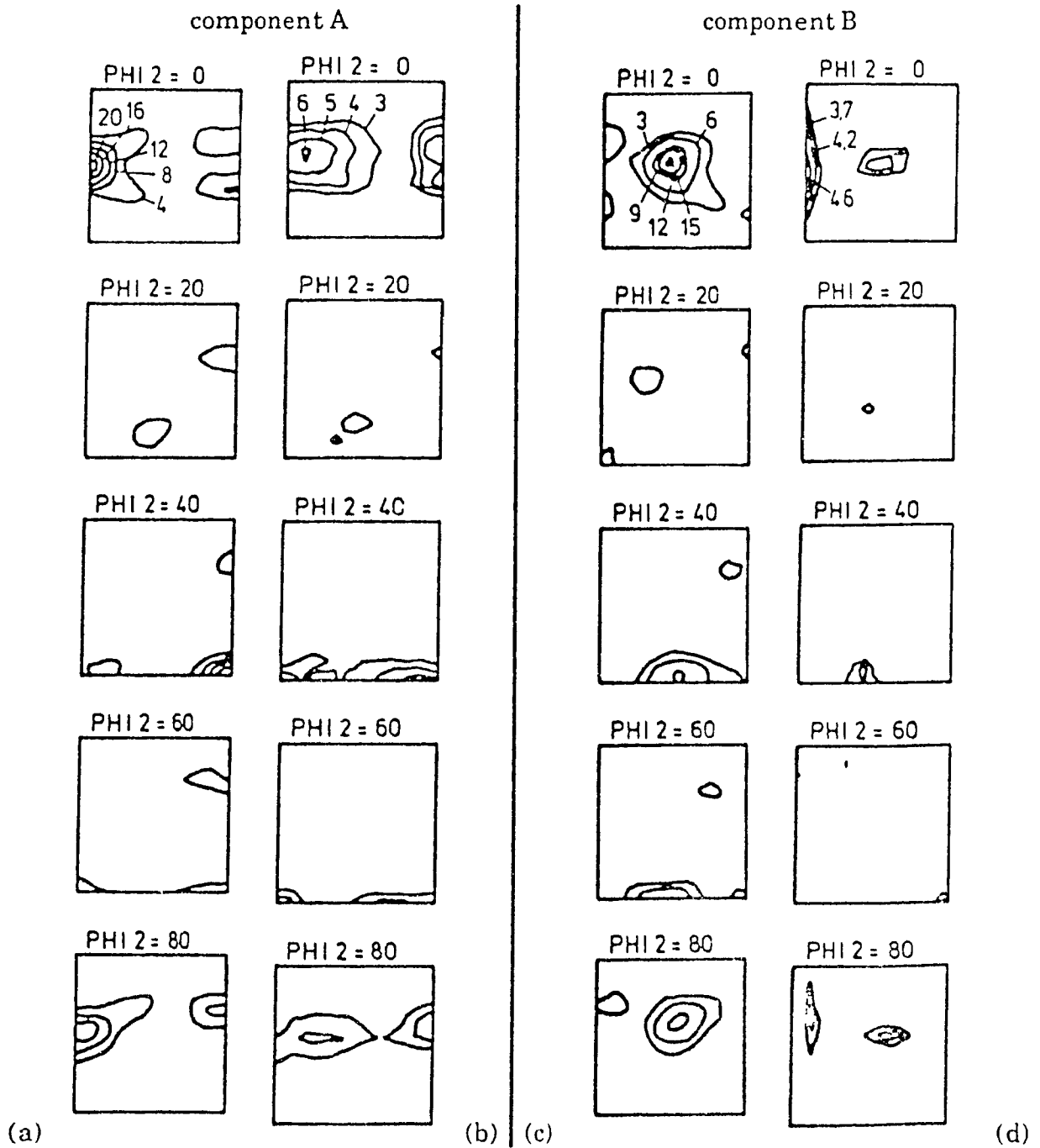


Figure 4-31 : Component A: (a) experimental, (b) NW predicted, component B: (c) experimental, (d) NW predicted.

relationship were given an equal probability of occurrence. Considerable discrepancy was also observed after 80% cross-rolling. On the other hand, in the case of a recrystallized specimen, an identical procedure led to the prediction of the classical

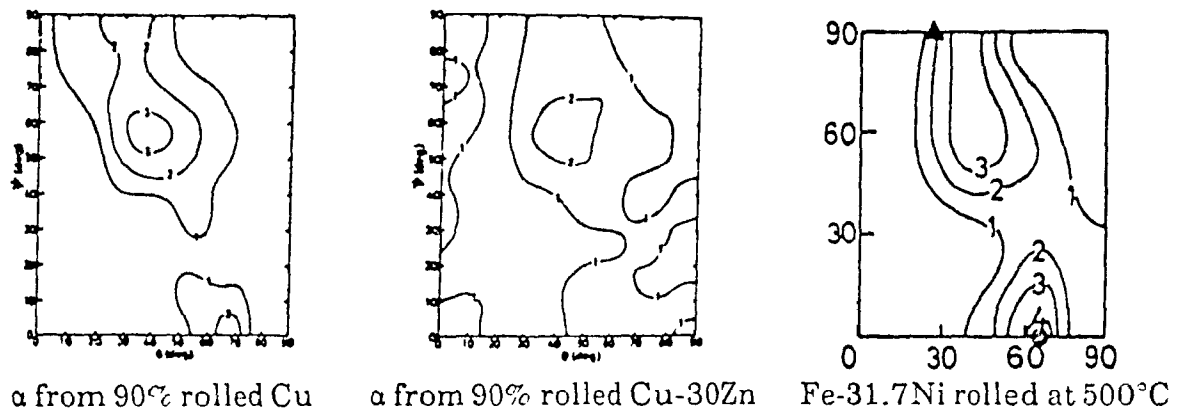


Figure 4-32 : $\phi = 45^\circ$ sections of observed and calculated ODF's.

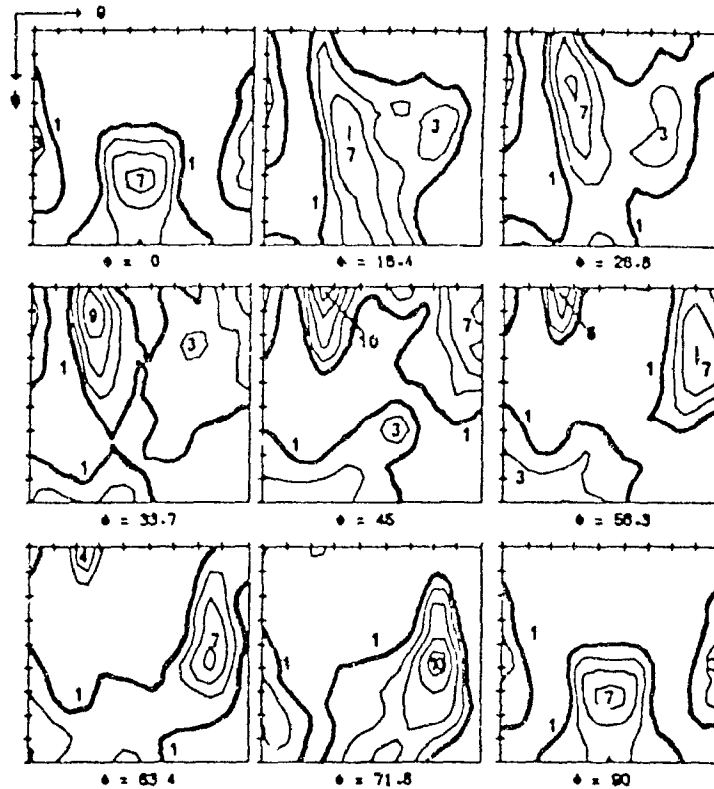


Figure 4-33 : Austenite ODF untransformed from Figure 4-23.

cube orientation. This difference was assumed to result from the high degree of symmetry of the initial cube and is likely to be a relatively rare event [31].

- MODF analysis :

The MODF can be used to determine the relationship between two textures related by an orientation dependent phase transformation provided a sufficiently high order of truncation is chosen. It should be noted that $\{100\}\langle 001 \rangle$ MODF components are produced by grains that have not undergone reorientation. The presence of peaks of significant intensity at other points is then clearly indicative of

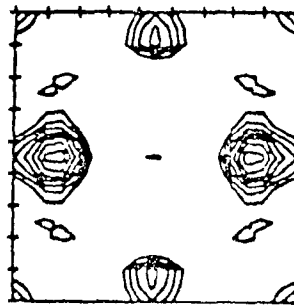


Figure 4-34 : MODF ($\phi = 0^\circ$) relating the two phases of an annealed Fe-30Ni alloy.

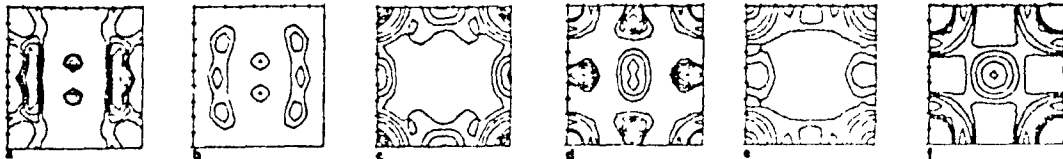


Figure 4-35 : MODF's ($\phi = 0^\circ$) relating the two phases of an Fe-30Ni alloy for prior reductions of (a) 50%, (b) 60%, (c) 70%, (d) 75%, (e) 80%, and (f) 90%.

the existence of an orientation relationship [55]. Figure 4-34 gives the $\phi = 0^\circ$ section of the MODF relating the martensite and austenite textures of an Fe-30Ni alloy 90% cold rolled and annealed. It tallies reasonably well with either KS or NW [41]. On the other hand, after cold rolling only, the agreement is poor or even bad and depends on the amount of deformation, as can be seen from Figure 4-35 [40].

- variant selection function analysis :

Variant selection functions have been calculated from the textures of the martensitic and austenitic phases of two samples of Fe-30Ni sheets rolled in different conditions assuming the KS crystallographic relationship (Figure 4-36). Starting

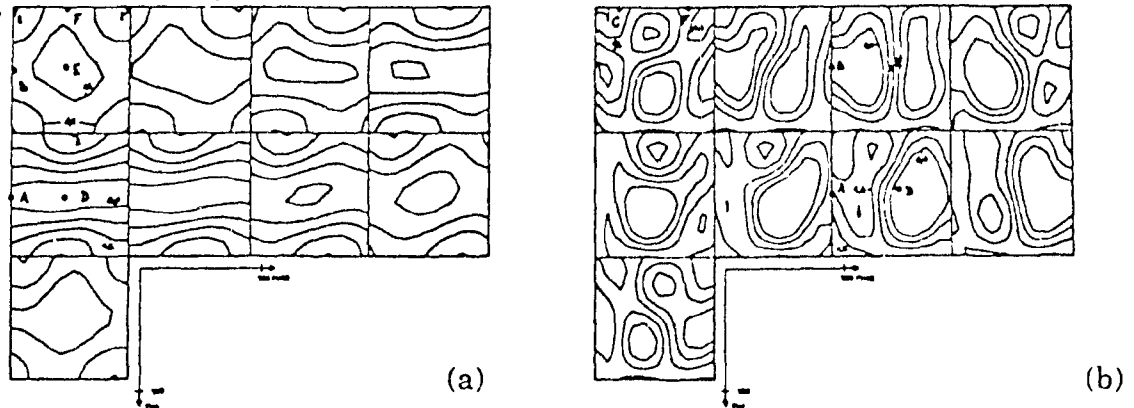


Figure 4-36: Variant selection functions after 10% rolling along (a) $\langle 100 \rangle$, (b) $\langle 110 \rangle$ with a quasi-ideal cube texture $\{100\} \langle 001 \rangle$, the first specimen was rolled 10% along the $\langle 100 \rangle$ direction and two of the variants (A and D) were found to occur with very weak weight. On the other hand, when rolled 10% along the $\langle 110 \rangle$ direction, the variants denoted E and B were weak [73].

IV.4.3 VARIANT SELECTION

In some cases it has been reported that the transformation approaches ideality with all variants equally favored [41,42,55,57,62,70,77,106,107], but most workers have needed to invoke a degree of variant selection [5,27,31,39-44,50,57,58,69,72,108], principally because the product textures do not contain peaks and are sharper than those predicted using all variants. A review of published results using selection rules is presented below. As currently formulated, it is not possible to apply weighting criteria to the continuous techniques of texture prediction. The following simulations were thus carried out either on ideal components or on a series of orientations chosen to represent the initial texture. The results presented below are classified according to the model on which they are based, as reviewed in III.3.2.

- practical illustration:

Applied stress or strain influences the rate of transformation and variant selection [33-35,65,68,71,109,110], although its effect seems to depend on the amount of deformation [103]. This seems particularly evident for shear transformations. As an illustration, the martensite textures of a recrystallized $\{100\}\langle 001 \rangle$ Fe-30Ni

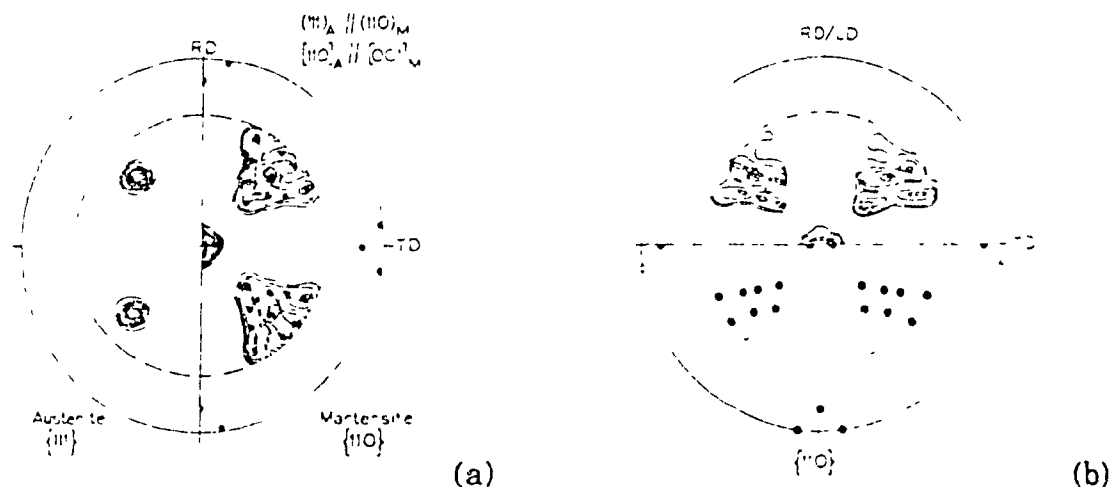


Figure 4-37 : Fe-30Ni textures (a) without load, (b) with load along RD (●:NW poles).

alloy, transformed with or without load along RD, are presented in Figure 4-37, with the corresponding active NW variants. It is apparent from these figures that some selection has occurred under the load. The strong influence of the *sense* of the applied stress has also been demonstrated [34,47]. Figure 4-38 represents the experimental and KS-predicted ODF's of an 80% rolled sheet of Fe-30Ni. The agreement is not satisfactory, although peaks coincide, proving the validity of such a derivation [72].

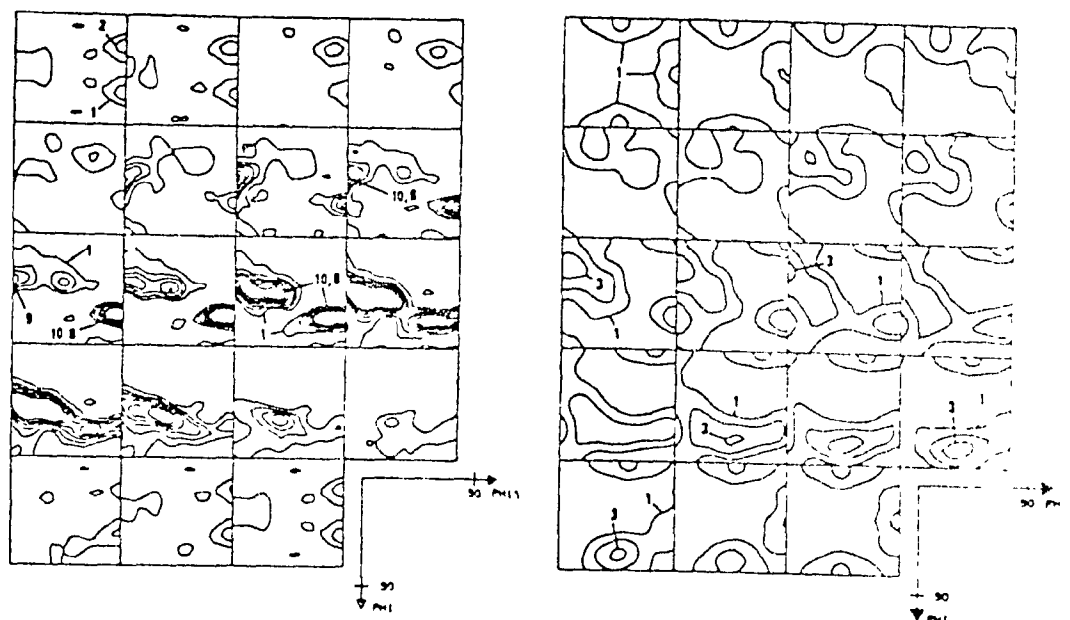


Figure 4-38 : Experimental and KS-predicted ODF's of Fe-30Ni rolled 80%

- the shape deformation model :

Studies employing this model have not led to successful results [34-36]. The effect of grain shape on variant selection has been shown to be weak, as illustrated in Figure 4-39, assuming 95% reduction [40].

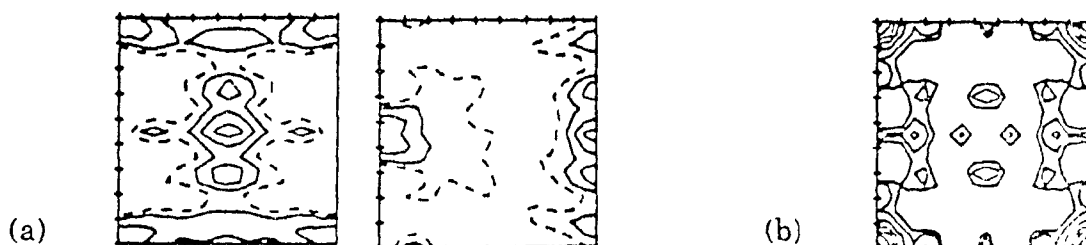


Figure 4-39 : (a) $\phi = 0^\circ$ and 45° ODF sections assuming a grain shape equivalent to 95% reduction, (b) associated $\phi = 0^\circ$ MODF.

- the Bokros-Parker model :

Studying an alloy with 12%Cr-6%Ni rolled 93% in the austenite phase, Borik *et al.* [39] have shown that it could be described best by $\{110\} \langle 225 \rangle$ and the transformed martensite by $\{568\} \langle 421 \rangle$. However, as shown in Figure 4-40 using all the KS variants, the predicted texture consisted of both the *actual* $\{568\} \langle 421 \rangle$ and a *missing* $\{100\} \langle 074 \rangle$ orientation, whose habit planes are normal to the active slip directions.

Predictions were also made under the assumption that the transformation took place on the variants associated with one, two or four of the most favored habit planes, taken to be of the form $\{3\ 10\ 15\}$, or even on all variants weighted in

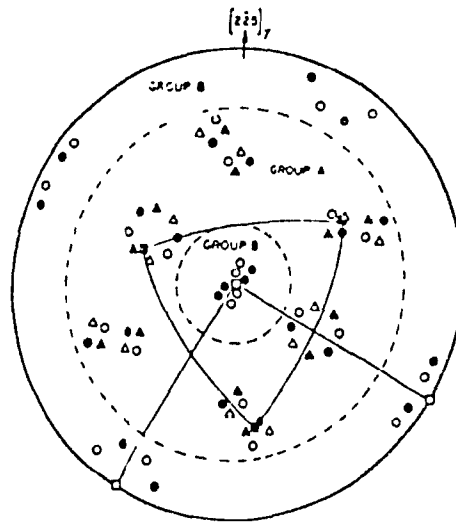


Figure 4-40 : (100) pole figure of the α orientations KS-derived from $(110)[2-25]_{\gamma}$.



Figure 4-41 : (a) $\Phi = 0^\circ$ and 45° ODF sections assuming the transformation to take place on the most favored habit plane, (b) associated $\Phi = 0^\circ$ MODF.

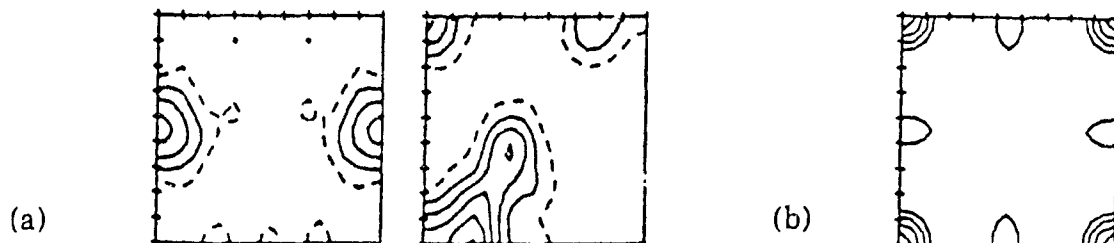


Figure 4-42 : (a) $\Phi = 0^\circ$ and 45° ODF sections assuming the transformation to take place on the two most favored habit planes, (b) associated $\Phi = 0^\circ$ MODF.

accordance with their habit planes [40]. The resulting $\Phi = 0^\circ$ and $\Phi = 45^\circ$ ODF and $\Phi = 0^\circ$ MODF sections are presented in Figures 4-41 to 4-44. All the predictions are less severe than the actual textures and show systematic, although not identical, deviations from experiment. This model is thus only partially successful.

- the active slip system model :

Haslam *et al* [44] used the ODF of 80% cold rolled copper to represent the austenite texture and transformed it using the KS relationship to predict ferrite textures. They did this by first fitting a large number of discrete orientations to the

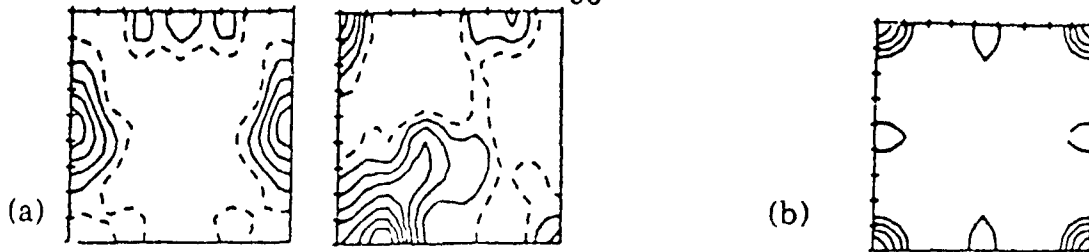


Figure 4-43 : (a) $\phi=0^\circ$ and 45° ODF sections assuming the transformation to take place on the four most favored habit planes, (b) associated $\phi=0^\circ$ MODF.

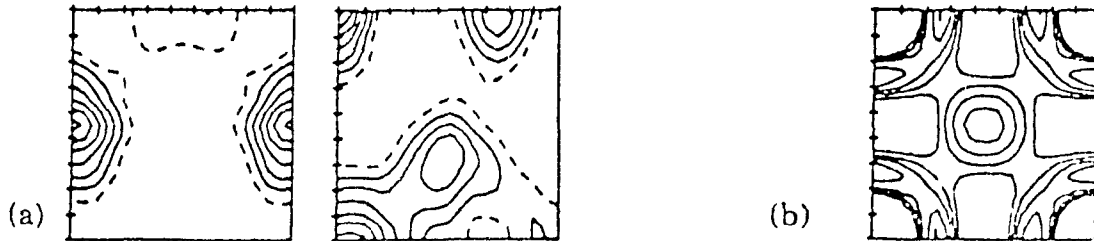


Figure 4-44 : (a) $\phi=0^\circ$ and 45° ODF sections assuming the transformation to take place on all weighted habit planes, (b) associated $\phi=0^\circ$ MODF section.

ODF and then operating on these orientations with selected KS variants. In this way, they were able to predict textures very similar to those of a range of hot rolled steels. Identical results were obtained with the NW relationship by pole figure analysis [66]. However, with this approach, no quantitative correlation was apparent.

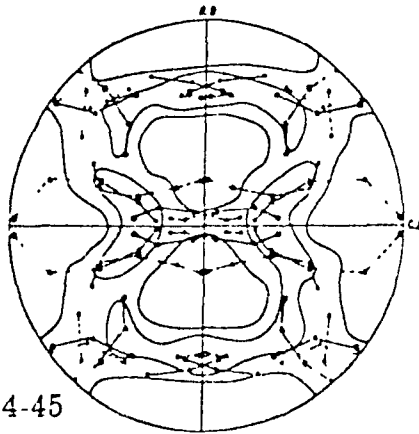


Figure 4-45

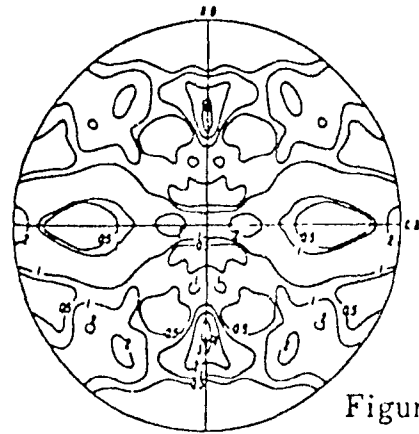


Figure 4-46

Figure 4-45 : (100) pole figure of the α orientations derived from $\{110\} \langle 112 \rangle$ (•), $\{123\} \langle 856 \rangle$ (▸), $\{112\} \langle 111 \rangle$ (●) by the variants associated with the slip systems upon which the largest shear stresses acted.

Figure 4-46 : (100) pole figure of Fe-25.7Ni derived with all 24 GT variants.

Figure 4-45 shows the (100) pole figure of the martensite phase of an Fe-25.7Ni alloy after 90% reduction at 400°C (levels 0.5 and 2 only) and the α poles derived from the main γ orientations ($\{110\} \langle 112 \rangle$, $\{123\} \langle 856 \rangle$ and $\{112\} \langle 111 \rangle$), using a Greninger-Troiano relationship [43]. The orientations derived from the variants corresponding to the two austenite slip systems which sustained the largest resolved

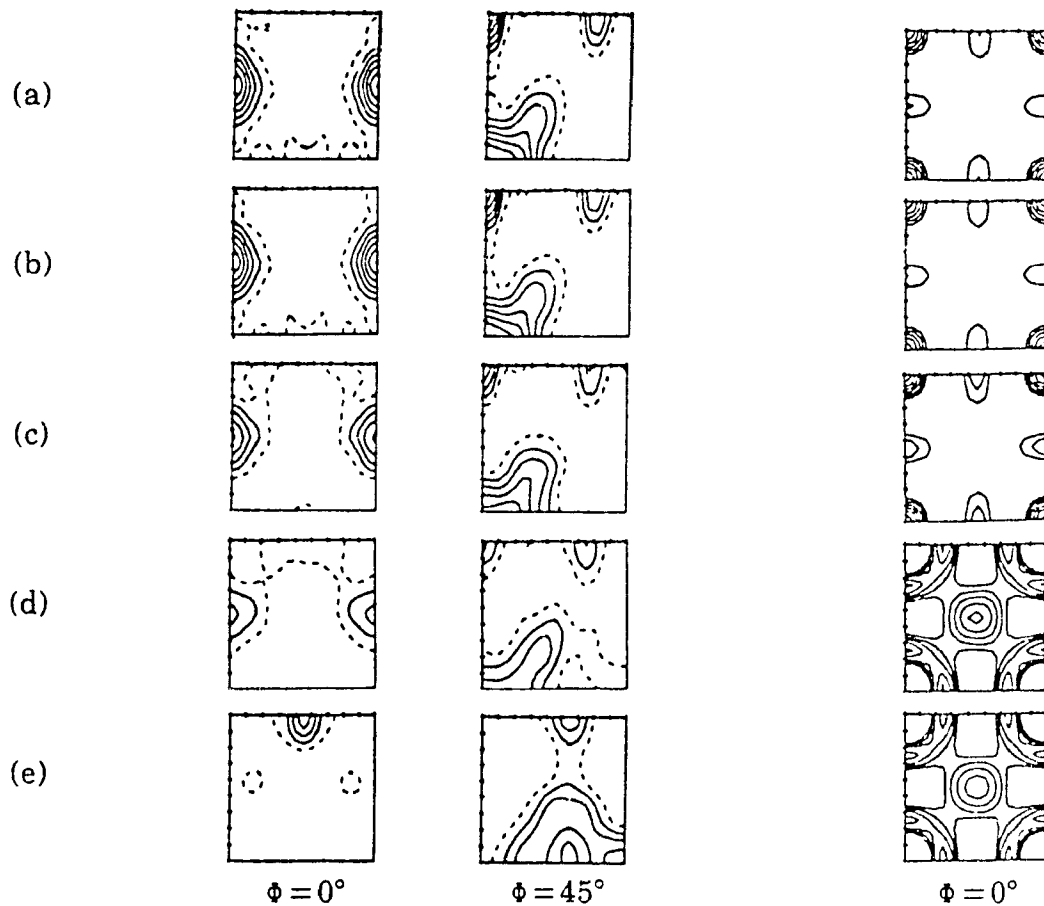


Figure 4-50 : $\phi = 0^\circ$, $\phi = 45^\circ$ ODF and $\phi = 0^\circ$ MODF sections predicted from 90% cold rolled austenite by means of the slip system/variant coincidence criterion assuming a rotation of the principal axes of the strain tensor about TD (shear) by (a) 0° (b) 5.6° (c) 13.2° (d) 22.5° (e) 45° .

compared to the equiprobable case, although it remains less sharp than the experimental ODF. For all reductions, variations were also systematically observed in the prediction of the relative weighting of components: the derived $\{113\}\langle 110 \rangle$ is always more severe than $\{112\}\langle 110 \rangle$ or $\{332\}\langle 113 \rangle$, which is not the case actually. In addition, $\{100\}\langle 011 \rangle$ is over- and $\{210\}\langle 120 \rangle$ under-predicted. By further including shear components, the predicted textures are modified but were not found closer to the experiment. It has also been noted that superficially similar ODF's could provide markedly different MODF's (Figures 4-50 (c) and (d)) [40].

- the Bain strain model:

Furubayashi *et al* [45,46,48,49] successfully simulated the martensite texture of an Fe-25.7Ni alloy rolled 90% at 400°C and air cooled, as shown in Figure 4-51. The metal-type austenite texture was decomposed into 360 grains and the model operated

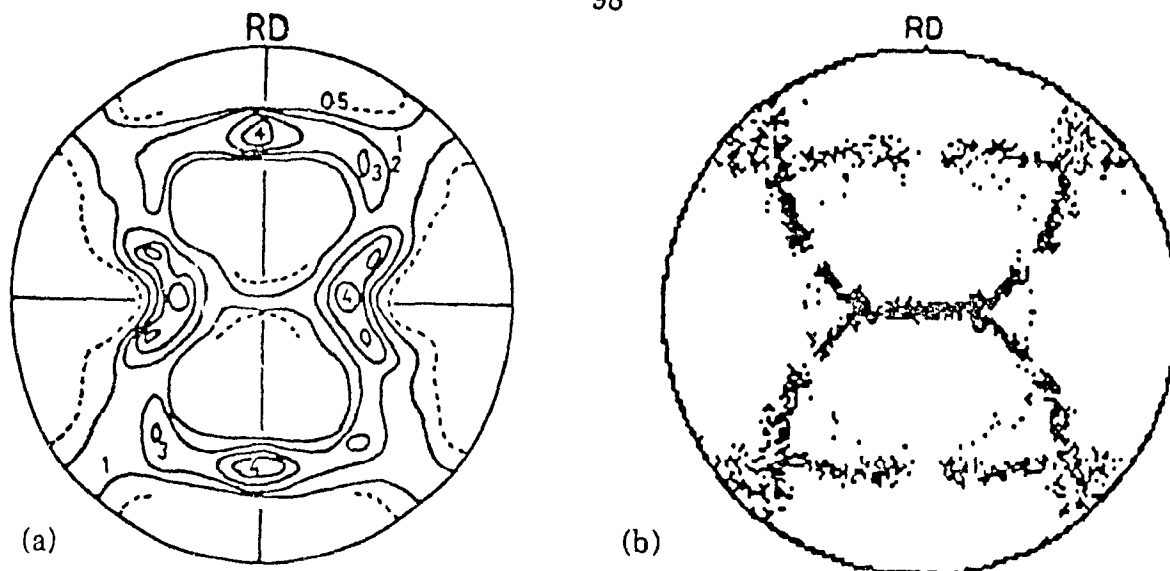


Figure 4-51: (a) Experimental, (b) simulated (100) pole figure for martensitic Fe-25.7Ni. on each individual orientation assuming that the variant having the maximum value for the parameter WB was selected among the three Bain variants.

- the geometrical parameters model:

Recently, Humbert *et al.* [50,72] have proposed a new type of model, based on optimum induced deformation, which gave reasonably good results in predicting the texture of an 80% rolled sheet of Fe-30Ni. Figure 4-52 presents the predicted ODF's assuming maximal deformation along ND and minimal deformation in the plane of the sheet, respectively. Comparison with the experiment (Figure 4-38) shows reasonably good agreement. The importance of dimensional parameters on the selection process was also emphasized by Hashimoto *et al.* [111,112].

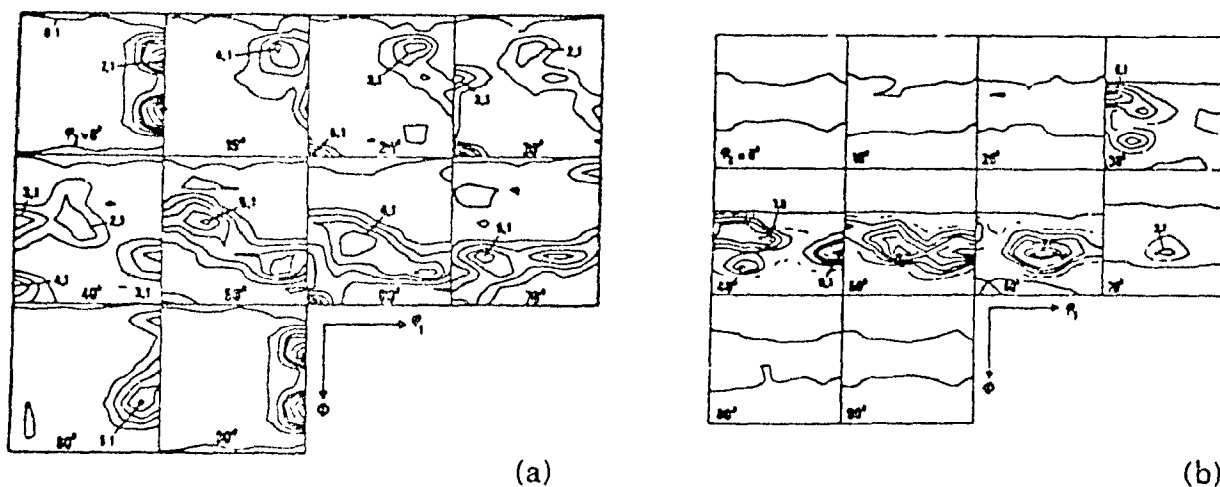


Figure 4-52: Simulated Fe-30Ni ODF's assuming (a) maximal deformation along ND, (b) minimal deformation in the sheet plane.

CHAPTER V

PREDICTION OF TRANSFORMATION TEXTURES

V.1	EXPERIMENTAL METHOD AND SIMULATIONS	101
V.1.1	CHOICE OF THE MATERIALS	101
	- stacking fault energy considerations	
	- considerations regarding the Periodic Table of the Elements	
	- compositions	
V.1.2	EXPERIMENTAL PROCEDURE	104
	- preparation of the starting materials	
	- final preparation	
	- texture measurement	
V.1.3	SIMULATIONS	105
	- discrete procedures	
	- continuous procedure	
V.2	RESULTS	108
V.2.1	EXPERIMENTAL RESULTS	108
	- main features	
	- influence of the cobalt content	
	- influence of rolling reduction	
V.2.2	RESULTS OF THE DISCRETE SIMULATIONS	114
	- transformation of common fcc components	
	- untransformation of common bcc components	

V.2.3	RESULTS OF THE CONTINUOUS SIMULATIONS	125
	- general observations regarding the simulated transformation textures	
	- detailed description of the ODF's obtained with the KS relationship	
	- influence of the choice of the orientation relationship	
V.3	DISCUSSION	151
V.3.1	COMPARISON WITH OBSERVED TEXTURES	151
	- ferrite in controlled rolled steels	
	- martensite	
	- cold rolled ferrite	
V.3.2	RELATIVE ASSESSMENT OF THE METHODS	168
	- transformation vs untransformation methods	
	continuous vs discrete methods	
V.3.3	INFLUENCE OF SIMULATION PARAMETERS	171
	- presence of ghosts in the starting texture	
	- order of truncation in the series expansions	
	- departures from the exact orientation relationships	

V.1 EXPERIMENTAL METHOD AND SIMULATIONS

As mentioned earlier, experimental difficulties often preclude texture determination of the austenite phase for most commercial steels, this is because they undergo phase transformation during cooling to room temperature. However, because of the existence of orientation relationships between parent and product phases, it is possible to infer the parent texture from the product texture, and vice versa.

V.1.1 CHOICE OF THE MATERIALS

In the course of this work, the austenite texture was assumed to be similar to that of other fcc materials and the corresponding ferrite textures were then simulated and compared to the experimental results of others. The problem was to make a judicious choice of the initial texture.

- stacking fault energy considerations :

In fcc metals and alloys, it is usual to distinguish between three different types of cold rolling texture depending on the stacking fault energy (SFE) level, namely (i) the brass or alloy type in low SFE materials, (ii) the copper or pure metal type in medium SFE materials, and (iii) the aluminum type in very high SFE materials. As summarized in Table 5-1, the brass type consists essentially of the brass component $\{110\}\langle 112 \rangle$ (Bs); in the copper type, the copper $\{112\}\langle 111 \rangle$ (Cu), $\{123\}\langle 634 \rangle$ (S) and brass components have nearly equal strengths; the S component seems to be predominant in the aluminum type [113]. In the literature, the γ rolling texture has generally been assumed to be similar to the textures of copper or aluminum.

The stacking fault energy of γ iron has been reported to be about 75mJ m^{-2} [114]. Accordingly, if the austenite rolling textures of low alloyed steels are to be simulated, they should be modelled by materials having comparable SFE's. However, the SFE of copper is only about 55mJ m^{-2} , whereas the SFE of aluminum is 200mJ m^{-2} [115]. An alternative is to make use of nickel-based alloys. The SFE of pure nickel is about 130mJ m^{-2} [116], but an addition of cobalt decreases the SFE [116,117], so that an alloy containing 30 weight per cent of cobalt is expected to have a stacking fault

energy of nearly 73.6 mJ/m^2 , which is similar to that of γ iron. The SFE values of some fcc metals and alloys are listed in Table 5-2.

SFE range	texture type	predominant components
low	brass or alloy	Bs $\{110\} \langle 112 \rangle$
intermediate	copper or pure metal	Cu $\{112\} \langle 111 \rangle$ Bs $\{110\} \langle 112 \rangle$ S $\{123\} \langle 634 \rangle$
very high	aluminum	S $\{123\} \langle 634 \rangle$

Table 5-1 : Classification of fcc textures as a function of SFE.

material	SFE (mJ/m^2)
Al	200
Ni	130
Ni-10Co	111.5
Ni-20Co	92.3
γ iron	75
Ni-30Co	73.6
Cu	55
Ni-40Co	53
Fe-30Ni	45
Ag	30
Ni-60Co	15
Ni-65Co	5.2

Table 5-2 : Some SFE values.

- considerations regarding the Periodic Table of the Elements

When considering the 'Periodic Table of the Elements' (Figure 5-1), it can be seen that Fe, Ni and Co belong to the same classification group (Group VIII) of the 4th period of the table and have similar physical data (Table 5-3). Their chemical properties and electrical behaviors might thus be expected to be rather close

	I	II	IIIb	IV	Vb	VI	VII		I	II	IIIa	IV	Va	VIa	VII	O
1																
2																
3																
4					V	Cr	M	Fe	Co	Ni	Cu	Zn				
					Nb											

Figure 5-1 : Extract of the 'Periodic Table of the Elements'.

	Fe	Co	Ni
atomic number	26	27	28
atomic weight	55.85	58.93	58.71
oxidation states	+ 2 and + 3	+ 2 and + 3	+ 2 and + 3
electron configuration	3s ² 3p ⁴ 4s ² 3d ⁶	3s ² 3p ⁴ 4s ² 3d ⁷	3s ² 3p ⁴ 4s ² 3d ⁸
melting point (°C)	1535	1495	1453
boiling point (°C)	2750	2870	2732
phases	δ, γ, α	-	δ, α

Table 5-3 . Comparison of some physical data for Fe, Ni and Co

- compositions:

From the two previous paragraphs, it seems reasonable to choose Ni-Co alloys to simulate austenite. The chemical compositions of the alloy employed in the present study are given in Table 5-4.

Alloy	Alloying elements						
	Co	C	S	Si	Cu	O ₂	Ni
Ni-10Co	11.15	0.006	0.003	0.03	0.03	0.005	balance
Ni-20Co	22.85	0.007	0.003	0.06	0.03	0.006	balance
Ni-30Co	30.90	0.006	0.003	0.03	0.03	0.009	balance
Ni-40Co	41.05	0.006	0.004	0.03	0.03	0.004	balance
Ni-60Co	60.50	0.006	0.004	0.06	0.03	0.007	balance

Table 5-4: Chemical compositions of the Ni-Co alloys (weight percent).

V.1.2 EXPERIMENTAL PROCEDURE

The preparation of the materials and the determination of the ODF's used in the simulations were carried out by Ray and Lucke [118]. Only a general overview of the procedure is given below.

- preparation of the starting materials:

The alloys were melted under vacuum and segregation was avoided by magnetic stirring during melting. The ingots were then cold rolled 50 per cent to a thickness of 10 mm and homogenized by an annealing treatment in vacuum at 1150°C for 24 hours. They were again cold rolled 50 per cent and annealed at 1100°C for 3 hours to yield starting materials of almost random texture and a grain size of about 0.1 mm.

- final preparation:

Final preparation consisted of cold rolling to 40, 70, 90 or 95 per cent reduction, using a laboratory mill with 250 mm diameter rolls. Reproducible textures were found over almost the whole thickness of the sheets, except for a narrow zone near the outermost surface.

- texture measurement:

The specimens were etched from one side of each sheet to the mid-thickness, on which the X-ray texture measurements were carried out. For each sample (area 24

mm x 14 mm), the texture was determined by plotting conventional pole figures as well as ODF's. For the latter purpose, four incomplete pole figures, namely the $\{111\}$, $\{200\}$, $\{220\}$ and $\{311\}$, were measured up to an azimuth of 85° . From these data, the ODF's were calculated following the series expansion method of Bunge [5,15] and using a computer program designed by Jura *et al* [119].

V 13 SIMULATIONS

Two main categories of prediction methods have been presented above based on the transformation and untransformation procedures, respectively. In each case, discrete and continuous simulations can be carried out, as presented in Chapter III. The practical principles of the derivations are given below

- discrete procedures:

As will be shown in the experimental results (see section V 2 1), the texture of cold rolled Ni-Co alloys can be roughly described by means of peak type components at $\{112\}\langle 111 \rangle$ (Cu), $\{110\}\langle 112 \rangle$ (Bs) and $\{123\}\langle 634 \rangle$ (S). In the literature, other orientations have also been reported when studying the rolling textures of fcc materials. These are all gathered in Table 5-5, together with the references in which they have been mentioned. The components produced by recrystallization are listed above the heavy line and those associated with deformation are tabulated below. The corresponding bcc orientations have been derived using the KS, B and NW relationships, as described in section III 4 1. All the calculated orientations have been retained; i.e. no selection rule was applied regarding the variants.

In a similar manner, rolled bcc materials can sometimes be described by a set of orientations, the most important of which are shown in Table 5-6. Again, with the exception of the cube texture (no.1), the recrystallization and rolling components are listed above and below the heavy line situated between orientations 4 and 5. On the basis of the untransformation method presented in section III 4 1, the fcc orientations corresponding to these bcc orientations have also been obtained using all the variants of the transformation laws (KS, B, NW). The procedure employed was similar to the discrete transformation, except that the operation was carried out in the reverse direction (from bcc to fcc).

number	symbol	γ orientation	references
1	?	$\{100\} \langle 001 \rangle$	31,55,62,65,104,124
2		$\{110\} \langle 111 \rangle$	42,43,124
3	'	$\{100\} \langle 012 \rangle$	42,43
4	($\{122\} \langle 212 \rangle$	102
5)	$\{113\} \langle 332 \rangle$	102
6	!	$\{112\} \langle 534 \rangle$	102
7	+	$\{112\} \langle 111 \rangle$	42,43,55,57,65,124
8	\times	$\{110\} \langle 112 \rangle$	41,44,55,57,65,124
9	o	$\{123\} \langle 634 \rangle$	124
10	\$	$\{110\} \langle 001 \rangle$	31,42,43,65,124
11	-	$\{123\} \langle 121 \rangle$	65
12	*	$\{123\} \langle 412 \rangle$	55,65,103
13	=	$\{123\} \langle 856 \rangle$	42,43
14	<	$\{146\} \langle 211 \rangle$	103
15	>	$\{233\} \langle 311 \rangle$	124
16	$\hat{\cdot}$	$\{168\} \langle 211 \rangle$	124
17	,	$\{135\} \langle 712 \rangle$	124

Table 5-5: Most important fcc recrystallization and rolling orientations.

- continuous procedure:

Better descriptions of textures are provided by complete ODF's. Therefore, the ODF's of the family of Ni-Co alloys were used to simulate austenites with a variety of stacking fault energy values and rolling reductions. The low temperature textures were then obtained on the basis of equation (3-55) in section III.4.2. As for the discrete derivations, no selection was made among the variants of the orientation

number	symbol	α orientation	references
1	?	$\{100\}\langle 001 \rangle$	
2	#	$\{100\}\langle 011 \rangle$	40,55,61
3	&	$\{110\}\langle 110 \rangle$	31
4	\$	$\{110\}\langle 001 \rangle$	31,61
5	a	$\{112\}\langle 110 \rangle$	31,40,60,74
6	c	$\{113\}\langle 110 \rangle$	41,43,54 59,63
7	e	$\{223\}\langle 110 \rangle$	40,74
8	n	$\{225\}\langle 110 \rangle$	
9	r	$\{111\}\langle 110 \rangle$	60,90
10	s	$\{111\}\langle 112 \rangle$	14,74
11	v	$\{332\}\langle 113 \rangle$	31,40,41,43,54 59,63
12	w	$\{554\}\langle 225 \rangle$	59,61,90
13	z	$\{201\}\langle 102 \rangle$	40

Table 5-6. Most important bcc texture components

relationships. From the experimental texture measurements, the CODB coefficients of the five Ni-Co alloys had been obtained in a previous study [118] for the four rolling reductions of 40%, 70%, 90% and 95%. These coefficients were used as the initial data in the present work. The bcc coefficients were simulated using the continuous procedure with the three classical transformation laws - KS, B and NW.

From the coefficients, the different ODF's were calculated following the series expansion method with Bunge's notation. The skeleton lines were also determined and plotted as a function of the Euler angle ϕ_1 . The typical bcc fibres, namely the α fibre with $\langle 110 \rangle$ // RD and the γ fibre with $\langle 111 \rangle$ // ND, were also calculated.

V.2 RESULTS

Because of the large volume of graphical results (over 150 ODF's), it has not been possible to reproduce all the corresponding figures within the limits of this thesis. The ones included below have been selected because they are representative of the results obtained and lead to clear illustrations of the points at stake. Tables containing some important characteristics, extracted from the ODF's and easier to compare, are also presented in support of the description of the results.

V.2.1 EXPERIMENTAL RESULTS

As they are the starting materials for the simulations, a brief description of the experimental ODF's obtained for the Ni-Co alloys seems necessary. It is usual to represent the textures of fcc metals and alloys by their ϕ_2 sections, since most of the important orientations lie in these sections. More detailed studies of fcc cold rolling textures can be found elsewhere [113,120-130].

- main features :

The complete ODF of Ni-30Co 95% cold rolled has been presented above in Figure 2-9 and the corresponding (200) pole figure and ND inverse pole figure in Figure 2-12 (Chapter II). Extracts of the ODF's for all the alloys with a reduction of 95% are presented in Figure 5-2. The $\phi_2 = 0^\circ$ and $\phi_2 = 45^\circ$ sections have been selected because they contain the ideal components $\{110\} \langle 112 \rangle$ (Bs) and $\{112\} \langle 111 \rangle$ (Cu), which are two of the most important orientations in fcc rolling textures. The S component $\{123\} \langle 634 \rangle$, which plays an equally important role in their description, falls at $\phi_2 = 63.4^\circ$, i.e. between the $\phi_2 = 60^\circ$ and $\phi_2 = 65^\circ$ sections. Therefore, these two sections have also been extracted from the complete ODF's. From Figure 5-2, it is apparent that the intensities are very high (maxima between 15 and 20) and that the peaks are generally not only sharp but also localized and rather narrow (little spread and no evidence for a fibre, even if they sometimes overlap partially).

- influence of the cobalt content :

In Figures 2-9 and 2-12 of Chapter II, the texture of Ni-30Co 95% cold rolled is shown to consist of three peaks at the Cu, Bs and S positions, with similar intensities.

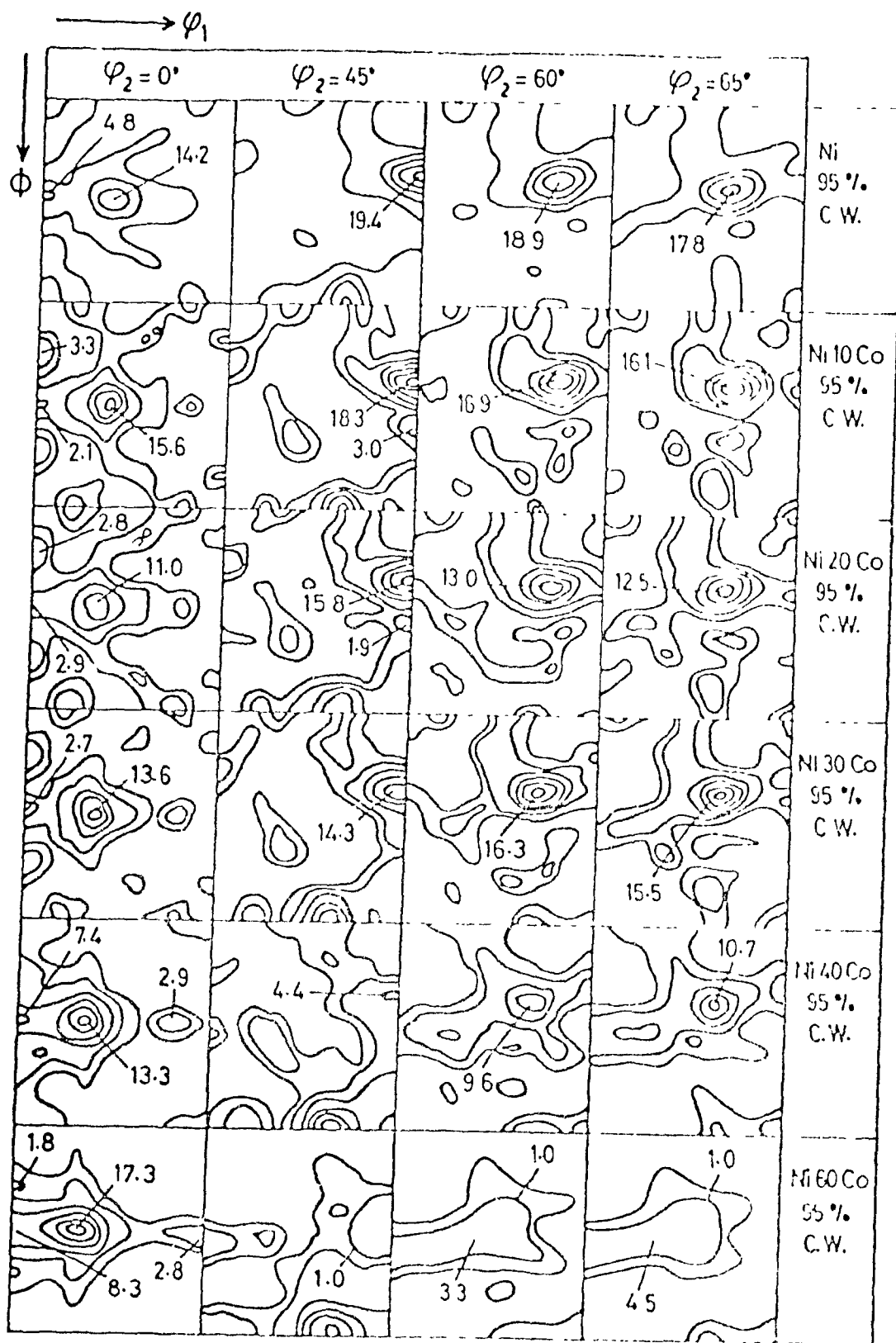


Figure 5-2: Partial ϕ_2 -section ODF's after 95% cold reduction for pure Ni and five of its alloys containing 10, 20, 30, 40 and 60 percent cobalt (levels 3, 6, 9, ...)

As expected from its intermediate SFE value ($\sim 72 \text{ mJ/m}^2$), this alloy thus has a pure metal type rolling texture. The influence of cobalt concentration, which controls the SFE level, is apparent from Figure 5-2. First, for 95% reduction, Ni-10Co and Ni-20Co are shown to be of the same type as Ni-30Co, with comparable peaks and severities.

When the Co content is increased to over 30%, i.e. when the SFE is decreased, the peaks at the Cu and S locations are drastically lowered and ultimately disappear in the case of Ni-60Co. On the other hand, the peak near the Bs component is almost insensitive to composition, although it sharpens at 60% cobalt, so that it finally becomes the maximum of the ODF for this particular alloy (brass or alloy type texture).

At the transition, Ni-40Co has a texture intermediate between that of the pure metal and the alloy; it consists of an absolute maximum near the Bs position, plus a second order maximum at S, with the Cu component barely visible. Moreover, the severity of this texture is less than those of both the pure metal and alloy types at a similar reduction.

These observations are fully consistent with expectations based on the SFE values and the classification of fcc textures presented earlier (see section V.1.1 regarding choice of the materials).

- influence of rolling reduction:

When studying the influence of rolling reduction, the three preceding types of textures (pure metal, alloy and intermediate) must again be differentiated.

The three alloys containing 10, 20 and 30 percent cobalt (pure metal type) have similar behaviors when the reduction is increased from 40 to 95% : the overall severities of the textures as well as the intensities of the three peaks (Bs, Cu, S) are increased homogeneously. Four ϕ_2 sections selected from the Ni-30Co ODF's after 40, 70, 90 and 95 % rolling reduction are presented in Figure 5-3. At lower reductions, it is apparent that the positions of the actual maxima are shifted so that they do not coincide exactly with the ideal positions of the Bs, Cu and S components. However, the textures can still be described by peaks and the angular differences between the observed and ideal positions always remain in the range 0° to 15° . Ultimately, from 95% reduction onwards, the two kinds of positions coincide.

The texture of Ni-40Co has been termed transitional for 95% cold reduction, with strong Bs and S components. At lower reduction levels, however, it exhibits a rather different texture (Figure 5-4). For reductions as low as 40%, the texture mainly

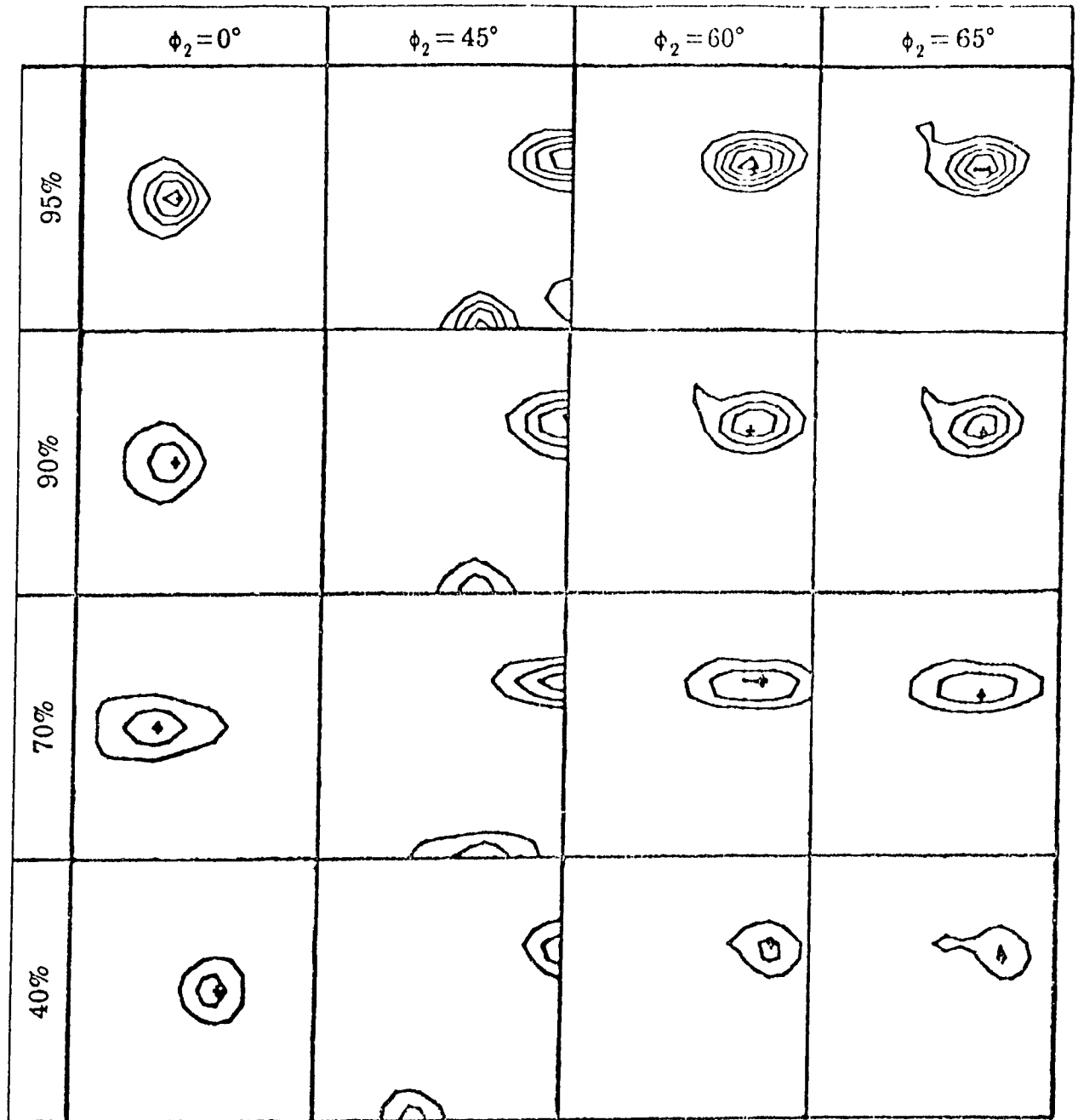


Figure 5-3 : Partial ϕ_2 -section ODF's for Ni-30Co cold rolled 40, 70, 90 and 95% (levels 3,6,9...).

consists of two maxima : one near the Goss position $\{110\}\langle 001 \rangle$ and the other 10° away from the Cu component. The S orientation only appears as a second order peak. When the reduction is increased, the components clustering around the Goss position rotate towards the Bs orientation, which gradually improves and then becomes the overall maximum after heavy reduction (90 to 95%). The texture is also sharpened

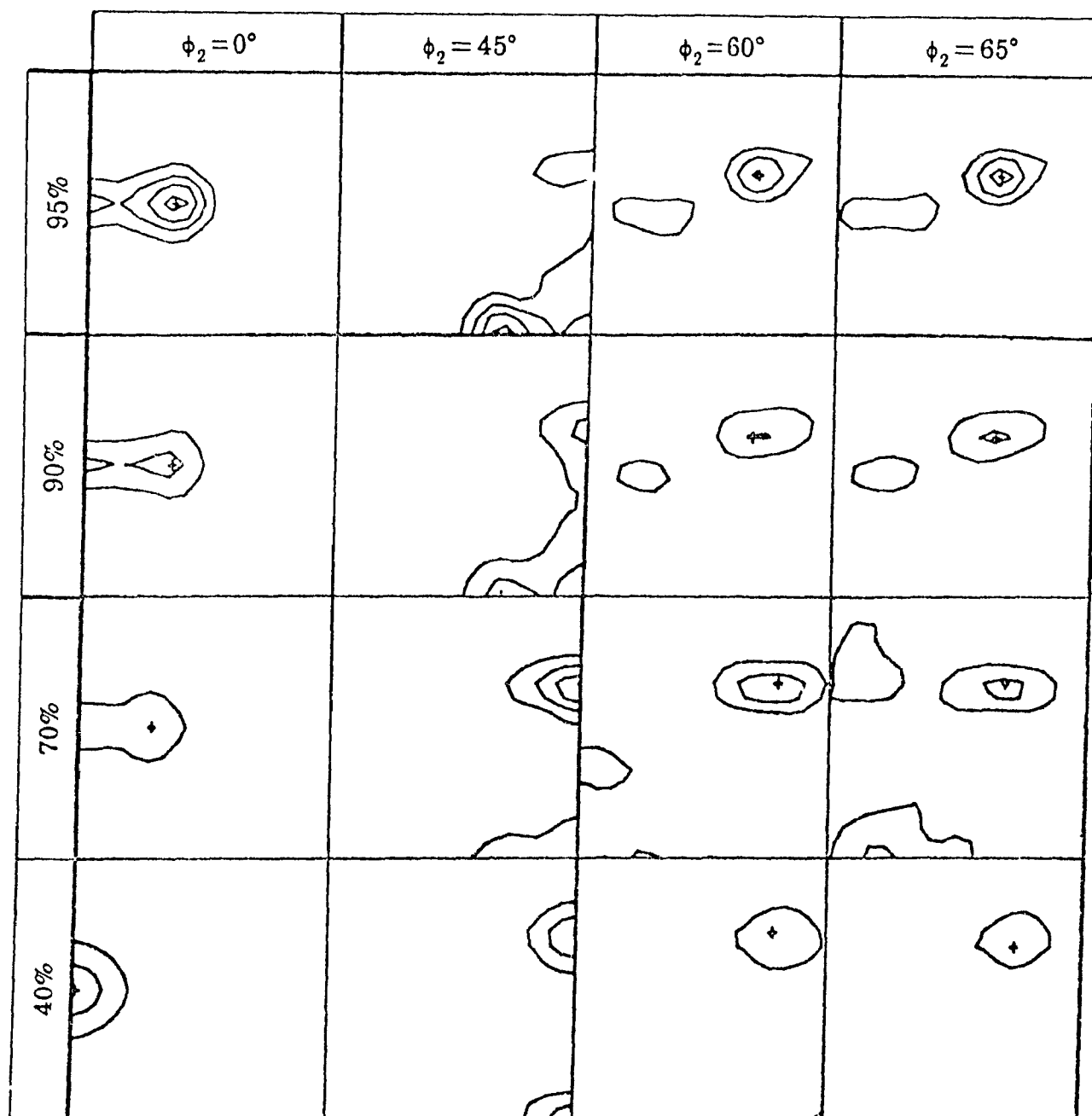


Figure 5-4 . Partial ϕ_2 -section ODF's for Ni-40Co cold rolled 40, 70, 90 and 95% (levels 3,6,9...).

near the S orientation and the severity is thus globally increased, even though the peak near Cu tends to disappear at reductions higher than 90%.

By contrast, an increase in rolling reduction has no influence on the texture of the Ni-60Co alloy other than producing a gradual sharpening, as shown in Figure 5-5. It always has a strong peak at Bs and a small one near the S position, which is

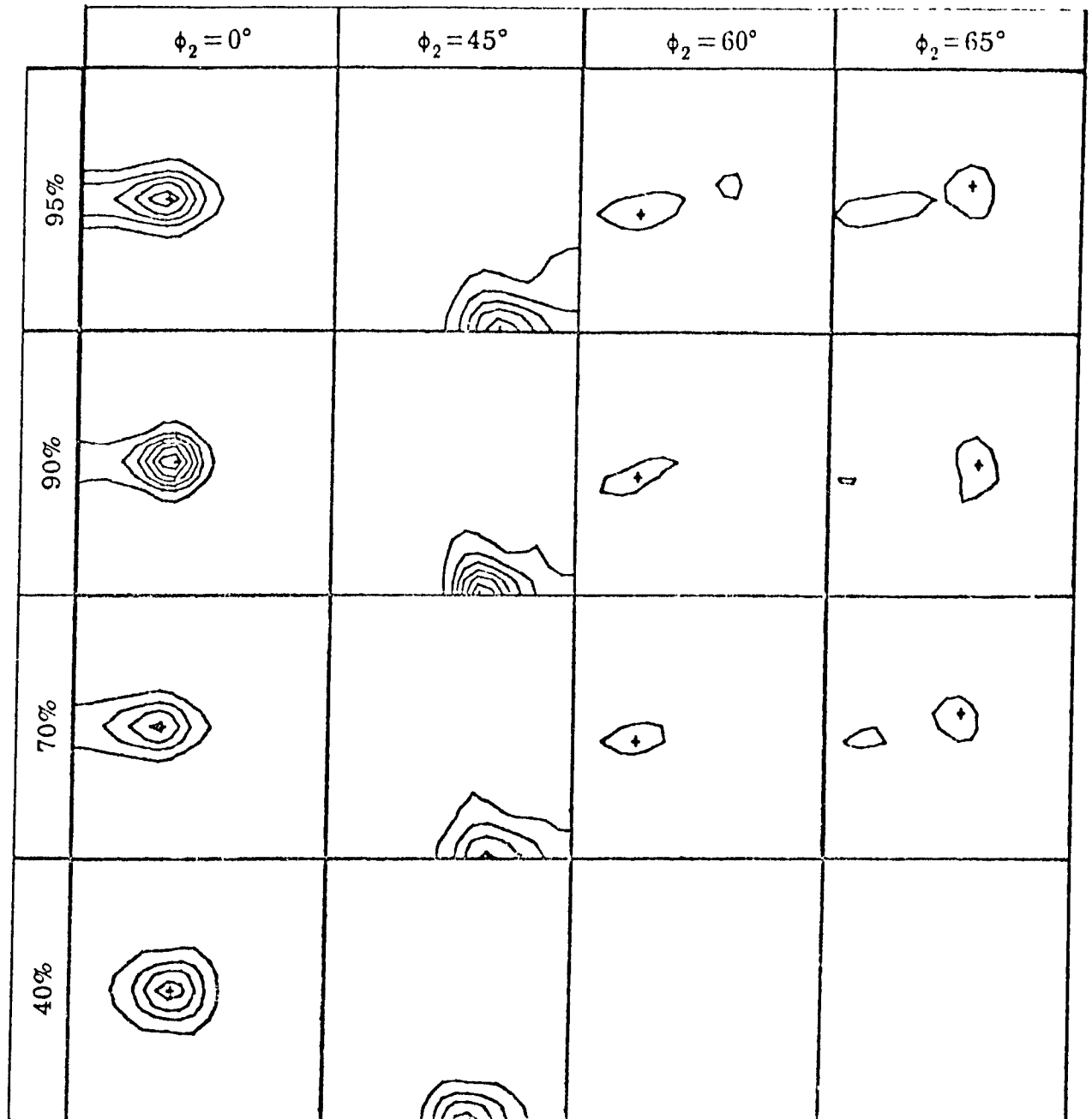


Figure 5-5 : Partial ϕ_2 -section ODF's for Ni-60Co cold rolled 40, 70, 90 and 95%
(levels 3,6,9...)

insensitive to the deformation state. The intensity in the vicinity of Bs increases with the amount of reduction until around 90% deformation and then decreases slightly with further deformation. However, the global severity of the texture is not reduced in the same manner.

V.2.2 RESULTS OF THE DISCRETE SIMULATIONS

In this study, ideal orientations were extracted from one phase and transformed to the other phase by the usual crystallographic relationships. This was done with the aim of using the discrete method to explain the main features of texture inheritance during phase transitions. In the following, the symbols used to represent the classical fcc and bcc components in Euler space are those introduced in Tables 5-5 and 5-6, respectively.

- transformation of common fcc components :

The most important orientations classically observed in fcc metals and alloys were used to simulate austenite. The corresponding bcc orientations were then derived. The results are presented on ϕ_1 sections of ODF frames and compared with the most relevant ideal components reported for rolled bcc materials. The latter are illustrated in Figure 5-6 (a).

Six fcc recrystallization texture components were transformed with the KS relationship. The derived orientations are shown in Figure 5-6 (b). Coincidence within a 10° range in Euler space is evident between some of these transformed components and the classical bcc ideal orientations presented in Figure 5-6 (a). As can be seen from Table 5-7, three of these (the $\{110\}\langle 111 \rangle$, $\{100\}\langle 001 \rangle$ and

initial fcc orientation	derived bcc orientation
$\{110\}\langle 111 \rangle$	$\{100\}\langle 011 \rangle$
$\{100\}\langle 001 \rangle$	$\{110\}\langle 001 \rangle$
	$\{100\}\langle 011 \rangle$
	$\{110\}\langle 110 \rangle$
$\{122\}\langle 212 \rangle$	$\{110\}\langle 001 \rangle$
	$\{100\}\langle 011 \rangle$
	$\{110\}\langle 110 \rangle$

Table 5-7 : List of bcc orientations KS-derived from fcc recrystallization components (Part 1).

$\{122\}\langle 212 \rangle$) lead to the Goss $\{110\}\langle 001 \rangle$, rotated-cube $\{100\}\langle 011 \rangle$ and rotated-Goss $\{110\}\langle 110 \rangle$ orientations, which have been reported among the bcc textures inherited from recrystallized γ [31,55,61]. These appear above the heavy line in

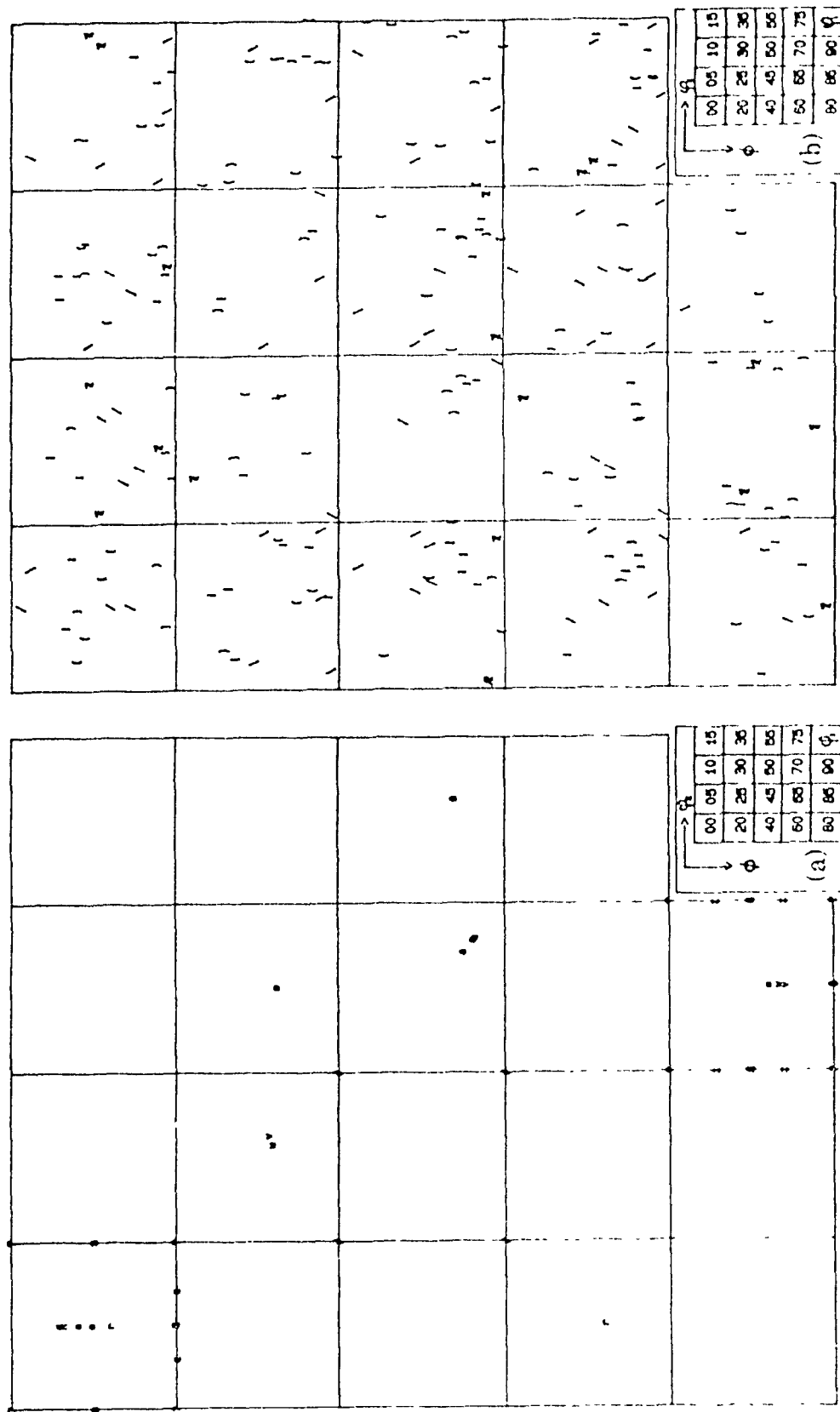


Figure 5-6 (a) and (b): (a) Some classical bcc texture components;
 (b) KS-related orientations transformed from some fcc recrystallization components

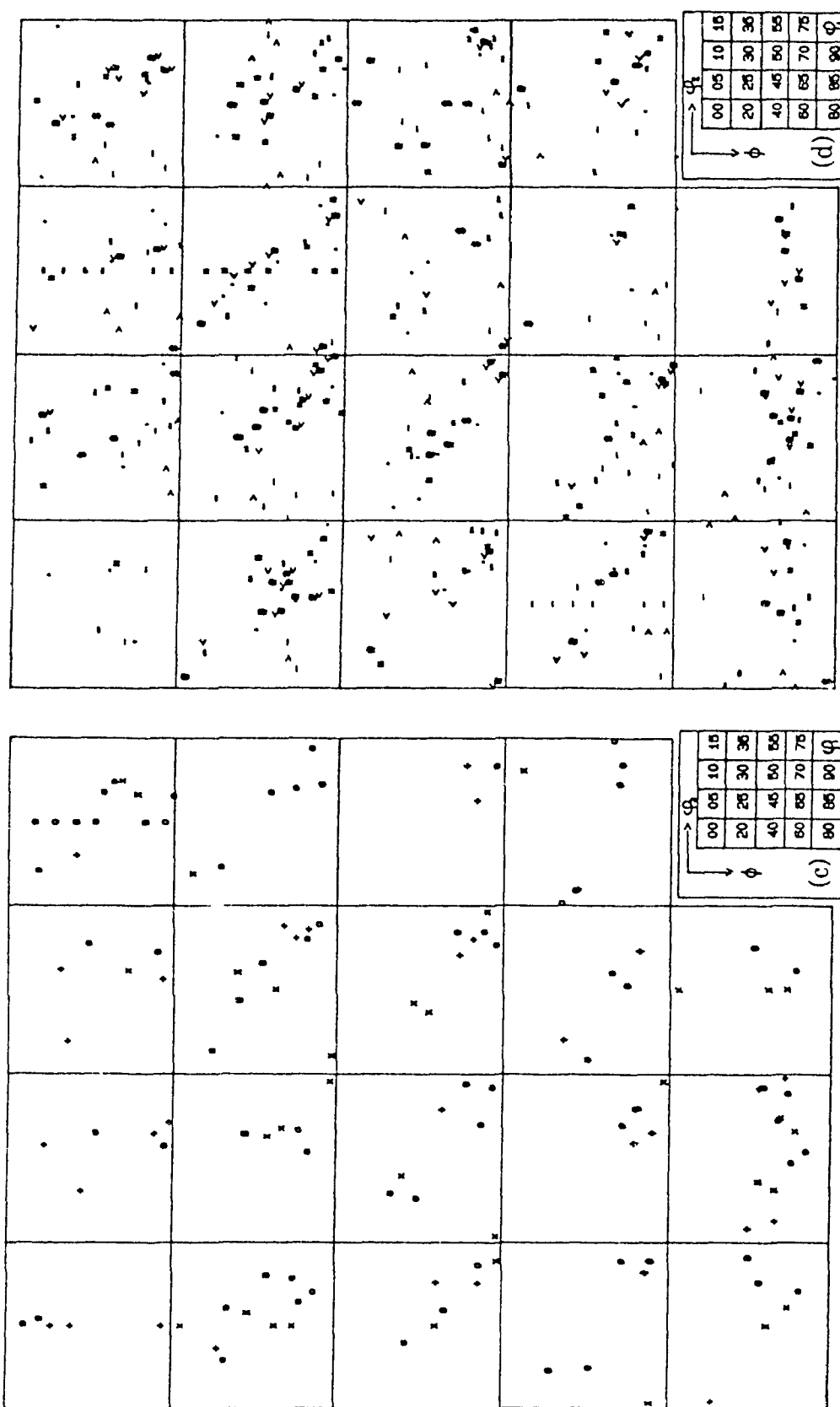


Figure 5-6 (c) and (d) : KS-related orientations transformed from (c) the three main fcc rolling components, and (d) some other fcc rolling components.

initial fcc orientation	derived bcc orientation
$\{110\}\langle 111 \rangle$	$\{111'\}\langle 110 \rangle$
$\{112\}\langle 534 \rangle$	$\{201\}\langle 102 \rangle$ $\{113\}\langle 110 \rangle$
$\{113\}\langle 332 \rangle$	$\{112\}\langle 110 \rangle$ $\{223\}\langle 110 \rangle$

Table 5-8 : List of bcc orientations KS-derived from fcc recrystallization components (Part 2).

Table 5-6. By contrast, three of the recrystallization components (i.e. the $\{110\}\langle 111 \rangle$, $\{112\}\langle 534 \rangle$ and $\{113\}\langle 332 \rangle$) are shown to transform into bcc *deformation* components, as can be seen from Table 5-8. These appear below the heavy line in Table 5-6.

The KS-transformation of the copper, brass and S orientations, the three main fcc rolling components, is illustrated in Figure 5-6 (c). The list of coincidences with the most common bcc orientations is given in Table 5-9. The $\{112\}\langle 111 \rangle$ (Cu) is seen to transform, not only into the classical $\{112\}\langle 110 \rangle$ and $\{113\}\langle 110 \rangle$ through two of the variants of the KS relationship, but also into $\{201\}\langle 102 \rangle$ and $\{110\}\langle 110 \rangle$ through two other variants. Here, the first three are bcc *deformation* components and

initial fcc orientation	derived bcc orientation
$\{112\}\langle 111 \rangle$	$\{112\}\langle 110 \rangle$ $\{113\}\langle 110 \rangle$ $\{201\}\langle 102 \rangle$ $\{110\}\langle 110 \rangle$
$\{110\}\langle 112 \rangle$	$\{332\}\langle 113 \rangle$ $\{111\}\langle 112 \rangle$ $\{100\}\langle 011 \rangle$
$\{123\}\langle 634 \rangle$	$\{113\}\langle 110 \rangle$ $\{332\}\langle 113 \rangle$ $\{110\}\langle 110 \rangle$

Table 5-9 : List of bcc orientations KS-derived from the three main fcc rolling components.

the last one ($\{110\}\langle 110\rangle$) is a *recrystallization* component. In the same manner, the $\{110\}\langle 112\rangle$ (Bs) leads to the classical $\{332\}\langle 113\rangle$ and $\{111\}\langle 112\rangle$ *deformation* components, as well as to $\{100\}\langle 011\rangle$, a *recrystallization* component. Moreover, the S component $\{123\}\langle 634\rangle$ transforms into both $\{113\}\langle 110\rangle$ (2 variants) and $\{332\}\langle 113\rangle$ (1 variant), as well as into the $\{110\}\langle 110\rangle$. Some other fcc deformation texture components were KS-transformed into the bcc phase. Coincidences with the classical bcc orientations, determined from Figure 5-6 (d), are gathered in Table 5-10. Thus, the set of fcc *recrystallization* components of Tables 5-7 and 5-8 as well as the set of fcc *deformation* components of Tables 5-9 and 5-10 each transform into both recrystallization and deformation bcc components

initial fcc orientation	derived bcc orientation
$\{110\}\langle 001\rangle$	$\{112\}\langle 110\rangle$ $\{111\}\langle 110\rangle$
$\{123\}\langle 856\rangle$	$\{100\}\langle 011\rangle$ $\{110\}\langle 110\rangle$
$\{146\}\langle 211\rangle$	$\{332\}\langle 113\rangle$ $\{100\}\langle 011\rangle$

Table 5-10: List of bcc orientations KS-derived from some other fcc rolling components.

As mentioned in Chapter III, the three orientation relationships (KS, Bain and NW), although rather different when expressed as parallelism conditions, are not far from one another in Euler space. This is confirmed in Figure 5-7, where the (100) pole figures of an initially cube-oriented grain, transformed according to these three laws, are presented and compared. In Figures 5-8 (b), (c) and (d), the three main fcc rolling components, namely the Cu, Bs and S, are transformed into the bcc state with the KS, Bain and NW orientation relationships, respectively. The corresponding (100) pole figures for the transformation of the S component are shown in Figures 5-9 (a) to (c). From a global point of view, the results obtained by the three types of derivation are thus similar. Each Bain-derived orientation is, however, surrounded by four NW- and eight KS-related orientations, respectively, in keeping with the relative number of variants of each law. An identical order is thus expected when the ODF's corresponding to these three relationships are classified according to their severity parameters.

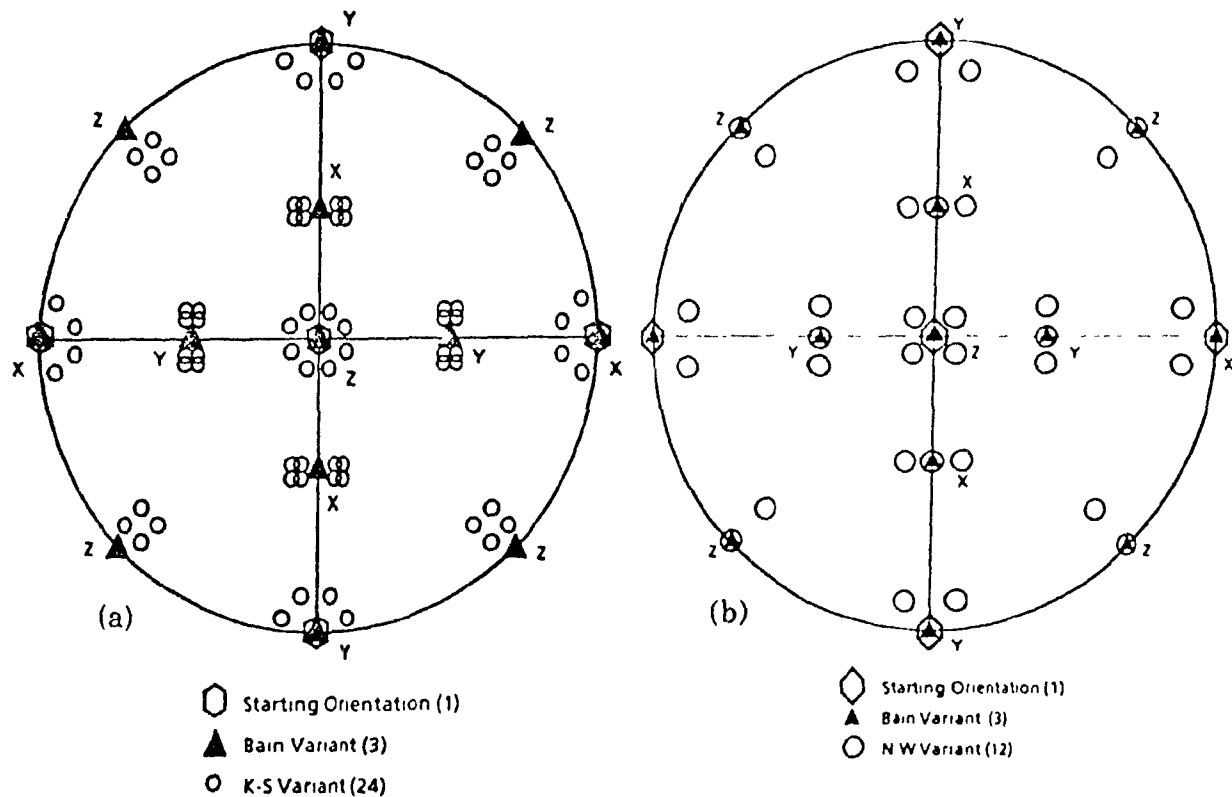


Figure 5-7 : Transformation of the fcc cube component (100 pole figures); comparison of the (a) Bain and KS orientations, and (b) Bain and NW orientations.

- untransformation of common bcc components.

The usual bcc ideal orientations of Table 5-6 have also been untransformed into the austenite state to ascertain their origins at high temperatures. The results are presented, in ϕ_2 sections, in Figures 5-10 (b) to (d) and compared with the classical fcc recrystallization and deformation components of Table 5-5 shown in Figure 5-10 (a). The descriptions given above for the transformation case are confirmed here, which is not unexpected, since transformation and untransformation are strictly equivalent operations when all the variants are considered identically.

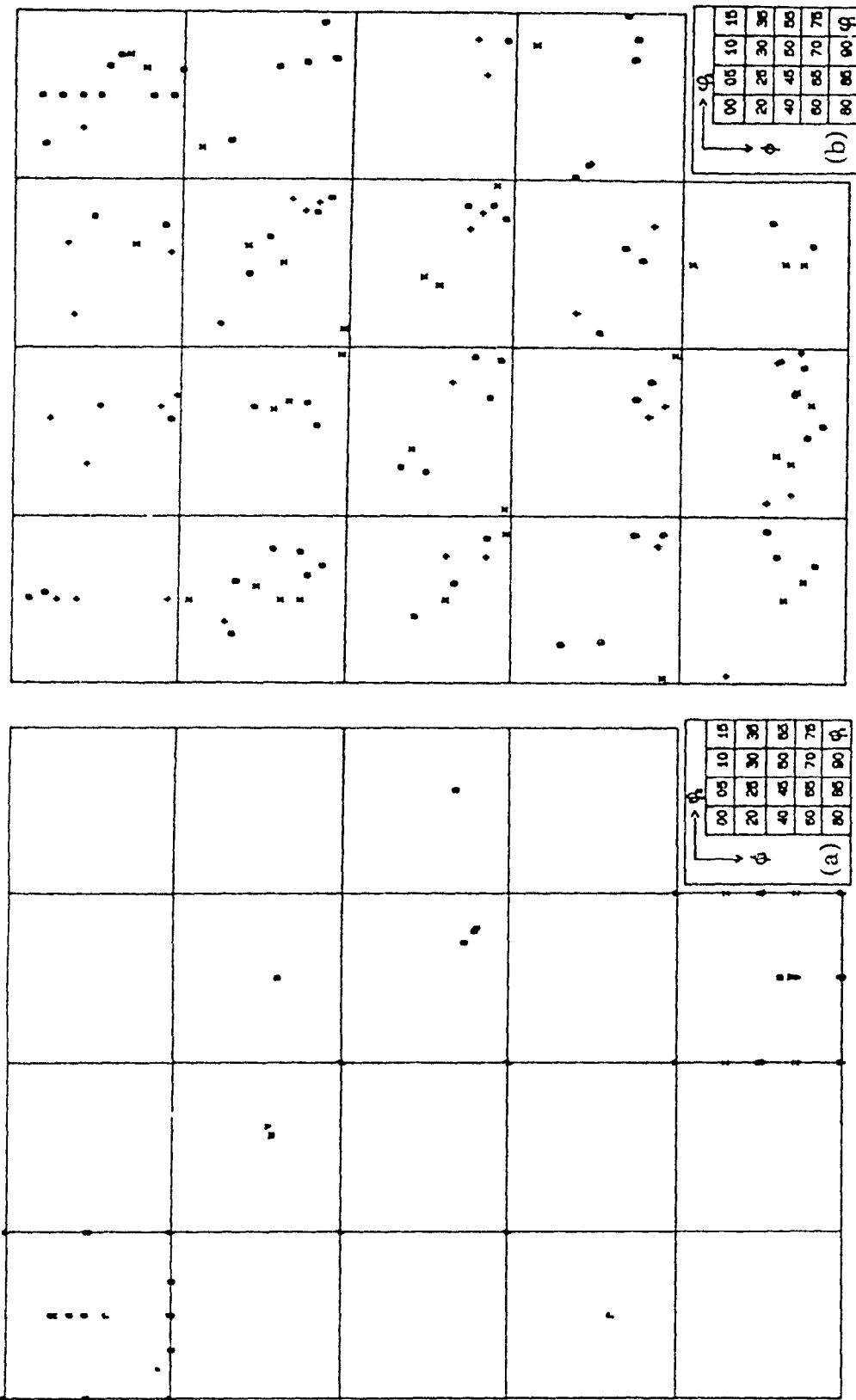


Figure 5-8 (a) and (b): (a) Some classical bcc texture components; (b) transformation of the three most important fcc rolling components with the KS relationship.

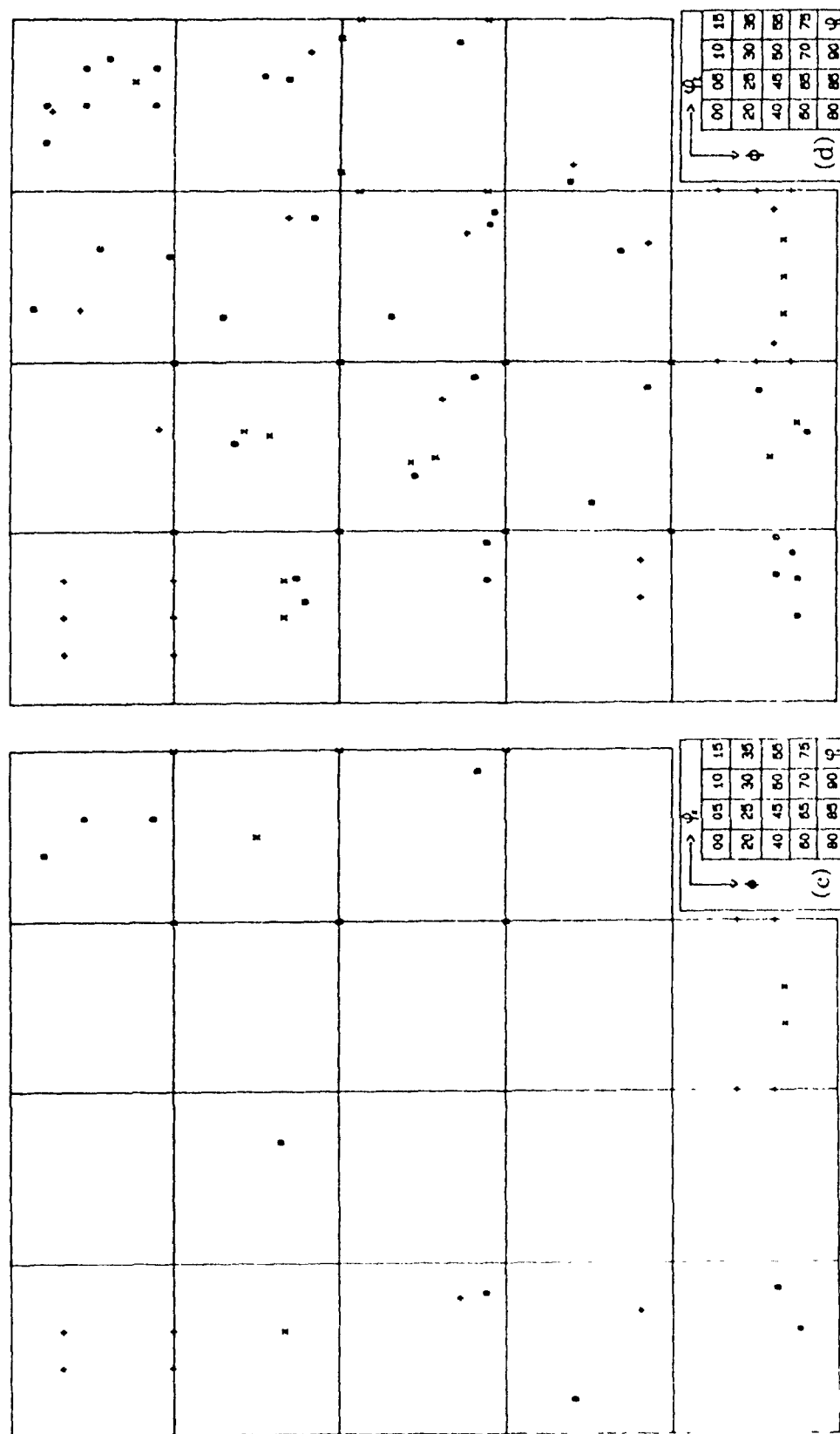


Figure 5-8 (c) and (d) : Transformation of the three most important fcc rolling components with the (c) Bain and (d) NW orientation relationships.

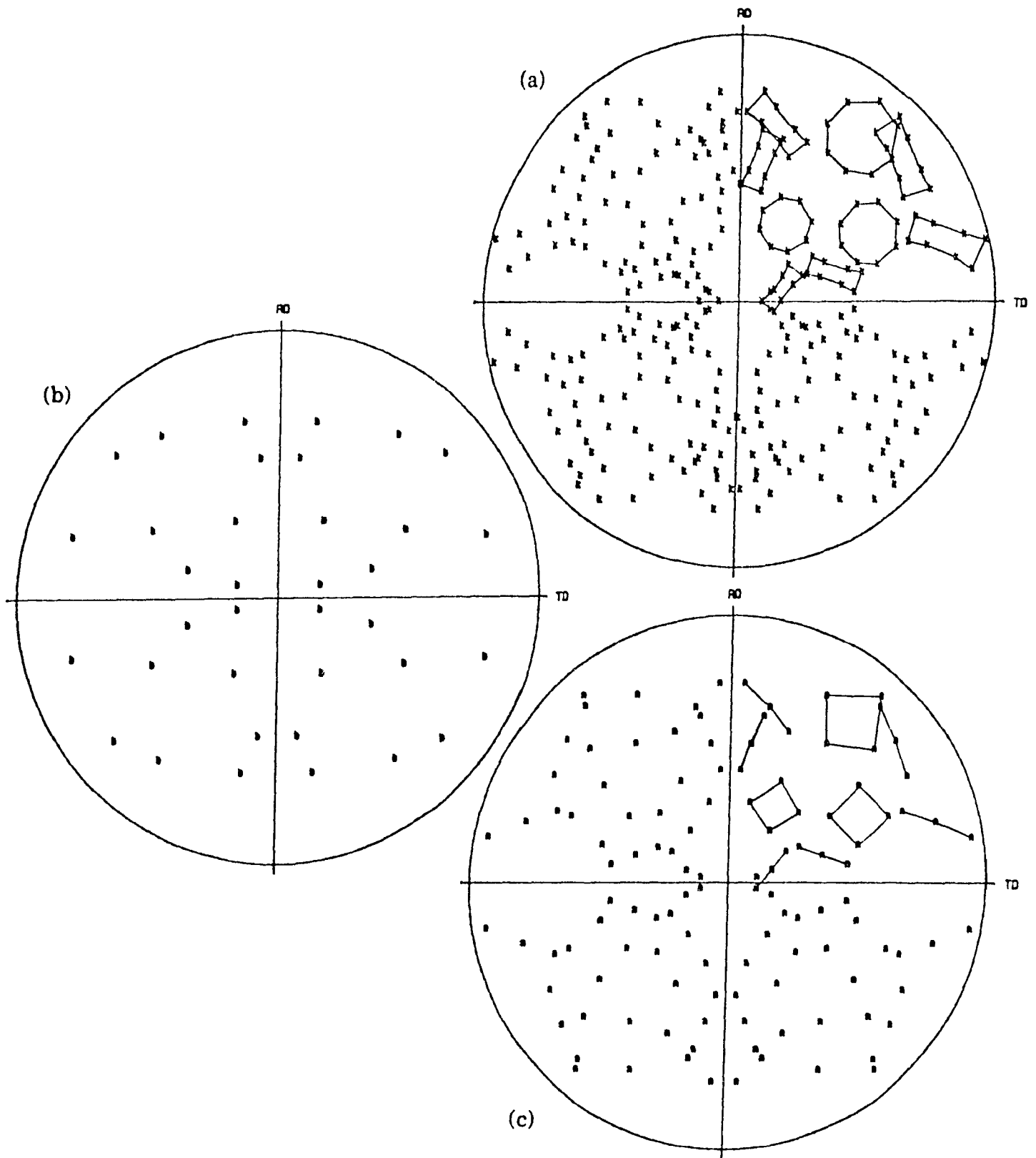


Figure 5-9: Transformation of the fcc S rolling component (100 pole figures) with the (a) KS, (b) Bain, and (c) NW orientation relationships.

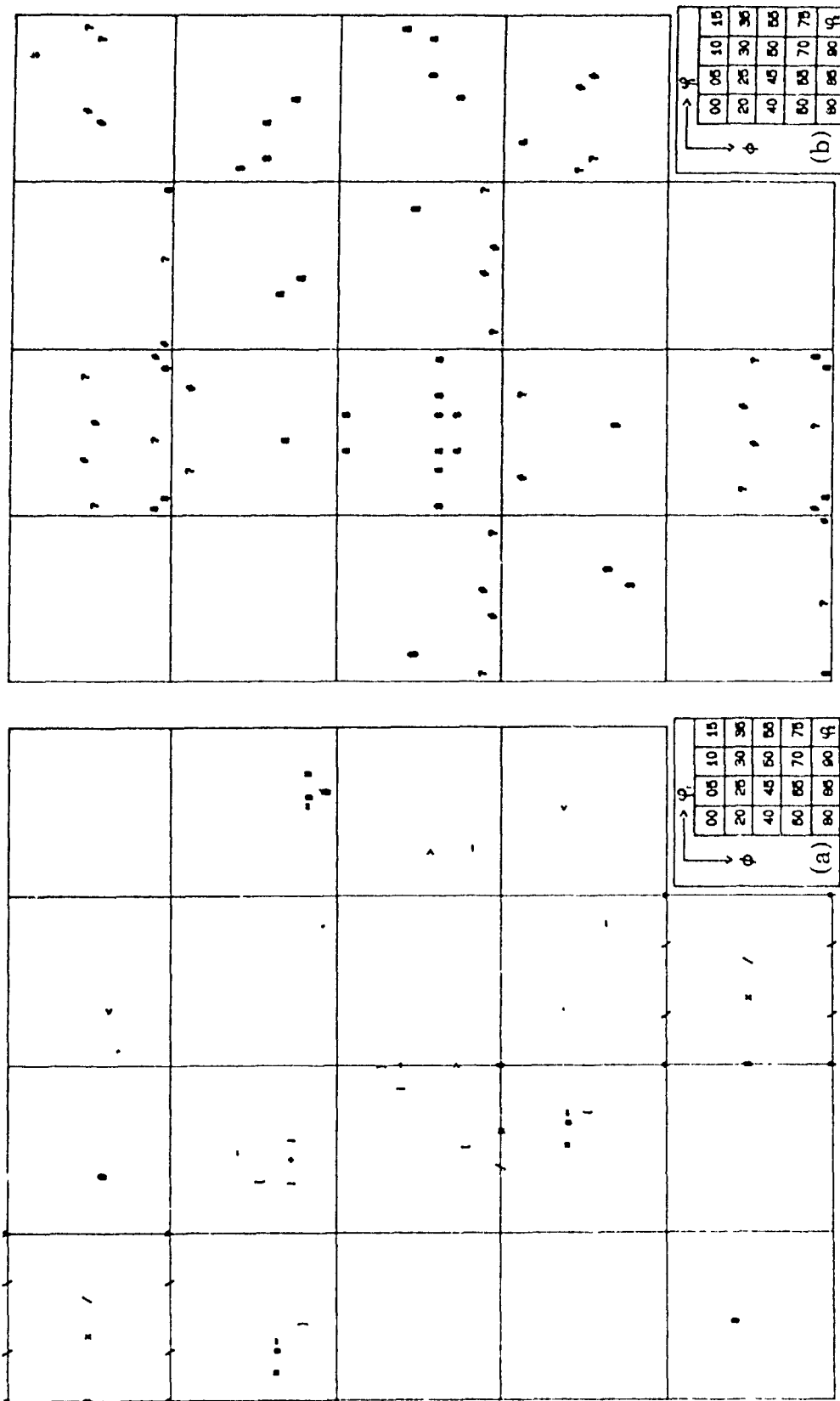


Figure 5-10 (a) and (b) : (a) Some classical fcc texture components; (b) KS-related orientations untransformed from the Cube Goss and associated rotated orientations.

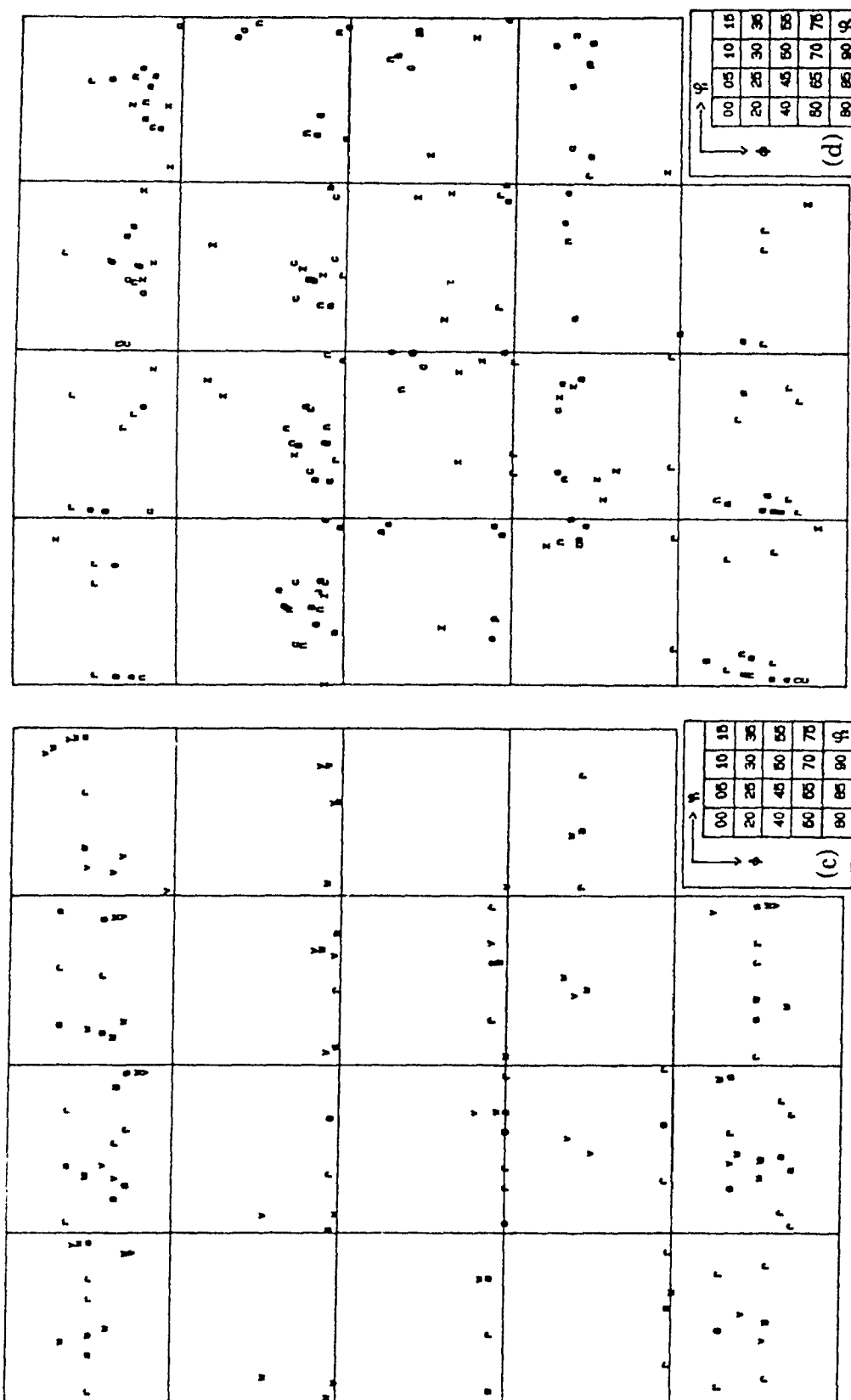


Figure 5-10 (c) and (d) : KS-related orientations untransformed from bcc rolling components (c) near the $\alpha = \langle 110 \rangle // \text{RD}$ fibre and (d) near the $\gamma = \langle 111 \rangle // \text{ND}$ fibre.

V.2.3 RESULTS OF THE CONTINUOUS SIMULATIONS

Unfortunately, a texture cannot be completely defined in terms of its peak type components and a full description by means of its orientation distribution function must therefore be employed. It has been assumed here that the ODF's of some Ni-Co alloys describe the rolling textures of austenites with comparable stacking fault energies. These were transformed according to the Bain, KS and NW relationships to yield textures corresponding to the bcc α obtained from the fcc γ by phase transformation. No variant selection rule was employed. The transformed ODF's are represented by their ϕ_1 sections, as is often the case for bcc textures, since most of the important orientations lie in these planes. In what follows, an ODF predicted using the KS transformation law is often termed KS-predicted, KS-selected or KS-derived, and similarly for the Bain and NW relationships.

- general observations regarding the simulated transformation textures:

It should first be noted, when comparing the simulated bcc textures with their fcc originals, that because of the multiplicity of variants in the transformation, the transformed ODF's always appear less intense than their parent γ textures. Also, all the predicted ODF's - except those corresponding to Ni-60Co - have similar characteristics (shape, maxima, intensities...). They are defined by two peaks, almost equally strong, in the vicinity of $\{332\}\langle 113 \rangle$ and $\{113\}\langle 110 \rangle$, but their relative importance as well as their exact locations depend on the amount of cobalt and the rolling reduction applied to the parent alloy.

This is not unexpected in the case of the textures derived from the Ni-Co alloys containing 10, 20 and 30 percent cobalt, since their respective SFE levels ensure a similar type of fcc rolling texture. Even the textures simulated from Ni-40Co (intermediate fcc texture) resemble those from the alloys with lower Co contents (pure metal type fcc texture). However, the intensity of the $\{113\}\langle 110 \rangle$ component is lowered and the $\{332\}\langle 113 \rangle$ peak is broadened compared to the Ni-10Co to Ni-30Co cases. On the other hand, the textures computed from Ni-60Co are of a different type. Two peaks still appear, but at markedly different positions: one at $\{111\}\langle 112 \rangle$, which is about 10 degrees away from $\{332\}\langle 113 \rangle$, and another near $\{100\}\langle 011 \rangle$. In general, the severity of the texture increases with the level of reduction, although the sharpness of the initial ODF is also a crucial parameter. The derived ODF's thus encompass the possible transformation textures that should be obtained from fcc γ with a range of SFE values and various rolling reductions.

The MODF's corresponding to the Bain, KS and NW orientation relationships have been employed in turn for the simulations and, although the general features of the three families of transformed ODF's are similar, the ones deduced from the Bain relation are always much sharper than those calculated from the other two. The NW-derived ODF's are detectably more intense (e.g. in terms of the severity parameters) than the KS-derived, in keeping with their respective numbers of variants.

- detailed description of the ODF's obtained with the KS relationship :

As stated in the presentation of the experimental results (V.2.1), the rolling textures of the Ni-Co alloys under study can be divided into three categories, depending on their stacking fault energies, namely the (i) pure metal, (ii) intermediate, and (iii) alloy type textures. Correspondingly, the simulated bcc textures were expected to fall into three groups, investigated in turn below. In all three cases, the derived bcc textures are less severe than those of their parent fcc structures.

(a) bcc textures transformed from pure metal type fcc rolling textures : These correspond to the textures derived from the Ni-Co alloys containing 10, 20 and 30 percent cobalt. Their ϕ_1 -section ODF's are shown in Figures 5-11, 5-12 and 5-13, respectively, for the four different rolling reductions (40, 70, 90 and 95%). The intensities along the α ($\langle 110 \rangle // RD$) and γ ($\langle 111 \rangle // ND$) fibres have also been plotted and are presented in Figures 5-14 and 5-15 as functions of the cobalt content, and in Figures 5-16 (a),(b),(c) and 5-17 (a),(b),(c) as functions of the amount of rolling deformation. Two maxima can be seen, irrespective of the alloy composition and of the degree of reduction before transformation. However, they gradually sharpen with rolling deformation. As a result, the severities of the ODF's derived from these three alloys, which are close at a given reduction, increase with the amount of prior reduction in the γ phase.

The positions of the two maxima in the transformation texture merely depend on the alloy composition and on its deformation level. As can be seen from Tables 5-11 and 5-12, for the lower Co contents (10 and 20% cobalt), the strongest peak first appears at the $\{112\} \langle 110 \rangle$ component after very light rolling in the γ phase and, as the deformation is increased, progressively shifts towards $\{225\} \langle 110 \rangle$, i.e. between $\{112\} \langle 110 \rangle$ and $\{113\} \langle 110 \rangle$ (Figures 5-16 (a) and (b)). It is also worth noting that this maximum, although of a peak type, is rather broad. A high degree of angular spread is thus involved. The width of the $\{225\} \langle 110 \rangle$ peak should not be confused

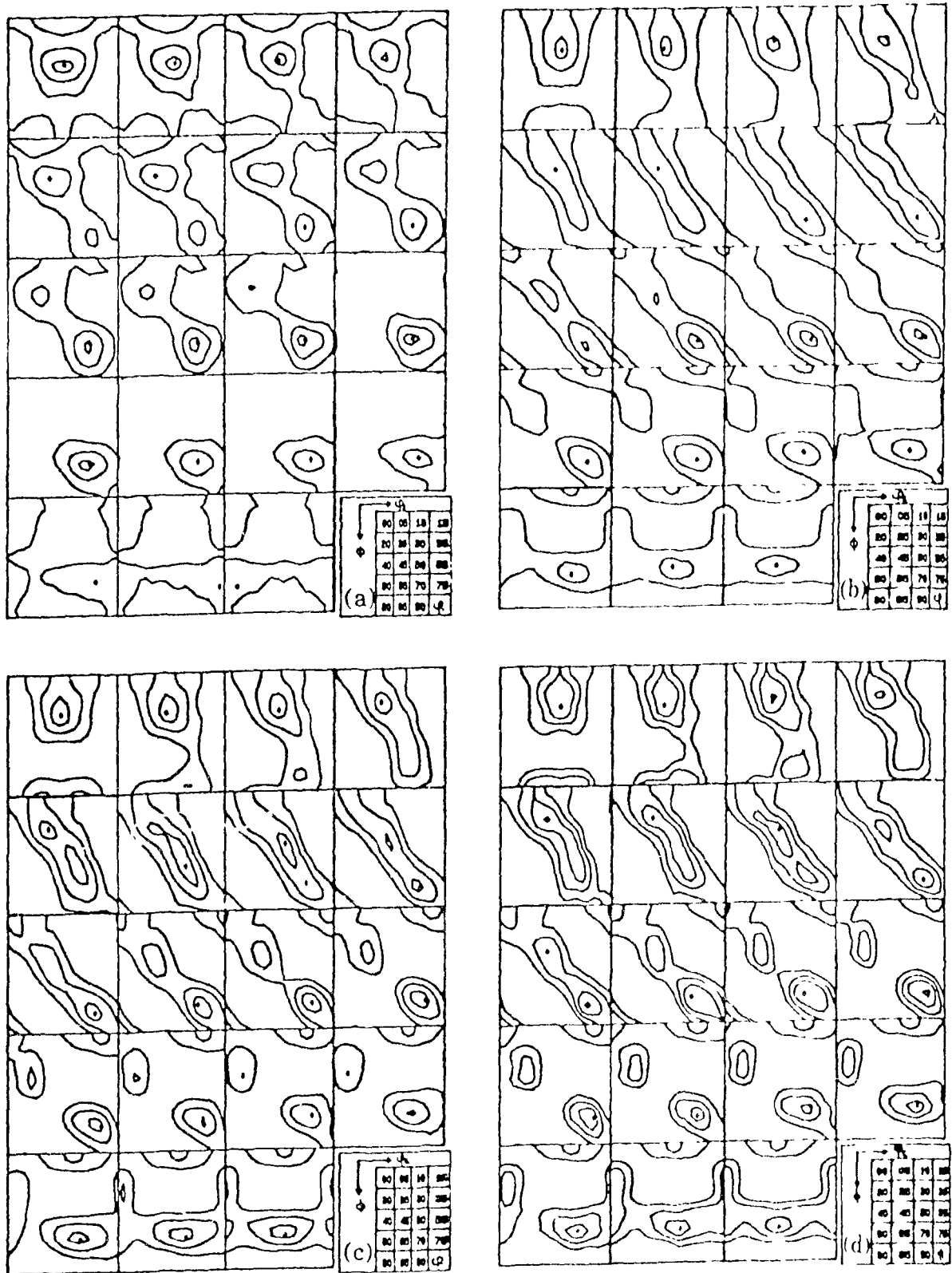


Figure 5-11 · ϕ_1 -section ODF's obtained by transforming the texture of Ni-10Co according to the KS relationship after (a) 40%, (b) 70%, (c) 90%, and (d) 95% reduction prior to transformation (levels 1,2,3...).

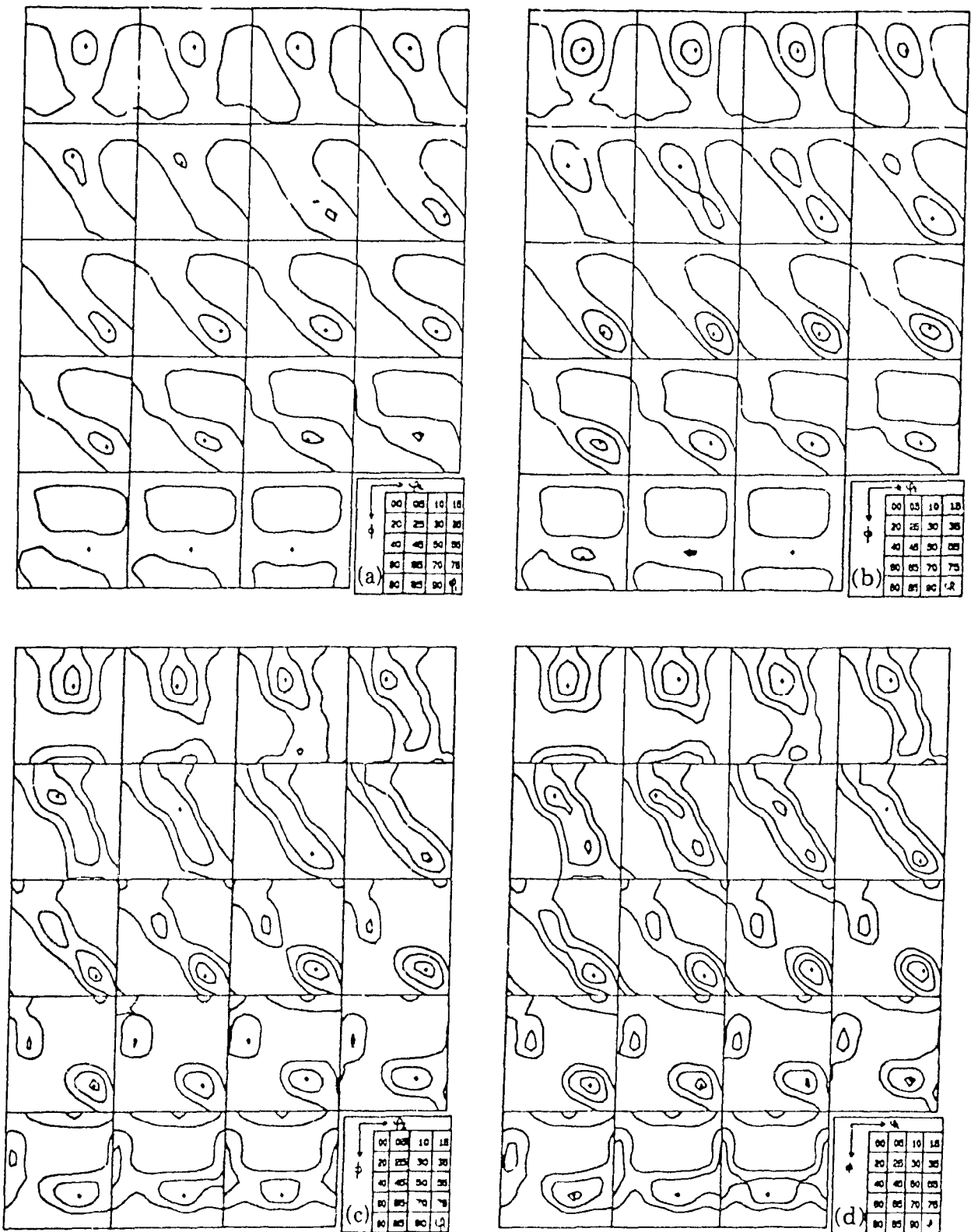


Figure 5-12 : ϕ_1 -section ODF's obtained by transforming the texture of Ni-20Co according to the KS relationship after (a) 40%, (b) 70%, (c) 90%, and (d) 95% reduction prior to transformation (levels 1,2,3...).

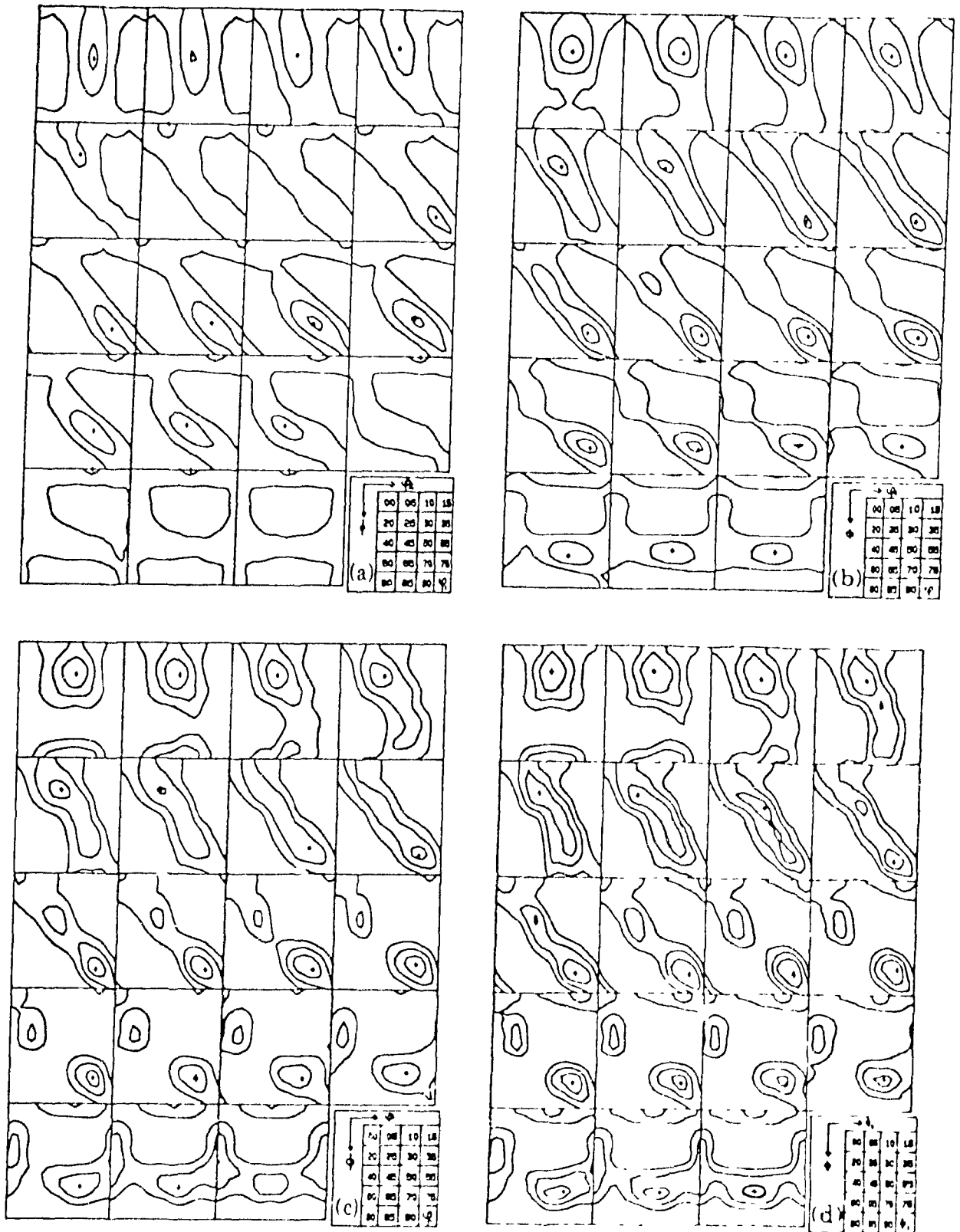


Figure 5-13 : ϕ_1 -section ODF's obtained by transforming the texture of Ni 30Co according to the KS relationship after (a) 40%, (b) 70%, (c) 90%, and (d) 95% reduction prior to transformation (levels 1,2,3 ...).

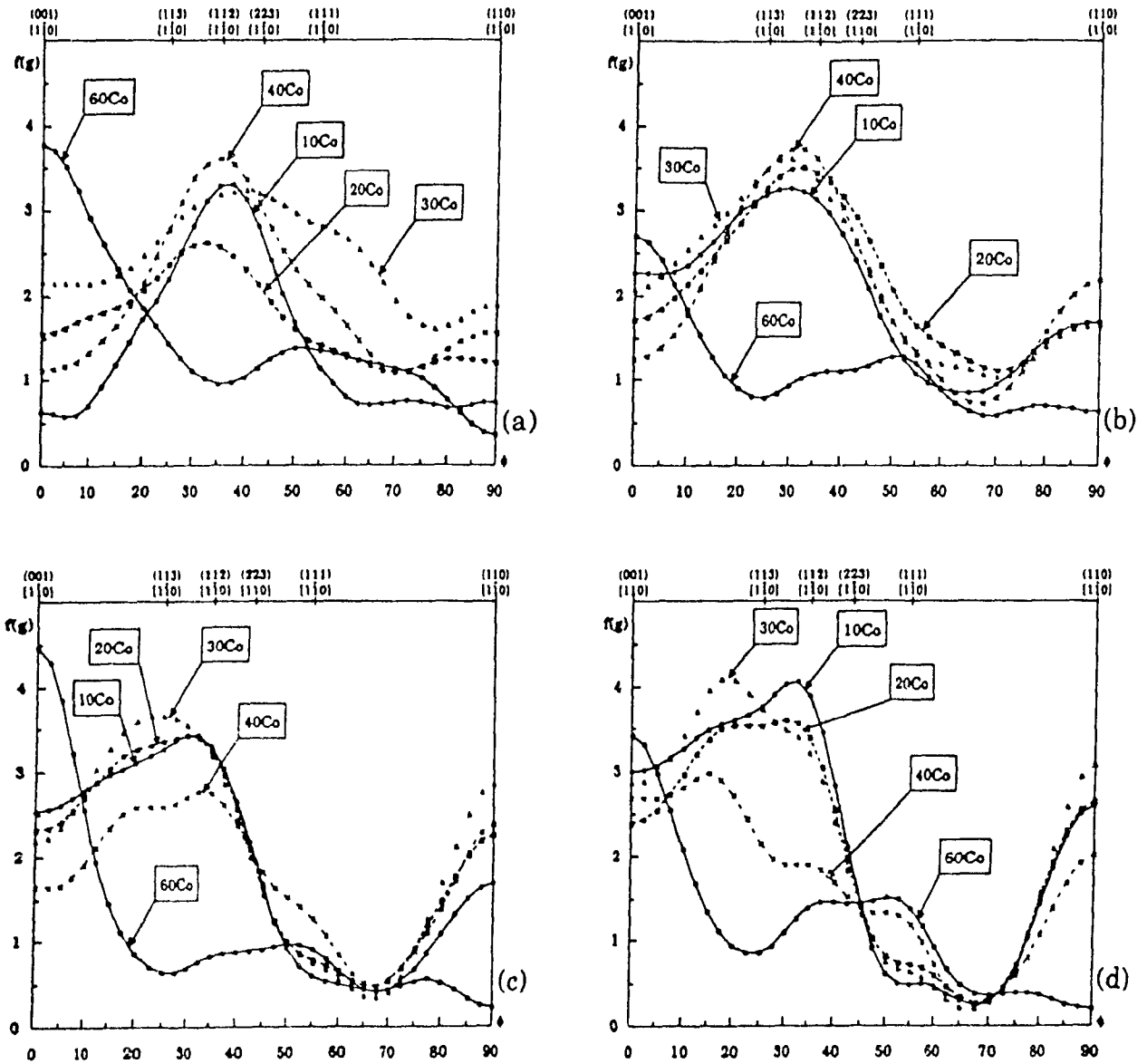


Figure 5-14: Ferrite α fibres deduced from the ODF's obtained by transforming the texture of the five Ni-Co alloys according to the KS relationship after (a) 40%, (b) 70%, (c) 90%, and (d) 95% reduction prior to transformation.

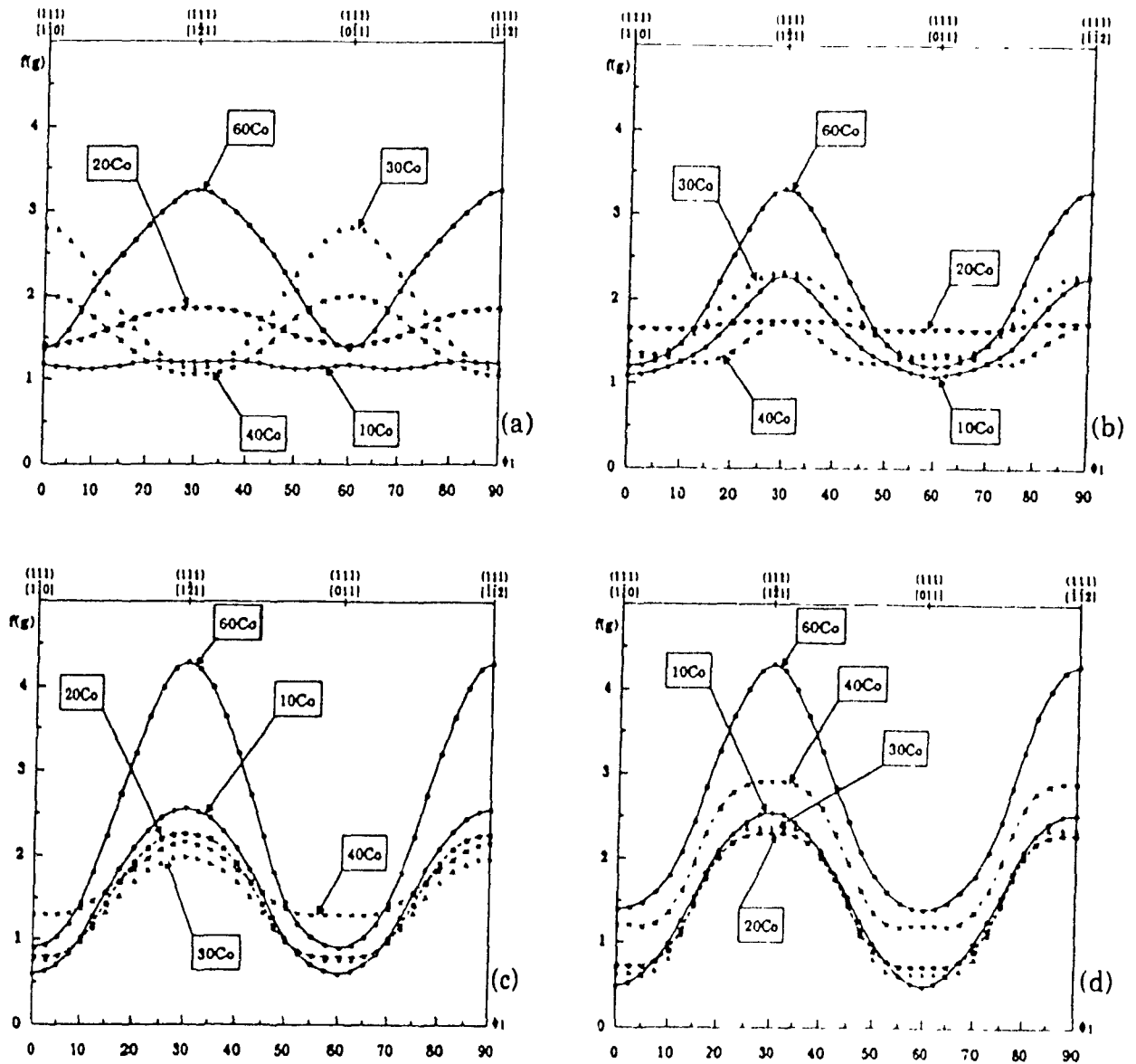


Figure 5-15: Ferrite γ fibres deduced from the ODF's obtained by transforming the texture of the five Ni-Co alloys according to the KS relationship after (a) 40%, (b) 70%, (c) 90%, and (d) 95% reduction prior to transformation

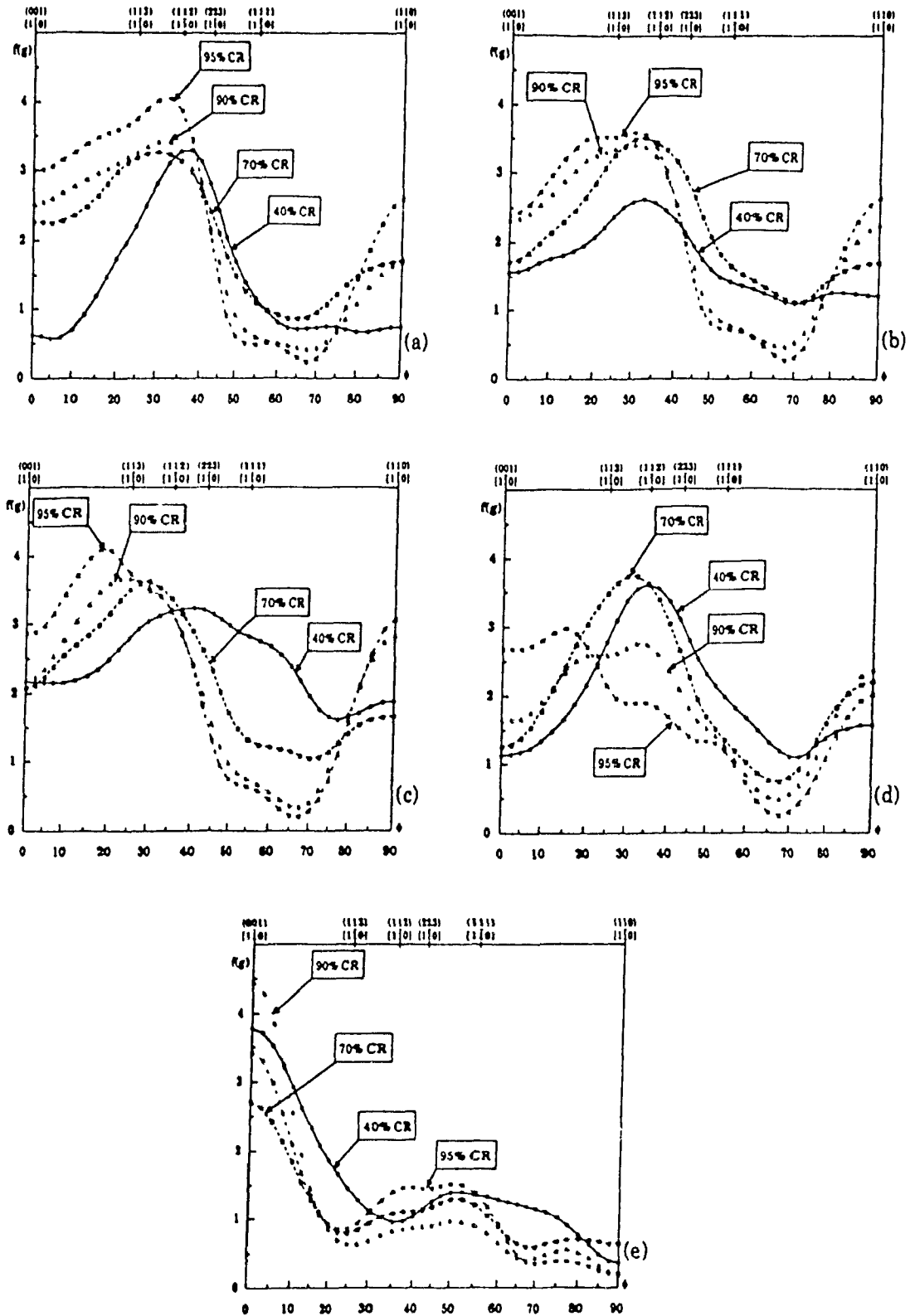


Figure 5-16 : Ferrite α fibres of the ODF's obtained by transforming the texture of (a)Ni-10Co, (b)Ni-20Co, (c)Ni-30Co (d)Ni-40Co, (e)Ni-60Co with the KS relationship.

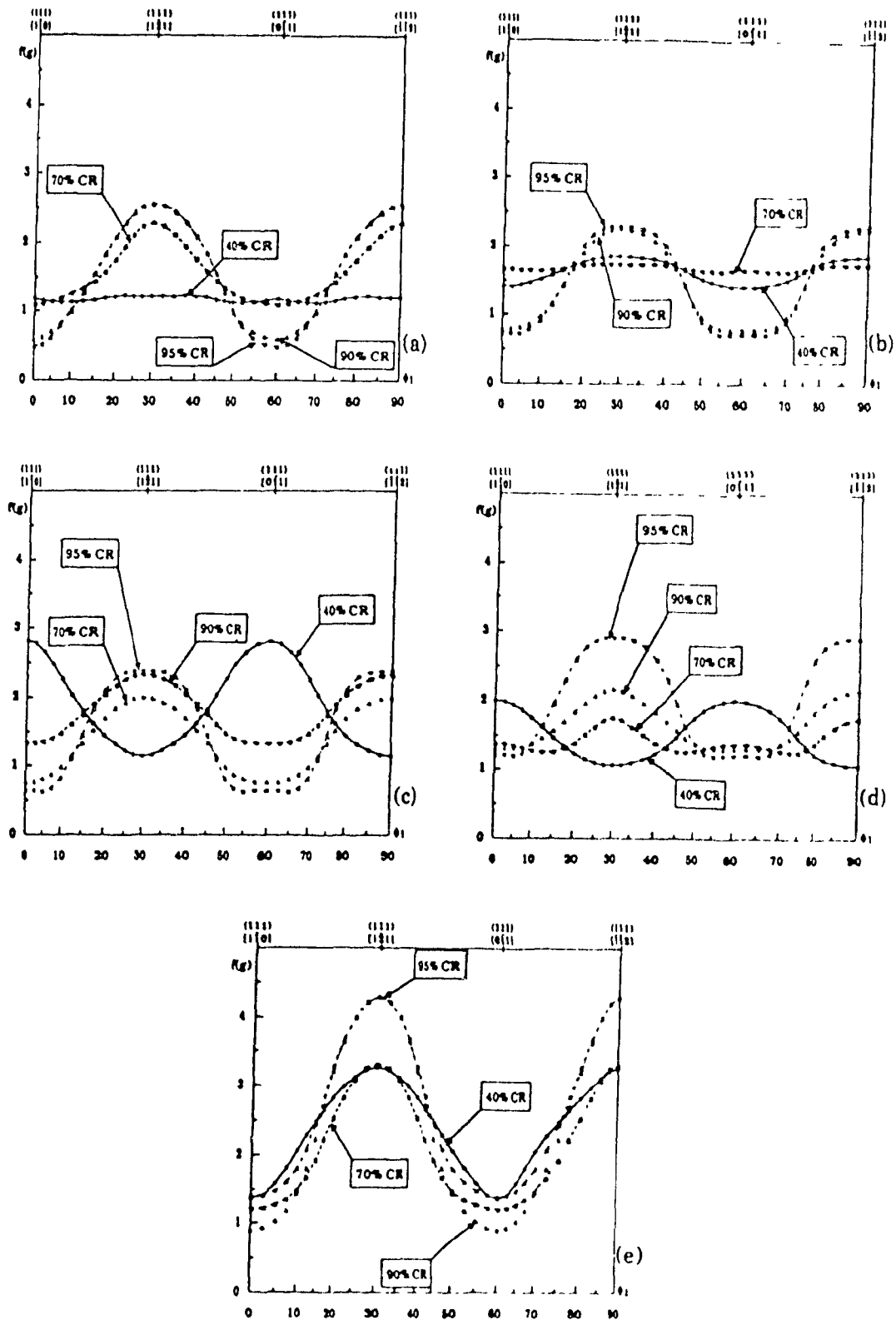


Figure 5-17 : Ferrite γ fibres of the ODF's obtained by transforming the texture of (a) Ni-10Co, (b) Ni-20Co, (c) Ni-30Co (d) Ni-40Co, (e) Ni-60Co with the KS relationship

reduction	40%		70%		90%		95%	
	location	I	location	I	location	I	location	I
severity	-	53	-	70	-	81	-	96
maxima	$\{112\} \langle 110 \rangle$	3 2	$\{225\} \langle 110 \rangle$	3 2	$\{225\} \langle 110 \rangle$	3 4	$\{225\} \langle 110 \rangle$	4 0
	-	-	$\{554\} \langle 225 \rangle$	3 5	$\{332\} \langle 113 \rangle$	3 5	$\{332\} \langle 113 \rangle$	3 5
2 nd order	-	-	$\{201\} \langle 102 \rangle$	1 5	$\{201\} \langle 102 \rangle$	2 0	$\{201\} \langle 102 \rangle$	2 5
maxima	-	-	$\{100\} \langle 011 \rangle$	2 5	$\{100\} \langle 011 \rangle$	2 5	$\{100\} \langle 011 \rangle$	2 5

Table 5-11: Main characteristics of the bcc textures KS-transformed from Ni-10Co.

reduction	40%		70%		90%		95%	
	location	I	location	I	location	I	location	I
severity	-	46	-	66	-	76	-	84
maxima	$\{112\} \langle 110 \rangle$	2 5	$\{225\} \langle 110 \rangle$	3 5	$\{225\} \langle 110 \rangle$	3 3	$\{225\} \langle 110 \rangle$	3 5
	-	-	$\{554\} \langle 225 \rangle$	2 0	$\{332\} \langle 113 \rangle$	2 5	$\{332\} \langle 113 \rangle$	2 5
2 nd order	-	-	-	-	$\{201\} \langle 102 \rangle$	2 2	$\{201\} \langle 102 \rangle$	2 5
maxima	-	-	-	-	$\{100\} \langle 011 \rangle$	2 5	$\{100\} \langle 011 \rangle$	2 5

Table 5-12: Main characteristics of the bcc textures KS-transformed from Ni-20Co.

with the presence of a fibre type component. On the contrary, the second most important peak of the texture, which also exhibits a peak form (i.e. no evidence for a fibre) in the vicinity of $\{332\} \langle 113 \rangle$, is narrower, as can be seen from the $\phi_1 = 90^\circ$ section of any of the KS-predicted ODF's in Figures 5-11 and 5-12, especially along the ϕ axis. Along the ϕ_2 axis, on the other hand, some overlapping is noted, with a minor component located near $\{201\} \langle 102 \rangle$. The exact position of this second maximum again varies with the amount of reduction prior to transformation. For the two alloys under consideration (Ni-10Co and Ni-20Co), $\{554\} \langle 225 \rangle$ gives a better description of the maximum at low deformations (up to 70%), but it finally shifts to $\{332\} \langle 113 \rangle$ after heavy γ rolling.

Compared to Ni-10Co and Ni-20Co, which have rather high SFE's, the textures derived from Ni-30Co, if analyzed in detail from Figure 5-13, already present some marked differences, although they still belong to the same overall category. For instance, as is evident from Table 5-13 and Figure 5-16 (c), their severities are less

reduction	40%		70%		90%		95%	
	location	I	location	I	location	I	location	I
severity	-	58	-	79		79		95
maxima	$\{112\} \langle 110 \rangle$	3 0	$\{225\} \langle 110 \rangle$	3 5	$\{113\} \langle 110 \rangle$	3 5	$\{114\} \langle 110 \rangle$	4 0
	-	-	$\{554\} \langle 225 \rangle$	2 5	$\{332\} \langle 113 \rangle$	2 5	$\{332\} \langle 113 \rangle$	3 0
2 nd order	-	-	-	-	$\{201\} \langle 102 \rangle$	2 5	$\{201\} \langle 102 \rangle$	3 0
maxima	$\{100\} \langle 011 \rangle$	2 0	$\{100\} \langle 011 \rangle$	2 0	$\{100\} \langle 011 \rangle$	2 0	$\{100\} \langle 011 \rangle$	2 5

Table 5-13: Main characteristics of the bcc textures KS-transformed from Ni-30Co.

sensitive to the amount of rolling: between 70% and 90% reduction, no major changes are observed in the severity parameter and the high intensity levels do not vary much either. At the same time, the position of the maximum becomes more sensitive to rolling: it is still located at $\{112\} \langle 110 \rangle$ for 40% γ rolling, as in the previous case, and again shifts to $\{225\} \langle 110 \rangle$ after 70% reduction. After 90%, however, it is to be found closer to $\{113\} \langle 110 \rangle$ and even moves towards $\{114\} \langle 110 \rangle$ when 95% deformation is carried out, as opposed to its position near $\{225\} \langle 110 \rangle$ for Ni-10 and 20 Co (see also Figures 5-14 and 5-15 for comparison with Ni-10Co and Ni-20Co).

In the simulated ODF's derived from the three alloys, second order maxima are often found near $\{201\} \langle 102 \rangle$ and $\{100\} \langle 011 \rangle$. Their strengths are sensitive to the amount of rolling reduction, so that they become significant after 90-95% deformation, as shown in Table 5-13.

(b) bcc textures transformed from intermediate type fcc rolling textures
When the ODF's simulated from Ni-40Co, which are illustrated in Figure 5-18, are compared with those derived from the pure metal type rolling textures just described, many similarities are evident. However, along the lines of the detailed analysis begun above, and in agreement with the tendencies shown by the Ni-30Co based

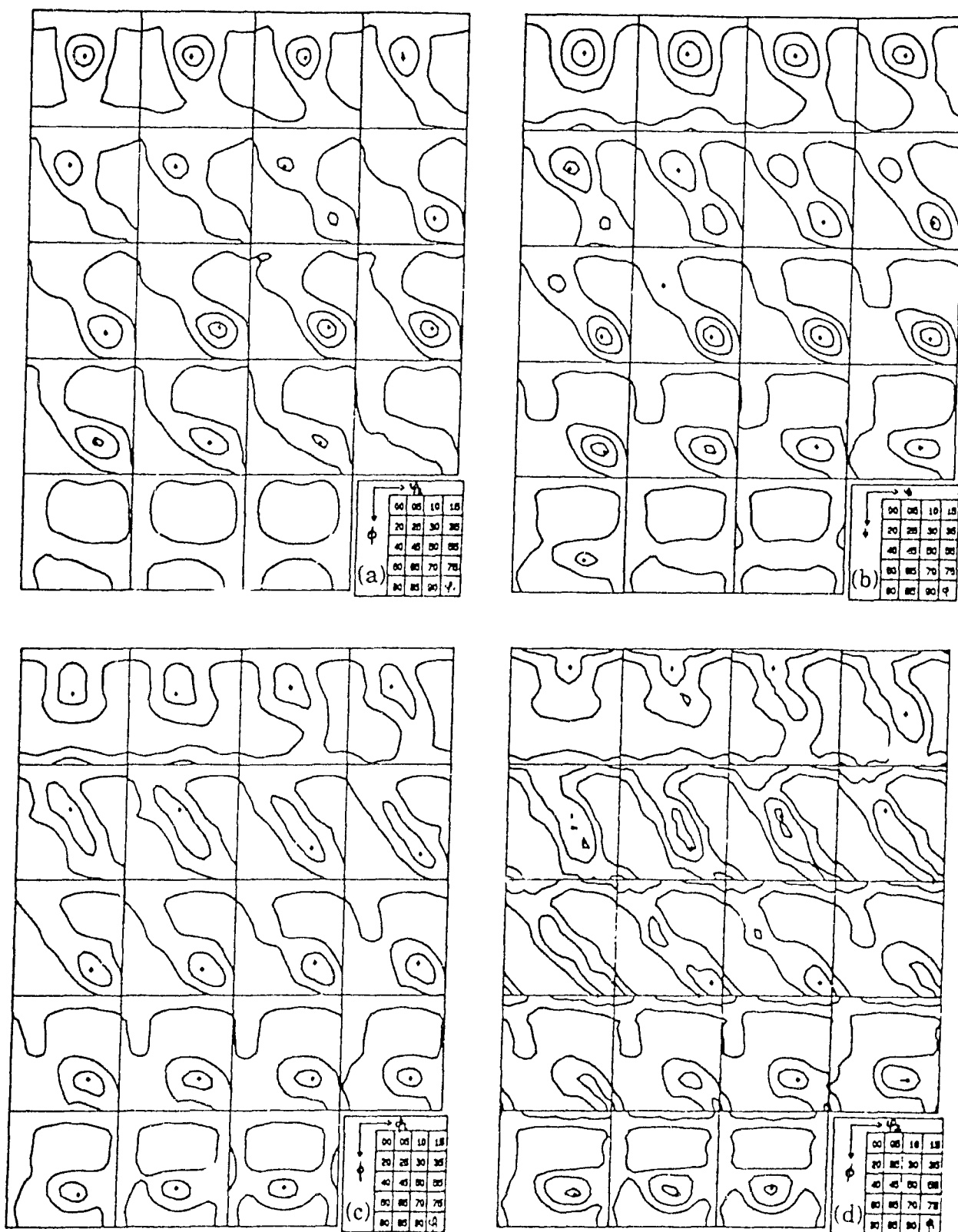


Figure 5-18 ϕ_1 -section ODF's obtained by transforming the texture of Ni-40Co according to the KS relationship after (a) 40%, (b) 70%, (c) 90%, and (d) 95% reduction prior to transformation (levels 1,2,3...).

reduction	40%		70%		90%		95%	
	location	I	location	I	location	I	location	I
severity	-	53	-	68	-	62	-	77
maxima	$\{112\} \langle 110 \rangle$	3.5	$\{225\} \langle 110 \rangle$	3.7	$\{225\} \langle 110 \rangle$	2.5	$\{114\} \langle 110 \rangle$	2.0
	-	-	-	-	$\{554\} \langle 225 \rangle$	2.5	$\{554\} \langle 225 \rangle$	3.0
2 nd order	-	-	$\{201\} \langle 102 \rangle$	2.0	$\{201\} \langle 102 \rangle$	2.0	$\{201\} \langle 102 \rangle$	2.0
maxima	-	-	-	-	-	-	$\{100\} \langle 011 \rangle$	1.5

Table 5-14. Main characteristics of the bcc textures KS-transformed from Ni-40Co.

ODF's, some differences can still be pointed out, e.g. in Figures 5-16 (d) and 5-17 (d), which illustrate the influence of the texture transition in the parent fcc structure.

The severities of the derived ODF's given in Table 5-14 also show a noticeable drop during intermediate rolling as the maximum near $\{112\} \langle 110 \rangle$ progressively disappears. $\{554\} \langle 225 \rangle$, which thus becomes the major component of the texture, does not sharpen sufficiently, however, to balance the decrease in severity, so that globally the ODF's become comparatively less severe at higher rolling reductions than those derived from pure metal type fcc textures. The $\{554\} \langle 225 \rangle$ peak is also broader in Ni-40Co than in the previous alloys.

The positions of the maxima change slightly from the case of Ni-30Co. The peak in the vicinity of $\{112\} \langle 110 \rangle$ after 40% reduction rotates to $\{225\} \langle 110 \rangle$, where it remains during the whole intermediate rolling process. Only after heavy deformation does it shift towards its ultimate position near $\{114\} \langle 110 \rangle$, also observed for the textures derived from Ni-30Co. On the other hand, $\{554\} \langle 225 \rangle$ is the best description of the other maximum. No rotation to $\{332\} \langle 113 \rangle$ is observed, even at very high rolling levels, as was the case for Ni-30Co. The second order maximum near $\{201\} \langle 102 \rangle$ is still apparent, although only in the spray of the $\{114\} \langle 110 \rangle$ after 95% γ rolling, whereas that in the vicinity of $\{100\} \langle 011 \rangle$ is hardly visible.

(c) bcc textures transformed from alloy type fcc rolling textures. In contrast to the two previous cases, the textures simulated from Ni-60Co differ significantly from those predicted for all the other alloys, as indicated in Figures 5-14 and 5-15.

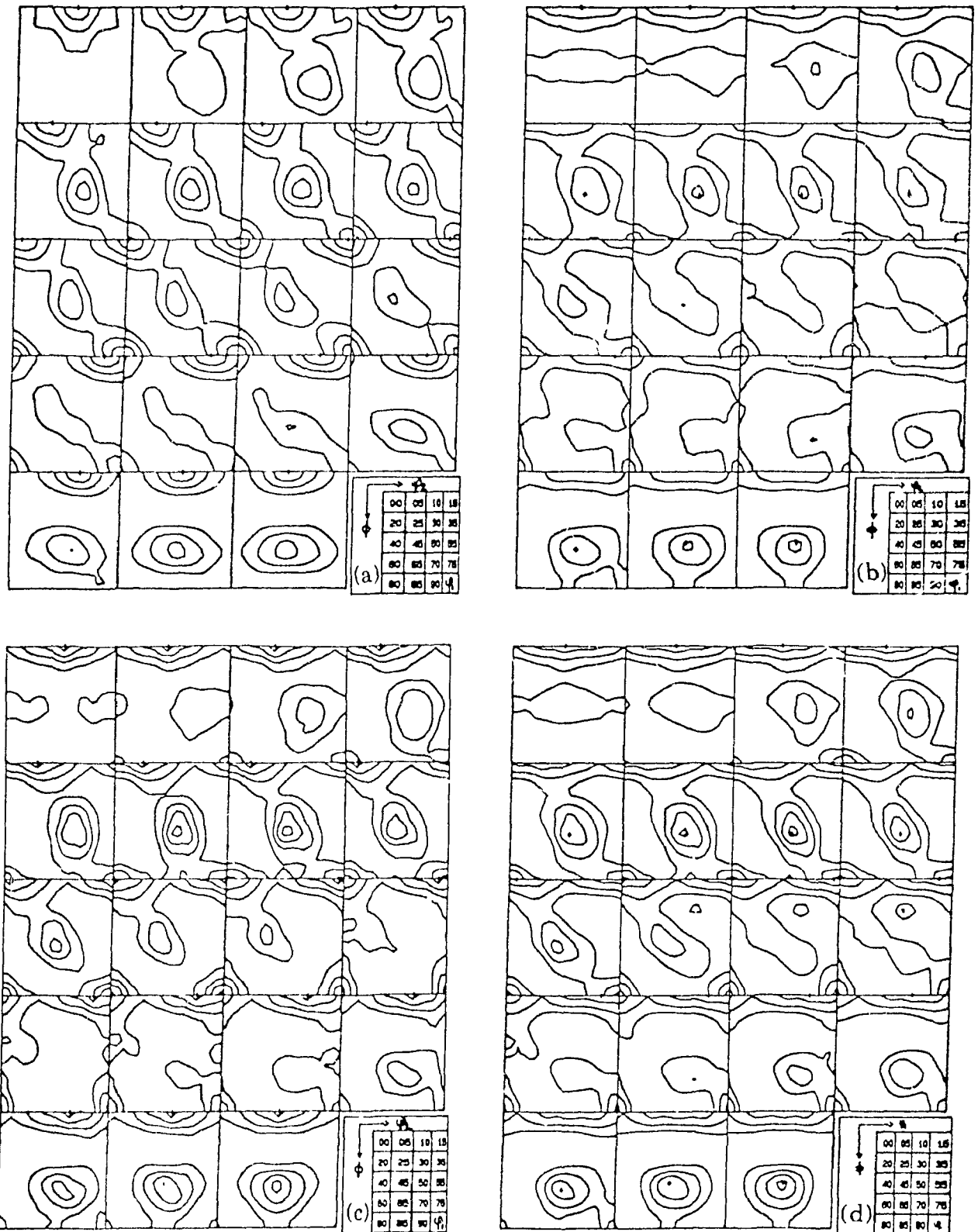


Figure 5-19 : ϕ_1 -section ODF's obtained by transforming the texture of Ni-60Co according to the KS relationship after (a) 40%, (b) 70%, (c) 90%, and (d) 95% reduction prior to transformation (levels 1,2,3...).

reduction	40%		70%		90%		95%	
	location	I	location	I	location	I	location	I
severity	-	77	-	63	-	87	-	90
maxima	{100}<011>	3.8	{100}<011>	2.7	{100}<011>	4.5	{100}<011>	3.4
	{111}<112>	3.2	{111}<112>	3.3	{111}<112>	4.3	{111}<112>	4.3
2 nd order	-	-	{100}<012>	2.0	{100}<012>	1.5	{100}<012>	2.0
maxima	-	-	-	-	-	-	-	-

Table 5-15 : Main characteristics of the bcc textures KS-transformed from Ni-60Co.

They still consist of two peaks, visible in Figure 5-19, but at the rather different locations reported in Table 5-15 : one at $\{111\}\langle 112 \rangle$, i.e. about 10 degrees away from $\{332\}\langle 113 \rangle$; its strength depends on the rolling reduction in an irregular manner. The other one always falls close to $\{100\}\langle 011 \rangle$, i.e. 15 degrees away from $\{113\}\langle 110 \rangle$ on the $\langle 100 \rangle // \text{RD}$ fibre, and its intensity increases with the deformation (Figure 5-16 (e)). Actually, this can be best described as a partial $\langle 100 \rangle // \text{ND}$ fibre, with maximum intensity at $\{100\}\langle 011 \rangle$, which develops with rolling. At low reductions, $\{100\}\langle 011 \rangle$ is already strong, and appears as a peak. There is also a second order peak near $\{100\}\langle 012 \rangle$ with an intensity which is almost independent of the amount of rolling.

- influence of the choice of the orientation relationship.

As stated earlier, for any alloy, the derived ODF's are always markedly more intense for the Bain orientation relationship than for the other two, and NW is always a little sharper than KS. In the following, the Bain and NW results are compared with the KS ones since the latter are generally reported to give the best description of actual transformations in steels.

(a) **Bain vs KS predictions** : Figures 5-20 (a) to (d) illustrate the Bain-predicted ODF's for the Ni-Co alloys containing 10, 20, 40 and 60% cobalt, respectively, and rolled to 95% reduction. Figure 5-21, on the other hand, shows the influence of the amount of reduction prior to transformation on the Bain-predicted ODF's for Ni-

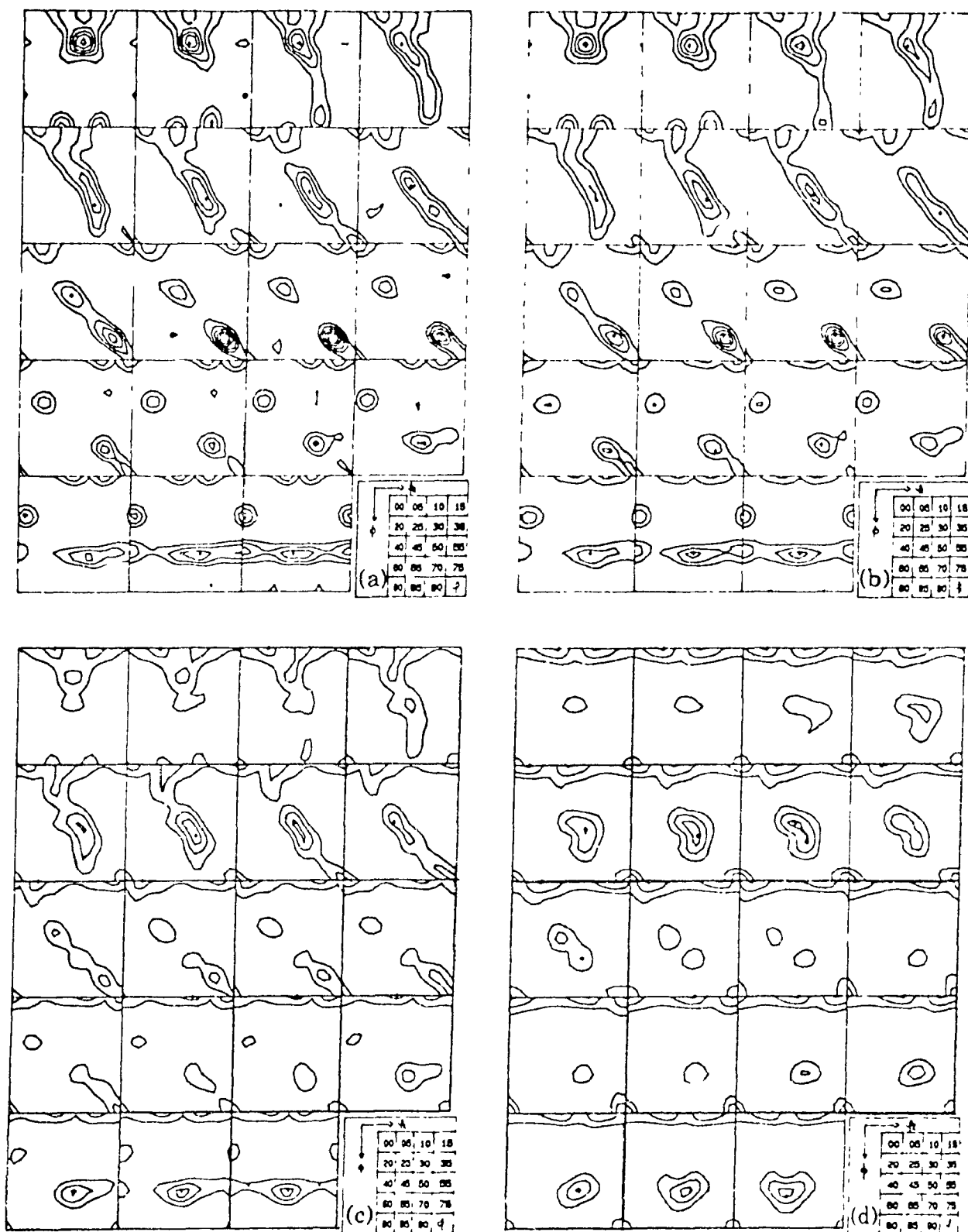


Figure 5-20: ϕ_1 -section ODF's obtained by transforming the texture of (a) Ni-10Co, (b) Ni-20Co, (c) Ni-40Co, (d) Ni-60Co after 95% prior reduction with the Bain orientation relationship (levels 2,4,6...).

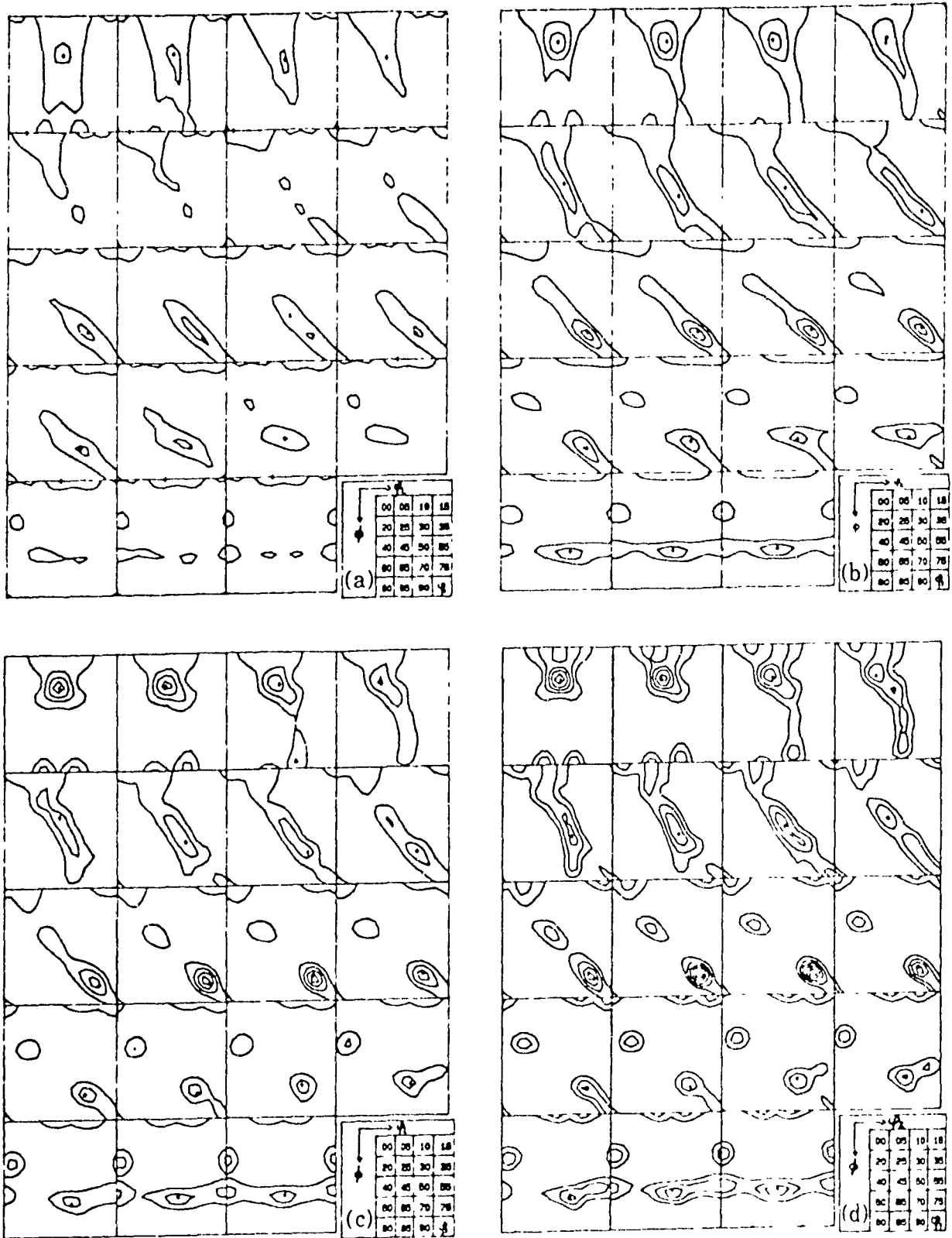


Figure 5-21 : ϕ_1 -section ODF's obtained by transforming the texture of Ni-30Co according to the Bain orientation relationship after (a) 40%, (b) 70%, (c) 90%, and (d) 95% reduction prior to transformation (levels 2,4,6...).

reduction	40%		70%		90%		95%	
	location	I	location	I	location	I	location	I
severity	-	97	-	1 39	-	1 32	-	1 71
maxima	{113}<110>	4	{113}<110>	7	{113}<110>	9	{113}<110>	12
	-	-	{554}<225>	5	{554}<225>	5	{554}<225>	8
2 nd order	{201}<102>	2	{201}<102>	4	{201}<102>	4	{201}<102>	5
maxima	{100}<011>	3	{100}<011>	3	{100}<011>	3	{100}<011>	4

Table 5-16 : Main characteristics of the bcc textures Bain-transformed from Ni-30Co.

reduction	40%		70%		90%		95%	
	location	I	location	I	location	I	location	I
severity	-	1 21	-	1 07	-	1 46	-	1 48
maxima	{100}<011>	6	{100}<023>	5	{100}<023>	7	{100}<023>	6
	{554}<225>	5	{332}<113>	5	{554}<225>	6 5	{554}<225>	6
2 nd order	-	-	-	-	-	-	-	-
maxima	-	-	-	-	-	-	-	-

Table 5-17 : Main characteristics of the bcc textures Bain-transformed from Ni-60Co.

30Co. For purposes of comparison with the KS results, the α and γ fibres were also calculated for the Bain transformation and are presented in Figures 5-22 to 5-25. The general trends of the two families of ODF's are similar to those obtained with the KS relationship, but close study of the severity, positions and intensities of their maxima reveals the differences. As an illustration, the severities and maxima locations and intensities obtained from the Bain transformation law are collected in Table 5-16 for Ni-30Co and in Table 5-17 for Ni-60Co. These two sets of data should be compared with those obtained from the KS derivation presented above in Tables 5-13 and 5-15, respectively. The maximum intensities in the Bain-related ODF's are between 2 and

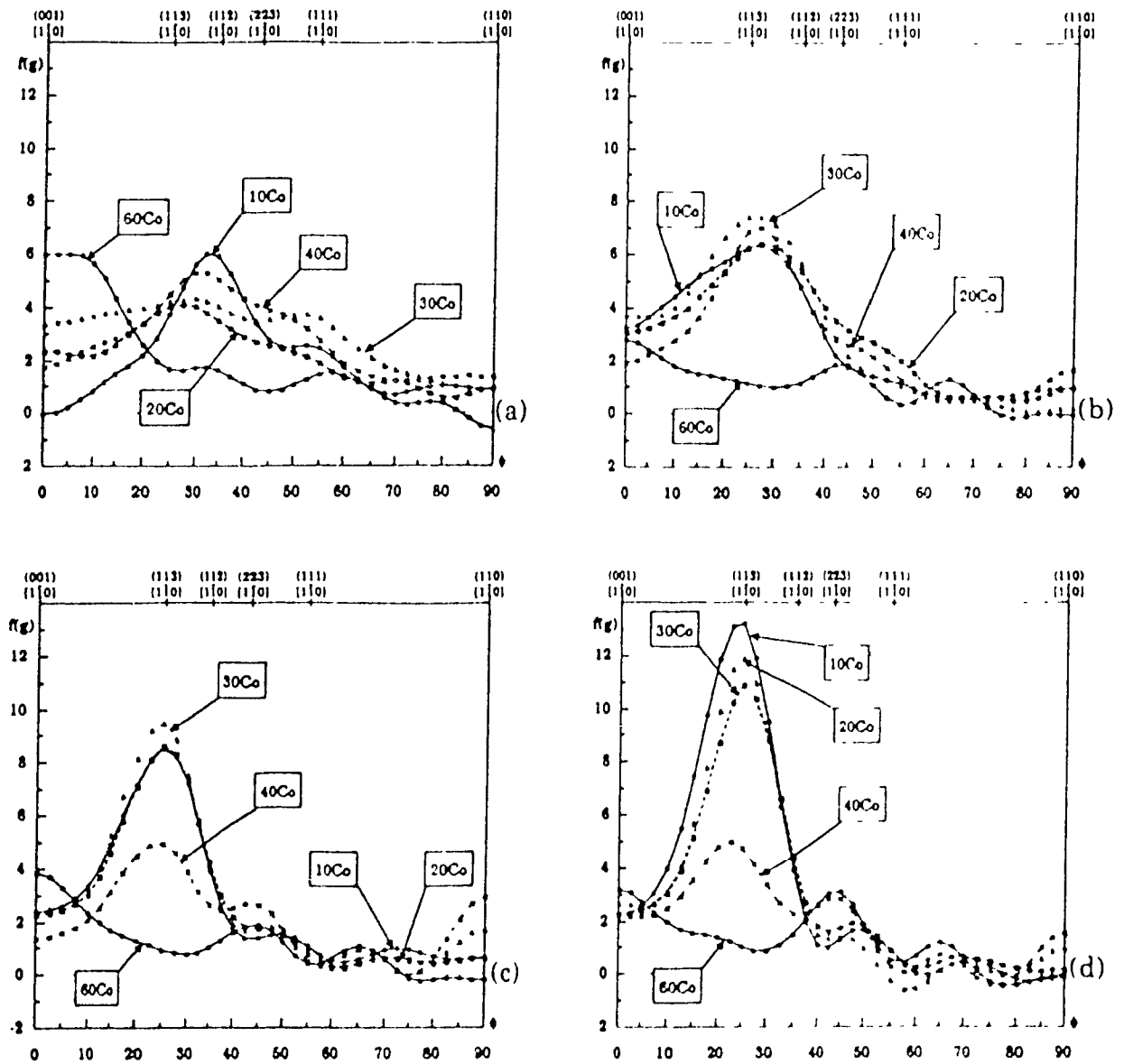


Figure 5-22: Ferrite α fibres deduced from the ODF's obtained by transforming the texture of the five Ni-Co alloys according to the Bain relationship after (a) 40%, (b) 70%, (c) 90%, and (d) 95% reduction prior to transformation.

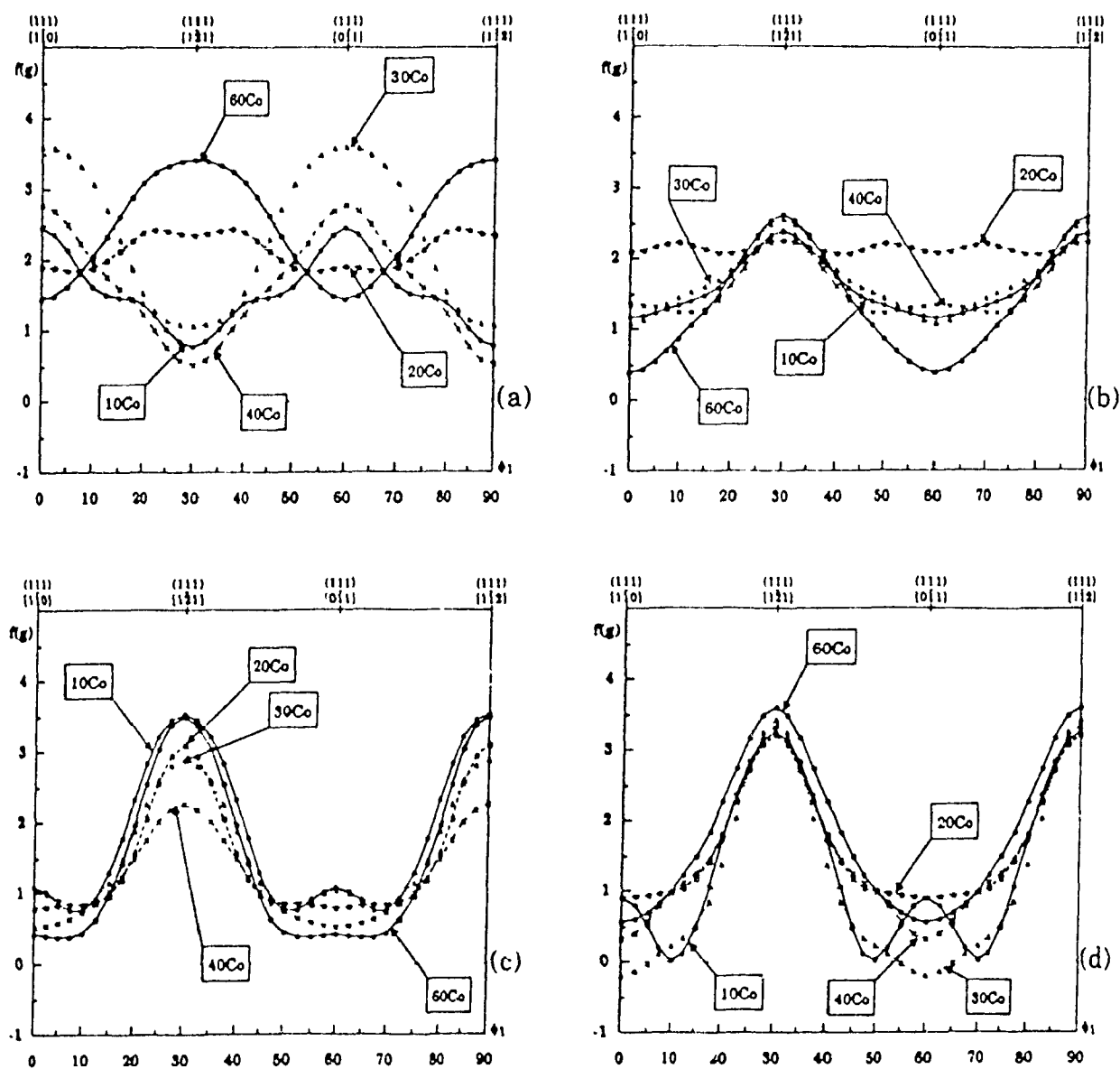


Figure 5-23 : Ferrite γ fibres deduced from the ODF's obtained by transforming the texture of the five Ni-Co alloys according to the Bain relationship after (a) 40%, (b) 70%, (c) 90%, and (d) 95% reduction prior to transformation.

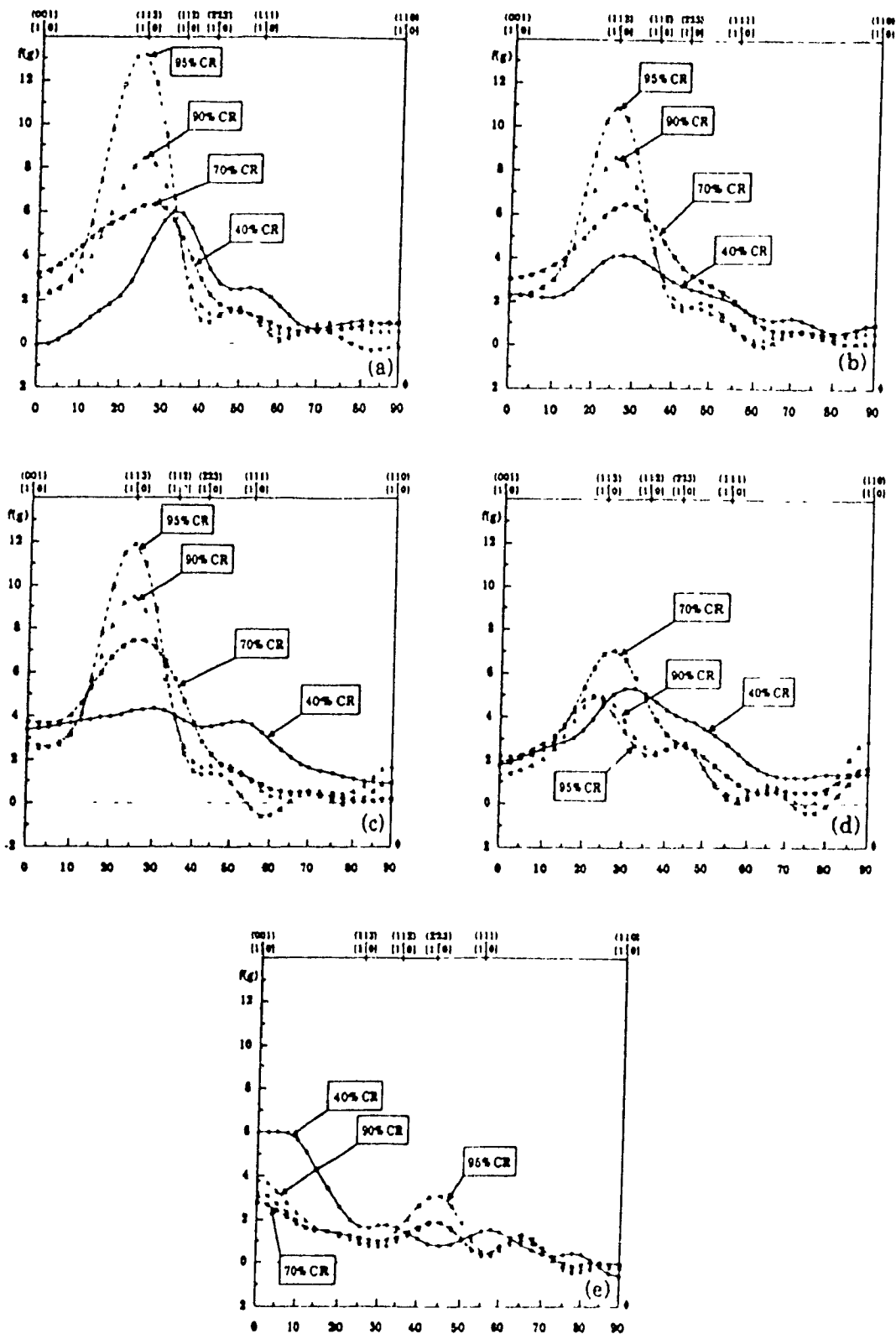


Figure 5-24 : Ferrite α fibres of the ODF's obtained by transforming the texture of (a) Ni-10Co, (b) Ni-20Co, (c) Ni-30Co, (d) Ni-40Co, (e) Ni-60Co with the Bain relationship.

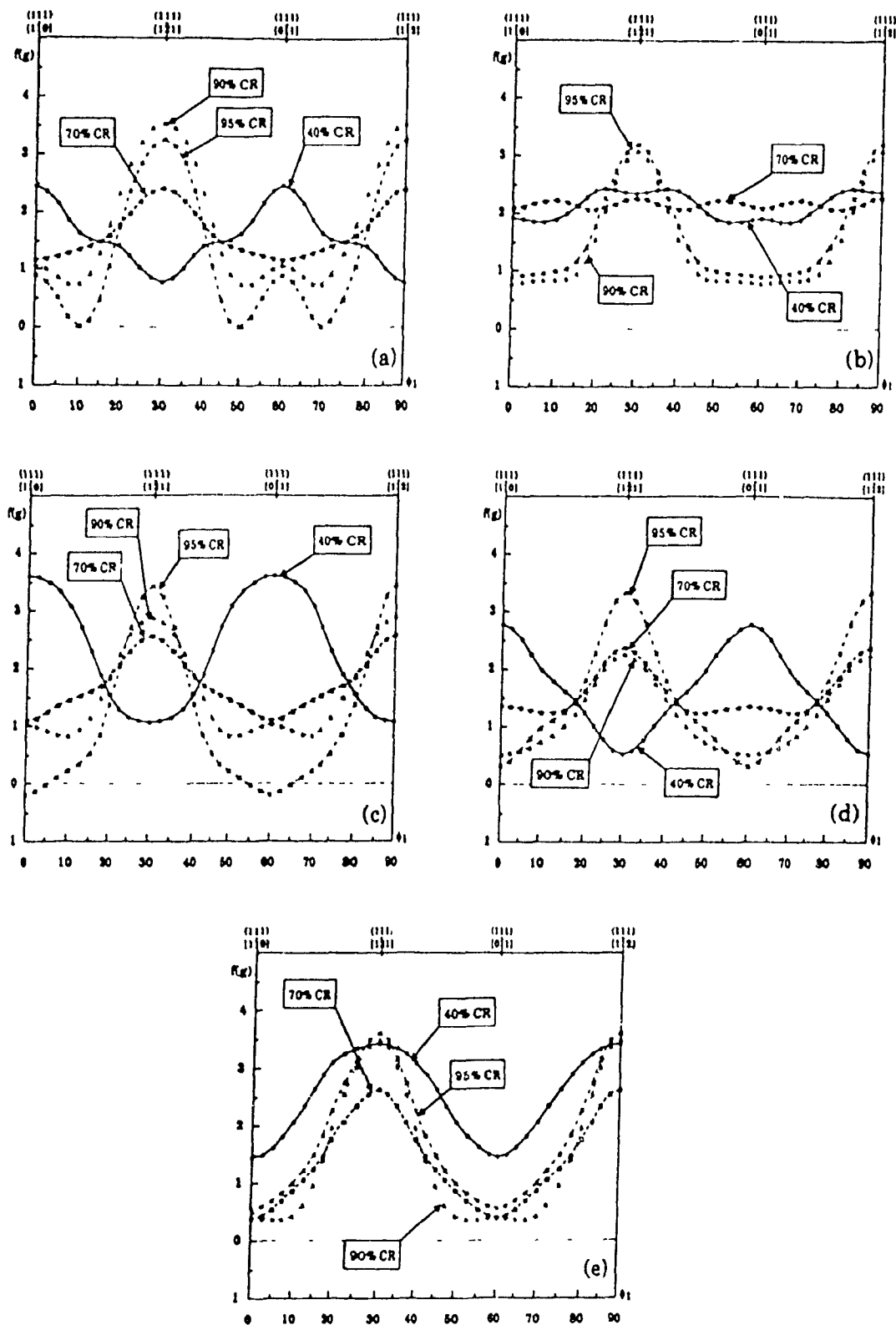


Figure 5-25 : Ferrite γ fibres of the ODF's obtained by transforming the texture of (a) Ni-10Co, (b) Ni-20Co, (c) Ni-30Co, (d) Ni-40Co, (e) Ni-60Co with the Bain relationship.

3 times the respective values for the KS ones. The sharper the texture (i.e. the larger the rolling reduction in the γ phase), the higher the ratio. For second order maxima, however, this ratio is reduced to a value between 1.5 and 2. The corresponding severity parameters, which give a measure of the average sharpness of the whole texture, and not only a measure of the intensities of the maxima, are around 1.7 times larger in the case of Bain than in that of KS. For very high reductions (95%), where the peaks attain higher levels and thus nearly define the entire texture, the severity parameter ratio Bain/KS tends towards a value near 2, which is closer to the coefficient relating the maxima in the two textures.

The predicted positions of the maxima are also slightly modified compared to the KS simulations. The $\{554\}\langle 225 \rangle$ component is almost always predicted using the Bain derivation. On the contrary, a KS prediction leads to the development of a maximum at a location best described by $\{332\}\langle 113 \rangle$, except for Ni-60Co, in which both types of law lead to a $\{554\}\langle 225 \rangle$ peak. In a similar manner, the second Bain-predicted maximum is most often found at $\{113\}\langle 110 \rangle$ for the ODF's simulated for the Ni-Co alloys containing 10, 20, 30 and 40 percent cobalt, using the KS relation, the corresponding peak for these alloys has been shown to fall at $\{112\}\langle 110 \rangle$ after low reductions and then, as the amount of reduction is increased, to move gradually to $\{225\}\langle 110 \rangle$ for Ni-10Co and Ni-20Co, or even to $\{113\}\langle 110 \rangle$, and ultimately to $\{114\}\langle 110 \rangle$ for Ni-30Co and Ni-40Co, respectively (Figures 5-22 and 5-24). For the derivations based on Ni-60Co, the second maximum is best described by $\{100\}\langle 023 \rangle$ if the Bain orientation relationship is employed, except at very low reductions where it is found at $\{100\}\langle 011 \rangle$, as predicted for all rolling levels using the KS relation.

Second order maxima also arise after a Bain transformation, except for Ni-60Co, where there is no real evidence for such a conclusion. As for the main peaks, their intensities are higher than those of the peaks resulting from a KS derivation. Their positions are also slightly shifted with respect to the KS case. $\{203\}\langle 302 \rangle$ is a better description here than $\{201\}\langle 102 \rangle$, and the $\{100\}\langle 011 \rangle$ of the former is moved by 10° along the $\langle 100 \rangle$ ND fibre.

(b) NW vs KS predictions. Figures 5-26 and 5-27 show the influence of cobalt content and rolling reduction on the NW-predicted ODF's. Again the two sets of simulated ODF's are similar and the resemblances are even more striking than with Bain. However, the maximum intensities as well as the severity parameters are about 10-15% higher in the NW-related ODF's compared to their respective levels for the corresponding KS-derived ones, as indicated in Tables 5-18 and 5-19 for Ni-30Co

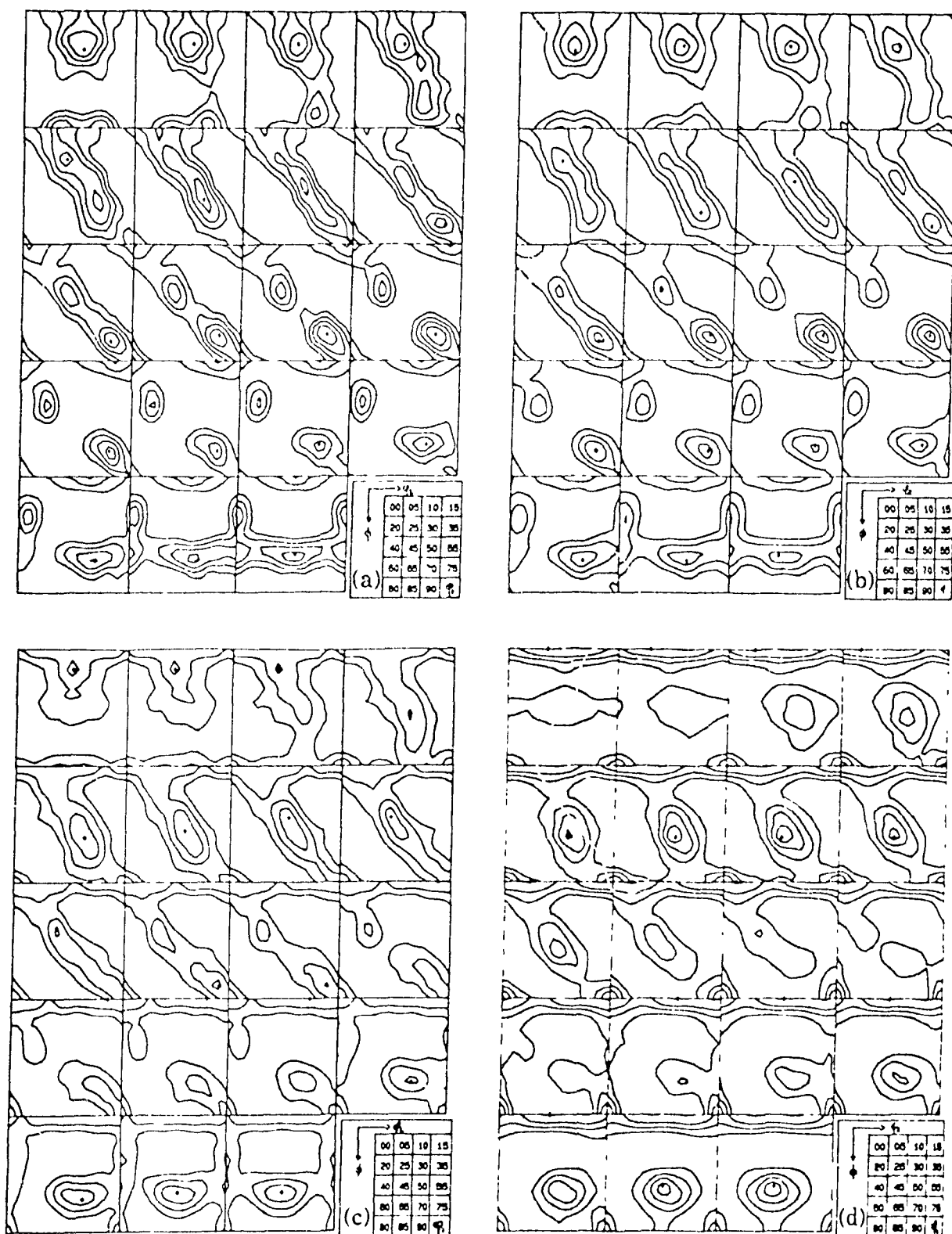


Figure 5-26 ϕ_1 -section ODF's obtained by transforming the texture of
 (a) Ni-10Co, (b) Ni-20Co, (c) Ni-40Co, (d) Ni-60Co after 95% prior reduction
 with the NW orientation relationship (levels 1,2,3...).



Figure 5-27 : ϕ_1 -section ODF's obtained by transforming the texture of Ni-30Co according to the NW orientation relationship after (a) 40%, (b) 70%, (c) 90%, and (d) 95% reduction prior to transformation (levels 1,2,3...).

reduction	40%		70%		90%		95%	
	location	I	location	I	location	I	location	I
severity	-	65	-	88	-	88	-	1 06
maxima	{113}<110>	3 0	{113}<110>	4 0	{113}<110>	4 0	{113}<110>	4 5
	-	-	{554}<225>	3 0	{554}<225>	2 5	{554}<225>	3 5
2 nd order	-	-	{201}<102>	2 0	{201}<102>	3 0	{201}<102>	3 0
maxima	{100}<011>	2 0	{100}<011>	2 0	{100}<011>	2 0	{100}<011>	3 0

Table 5-18 : Main characteristics of the bcc textures NW-transformed from Ni-30Co.

reduction	40%		70%		90%		95%	
	location	I	location	I	location	I	location	I
severity	-	87	-	75	-	1 05	-	81
maxima	{100}<011>	4 0	{100}<011>	3 0	{100}<011>	5 0	{100}<011>	2 0
	{554}<225>	4 0	{554}<225>	3 0	{554}<225>	5 0	{554}<225>	4 0
2 nd order	-	-	{100}<012>	3 0	{100}<012>	2 0	{100}<012>	2 0
maxima	-	-	-	-	-	-	-	-

Table 5-19 : Main characteristics of the bcc textures NW-transformed from Ni-60Co.

and Ni-60Co, respectively. The positions of the maxima are globally in agreement, except that {554}<225> rather than {332}<113> is predicted for heavily cold rolled Ni-10Co and Ni-20Co and for Ni-30Co irrespective of the rolling reduction (Figure 5-27). Also, {554}<225> is NW-predicted for Ni-60Co as opposed to {111}<112> with the KS relation. Lastly, for Ni-30Co, the NW orientation relationship predicts a maximum at {113}<110>, irrespective of the amount of prior reduction, whereas KS predicts {112}<110> after 40% reduction, which gradually rotates to {114}<110> through {113}<110> with increasing degrees of rolling.

V.3 DISCUSSION

In this section, three points of particular interest are discussed in turn : (i) the analytically predicted textures are first compared with experimental ODF's in order to evaluate the assumptions and methods used; (ii) the different types of simulation methods are then compared briefly; and finally (iii) the influence of some simulation parameters on the resulting transformation textures is presented.

V.3.1 COMPARISON WITH OBSERVED TEXTURES

The transformation textures presented above, predicted from the series of Ni-Co alloys, will now be compared with three kinds of experimental ODF's measured on :

(i) ferrite in controlled rolled steels, (ii) martensite, and (iii) cold rolled ferrite.

- ferrite in controlled rolled steels :

The extent of correspondence between the analytically predicted bcc ODF's and experimental textures determined on HSLA steels will now be considered. Here, the Roe notation (ψ, θ, ϕ) is employed for the Euler angles, as in the original publications. For this purpose, the ODF reported by Inagaki for a controlled rolled 0.10C-1.24Mn-0.03Nb-0.067V steel [57] has been selected and is presented in Figure 5-28 (a). This Nb-V steel was first hot rolled in the recrystallized γ range and then controlled rolled to a total reduction of about 85 percent at a finishing temperature of 850°C. The presence of Nb and V ensured that the γ rolling texture was retained before transformation into α . Moreover, as mentioned previously (V 1.1.), the stacking fault energies of the fcc Ni-30Co alloy and the austenite of the experimental steel are expected to be comparable. The ψ -section ODF's calculated for the Ni-30Co alloy, after 95% reduction prior to transformation, are illustrated in Figures 5-28 (b), (c) and (d) for the KS, Bain and NW orientation relationships, respectively.

Although the general features of the textures represented by these four figures are similar, the intensity levels in the experimental steel correspond best with those calculated from the KS or NW relations and are somewhat sharper than predicted. The maximal intensities in each section of the Bain-related ODF are about 2 to 2.5 times the respective values for the experimental texture, in agreement with what was said earlier about the relative number of variants associated with the three

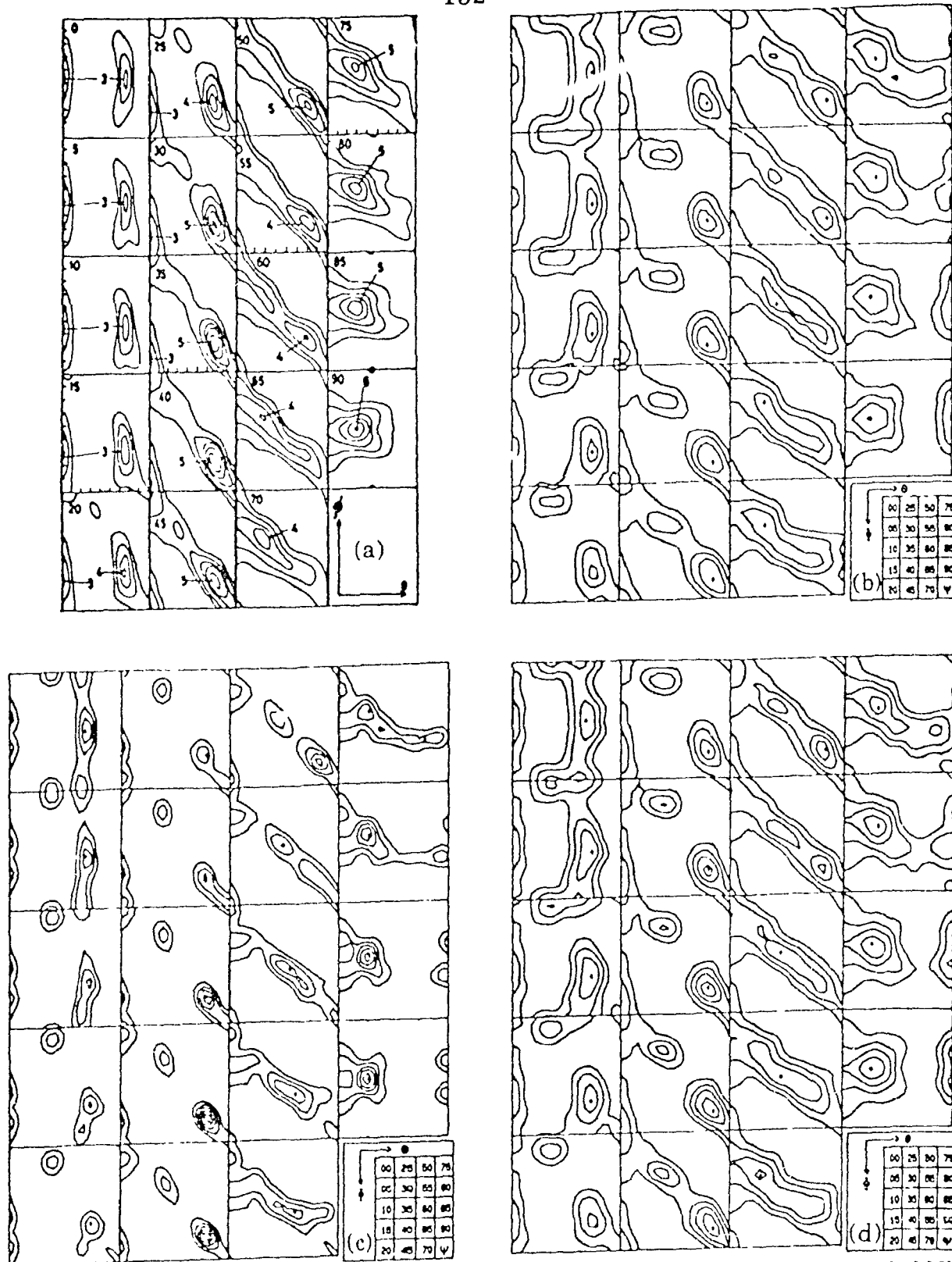


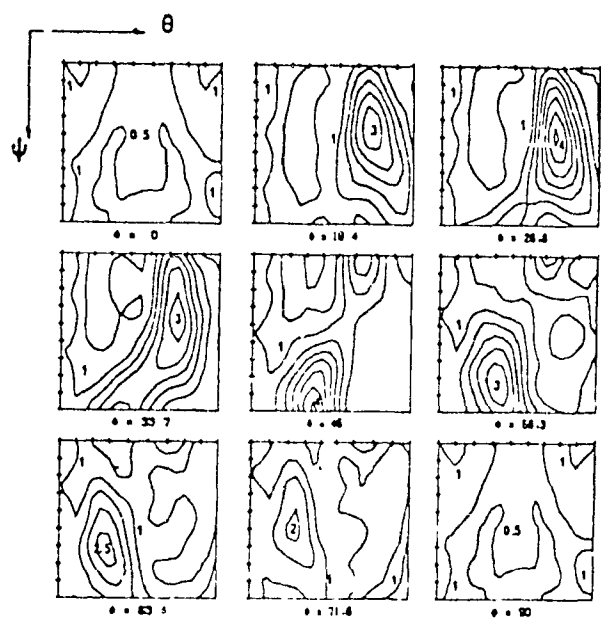
Figure 5-28 : (a) experimental ψ -section ODF (Roe notation) for a controlled rolled Nb steel containing 1.24% Mn; (b), (c), and (d) . ψ -section ODF's (Roe notation) obtained by transforming the texture of the 95% cold rolled Ni-30Co alloy according to the KS (levels 1,2,3...), Bain (levels 2,4,6...) and NW (levels 1,2,3...) relationships, respectively.

transformation laws. The global dispositions and shapes of the iso-density lines, however, are nearly identical in the four textures. The NW and KS simulations can hardly be differentiated from each other, except that the NW-predicted textures are always slightly more severe than the corresponding KS ones, as can be noted from their respective severity parameters. The positions of the two peaks, experimentally measured near $\{332\}\langle 113 \rangle$ and $\{113\}\langle 110 \rangle$, are equally well predicted by the three orientation relationships, but their surrounding angular spreads are about twice narrower in the Bain-related ODF than in either the KS or the NW, which correspond better to reality (see the $\psi = 0^\circ$ and $\psi = 45^\circ$ sections, for instance).

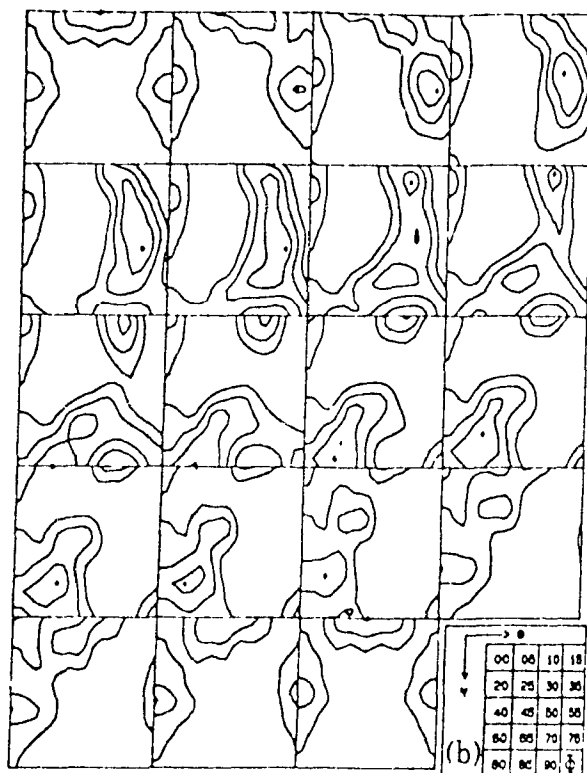
All the experimental peaks appear on the simulated ODF's but, conversely, one of the maxima of secondary importance predicted by the three types of derivation does not exist in the experimental texture. As reported in the section dealing with the continuous results (V.2.3), a second order peak is exhibited at $\{201\}\langle 102 \rangle$ in nearly all the simulations. However, this calculated peak is not visible on the experimental ODF, as can be seen from a comparison of the experimental and simulated $\psi = 90^\circ$ sections, for example. On the other hand, the other second order maximum described in section V.2.3 and predicted near $\{100\}\langle 011 \rangle$ is effectively present experimentally with a shape and spread close to those predicted by the KS- and NW-related textures ($\psi = 0^\circ$ sections). The Bain orientation relationship predicts narrower and sharper second order peaks, as already pointed out for the calculated intensities and shapes of the overall maxima.

The above considerations justify the description of the austenite texture by that of an fcc alloy with a similar SFE, and also give strong support to the general view that ferrite does indeed transform from austenite according to the KS relationship, even after heavy deformation. Similar conclusions could also have been drawn from the ODF's of a 0.18C-1.28Mn-0.031Nb-0.042V steel finish rolled at 750°C [57], a 0.1C-1.3Mn-0.03Nb steel controlled rolled with $T_f = 800^\circ\text{C}$ [58], or a 0.12C-1.47Mn-0.051Nb steel finish rolled at 815°C after 80% reduction, as shown for the latter in Figure 5-29 (ϕ -section ODF's).

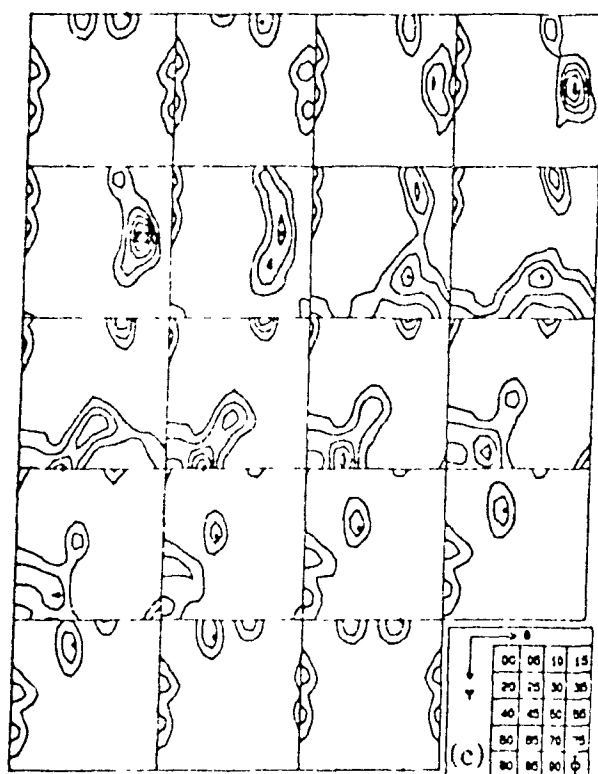
Comparisons can also be drawn between the experiments and the textures derived analytically for Ni-30Co after lower reductions prior to transformation. In the same manner as for Figure 5-28, the simulated ODF's after 40%, 70% and 90% rolling in the fcc phase are compared to the texture of the controlled rolled steel reported by Inagaki [57] in Figures 5-30, 5-31 and 5-32, respectively. As pointed out during the presentation of the results, the severity of the transformed textures merely depend on the amount of reduction given to the material before transformation. However, the



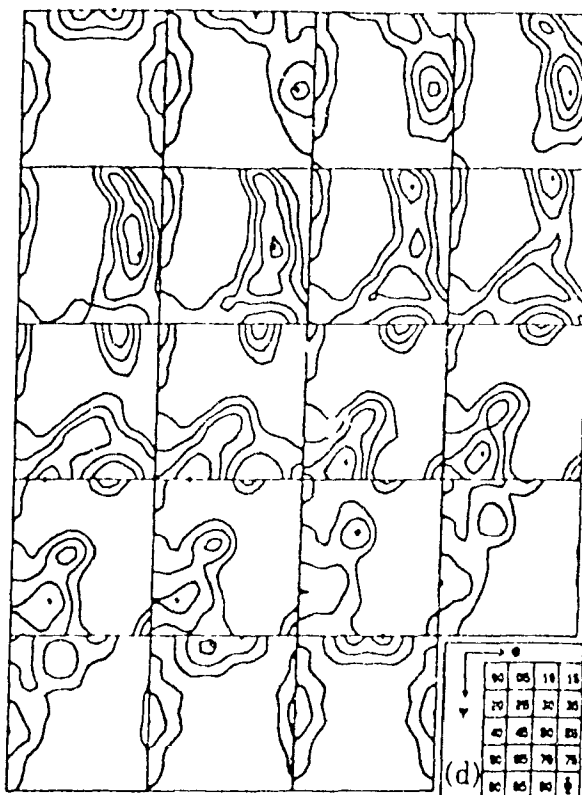
(a)



(b)



(c)



(d)

Figure 5-29 (a) experimental ϕ -section ODF (Roe notation) for a hot rolled Nb steel containing 1.47% Mn; (b), (c), and (d) ϕ -section ODF's (Roe notation) obtained by transforming the texture of the 95% cold rolled Ni-30Co alloy according to the KS (levels 1,2,3..), Bain (levels 2,4,6..) and NW (levels 1,2,3..) relationships, respectively.

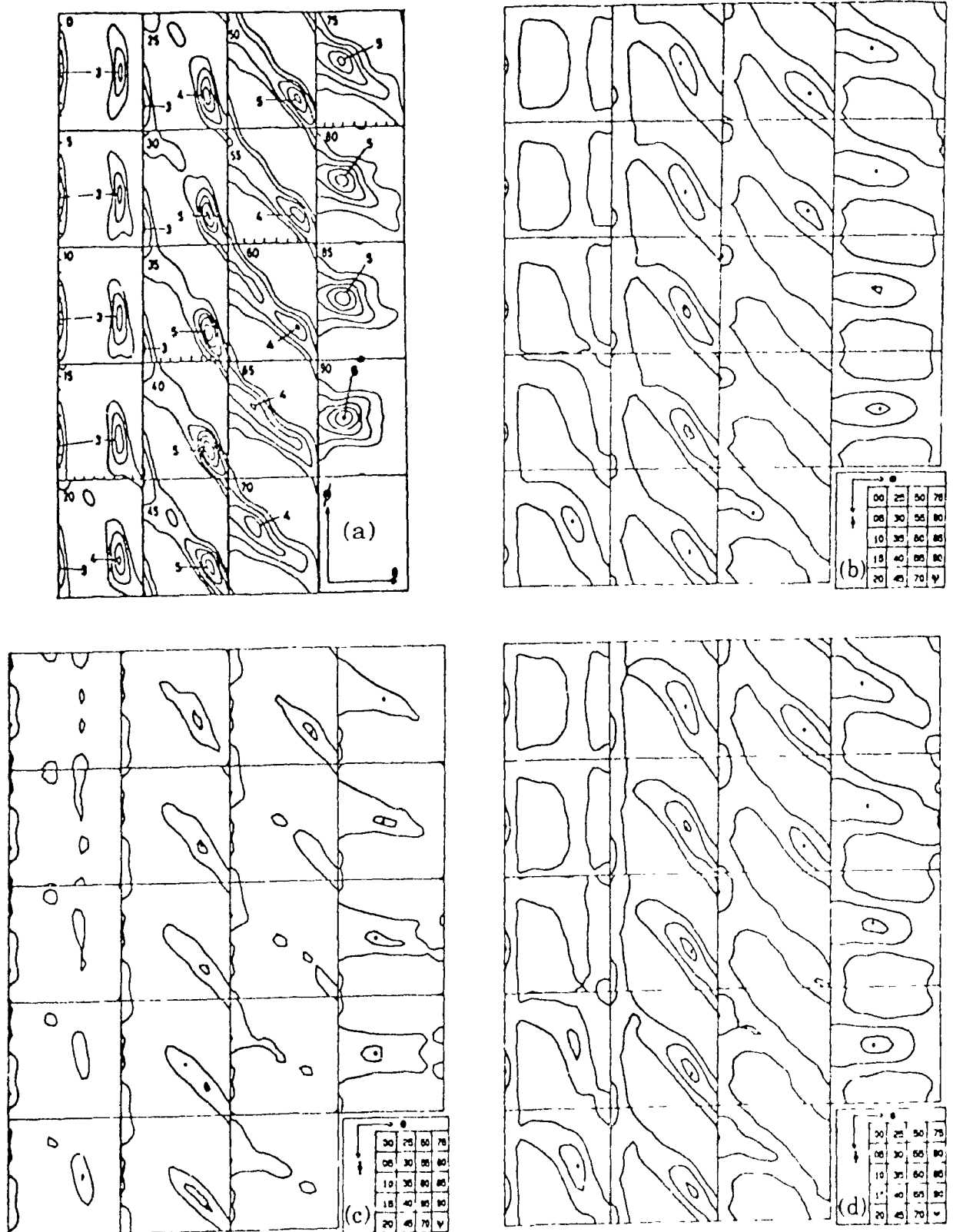


Figure 5-30 : (a) experimental ψ -section ODF (Roe notation) for a controlled rolled Nb steel containing 1.24% Mn; (b), (c), and (d) ψ -section ODF's (Roe notation) obtained by transforming the texture of the 40% cold rolled Ni-30Co alloy according to the KS (levels 1,2,3..), Bain (levels 2,4,6..) and NW (levels 1,2,3..) relationships, respectively.

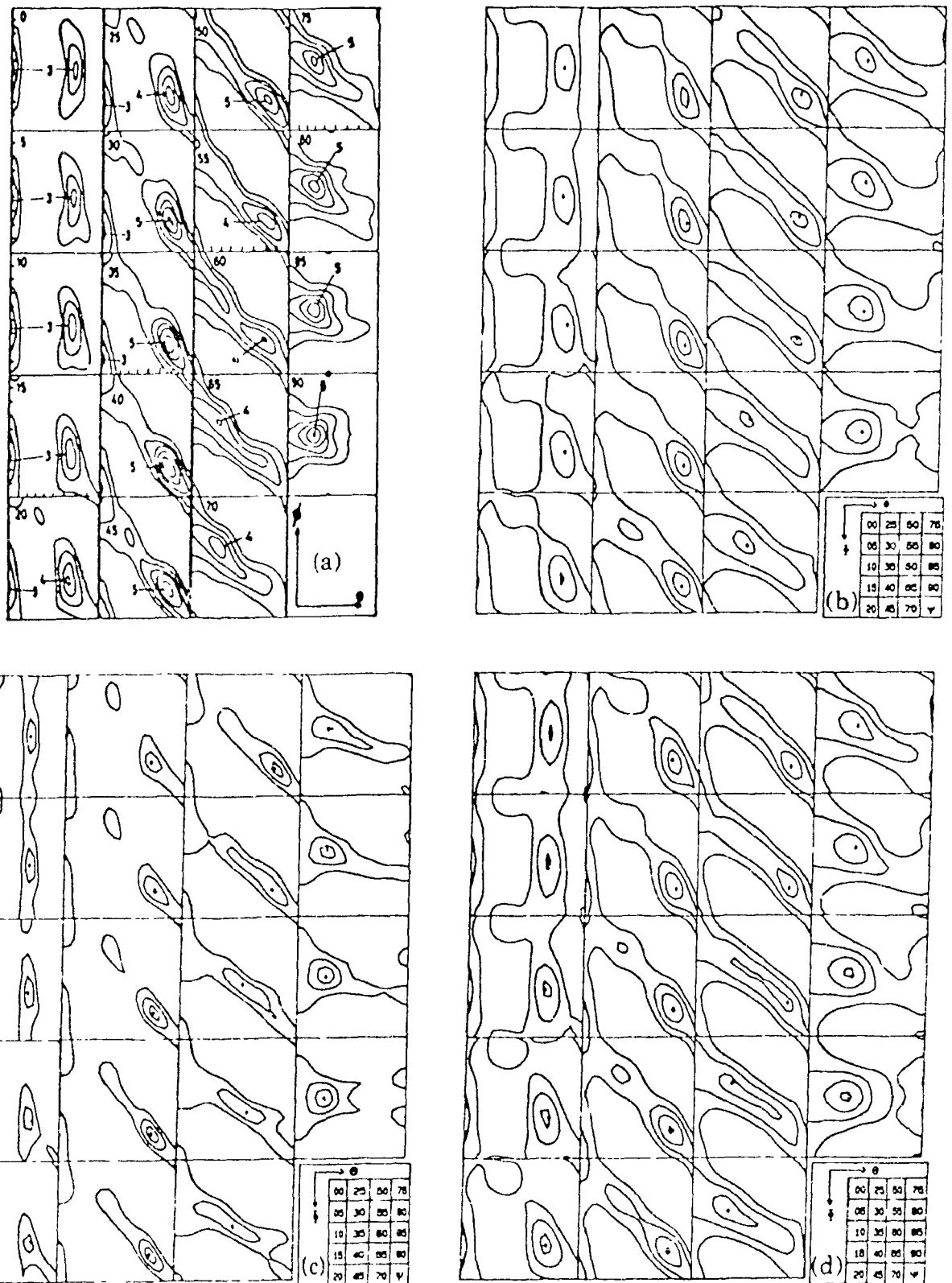


Figure 5-31 : (a) experimental ψ -section ODF (Roe notation) for a controlled rolled Nb steel containing 1.24% Mn; (b), (c), and (d) ψ -section ODF's (Roe notation) obtained by transforming the texture of the 70% cold rolled Ni-30Co alloy according to the KS (levels 1,2,3..), Bain (levels 2,4,6..) and NW (levels 1,2,3..) relationships, respectively.

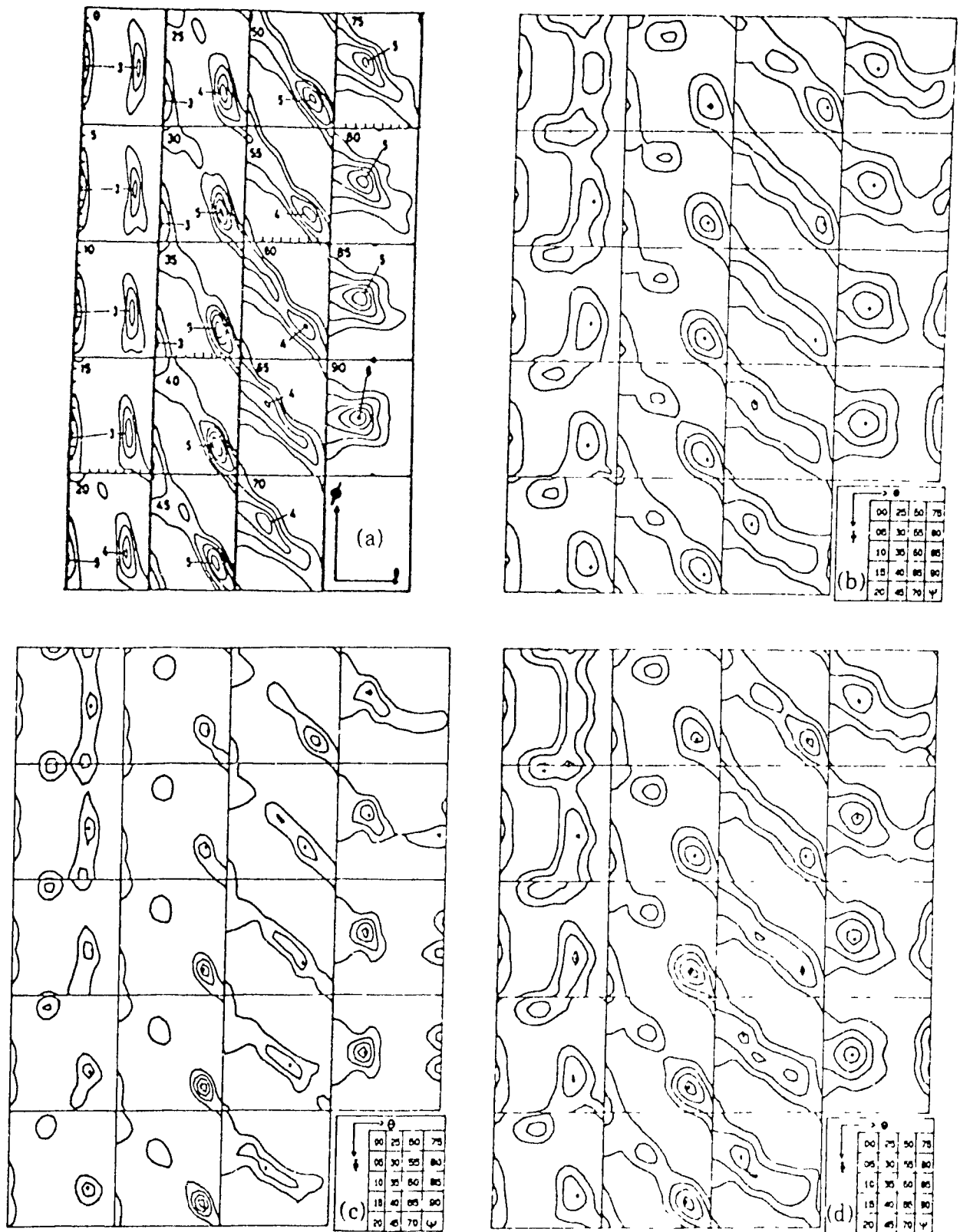


Figure 5-32. (a) experimental ψ -section ODF (Roe notation) for a controlled rolled Nb steel containing 1.24% Mn; (b), (c), and (d) ψ -section ODF's (Roe notation) obtained by transforming the texture of the 90% cold rolled Ni-30Co alloy according to the KS (levels 1,2,3..), Bain (levels 2,4,6..) and NW (levels 1,2,3..) relationships, respectively.

correspondence with experiment remains valid to a reasonable extent even if the level of reduction is lowered to 90% or 70% before transformation, as can be seen from Figures 5-31 and 5-32. After 40% prior deformation, on the other hand, the transformation textures are inherited from less marked fcc textures (lower intensity, less pronounced peaks ...) and it leads to poorer agreement with the ODF of the controlled rolled steel (Figure 5-30).

The major components of the transformation texture, namely the $\{332\}\langle 113 \rangle$ and $\{113\}\langle 110 \rangle$, have been suggested as originating from the $\{110\}\langle 112 \rangle$ (Bs) and $\{112\}\langle 111 \rangle$ (Cu) components, respectively, of the texture in the γ phase [54,57]. This is supported by the results of the present study, where the repeated high intensity of the $\{332\}\langle 113 \rangle$ component in the derived α textures is associated with the high intensity of the Bs component, $\{110\}\langle 112 \rangle$, in the original rolling texture of all the Ni-Co alloys. Similarly, the strong $\{113\}\langle 110 \rangle$ α texture component can be linked to the presence of a strong Cu peak, $\{112\}\langle 111 \rangle$, in the starting ODF, and a low $\{113\}\langle 110 \rangle$ with its absence.

The experimental ψ -section ODF for a controlled rolled steel containing 2.48% Mn [57] is shown in Figure 5-33 (a). As for the previous steel, it can be compared with the textures derived analytically from Ni-30Co 95% cold rolled according to the KS, Bain and NW orientation relationships, which are represented in Figures 5-33 (b), (c) and (d), respectively. The experimental texture was measured on a 0.08C-2.48Mn-0.050Nb-0.010V steel finish rolled at 800°C (i.e. well below the no-recrystallization temperature of austenite T_{nr} , though higher than the transformation temperature A_{r3}). From Figure 5-33 (a), it should first be noted that the sharpness of the measured texture is much higher in the case of the 2.48% Mn steel than in the 1.28% Mn grade shown in Figure 5-28 (a), although the two ODF's are of the same type. The KS- and NW-simulated ODF's obtained from 95% cold rolled Ni-30Co thus do not show the same good agreement with experiment, because the calculated intensities are about three times too low. The Bain-simulated ODF, on the contrary, predicts these high intensity levels, centered on the $\{332\}\langle 113 \rangle$ and $\{113\}\langle 110 \rangle$ positions, more accurately. However, the difference in severity between the measured and derived textures is not likely to be related to selection between the variants of the transformation law. By comparing the discrete orientations derived from the fcc Cu and Bs components with the peaks of the experimental ODF's, the original austenite textures of the two steels are both seen to be of the pure metal type [57]. Moreover, the second order maximum, predicted by the three laws to be near $\{201\}\langle 102 \rangle$, is indeed observed on the actual ODF of the 2.48% Mn steel as an independent peak,

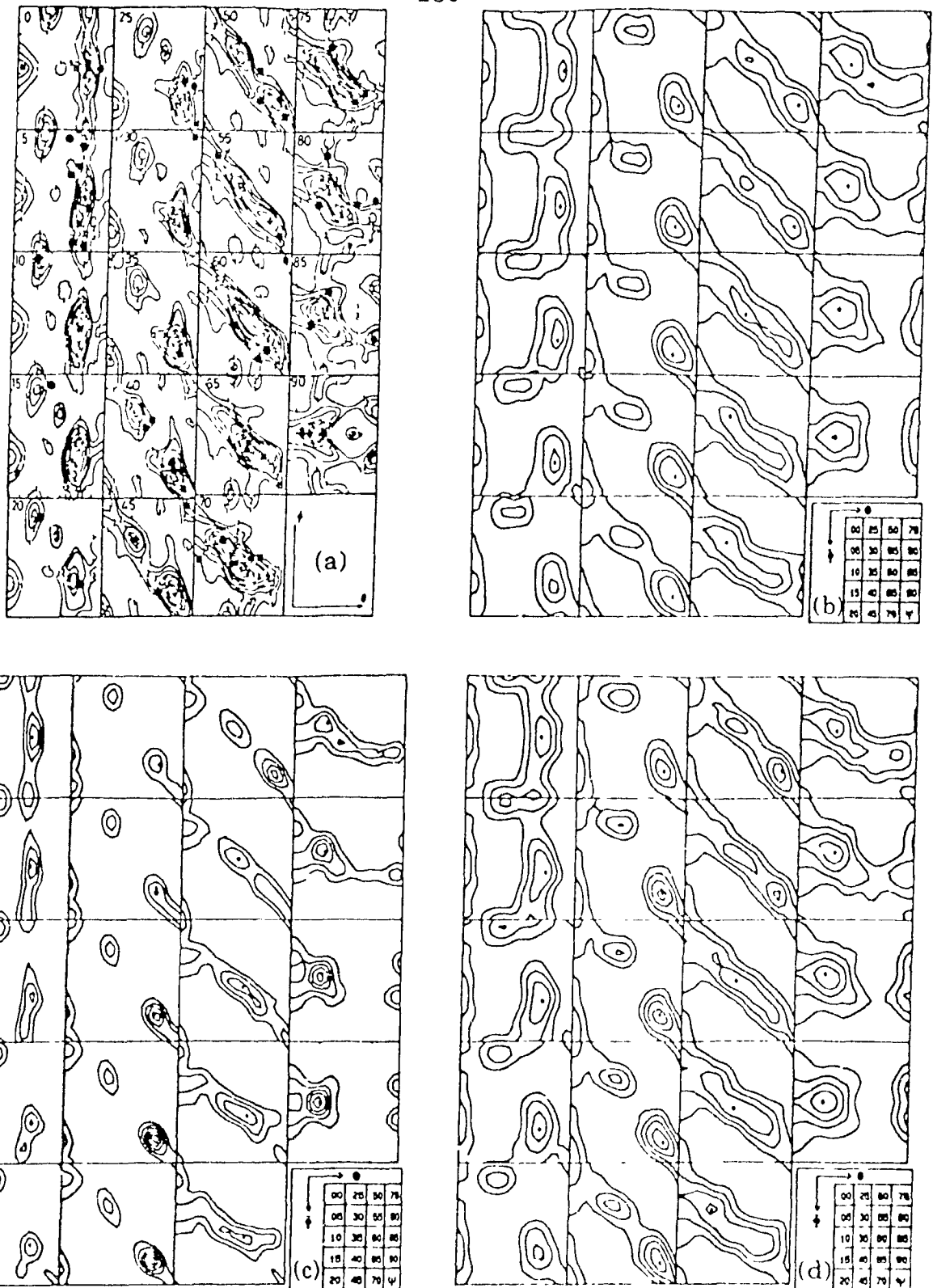


Figure 5-33 : (a) experimental ψ -section ODF (Roe notation) for a controlled rolled Nb steel containing 2.48% Mn; (b), (c), and (d) ψ -section ODF's (Roe notation) obtained by transforming the texture of the 95% cold rolled Ni-30Co alloy according to the KS (levels 1,2,3..), Bain (levels 2,4,6..) and NW (levels 1,2,3..) relationships, respectively.

which was not the case for the steel containing 1.28% Mn. The experimental texture is thus simply more severe than predicted, and this therefore indicates that the effect of Mn as an alloying element is far more important on the transformation itself than on the transition of the γ rolling texture from the pure metal to the alloy type.

- martensite:

An attempt is made here to compare experimentally determined martensite textures with the analytically predicted α textures for the Ni-40Co alloy. The SFE of Fe-30Ni is expected to be about 45 mJ m^{-2} [114], this is not very different from that of the present Ni-40Co alloy, which is about 53 mJ m^{-2} [116,117] (see also Table 5-2). Figure 5-34 (a) presents the ϕ_2 -section ODF of an Fe-30Ni alloy rolled in the austenite phase to a total reduction of 80 percent and transformed into martensite [72]. The ϕ_2 -section ODF's predicted from the texture of the Ni-40Co alloy using the KS, Bain and NW relations are shown in Figures 5-34 (b), (c) and (d), respectively.

It is apparent from this figure that, although the overall intensity maxima in the experimental and predicted textures appear at about the same locations in orientation space, namely near $\{332\}\langle 113 \rangle$ and $\{113\}\langle 110 \rangle$, they are much weaker in the simulated textures than in the measured one. Even certain second order maxima, e.g. near $\{201\}\langle 102 \rangle$ in the $\phi_2 = 0^\circ$ or $\phi_2 = 90^\circ$ section, are under-predicted compared to the experiment. Furthermore, there are additional peaks in the simulated ODF's, especially along the $\langle 100 \rangle$ //ND fibre (along the $\phi = 0^\circ$ axis in every $\phi_2 = \text{constant}$ section), which are not present in the experimental texture.

This is confirmed in Figure 5-35 by comparing the $\phi_2 = 0^\circ$ and $\phi_2 = 45^\circ$ sections of an experimental ODF for the martensite formed from an Fe-30Ni alloy rolled 70 percent in the γ phase [40,41] (Figure 5-35 (a)) with the corresponding simulated sections predicted from the Ni-40Co alloy 95 percent cold rolled according to the KS and Bain relationships, shown in Figures 5-35 (b) and (c), respectively. Again the peaks are sharper in the measured texture ($\phi_2 = 45^\circ$ section for the overall maximum and $\phi_2 = 0^\circ$ section for some second order peaks). An extra peak is observed experimentally near the $\{100\}\langle 011 \rangle$ component, which was not visible in Figure 5-34 (a) in the case of the Fe-30Ni texture reported by Humbert *et al.* after 80% rolling reduction in the austenite range [72]. It is, however, narrower and stronger than the KS-predicted one. The Bain-related $\phi_2 = 0^\circ$ section, on the other hand, exhibits a broad peak of secondary importance at a location best described by $\{100\}\langle 012 \rangle$, compared to the observed $\{100\}\langle 011 \rangle$ (rotated-cube component) also visible in the corner of the $\phi_2 = 45^\circ$ section and predicted by the KS transformation law.

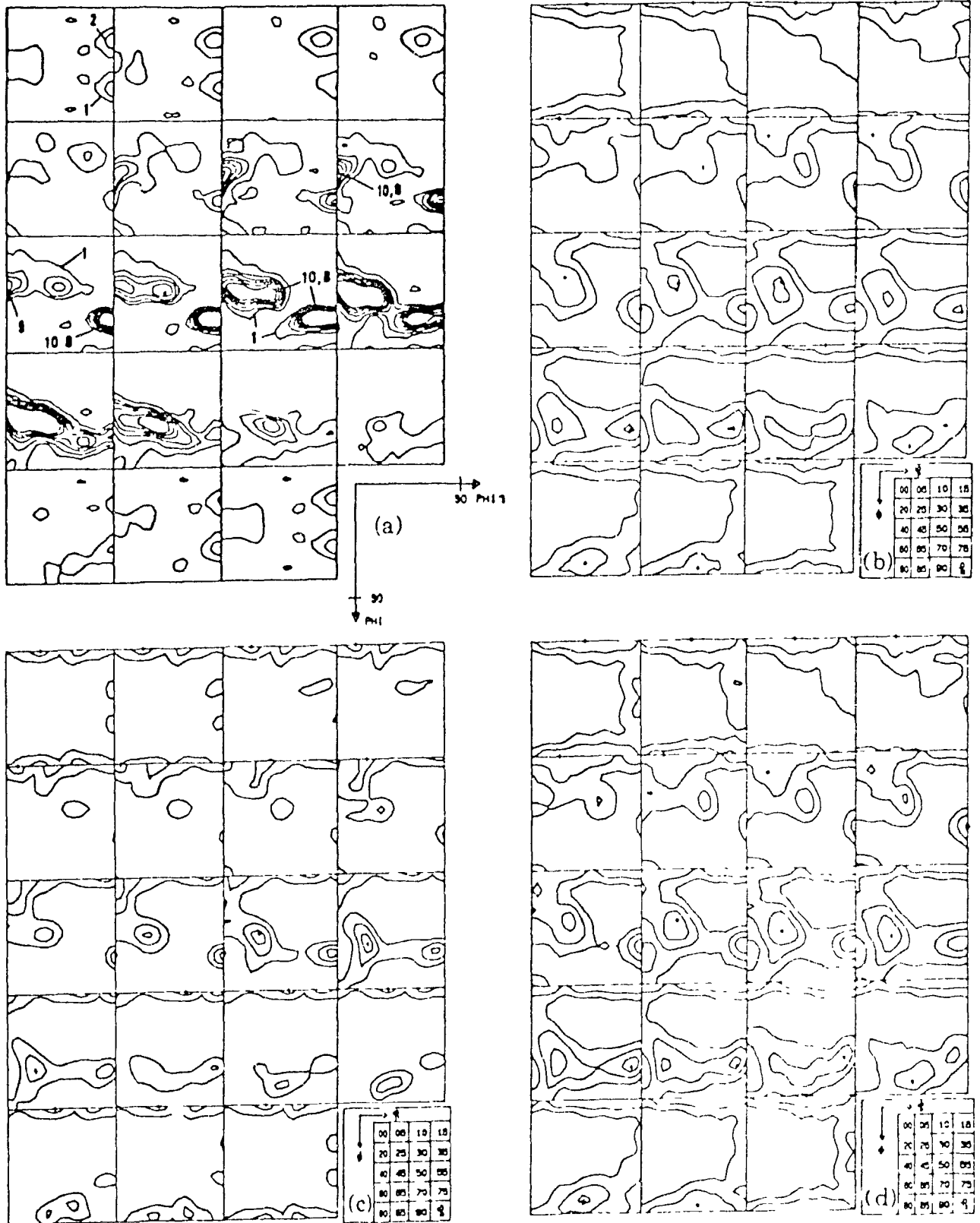


Figure 5-34: (a) experimental ϕ_2 -section ODF for the martensite formed from an 80% γ rolled Fe-30Ni alloy; (b), (c), and (d) ϕ_2 -section ODF's obtained by transforming the texture of the 95% cold rolled Ni-40Co alloy according to the KS (levels 1,2,3...), Bain (levels 2,4,6...) and NW (levels 1,2,3...) relationships, respectively.

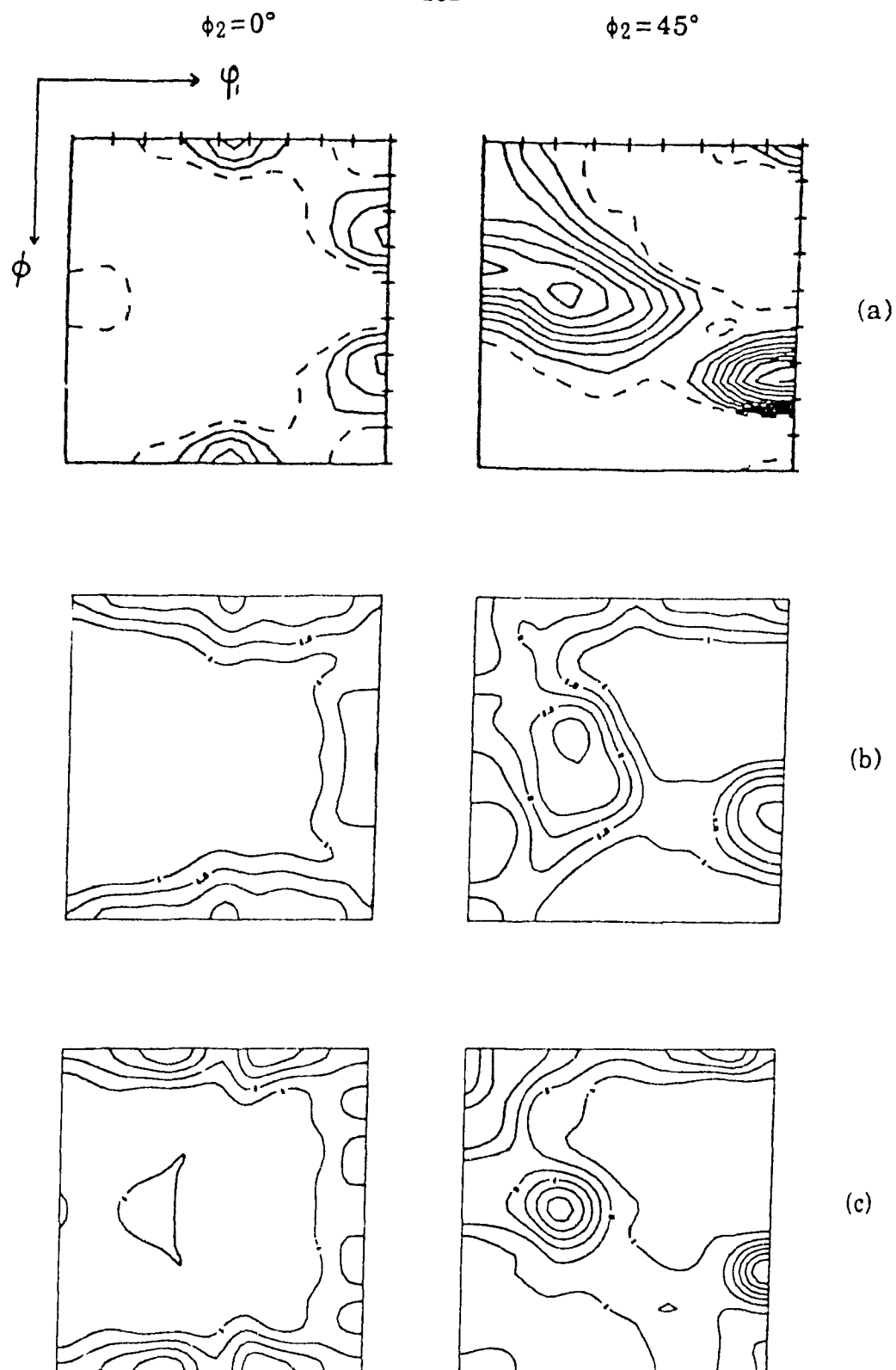


Figure 5-35 : $\phi_2 = 0^\circ$ and $\phi_2 = 45^\circ$ sections from (a) the experimental ODF for the martensite formed from a 70% γ rolled Fe-30Ni alloy; (b) and (c) the textures obtained by transforming the ODF of the 95% cold rolled Ni-40Co alloy according to the KS (levels 1,2,3..) and Bain (levels 2,4,6..) relationships, respectively.

These results indicate that variant selection is likely to take place during martensite formation, in agreement with the conclusions of Humbert *et al* [50,72], Davies and Bateman [40,41] and others [e.g. 31].

- cold rolled ferrite :

The analytically predicted transformation textures derived from the series of Ni-Co alloys, represented by their $\phi_1 = \text{constant}$ sections, exhibit some points of similarity with certain experimental ODF's observed in cold rolled steels and iron alloys. As an illustration, two experimental cold rolled bcc textures are presented in Figure 5-36 : the ϕ_1 -section ODF of an Armco iron, rolled 90% at room temperature [131,132], is shown in Figure 5-36 (a) and the ϕ_1 -section ODF of a 70% cold rolled low carbon steel [133] is illustrated in Figure 5-36 (b). In Figures 5-36 (c) and (d), on the other hand, the simulated textures derived from Ni-30Co 95 % cold rolled according to the KS and Bain orientation relationships, respectively, are presented for comparison.

The general trend of the four figures shows some degree of correspondence between the textures of the bcc materials obtained by (i) deformation + transformation, and (ii) transformation + deformation. However, the severity is higher in the cold rolled materials, as confirmed by others workers [e.g. 134-137]. It also appears that the nature of the maxima are different in the two processes : the simulated ODF's have been described earlier by a set of ideal orientations of various strengths. On the contrary, the experimental cold rolled textures are best described by fiber type components, as shown in Figure 5-37, which compares the ϕ -section ODF's (Roe notation) for an 80% cold rolled low carbon steel [138] with that KS-predicted from Ni-30Co 95% cold rolled.

Figure 5-38 confirms this result by comparing the $\phi_2 = 45^\circ$ sections of a 72% cold rolled Nb containing steel [137] with the corresponding section extracted from Figure 5-37 (b). A partial α and a complete γ fibre therefore appear as better descriptions of the cold rolled textures than two ideal orientations in the vicinity of $\{332\} \langle 113 \rangle$ and $\{113\} \langle 110 \rangle$. The α and γ fibres corresponding to the textures shown in Figure 5-36 are illustrated in Figure 5-39. From this figure, it can clearly be seen that, in cold rolled steels, (i) the intensity is globally higher, (ii) the nature of the main components is more of a fibre type, and (iii) the position of the maximum is shifted from near $\{113\} \langle 110 \rangle$ towards about $\{223\} \langle 110 \rangle$, compared to the present simulated results.

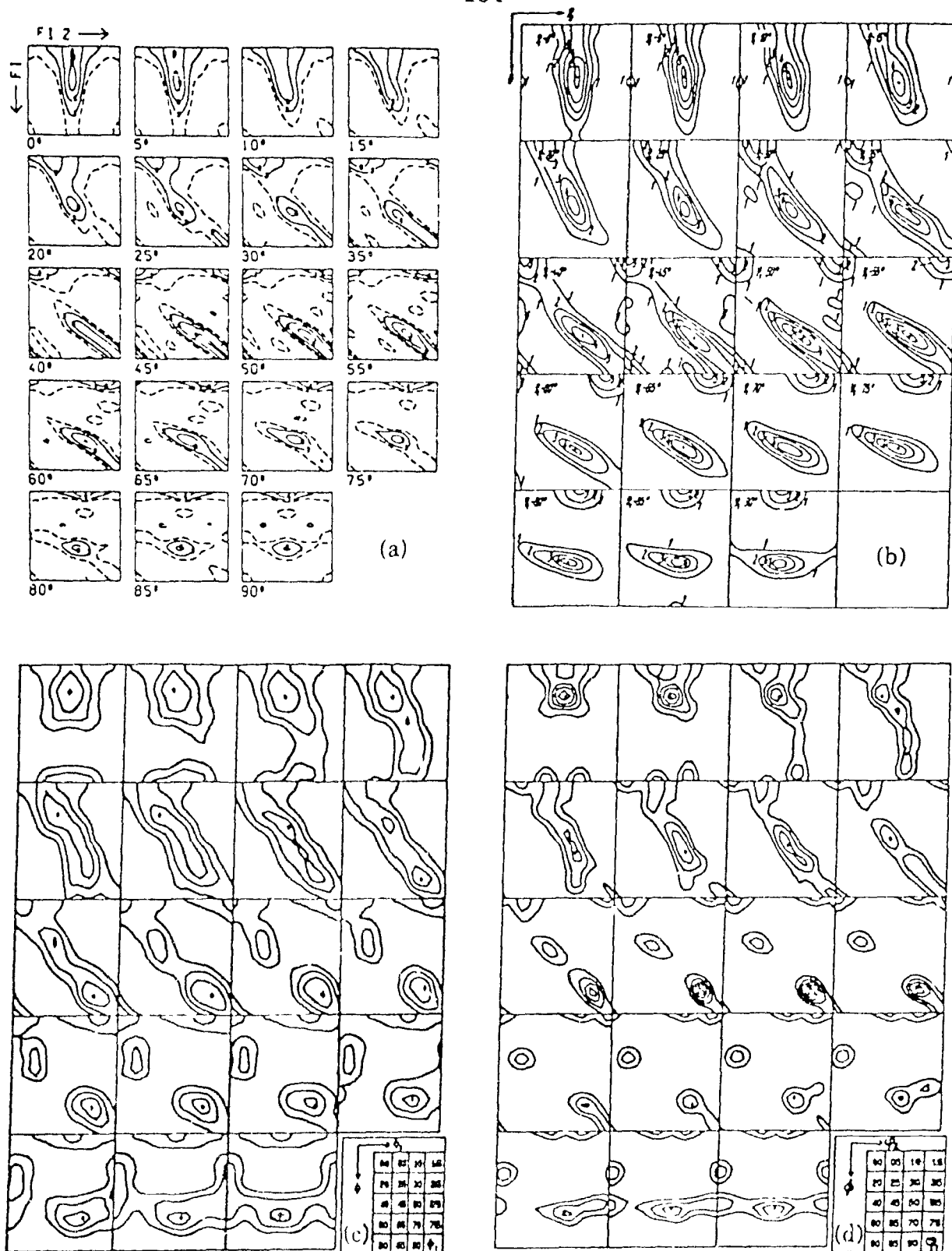
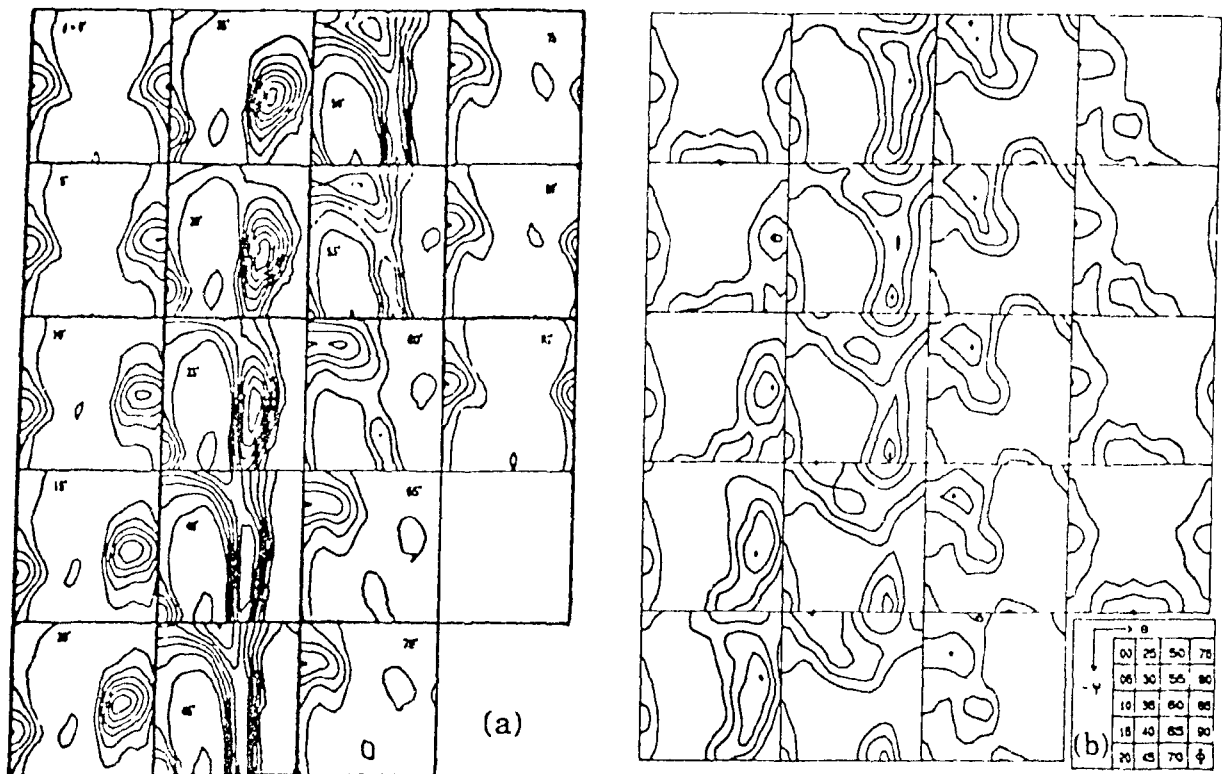


Figure 5-36 ϕ_1 -section ODF's of (a) an Armco iron, rolled 90% at room temperature; (b) a 70% cold rolled low carbon steel; (c) and (d) the textures obtained by transforming the ODF of the 95% cold rolled Ni-30Co alloy according to the KS (levels 1,2,3..) and Bain (levels 2,4,6..) relationships, respectively.



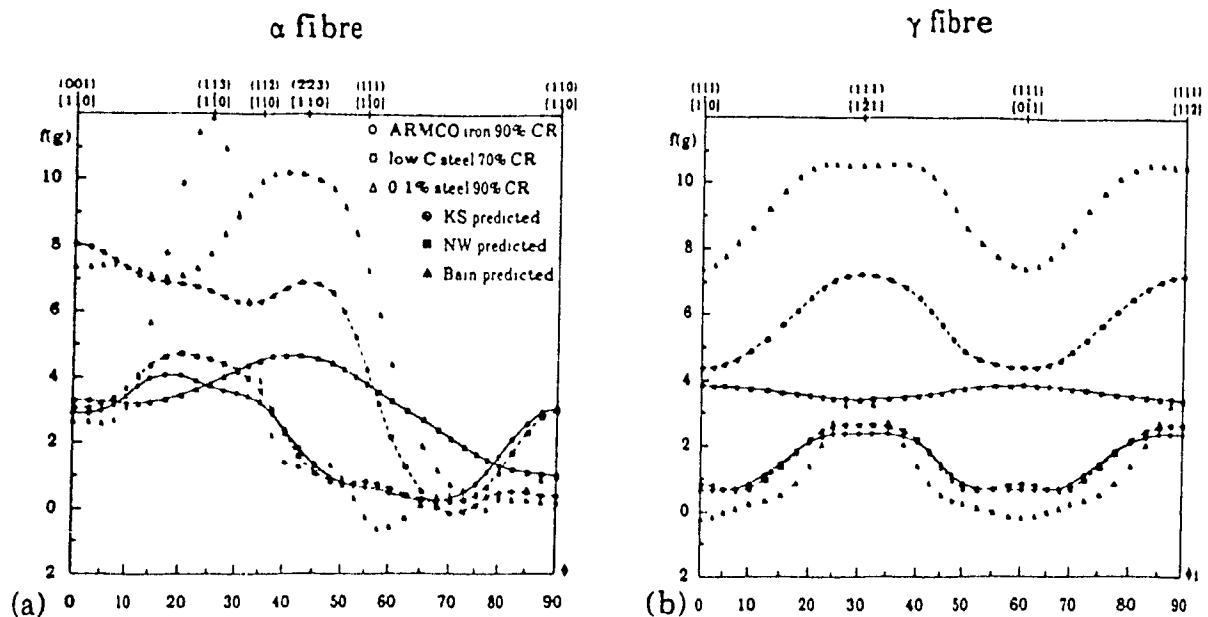


Figure 5-39 : Orientation density along the (a) α fibre and (b) γ fibre of the textures shown in Figure 5-36.

Finally, the simulated textures are compared with the results reported by Schlippenbach et al. [134,135] in the form of the respective α fibres. In their work, the latter authors studied an Armco iron (AI), an aluminum killed (AK) and an interstitial free (IF) steel, each with 80% cold reduction, and a vacuum degassed (VD) steel rolled to different reductions. The α fibres are shown in Figure 5-40. Again, the same differences appear between the materials produced by the two different processes.

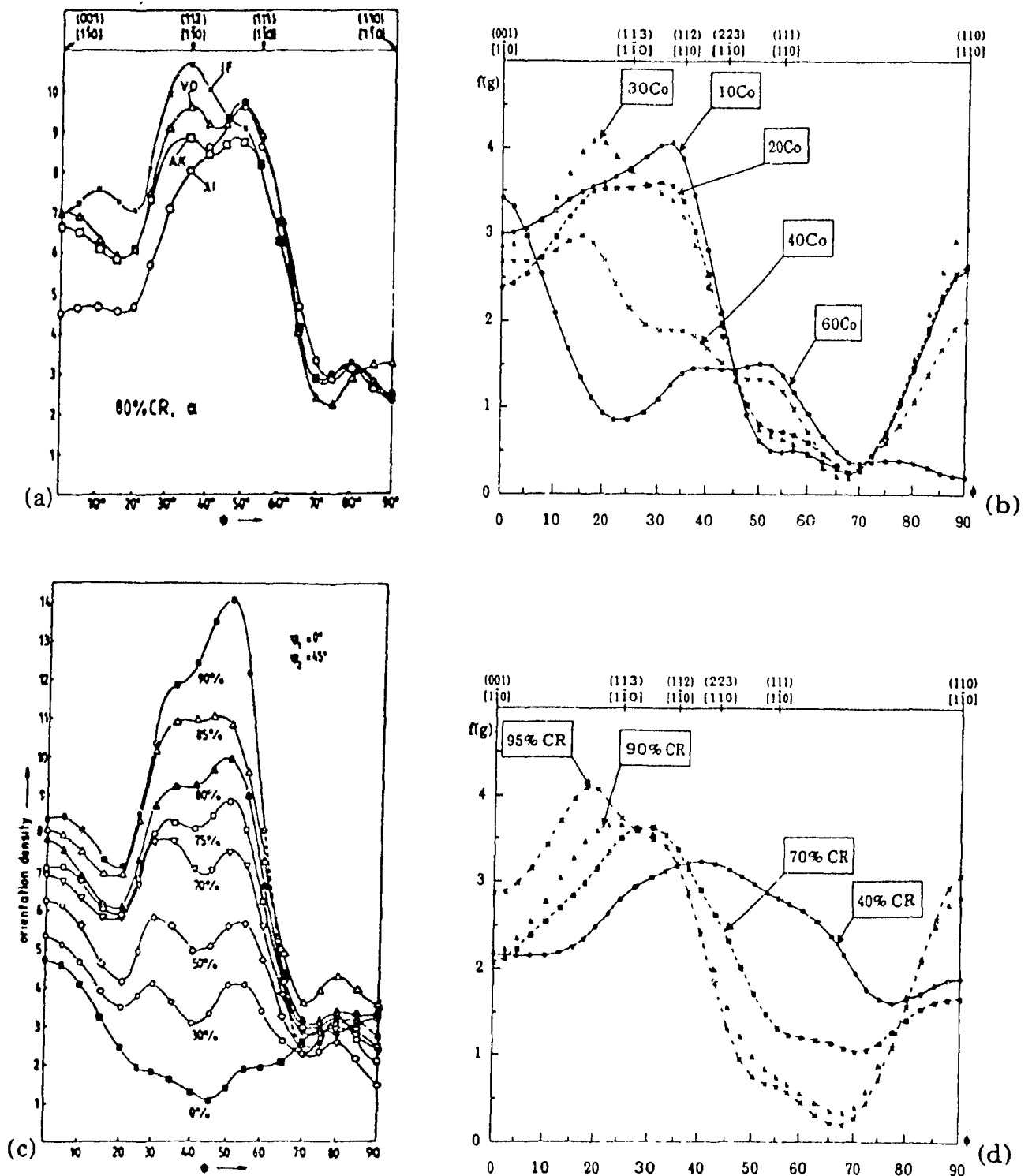


Figure 5-40 : Orientation density along the α fibre for : (a) four 80% cold rolled steels; (b) the textures KS-related to 95% cold rolled Ni-Co alloys with various Co contents; (c) a vacuum degassed steel with various cold rolling reductions; and (d) the textures KS-derived from the Ni-30Co alloy with various cold rolling reductions.

V.3.2 RELATIVE ASSESSMENT OF THE METHODS

As discussed above, the simulation techniques for the study of transformation textures can be divided into the *transformation* and *untransformation* methods and also between the *discrete* and *continuous* methods. These two types of approaches are compared briefly in turn below.

- transformation vs untransformation methods :

In the present work, the untransformation procedure was only used to confirm the origin in the austenite of some well-defined ferrite ideal orientations, such as the $\{332\}\langle 113 \rangle$ and $\{113\}\langle 110 \rangle$. As expected, such specific derivations, carried out in an identical manner for each variant of the transformation law, did not lead to any new results compared to those of the direct transformation method. No continuous untransformation simulations were, however, attempted in the course of this research. Nevertheless, these are expected to produce results similar to those obtained from the transformation procedure, as long as no variant selection is involved. Kallend *et al* have indeed reported such global agreement between the two types of methods [55], although a detailed analysis shows some minor differences between the analytical ODF untransformed from that of a ferritic steel and an fcc pure metal type rolling texture.

- continuous vs discrete methods :

Methods based on both continuous and discrete descriptions of the ODF have been used to derive simulated transformation textures. It is the aim of this section to compare such results. As recalled earlier, Inagaki [54,57] suggested that the $\{332\}\langle 113 \rangle$ and $\{113\}\langle 110 \rangle$ orientations, observed in controlled rolled steels, originate from the $\{110\}\langle 112 \rangle$ (Bs) and $\{112\}\langle 111 \rangle$ (Cu) components of the γ phase texture, respectively. This result has been confirmed by the present research and the analysis has been extended to the role of the $\{123\}\langle 634 \rangle$ (S) component.

To illustrate these relationships, it was assumed that the γ rolling texture consists solely of the Bs, Cu and S components. The orientations obtained by transforming these three components according to the KS relationship are shown in Figure 5-41, superimposed on the ODF calculated by transforming the texture of the 95% cold rolled Ni-30Co alloy using the same transformation law. The most important feature of this diagram is that the major orientation density maxima in

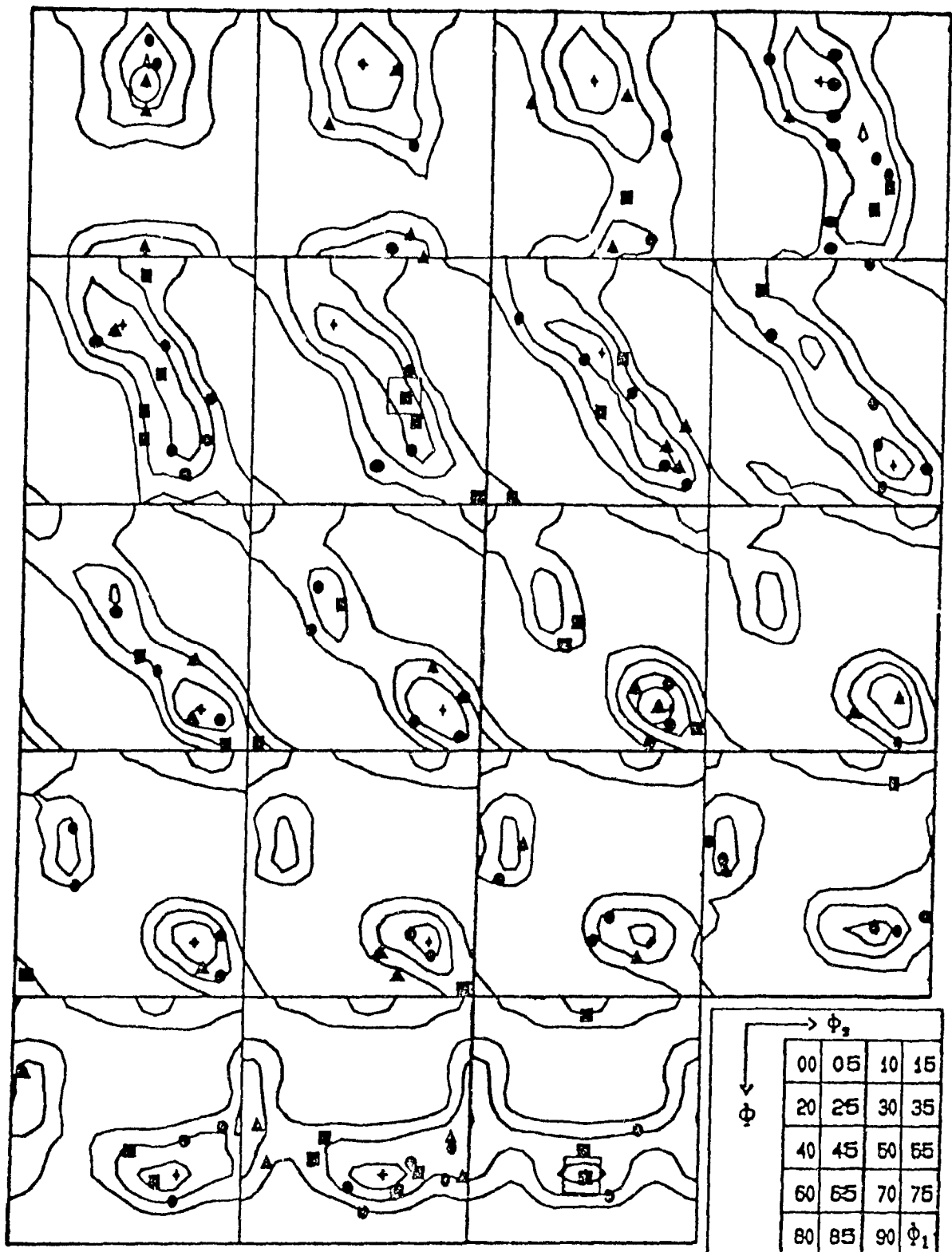


Figure 5-41: Orientations derived from the three principal fcc rolling texture components (Cu, Bs and S) according to the KS relationship. These are superimposed on the ODF obtained with the same transformation law from the texture of the 95% cold rolled Ni-30Co alloy (levels 1,2,3..).

the different $\phi_1 = \text{constant}$ sections are made up of the transformed Bs, Cu and S orientations. In addition, many of the minor maxima are also accounted for.

One of the twelve orientations transformed from the Bs is the $\{332\} \langle 113 \rangle$, whereas $\{113\} \langle 110 \rangle$ is one of the twelve obtained from the Cu. Also, in each case, three of the remaining transformed Bs and Cu orientations lie within 10° in Euler space from the $\{332\} \langle 113 \rangle$ and $\{113\} \langle 110 \rangle$. In addition, two out of the twenty four orientations transformed from the S lie close to the above orientations.

Some other findings, summarized in Tables 5-7 to 5-10 above, are worth noting. The $\{201\} \langle 102 \rangle$ orientation is seen to be produced from the $\{112\} \langle 111 \rangle$ (Cu) and also from the $\{112\} \langle 534 \rangle$, which is close to the Cu component. The presence in the transformation textures of a second order peak near $\{201\} \langle 102 \rangle$ is not therefore surprising, as long as there is no variant selection in the transformation law. The other maximum of secondary importance observed on the ODF's near $\{100\} \langle 011 \rangle$ can be explained by the fact that the Bs and S components both lead to the $\{100\} \langle 011 \rangle$ (rotated-cube) orientation. The KS-derivation of the fcc recrystallization components also forms this orientation.

Finally, the discrete transformation of the main components of the γ rolling texture leads directly to the formation of the important $\{332\} \langle 113 \rangle$ and $\{113\} \langle 110 \rangle$ orientations, observed in controlled rolled steels and well predicted by the continuous method. The origins of these peaks are clearly established in this way, as demonstrated above. In addition, with the aid of the discrete technique, the maxima of secondary importance derived by the series expansion method near $\{201\} \langle 102 \rangle$ and $\{100\} \langle 011 \rangle$ are also shown to be formed from these fcc rolling components. Discrete simulations thus help to ascertain qualitatively the fcc parents of the major bcc orientations, whereas continuous methods give quantitative relations between the two complete ODF's.

V.3.3 INFLUENCE OF SIMULATION PARAMETERS

Finally, the role and importance of certain parameters of the simulation will now be presented and their influence on the derived results emphasized. Attention will be focussed on the Ni-30Co alloy, 95% cold rolled and KS-transformed, as this material has an SFE close to that of γ -iron and its texture after KS-transformation compares well with actual transformation textures in steels. The conclusions drawn below, however, apply equally to any of the simulations carried out in the course of this research.

- presence of ghosts in the starting texture :

Since the correct representation of ODF's requires consideration of both the even and odd terms in the series expansion, and since pole figures are determined only by the even terms, it is not in principle possible to produce true ODF's from experimental pole figures [e.g. 139]. Although the correct positions of the strongest maxima are yielded in a satisfactory manner when only the even coefficients are used, the ODF's reproduced from pole figures in this way also contains false peak profiles and strong fluctuations which suggest non-existent maxima. These are denoted as "ghosts".

The "ghost" phenomenon also affects transformation textures. Two methods were used to correct the experimental ODF's measured for the Ni-Co alloys : first, each ODF was analyzed in terms of a limited number of "gaussian" components g_i , each with a statistical weight M_i and an angular spread ω_{0i} . This family (g_i, M_i, ω_{0i}) was then used to calculate the odd $C_l^{\mu\nu}$ coefficients [e.g. 13,140,141]. An iterative positivity method [142] was also employed, which basically develops the negative regions of the ODF into a series of odd coefficients. This second method was applied in turn to the experimental fcc and simulated bcc textures to see whether any major difference arose depending on the location of the correction in the simulation procedure.

The ϕ_1 -section ODF obtained by transforming the texture of the 95% cold rolled Ni-30Co alloy according to the KS relationship with no correction (Figure 5-42 (a)) is compared with the ODF's resulting from the three types of correction described above in the following figures : (i) the gaussian peak method (Figure 5-42 (b)); the iterative zero condition technique applied (ii) before (Figure 5-42 (c)) and (iii) after (Figure 5-42 (d)) transformation. Figures 5-43 and 5-44 illustrate the same points in terms of the NW and Bain relations, respectively. The α and γ fibres are also compared, for the

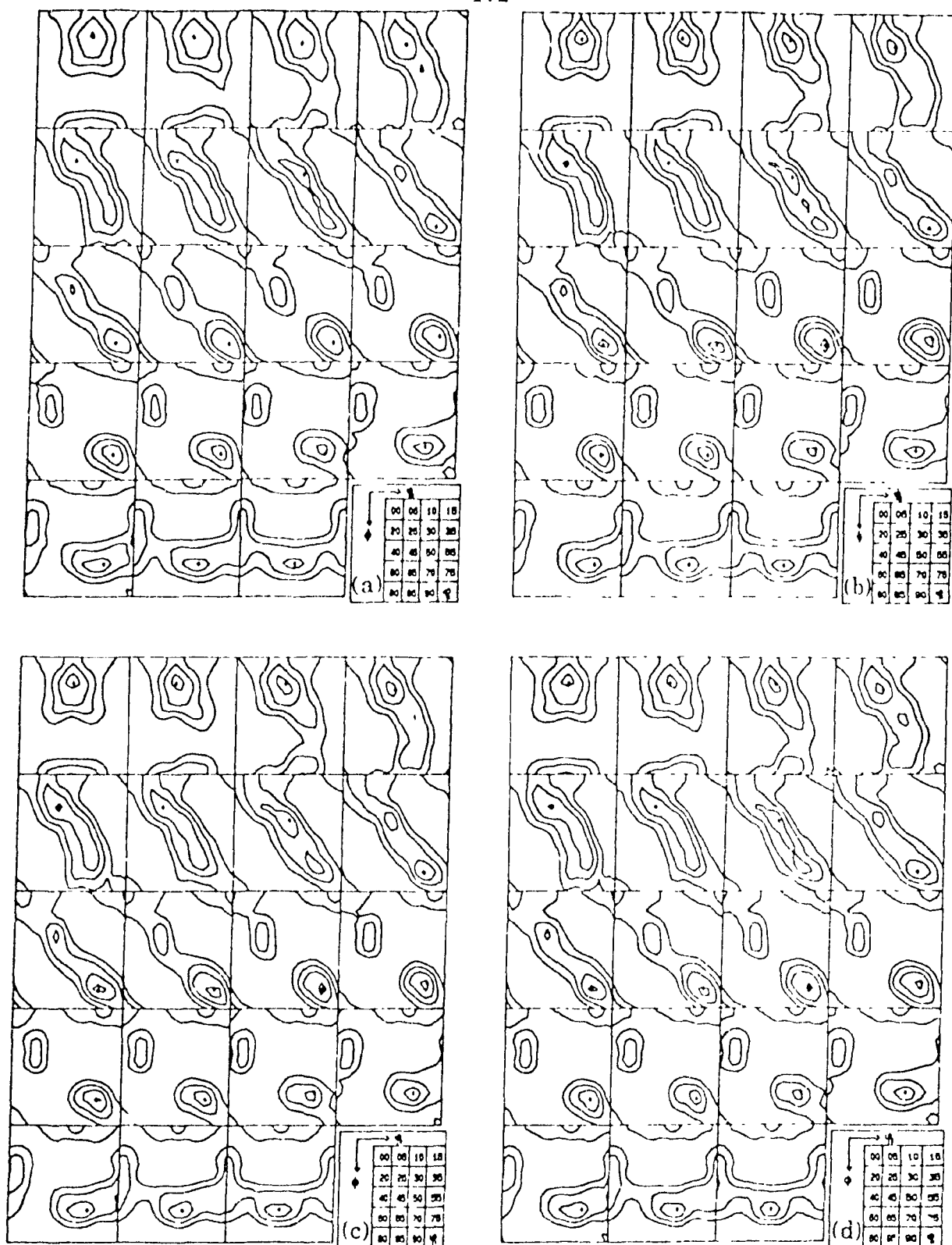


Figure 5-42 : ϕ_1 -section ODF's obtained by transforming the texture of the 95% cold rolled Ni-30Co alloy according to the KS relationship : (a) without ghost correction; (b) corrected with a gaussian peak method; and corrected with an iterative positivity method (c) before and (d) after transformation (levels 1,2,3..).

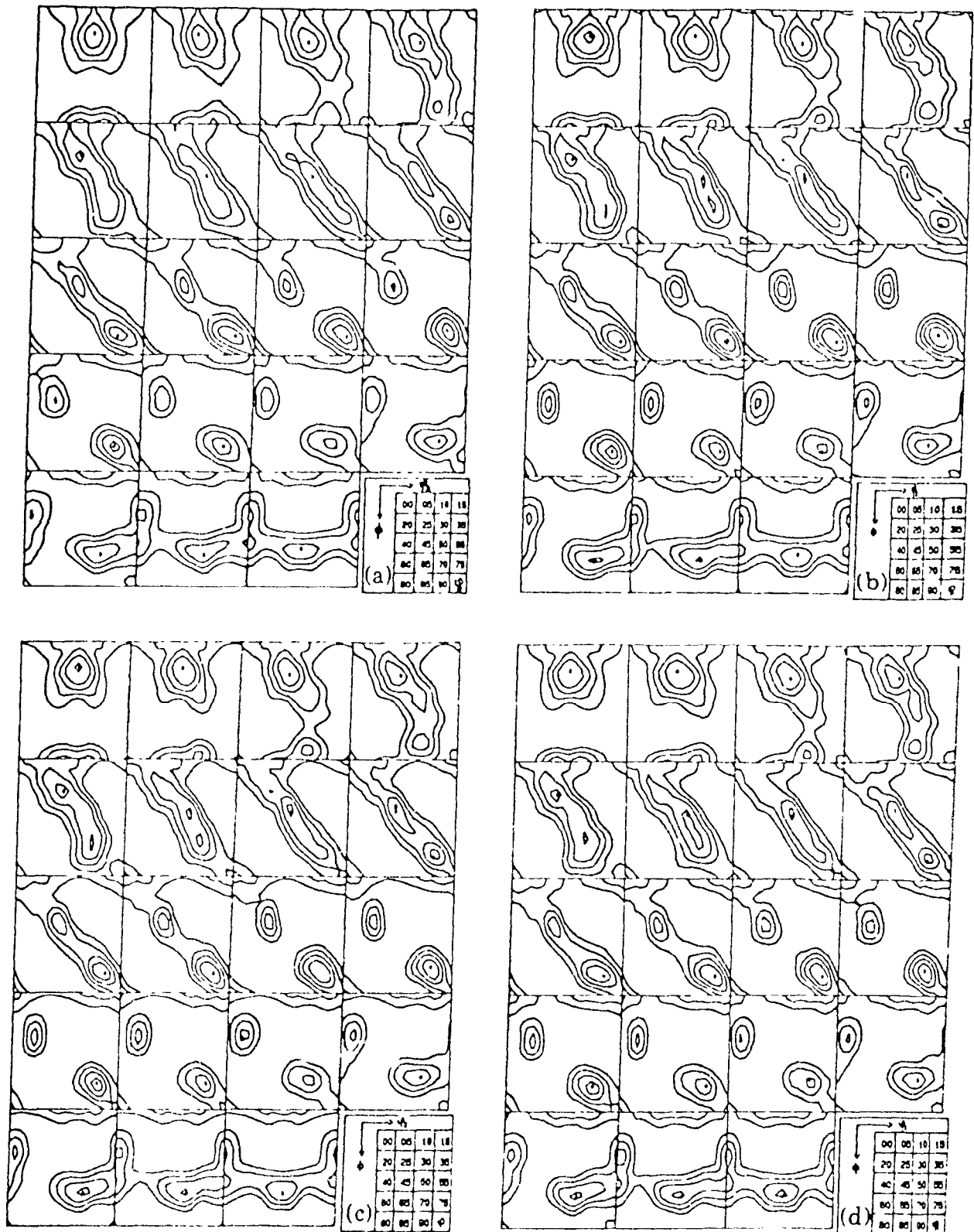


Figure 5-43 : ϕ_1 -section ODF's obtained by transforming the texture of the 95% cold rolled Ni-30Co alloy according to the NW relationship : (a) without ghost correction; (b) corrected with a gaussian peak method; and corrected with an iterative positivity method (c) before and (d) after transformation (levels 1,2,3...).

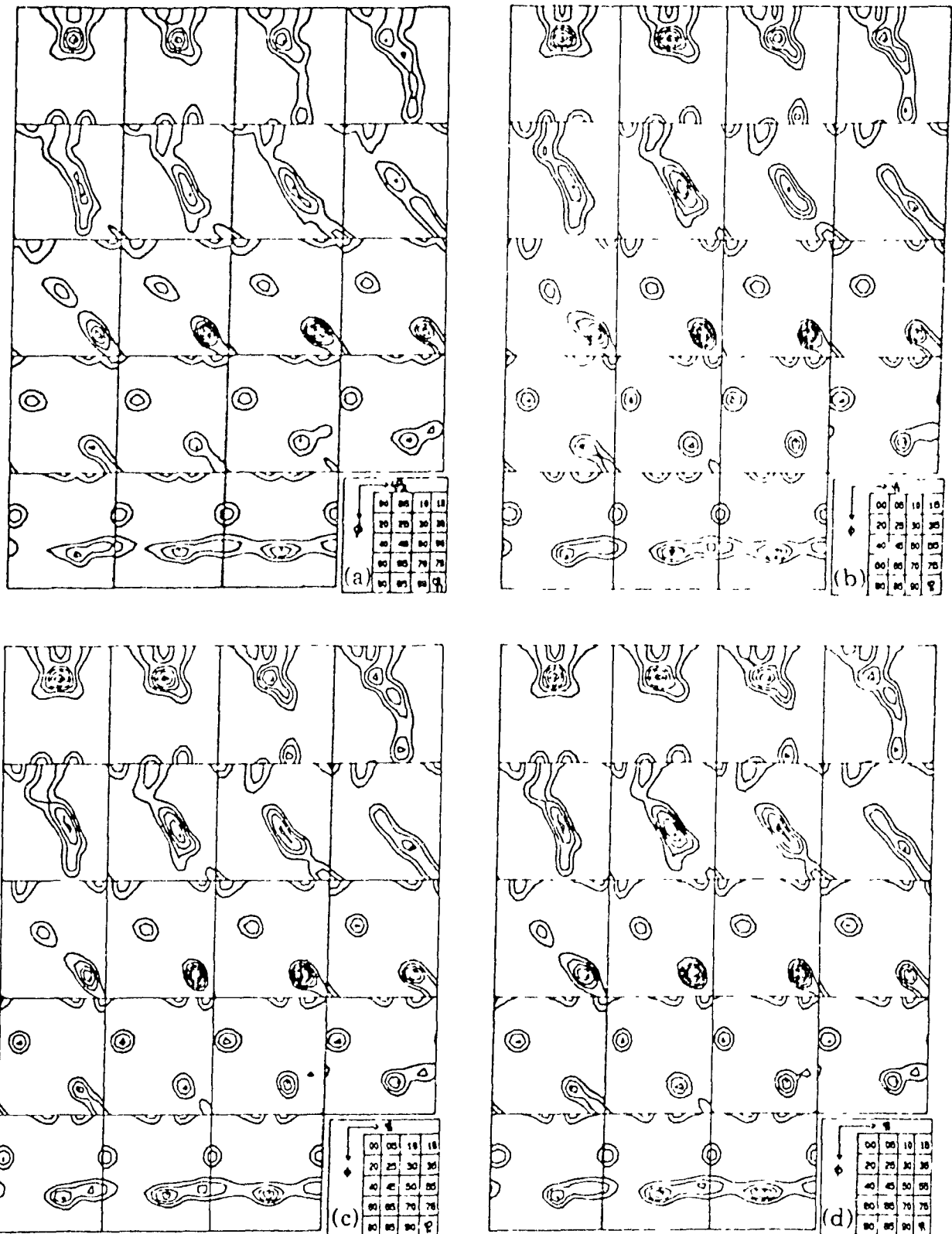


Figure 5-44 : ϕ_1 -section ODF's obtained by transforming the texture of the 95% cold rolled Ni-30Co alloy according to the Bain relationship : (a) without ghost correction; (b) corrected with a gaussian peak method; and corrected with an iterative positivity method (c) before and (d) after transformation (levels 2,4,6..).

four conditions, in Figures 5-45 (a), (b) and (c) for the KS, NW and Bain transformation laws, respectively.

The main influence of the ghost correction process thus appears to be that the severity of the transformation texture is increased slightly compared to the case where no correction is applied. No major change is observed in the ϕ_1 -section ODF's, except that the maxima are somewhat sharpened. The negative intensities are not represented on the $\phi_1 = \text{constant}$ sections, so that the effect of the correction procedure cannot be fully appreciated. These observations are confirmed by the plots of the orientation densities along the α and γ fibres. The gaussian type correction seems to sharpen the final texture more than the two iterative positivity methods, which in turn give similar results. The strong maxima are further strengthened and certain second order peaks are lowered.

Finally, although some modifications are apparent, they remain far below the degree of certainty of the experimental measurements, so that the ghost phenomenon can be concluded to have little influence on the study of transformation textures by such types of simulations.

- order of truncation in the series expansions:

In the series expansion method, the summations on the first index - denoted l - should range from zero to infinity. However, they are generally truncated at $l_{\text{max}} = 22$ for simplicity and because the weight of the higher order indices is well below the degree of precision of the orientation density $f(g)$. The influence of truncation at a lower level was therefore investigated on the transformation texture KS-derived from the 95% cold rolled Ni-30Co data.

Here, the limitation on l can originate from any of the three harmonic functions involved in the simulation of transformation textures: (i) the ODF of the parent fcc phase, (ii) the MODF of the orientation relationship, or (iii) the ODF of the product bcc phase. These three functions, when expanded into series form, can *a priori* be truncated at three different values of the first index, l . The transformation relation, which relates the corresponding three types of coefficients, however, takes the smallest l_{max} into account, the coefficients of higher order being annihilated.

The ϕ_1 -section ODF's KS-derived from 95% cold rolled Ni-30Co are presented in Figure 5-46 with different orders of truncation ($l_{\text{max}} = 22, 18, 12$ and 6). The corresponding orientation densities along the α and γ fibres are illustrated in Figures 5-47 (a) and (b), respectively. The severity of the transformation textures increases with l_{max} , although the strengths of certain peaks can be influenced in different

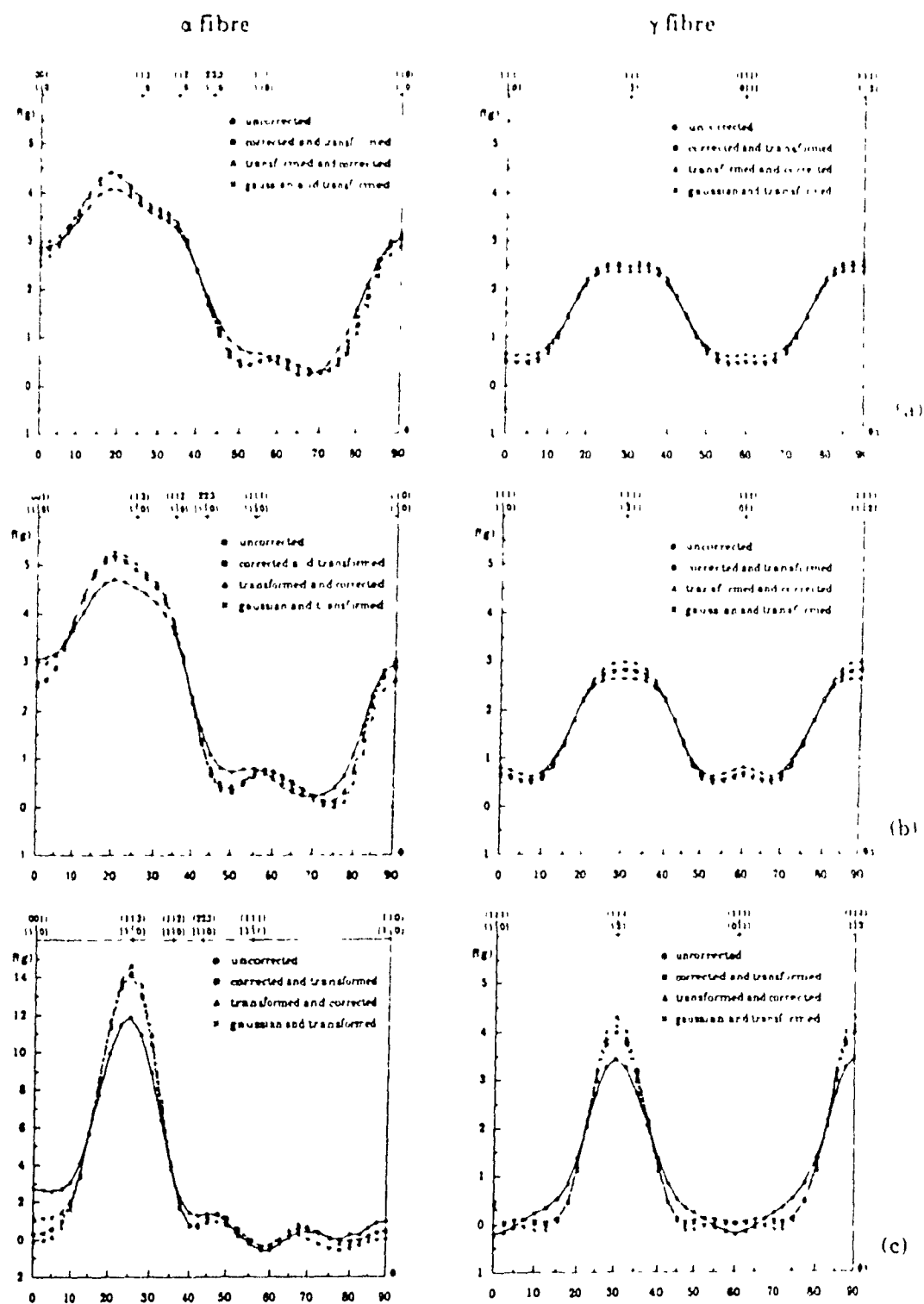


Figure 5-45 : Orientation density along the α and γ fibres of the textures shown in Figures 5-42 to 5-44 pertaining to the : (a) KS, (b) NW, and (c) Bain relationships.

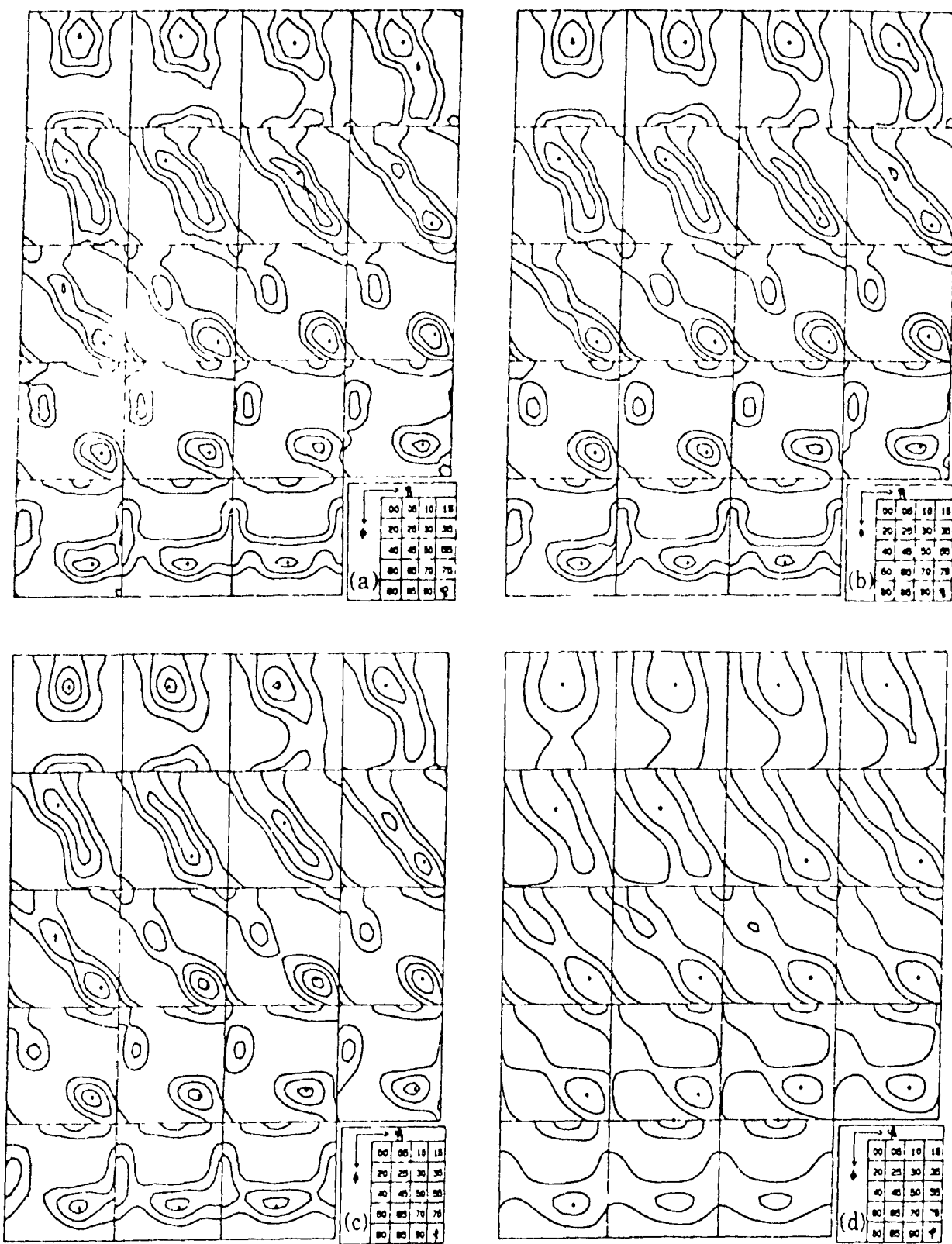


Figure 5-46: ϕ_1 -section ODF's obtained by transforming the texture of the 95% cold rolled Ni-30Co alloy according to the KS relationship with different orders of truncation. (a) $l_{\max}=22$, (b) $l_{\max}=18$, (c) $l_{\max}=12$, and (d) $l_{\max}=6$ (levels 1,2,3..).

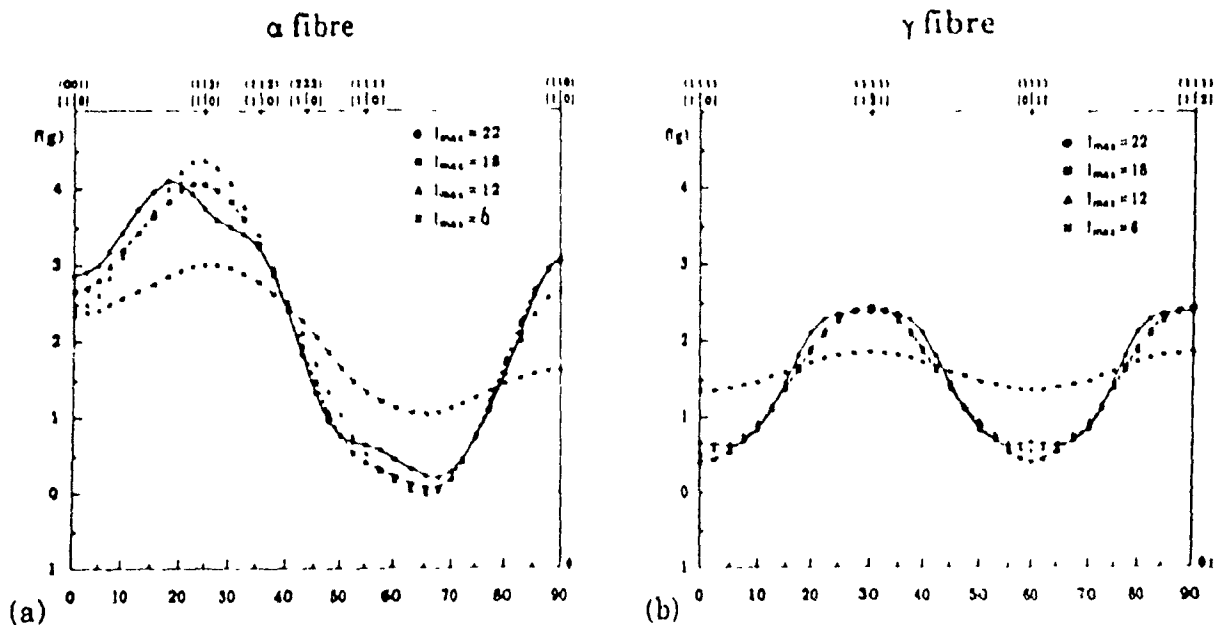


Figure 5-47: Orientation density along the (a) α fibre and (b) γ fibre of the textures shown in Figure 5-46.

ways. The above remarks do not apply perhaps to the $l_{\max}=6$ case, which differs somewhat from the others, probably because of the over simplification of the description of the texture.

- departures from the exact orientation relationships.

In the course of this work, the orientation relationship was always assumed to apply strictly and identically to each individual grain. It has been said, however, that phase transformations are seldom characterized by such high degrees of ideality. Certain discrepancies can therefore be introduced into the simulations when calculating the MODF coefficients of the transformation law - (i) a gaussian angular spread ω_0 about the ideal value Δg of the orientation relationship can be assumed, and/or (ii) a percentage p_r of the transformation can be carried out in a random manner. The effects of these two parameters - ω_0 and p_r - are presented below on the transformation texture KS-derived from 95% cold rolled Ni-30Co.

(a) influence of a gaussian spread in the orientation relationship on the simulated transformation texture : In Figure 5-48, the ϕ_1 -section ODF's are shown for different values of the angular spread ω_0 (0° , 5° , 10° and 15°) and the corresponding orientation densities along the α and γ fibres are presented in Figure

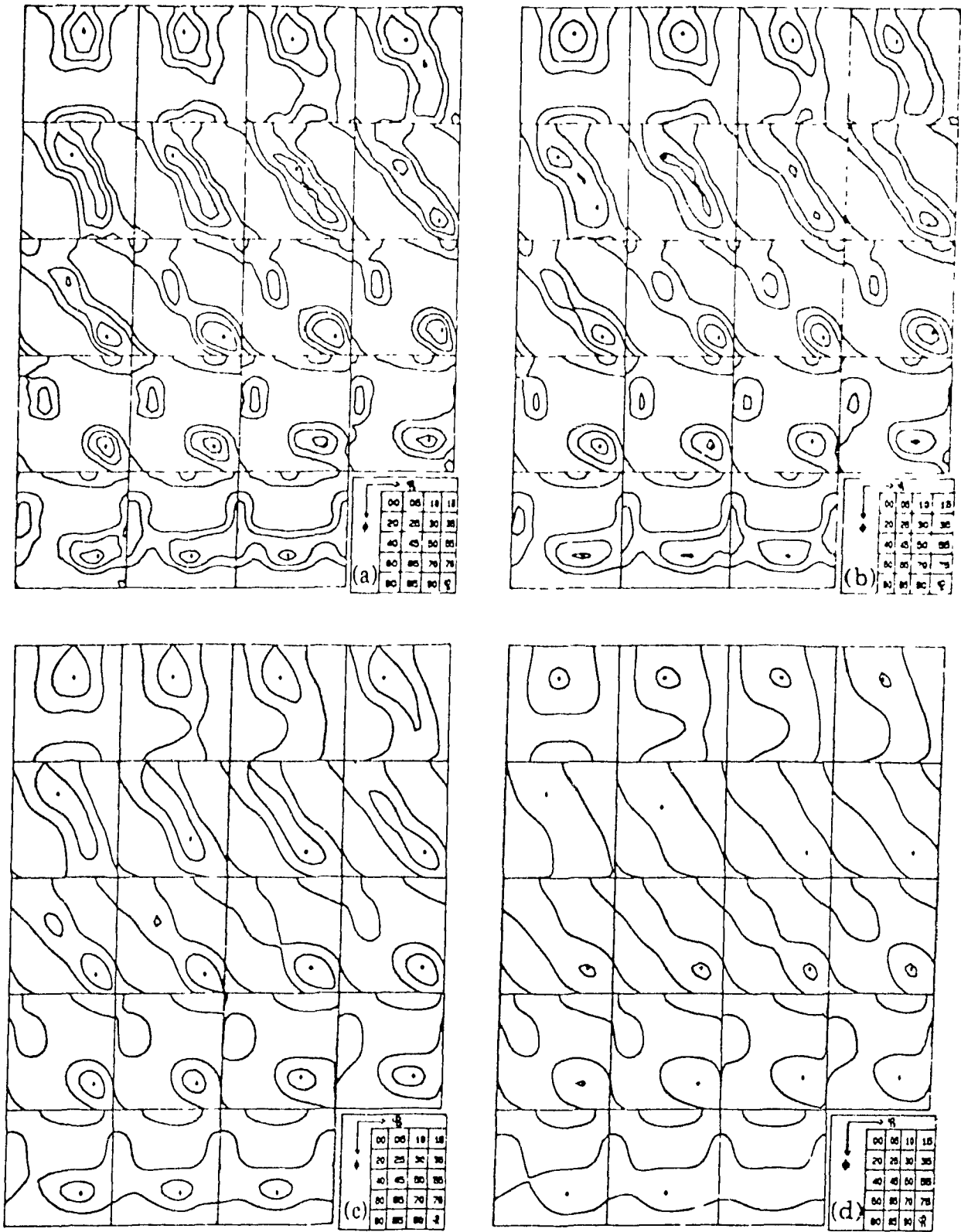


Figure 5-48 : ϕ_1 -section ODF's obtained by transforming the texture of the 95% cold rolled Ni-30Co alloy according to the KS relationship with four angular spreads away from the exact law : (a) $\omega_0 = 0^\circ$, (b) $\omega_0 = 5^\circ$, (c) $\omega_0 = 10^\circ$ and (d) $\omega_0 = 15^\circ$ (levels 1,2,3,..).

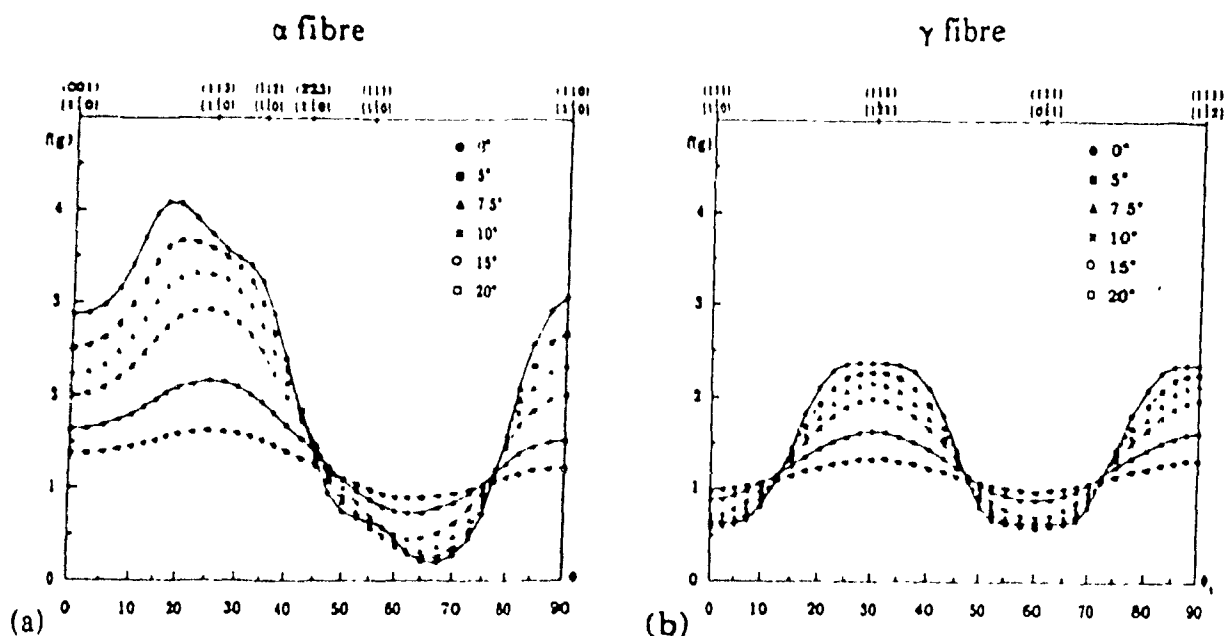


Figure 5-49 : Orientation density along the (a) α fibre and (b) γ fibre of the textures shown in Figure 5-48.

5-49. The severity of the texture decreases with ω_0 and the peak profiles become smoother. The positions of the maxima are only slightly modified, but their strengths are significantly lowered compared to the exact transformation. This applies to the overall maxima of the texture, as well as to the peaks of secondary importance. From Figure 5-49 (a), it is also evident that the location of the strongest maximum gradually shifts towards the $\{113\} \langle 110 \rangle$ orientation as the angular spread goes from 0° to 7.5° ; it then remains in this position for higher values of the ω_0 parameter. For ω_0 greater than about 20° , the simulated textures exhibit intensities close to the random distribution.

All these findings are in agreement with the fact that the spectrum of the transformation law is enlarged when ω_0 is increased, so that the product orientations are distributed over a wider range of Euler space than in the case of a strict orientation relationship.

(b) influence of a percentage of random transformation on the simulated transformation texture : The ϕ_1 -section ODF's obtained by transforming the texture of 95% cold rolled Ni-30Co according to the KS orientation relationship with different percentages of randomness in the transformation (0%, 15%, 25%, and 40%) are shown in Figure 5-50. In the 15% random case, for example, 85% of the initial

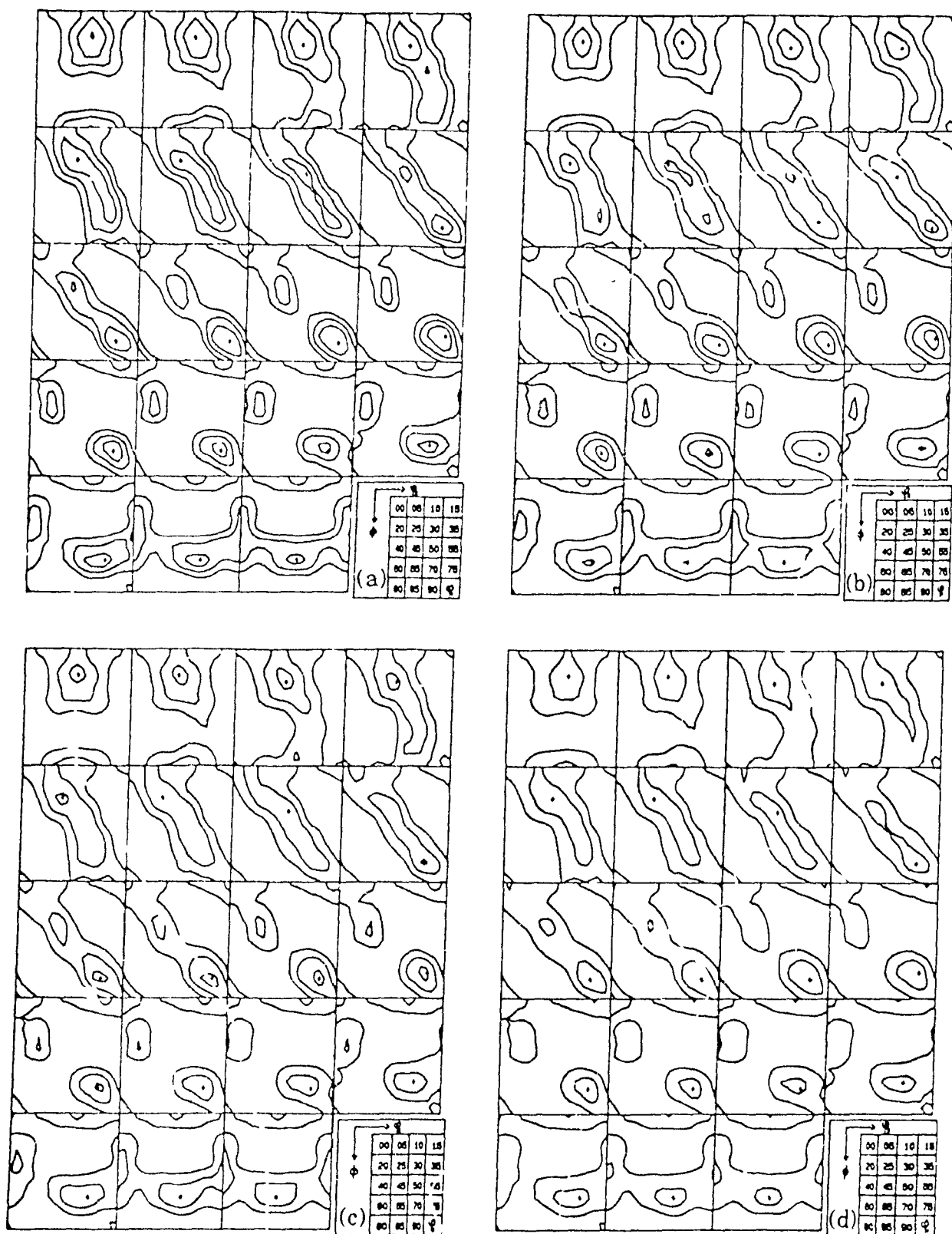


Figure 5-50 : ϕ_1 -section ODF's obtained by transforming the texture of the 95% cold rolled Ni-30Co alloy according to the KS relationship with four percentages of randomness : (a) $p_r = 0\%$, (b) $p_r = 15\%$, (c) $p_r = 25\%$, and (d) $p_r = 40\%$ (levels 1,2,3...).



texture is transformed according to KS and 15% in a random manner. Similar figures apply to the other random levels. The corresponding orientation densities along the α and γ fibres are presented in Figure 5-51.

As can be seen from Figures 5-50 and 5-51, the main influence of randomness is to lower the intensity of the transformed ODF. The severity of the texture decreases regularly as p_r increases. However, this strength reduction is not accompanied by any change in the position of the maxima of the ODF, as was the case with ω_0 ; the overall maxima and second order peaks are decreased in intensity but do not undergo any shift compared to the $p_r = 0\%$ case (i.e. the transformation according to the strict KS relationship). The transformation texture keeps its initial form, even with a random component as high as 40%.

Finally, the influence of the above departures from the strict orientation relationship is mainly to lower the intensities of the derived transformation textures, as can be seen from Figures 5-52 (a) and (b), which show the dependence of the severity parameter on the two simulation parameters ω_0 and p_r , respectively.

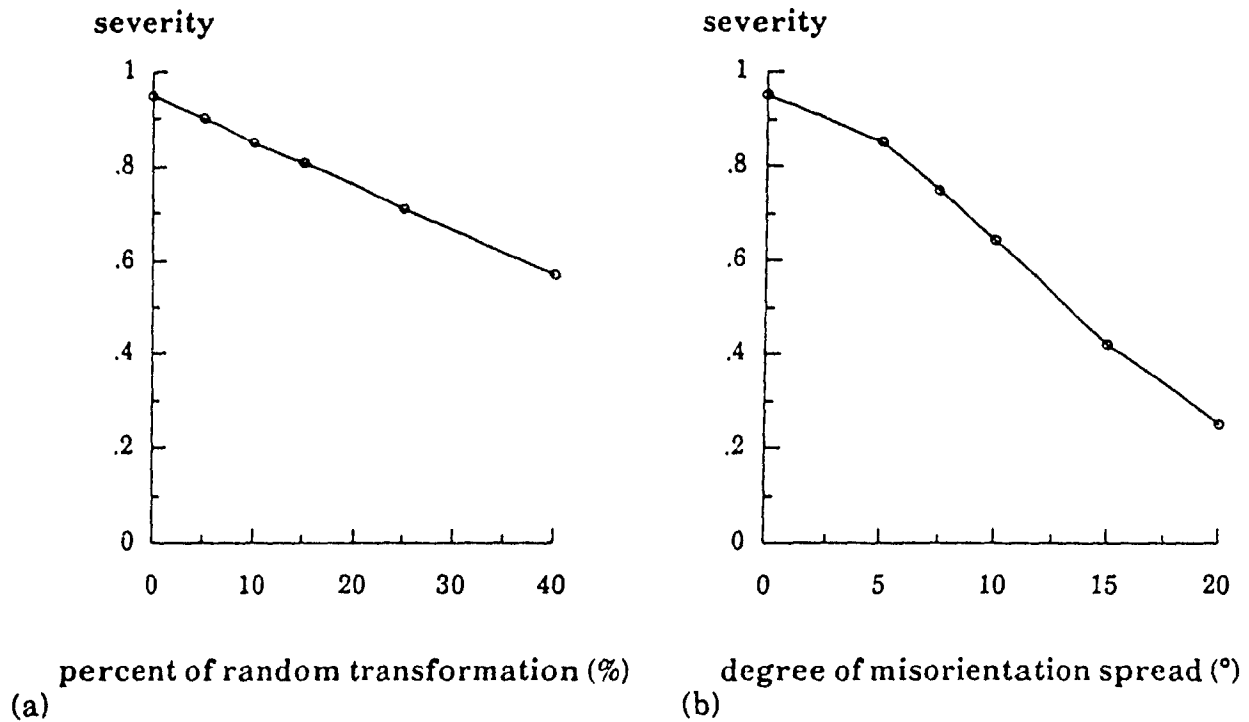


Figure 5-52 : Dependence of the severity parameter of the transformation texture on the (a) percentage of randomness, and (b) degree of misorientation in the transformation.

CHAPTER VI

CONCLUSIONS

The main purpose of this work was to describe the theoretical basis for the investigation of transformation textures, with particular reference to the case of controlled rolled steels. The mathematical formulation of phase transformation, as applied to texture evolution, has been reviewed, from both a discrete and a continuous point of view, by means of the orientation of individual crystals and the statistical concept of the orientation distribution function, respectively. The classical orientation relationships considered to be valid during the γ -to- α transition in steels have also been reviewed, as well as some of the variant selection models. An analysis of the most important problems related to the existence of several variants of a transformation law, as a result of crystal symmetry, has been attempted. Methods, based on the discrete and continuous formalisms, have then been presented for investigating the inheritance of a texture during the phase transition, both during the transformation ($\gamma \rightarrow \alpha$) and the untransformation ($\alpha \leftarrow \gamma$) process.

The different kinds of transformation textures normally encountered in steels have been discussed and the effects of compositional and processing variables on their development have been enumerated. The correspondence obtained in earlier studies between analytically predicted and experimental textures has also been presented in some detail. In the present investigation, transformation textures in steels have been estimated by transforming the ODF's according to certain crystallographic relationships for a series of cold rolled Ni-Co alloys, taken as representative of the austenite.

From this work, the following major conclusions can be drawn :

- (1) Both discrete and continuous models are available for the simulation of transformation textures. However, detailed analysis requires the use of the complete ODF and MODF descriptions rather than that of ideal orientations and crystallographic relationships, so that the continuous series expansion method gives the best results.

- (2) The transformation ODF's obtained from the Bain relation are much sharper than the ODF's deduced from those of Kurdjumow-Sachs or Nishiyama-Wassermann. In all three cases, however, due to the multiplicity of the transformation variants, the transformed textures are invariably weaker than those of their austenite parents.
- (3) The ferrite textures determined in controlled rolled steels heavily deformed in the austenite range generally agree with the ODF predicted on the basis of the KS relation, without variant selection, from the cold rolled Ni-Co alloy with similar stacking fault energy.
- (4) The two major texture components of the ferrite derived from deformed austenite are the $\{332\}\langle 113 \rangle$ and $\{113\}\langle 110 \rangle$; these originate from the $\{110\}\langle 112 \rangle$ (Bs) and $\{112\}\langle 111 \rangle$ (Cu) orientations, respectively, which are the two major rolling components of fcc materials. Several of the transformed orientations derived from the third most important fcc rolling component, the $\{123\}\langle 634 \rangle$ (S), also lie close to the above ferrite orientations. In addition, the transformation of these three components partially predicts some of the second order maxima observed in experimental textures.
- (5) The overall severity of the texture predicted from the Ni-Co alloys and the exact positions of their maxima, in the vicinity of $\{332\}\langle 113 \rangle$ and $\{113\}\langle 110 \rangle$, vary with the amount of rolling reduction prior to transformation.
- (6) Comparison between the martensite textures inherited from deformed austenites and those derived from the Ni-Co alloys indicates that variant selection plays a role in this kind of transformation.
- (7) Although some of the features of the ϕ_1 -section ODF's pertaining to cold rolled steels resemble those derived from the Ni-Co alloys, the former are generally more severe and best described by fiber type components (mainly the α and γ fibres) rather than by peak type maxima. As a result, the two processes of

deformation + transformation and transformation + deformation do not appear to be equivalent.

- (8) The presence of ghosts in the parent austenite textures does not modify the general conclusions drawn from the above simulations, although their correction slightly sharpens the intensities of the derived maxima. Certain simulation parameters, such as the order of truncation and departures from the exact orientation relationship (gaussian spread and the presence of a random component), also modify the severity of the predicted textures without altering their major characteristics.

REFERENCES

1. H.R. Wenk, H.-J. Bunge, J.S. Kallend, K. Lucke, S. Matthies, J. Pospiech and P. Van Houtte, "Eighth International Conference on Textures of Materials", Conf. Proc. ICOTOM-8, J.S. Kallend and G. Gottstein eds., The Metallurgical Society of AIME, Santa Fe, New Mexico, U. S. A., 1988, p. 17.
2. H.-J. Bunge, "Texture Analysis in Materials Science", Butterworths, London, 1982.
3. R.J. Roe, J. Appl. Phys., **36** (1965), 2024.
4. R.J. Roe, J. Appl. Phys., **37** (1966), 2069.
5. H.-J. Bunge, Zeitschrift für Metallkunde, **56** (1965), 872.
6. D. Ruer, Thèse, Université de Metz, France, 1976.
7. A. Vadon, Thèse, Université de Metz, France, 1981.
8. S. Matthies, Phys. Stat. Sol. (B), **92** (1979), K135.
9. J. Muller, C. Esling and H.-J. Bunge, J. Phys., **42** (1981), 161.
10. J. Imhof, Textures and Microstructures, **4** (1982), 189.
11. J. Starkey, Can. J. Earth. Sci., **20** (1983), 932.
12. R.O. Williams, Trans. Metall. Soc. AIME, **242** (1968), 104.
13. W. Truszkowski, J. Pospiech, J. Jura and B. Major, "3^{eme} Colloque Européen sur les Textures de Déformation et de Recristallisation des Métaux et leurs Applications Industrielles", Conf. Proc. ICOTOM-3, R. Penelle ed., Société Française de Métallurgie, Pont-à-Mousson, France, 1973.
14. C. Esling and E. Bechler-Ferry, "Quantitative Texture Analysis", H.-J. Bunge and C. Esling eds., Deutsche Gesellschaft für Metallkunde, Verlag, Germany, 1982, p. 427.
15. H.-J. Bunge, "Mathematische Methoden der Texturanalyse", Akademie-Verlag, Berlin, 1969.
16. C.M. Sargent, Scripta Metall., **8** (1974), 821.
17. H.-J. Bunge, M. Humbert and P.I. Welch, Scripta Metall., **17** (1983), 1403.
18. M. Humbert, P.I. Welch and H.-J. Bunge, "Seventh International Conference on Textures of Materials", Conf. Proc. ICOTOM-7, Netherlands Society for Materials Science, Noordwijkerhout, The Netherlands, 1984, p. 321.
19. E.C. Bain, Trans. AIME, **70** (1924), 25.
20. G. Kurdjumow and G. Sachs, Zeitschrift für Physik, **64** (1930), 325.
21. Z. Nishiyama, Sci. Rep. Tohoku Imperial University, **23** (1934), 637.

22. Z. Nishiyama, Sci. Rep. Tohoku Imperial University, **25** (1936), 94.
23. G. Wassermann, Archiv für das Eisenhüttenwesen, **6** (1933), 347.
24. A.B. Greninger and A.R. Troiano, Metals Transactions, **185** (1949), 590.
25. W. Pitsch, J. Inst. Metals, **87** (1959), 444.
26. P. Coulomb, "Les Textures dans les Métaux de Réseau Cubique", Dunod, Paris, 1972, p. 117.
27. F. Wagner, H.W. Bergmann, M. Humbert and C. Esling, "The Sixth International Conference on Textures of Materials", Conf. Proc. ICOTOM-6, Vol. 1, The Iron and Steel Institute of Japan, Tokyo, Japan, 1981, p. 714.
28. A.D. King and T. Bell, Metall. Transactions, **6A** (1975), 1419.
29. H. Hu, Trans. Metall. Soc. AIME, **233** (1965), 1071.
30. H.-J. Bunge, M. Humbert and P.I. Welch, Textures and Microstructures, **6** (1984), 81.
31. H. Hu and J.S. Kallend, "The Sixth International Conference on Textures of Materials", Conf. Proc. ICOTOM-6, Vol. 1, The Iron and Steel Institute of Japan, Tokyo, Japan, 1981, p. 164.
32. J.R. Patel and M. Cohen, Acta Metall., **1** (1953), 531.
33. D. Goodchild, W.T. Roberts and D.V. Wilson, Acta Metall., **18** (1970), 1137.
34. G. Stone and G. Thomas, Metall Transactions, **5** (1974), 2095.
35. M. Kato and T. Mori, Acta Metall., **24** (1976), 853.
36. M. Kato and T. Mori, Acta Metall., **25** (1977), 951.
37. J.C. Bokros and E.R. Parker, Acta Metall., **11** (1963), 1291.
38. T.N. Durlu and J.W. Christian, Acta Metall., **27** (1979), 663.
39. F. Borik and R.H. Richman, Trans. Metall. Soc. AIME, **239** (1967), 675.
40. R.M. Bateman and G.J. Davies, "The Sixth International Conference on Textures of Materials", Conf. Proc. ICOTOM-6, Vol. 1, The Iron and Steel Institute of Japan, Tokyo, Japan, 1981, p. 690.
41. G.J. Davies and R.M. Bateman, "The Sixth International Conference on Textures of Materials", Conf. Proc. ICOTOM-6, Vol. 1, The Iron and Steel Institute of Japan, Tokyo, Japan, 1981, p. 132.
42. H. Abe, K. Ito and R. Fukumoto, J. Japan Inst. Metals, **31** (1967), 37.
43. H. Abe and K. Ito, J. Japan Inst. Metals, **31** (1967), 1300.
44. K. Haslam, T. Coleman, D. Dulieu and I.L. Dillamore, "3^{ème} Colloque Européen sur les Textures de Déformation et de Recristallisation des Métaux et leurs Applications Industrielles", Conf. Proc. ICOTOM-3, R. Penelle ed., Société Française de Métallurgie, Pont-a-Mousson, France, 1973, p. 369.

45. E. Furubayashi, Tetsu to-Hagané, 71 (1985), 1155.
46. E. Furubayashi, Tetsu-to-Hagané, 71 (1985), 1359.
47. Y. Higo, F. Lacroisey and T. Mori, Acta Metall., 22 (1974), 313.
48. E. Furubayashi, H. Miyaji and M. Nobuki, Trans. ISIJ, 27 (1987), 513.
49. H. Miyaji, M. Nobuki, N. Sakuma, T. Mitsui, H. Nakajima and E. Furubayashi, "International Conference on Physical Metallurgy of Thermomechanical Processing of Steels and Other Metals". Conf. Proc. THERMEC-88, Vol. 2, The Iron and Steel Institute of Japan, Tokyo, Japan, 1988, p. 815.
50. M. Humbert, F. Wagner, W.P. Liu, C. Esling and H.-J. Bunge, "Eighth International Conference on Textures of Materials", Conf. Proc. ICOTOM-8, J.S. Kallend and G. Gottstein eds., The Metallurgical Society of AIME, Santa Fe, New Mexico, U. S. A., 1988, p. 743.
51. P. Van Houtte, Textures and Microstructures, 7 (1987), 187.
52. M. Semchysen and G.A. Timmons, Trans. Metall. Soc. AIME, 194 (1952), 297.
53. H.-J. Bunge and C. Esling, J. Phys. Lett., 40 (1979), L-627.
54. H. Inagaki, "Fifth International Conference on Textures of Materials", Conf. Proc. ICOTOM-5, Vol. 2, G. Gottstein and K. Lucke eds., Springer Verlag, Berlin, Germany, 1978, p. 157.
55. J.S. Kallend, P.P. Morris and G.J. Davies, Acta Metall., 24 (1976), 361.
56. G.J. Davies, "Fifth International Conference on Textures of Materials", Conf. Proc. ICOTOM-5, Vol. 2, G. Gottstein and K. Lucke eds., Springer Verlag, Berlin, Germany, 1978, p. 121.
57. H. Inagaki, Trans. ISIJ, 17 (1977), 166.
58. H. Inagaki, "The Sixth International Conference on Textures of Materials", Conf. Proc. ICOTOM-6, Vol. 1, The Iron and Steel Institute of Japan, Tokyo, Japan, 1981, p. 149.
59. H. Inagaki, K. Kurihara and I. Kozasu, Trans. I. S. I. J., 17 (1977), 75.
60. G.J. Davies, J.S. Kallend and P.P. Morris, "The Hot Deformation of Austenite", AIME, New York, U. S. A., 1977, p. 559.
61. H. Inagaki, Zeitschrift fur Metallkunde, 74 (1983), 716.
62. A. Jones and B. Walker, Metal Sci., 8, (1974), 397.
63. T. Yutori and R. Ogawa, "The Sixth International Conference on Textures of Materials", Conf. Proc. ICOTOM-6, Vol. 1, The Iron and Steel Institute of Japan, Tokyo, Japan, 1981, p. 669.
64. R.K. Ray and J.J. Jonas, Inter. Materials Reviews, to be published.

65. E.B. Kula and S.L. Lopata, Trans. Metall. Soc. AIME, 215 (1959), 980.
66. C. Vlad, "Directionality of Properties in Wrought Products", The Metals Society, London, 1976, p. 311.
67. J. Pospiech, J. Jura and A. Maciosowski, "3^{ème} Colloque Européen sur les Textures de Déformation et de Recristallisation des Métaux et leurs Applications Industrielles", Conf. Proc. ICOTOM-3, R. Penelle ed. , Société Française de Métallurgie, Pont-à-Mousson. France, 1973, p. 117.
68. J. Grewen and G. Wassermann, Texture, 2 (1975), 45.
69. H. Kubotera, K. Nakaoka and T. Nagamine, Nippon Kokan Tech Rep., May 1968, p. 19.
70. C.M. Vlad and D. Grzesik, "Texture and the Properties of Materials", The Metals Society, London, 1976, p. 311.
71. H.-P. Sattler and G. Wassermann, J. Less-Common Metals, 28 (1972), 119.
72. M. Humbert, to be published.
73. M. Humbert, P.I. Welch and H.-J. Bunge, "Theoretical Methods of Texture Analysis", H.-J. Bunge eds. , Deutsche Gesellschaft für Metallkunde, Verlag, Germany, 1987, p. 327.
74. H. Inagaki and M. Kodama, Tetsu-to-Hagane, 67 (1981), S640.
75. I. Kozasu, H. Inagaki, K. Kurihara and T. Sampei, Tetsu-to-Hagane, 61 (1975), S209.
76. I. Kozasu, H. Inagaki, K. Kurihara and T. Sampei, Tetsu-to-Hagane, 61 (1975), S210.
77. G.J. Davies, J.S. Kallend and P.P. Morris, Acta Metall., 24 (1976), 159.
78. U. Lotter, L. Meyer and D. Knorr, Archiv für das Eisenhüttenwesen, 47 (1976), 259.
79. U. Lotter and L. Meyer, Metals Tech., 4 (1977), 21.
80. C.M. Vlad and D. Grzesik, "Texture and the Properties of Materials", The Metals Society, London, 1976, p. 255.
81. T. Gladman and D. Dulieu, Met. Sci., 8 (1974), 167.
82. I.L. Dillamore, R.F. Dewsnap and M.G. Frost, Metals Tech., 2 (1975), 294.
83. C.M. Vlad and H.-J. Bunge, "The Sixth International Conference on Textures of Materials", Conf. Proc. ICOTOM-6, Vol. 1, The Iron and Steel Institute of Japan, Tokyo, Japan, 1981, p. 639.
84. T. Coleman, D. Dulieu and A. Grouch, "The Microstructure and Design of Alloys", The Metals Society, London, 1973, p. 70.

85. B.L. Bramfit and A.R. Marder, "Processing and Properties of Low Carbon Steels", A. I. M. E. , New York, U. S. A. , 1973, p. 191.
86. T. Tanaka, N. Nabata, T. Hatomura and C. Shiga, "Microalloying '75", Union Carbide Corp. , New York, U. S. A. , 1977, p. 107.
87. J.H. Little, J.A. Chapman, W.B. Morrison and B. Mintz, "The Microstructure and Design of Alloys", The Metals Society, London, 1973, p. 70.
88. D.N. Hawkins, Metals Tech. , 3 (1976), 417.
89. H. Inagaki, T. Suda, Texture, 1 (1972), 129.
90. T. Tanaka and N. Tabata, Tetsu-to-Hagané, 64 (1978), 1353.
91. C.A. Stickles, Trans. Metall. Soc. AIME, 239 (1967), 1857.
92. R.O. Williams, Trans. Metall. Soc. AIME, 224 (1962), 129.
93. I.L. Dillamore and W.T. Roberts, J. Inst. Metals, 92 (1963/64), 193.
94. M. Matsuo, T. Sakai and Y. Suga, Metall. Transactions, 17A (1986), 1313.
95. T. Yutori and R. Ogawa, Tetsu-to-Hagané, 65 (1979), 1747.
96. I. Kozasu, H. Inagaki, K. Kurihara, T. Sampei and T. Ohkita, Tetsu-to-Hagané, 59 (1973), A49.
97. I.L. Dillamore and W.T. Roberts, Acta Metall. , 12 (1964), 281.
98. R. Penelle, J. Mihon and P. Lacombe, "7ème Colloque de Métallurgie, Ecrouissage, Restauration, Recristallisation", Paris, 1963, p. 153.
99. H. Borchers and K. Klinge, Archiv für das Eisenhüttenwesen, 39 (1968), 369.
100. R.S. Schoefield, G. Rawntree, N.V. Sarma and T. Weiner, Metals Tech. , 1 (1974) 325.
101. H. Inagaki, Trans. ISIJ, 23 (1983), 1059.
102. S.R. Goodman and H. Hu, Trans. Metall. Soc. AIME, 233 (1965), 103.
103. S.R. Goodman and H. Hu, Trans. Metall. Soc. AIME, 230 (1964), 1413.
104. G.J. Davies, J.S. Kallend and T. Ruberg, Met. Sci. , 9 (1975), 421.
105. H.W. Bergmann, E. Bechler-Ferry and C. Esling, "The Sixth International Conference on Textures of Materials", Conf. Proc. ICOTOM-6, Vol. 1, The Iron and Steel Institute of Japan, Tokyo, Japan, 1981, p. 703.
106. C. Esling, F. Wagner, R. Baro and M. Englander, "Fifth International Conference on Textures of Materials", Conf. Proc. ICOTOM-5, Vol. 2, G. Gottstein and K. Lucke eds. , Springer Verlag, Berlin, Germany, 1978, p. 221.
107. B.B. Rath, J.S. Kallend, C.L. Vold, R.A. Masura and A. Imam, "Seventh International Conference on Textures of Materials", Conf. Proc. ICOTOM-7, Netherlands Society for Materials Science, Noordwijkerhout, The Netherlands, 1984, p. 339.

108. N. Inakazu and H. Yamamoto, "The Sixth International Conference on Textures of Materials", Conf. Proc. ICOTOM-6, Vol. 1, The Iron and Steel Institute of Japan, Tokyo, Japan, 1981, p. 327.
109. H. Neerfeld and K. Mathieu, Archiv fur das Eisenhüttenwesen, **20** (1949), 69.
110. K.W. Andrews, J. Iron and Steel Inst., **184** (1956), 274.
111. O. Hashimoto, S. Satoh and T. Tanaka, Trans. ISIJ, **27** (1987), 746.
112. O. Hashimoto, S. Satoh and T. Tanaka, Trans. ISIJ, **23** (1983), 1028.
113. K. Lucke, "The Sixth International Conference on Textures of Materials", Conf. Proc. ICOTOM-6, Vol. 1, The Iron and Steel Institute of Japan, Tokyo, Japan, 1981, p. 14.
114. W. Charnock and J. Nutting, Metal Sci. J., **1** (1967), 123.
115. P.C.J. Gallagher, Metall Transactions, **1A** (1970), 2429.
116. P. Haasen, "Physical Metallurgy", Cambridge University Press, 1978, p. 116.
117. B.E.P. Beeston and L.K. France, J. Inst. Metals, **96** (1968), 105.
118. R.K. Ray and K. Lucke, unpublished research.
119. J. Jura and J. Pospiech, Texture, **3** (1978), 1.
120. B. Bacroix, "Prediction of high temperature deformation textures in FCC metals", Ph. D. Thesis, McGill University, Montreal Canada, 1986, p. 17.
121. J. Hirsch, K. Lucke and H. Mecking, "Seventh International Conference on Textures of Materials", Conf. Proc. ICOTOM-7, Netherlands Society for Materials Science, Noordwijkerhout, The Netherlands, 1984, p. 83.
122. J. Hirsch, K.H. Virnich and K. Lucke, "The Sixth International Conference on Textures of Materials", Conf. Proc. ICOTOM-6, Vol. 1, The Iron and Steel Institute of Japan, Tokyo, Japan, 1981, p. 375.
123. J. Hirsch and K. Lucke, "Theoretical Methods of Texture Analysis", H.-J. Bunge eds., Deutsche Gesellschaft für Metallkunde, Verlag, Germany, 1987, p. 307.
124. J. Hirsch and K. Lucke, Acta Metall., **11** (1988), 2863.
125. M. Hatherly, A.S. Malin, C.M. Carmichael, F.J. Humphreys and J. Hirsch, Acta Metall., **34** (1986), 2247.
126. H. Hu, R.S. Cline and S.R. Goodman, J. Appl. Phys., **32** (1961), 1392.
127. A. Mucklich, J. Tobisch, K. Kleinstück and K. Hennig, "Fifth International Conference on Textures of Materials", Conf. Proc. ICOTOM-5, Vol. 1, G. Gottstein and K. Lucke eds., Springer Verlag, Berlin, Germany, 1978, p. 237.
128. H. Mecking, "Theoretical Methods of Texture Analysis", H.-J. Bunge eds., Deutsche Gesellschaft für Metallkunde, Verlag, Germany, 1987, p. 232.

129. P. Coulomb, "Les textures dans les métaux de réseau cubique", Dunod, Paris, 1972, p. 97.
130. K.H. Virnich and K. Lucke, "Fifth International Conference on Textures of Materials", Conf. Proc. ICOTOM-5, Vol. 1, G. Gottstein and K. Lucke eds., Springer Verlag, Berlin, Germany, 1978, p. 397.
131. R. Kern and H.-J. Bunge, "Seventh International Conference on Textures of Materials", Conf. Proc. ICOTOM-7, Netherlands Society for Materials Science, Noordwijkerhout, The Netherlands, 1984, p. 89.
132. R. Kern, H.P. Lee and H.-J. Bunge, Metal Working, 11 (1986), 563.
133. H.-J. Bunge, Phys. Stat. Sol., 26 (1968), 167.
134. U. von Schluppenbach, F. Emren and K. Lucke, Acta Metall., 34 (1986), 1289.
135. U. von Schluppenbach, K. Lucke, "Seventh International Conference on Textures of Materials", Conf. Proc. ICOTOM-7, Netherlands Society for Materials Science, Noordwijkerhout, The Netherlands, 1984, p. 159.
136. W. Osterle, "Seventh International Conference on Textures of Materials", Conf. Proc. ICOTOM-7, Netherlands Society for Materials Science, Noordwijkerhout, The Netherlands, 1984, p. 123.
137. D.J. Willis and M. Hatherly, "Fifth International Conference on Textures of Materials", Conf. Proc. ICOTOM-5, Vol. 1, G. Gottstein and K. Lucke eds., Springer Verlag, Berlin, Germany, 1978, p. 465.
138. H. Hu, Texture Cryst. Solids, 4 (1980), 13.
139. K. Lucke, J. Pospiech, K.H. Virnich and J. Jura, Acta Metall., 29 (1981), 167.
140. K.H. Virnich, J. Pospiech, A. Flemmer and K. Lucke, "Fifth International Conference on Textures of Materials", Conf. Proc. ICOTOM-5, Vol. 1, G. Gottstein and K. Lucke eds., Springer Verlag, Berlin, Germany, 1978, p. 129.
141. J. Hirsch and K. Lucke, "Theoretical Methods of Texture Analysis", H.-J. Bunge eds., Deutsche Gesellschaft für Metallkunde, Verlag, Germany, 1987, p. 53.
142. H.-J. Bunge, "Eighth International Conference on Textures of Materials", Conf. Proc. ICOTOM-8, J.S. Kallend and G. Gottstein eds., The Metallurgical Society of AIME, Santa Fe, New Mexico, U. S. A., 1988, p. 69.

APPENDIX A

LIST OF THE VARIANTS OF SOME TRANSFORMATION LAWS

variant	Euler angles	rotation	
		axis	angle
1	(0°, 45°, 0°)	[100]	45°
2	(90°, 45°, -90°)	[010]	45°
3	(45°, 0°, 0°)	[001]	45°

Table A-1: Variants of the Bain orientation relationship

variant	Euler angles	rotation	
		axis	angle
1	(45°, 90°, -9.74°)	[uvw]	95.26°
2	(-174.23°, 48.19°, 95.77°)	[uvw]	95.26°
3	(174.23°, 48.19°, -95.77°)	[uvw]	95.26°
4	(5.77°, 48.19°, -84.23°)	[uvw]	95.26°
5	(138.77°, 80.41°, -94.36°)	[uvw]	95.26°
6	(41.23°, 80.41°, -85.64°)	[uvw]	95.26°
7	(-41.23°, 80.41°, 85.64°)	[uvw]	95.26°
8	(-138.77°, 80.41°, 94.36°)	[uvw]	95.26°
9	(4.36°, 80.41°, -48.77°)	[uvw]	95.26°
10	(175.64°, 80.41°, -131.23°)	[uvw]	95.26°
11	(-175.64°, 80.41°, 131.23°)	[uvw]	95.26°
12	(-4.36°, 80.41°, 48.77°)	[uvw]	95.26°

Table A-2: Variants of the Nishiyama-Wassermann orientation relationship

$$h = -1 + \sqrt{2} + \sqrt{3} \quad k = 1 + \sqrt{2} + \sqrt{3} \quad l = \sqrt{2}$$

variant	Euler angles	rotation	
		axis	angle
1	$(-5.77^\circ, 48.19^\circ, 84.23^\circ)$	[1-12]	90°
2	$(-174.23^\circ, 48.19^\circ, 95.77^\circ)$	[-1-1-2]	90°
3	$(174.23^\circ, 48.19^\circ, -95.77^\circ)$	[-112]	90°
4	$(5.77^\circ, 48.19^\circ, -84.23^\circ)$	[11-2]	90°
5	$(138.77^\circ, 80.41^\circ, -94.36^\circ)$	[-121]	90°
6	$(41.23^\circ, 80.41^\circ, -85.64^\circ)$	[12-1]	90°
7	$(-41.23^\circ, 80.41^\circ, 85.64^\circ)$	[1-21]	90°
8	$(-138.77^\circ, 80.41^\circ, 94.36^\circ)$	[-1-2-1]	90°
9	$(4.36^\circ, 80.41^\circ, -48.77^\circ)$	[21-1]	90°
10	$(175.64^\circ, 80.41^\circ, -131.23^\circ)$	[-211]	90°
11	$(-175.64^\circ, 80.41^\circ, 131.23^\circ)$	[-2-1-1]	90°
12	$(-4.36^\circ, 80.41^\circ, 48.77^\circ)$	[2-11]	90°
13	$(131.23^\circ, 80.41^\circ, -175.64^\circ)$	[-21-1]	90°
14	$(48.77^\circ, 80.41^\circ, -4.36^\circ)$	[211]	90°
15	$(-48.77^\circ, 80.41^\circ, 4.36^\circ)$	[2-1-1]	90°
16	$(-131.23^\circ, 80.41^\circ, 175.64^\circ)$	[-2-11]	90°
17	$(-94.36^\circ, 80.41^\circ, 138.77^\circ)$	[-1-21]	90°
18	$(-85.64^\circ, 80.41^\circ, 41.23^\circ)$	[1-2-1]	90°
19	$(85.64^\circ, 80.41^\circ, -41.23^\circ)$	[121]	90°
20	$(94.36^\circ, 80.41^\circ, -138.77^\circ)$	[-12-1]	90°
21	$(-84.23^\circ, 48.19^\circ, 5.77^\circ)$	[1-1-2]	90°
22	$(-95.77^\circ, 48.19^\circ, 174.23^\circ)$	[-1-12]	90°
23	$(95.77^\circ, 48.19^\circ, -174.23^\circ)$	[-11-2]	90°
24	$(84.23^\circ, 48.19^\circ, -5.77^\circ)$	[112]	90°

Table A-2 Variants of the Kurdjumov-Sachs orientation relationship

APPENDIX B

SPLITTING THE ODF INTO 18 SECTIONS

The objective is to calculate the contribution of the 18 ϕ_2 -sections of an ODF to the overall integral

$$I = \int_{[0,90]^3} f(g) \, dg \quad (\text{B-1})$$

B-1/ The ODF is defined by :

$$f(\phi_1, \Phi, \phi_2) = \sum_{l\mu\nu} C_l^{\mu\nu} \dot{T}_l^{\mu\nu}(\phi_1, \Phi, \phi_2) \quad (\text{B-2})$$

so that its integral I_i over section number "i" can be calculated from :

$$I_i = \frac{1}{8\pi^2} \int_0^{90^\circ} d\phi_1 \int_0^{90^\circ} \sin\Phi \, d\Phi \int_{\phi_2^{\min}}^{\phi_2^{\max}} f(\phi_1, \Phi, \phi_2) \, d\phi_2 \quad (\text{B-3})$$

where

$\phi_2^{\min} = 0^\circ$	and	$\phi_2^{\max} = 2.5^\circ$	if $i = 0$ (1 st half),
$\phi_2^{\min} = 87.5^\circ$	and	$\phi_2^{\max} = 90^\circ$	if $i = 0$ (2 nd half),
$\phi_2^{\min} = (5i - 2.5)^\circ$	and	$\phi_2^{\max} = (5i + 2.5)^\circ$	for $i = 1, \dots, 17$.

B-2/ In each section, the integrals of the $\dot{T}_l^{\mu\nu}$ functions are introduced. Strictly, the volume quantities $V_{l\mu\nu}$ should be calculated, but if $\dot{T}_l^{\mu\nu}$ is assumed to be independent of ϕ_2 , the surface integral $S_{l\mu\nu}$ is a good approximation of $V_{l\mu\nu}$. These quantities can be computed once for all, and stored.

$$V_{l\mu}^i = \frac{1}{8\pi^2} \int_0^{90^\circ} \sin\Phi \, d\Phi \int_0^{90^\circ} d\phi_1 \int_{\phi_2^{\min}}^{\phi_2^{\max}} \dot{T}_l^{\mu}(\phi_1, \Phi, \phi_2) \, d\phi_2 \quad (\text{B-4a})$$

$$S_{l\mu}^i = \frac{(\phi_2^{\max} - \phi_2^{\min})}{8\pi^2} \int_0^{90^\circ} \sin\Phi \, d\Phi \int_0^{90^\circ} \dot{T}_l^{\mu}(\phi_1, \Phi, \phi_2) \, d\phi_1 \quad (\text{B-4b})$$

B-3/ As a result of these definitions, I_l can be expressed either as :

$$I_l = \sum_{l\mu\nu} C_l^{\mu\nu} V_{l\mu\nu}^l \quad (\text{B-5a})$$

or, in a simplified manner, as :

$$I_l \approx \sum_{l\mu\nu} C_l^{\mu\nu} S_{l\mu\nu}^l \quad (\text{B-5b})$$

The normalization condition, defined for the entire Euler space, can be expressed for (ϕ_1, ϕ, ϕ_2) restricted to ranges between 0 and 90° as follows :

$$dg = \frac{1}{8\pi^2} \sin\Phi \, d\phi_1 \, d\Phi \, d\phi_2 \quad , \quad \int_{(0,2\pi] \times (0,\pi] \times (0,2\pi]} dg = 1 \quad , \quad \int_{[0,90^\circ]^3} dg = \frac{1}{32} \quad (\text{B-6})$$

so that

$$\int_{[0,90^\circ]^3} f(g) \, dg = \frac{1}{32} \quad (\text{B-7})$$

and using the definition of $f(g)$ given in (B-2)

$$C_0^{11} \frac{1}{32} + \sum_{l \neq 0} \sum_{\mu,\nu} C_l^{\mu\nu} \int_{[0,90^\circ]^3} \ddot{T}_l^{\mu\nu}(g) \, dg = \frac{1}{32} \quad (\text{B-8})$$

$$\sum_{l \neq 0} \sum_{\mu,\nu} C_l^{\mu\nu} \int_{[0,90^\circ]^3} \ddot{T}_l^{\mu\nu}(g) \, dg = 0 \quad (\text{B-9})$$

Applied to the system of orthogonal functions $\ddot{T}_l^{\mu\nu}$, the normalization condition relation (B-7) thus leads to :

$$\int_{[0,90^\circ]^3} \ddot{T}_0^{11}(g) \, dg = \frac{1}{32} \quad \text{and} \quad \int_{[0,90^\circ]^3} \ddot{T}_l^{\mu\nu}(g) \, dg = 0 \quad \text{for } l \neq 0 \quad (\text{B-10})$$

Consequently :

$$\sum_{i=1}^N V_{011}^i = \frac{1}{32} \quad \text{and} \quad \sum_{i=1}^N V_{l\mu\nu}^i = 0 \quad \text{for } l \neq 0 \quad (\text{B-11a})$$

and, to a lesser extent,

$$\sum_{i=1}^N S_{011}^i \approx \frac{1}{32} \quad \text{and} \quad \sum_{i=1}^N S_{l\mu\nu}^i \approx 0 \quad \text{for } l \neq 0 \quad (\text{B-11b})$$

As a means of verification, ΣI_i can be calculated in two different ways :

$$\sum_{i=1}^N I_i = \int_{(0,90^\circ)} f(g) dg = \frac{1}{32} \quad (\text{B-12a})$$

and

$$\sum_{i=1}^N I_i = \sum_{i=1}^N \sum_{l,\mu,\nu} C_l^{\mu\nu} V_{l\mu\nu}^i = \sum_{l,\mu,\nu} C_l^{\mu\nu} \sum_{i=1}^N V_{l\mu\nu}^i = \frac{1}{32} C_{11}^{\mu\nu} = \frac{1}{32} \quad (\text{B-12b})$$

Note B-1: The calculation of the mathematical quantities $V_{l\mu\nu}$ and $S_{l\mu\nu}$ is based on Simpson's rule for integration, which reads

$$\int_a^b f(x) dx = \frac{h}{3} \left[f(a) + 4f(a+h) + 2f(a+2h) + \dots + 2f(a+(2n-2)h) + 4f(a+(2n-1)h) + f(b) \right] \quad (\text{B-13})$$

with $h = (b-a)/2n$

Note B-2: The $S_{l\mu\nu}$ and $V_{l\mu\nu}$ have been found to be identically equal to zero in 2 cases :

- for $l=9,13,15,17,19,21$ and $\nu=1$, because $B_l^{01}=0$,
 - for $\nu=3,5,7,9,11$, recalling that $n=2(\nu-1)$ or $\nu=n/2+1$
- for which the explanation reads as follows :

$$S_{l\mu\nu}^i = \frac{\varepsilon_n \sqrt{2\pi}}{4\pi} \sum_{m=0}^{l/4} B_l^{4m\mu} \int_0^{90^\circ} d\phi_1 \int_0^{90^\circ} S_l^{4m\mu}(\phi_1) \sin\phi \quad (\text{B-14})$$

with

$$S_l^{4mn} = C_1 \cos(n\phi_1) + C_2 \sin(n\phi_1) \quad (\text{B-15})$$

so that, for $n > 1$

$$\int_0^{90^\circ} S_l^{4mn} d\phi_1 = \frac{C_1}{n} \sin \frac{n\pi}{2} + \frac{C_2}{n} \left(1 - (-1)^{\frac{n\pi}{2}}\right) \quad (\text{B-16})$$

Finally, this integral is identically equal to zero for $n=4,8,12,16,20$, or $\nu=3,5,7,9,11$. Moreover, in the $\phi_2=0^\circ$ and $\phi_2=90^\circ$ sections (which by the way are identical), other coefficients are also zero

APPENDIX C

THE GENERATION OF ORIENTATIONS IN ONE ODF SECTION

The objective is to distribute N grains among the 18 ϕ_2 -sections of an ODF according to their respective contributions to the overall integral

$$I = \int_{[0,90^\circ]^3} f(g) \, dg \quad (C-1)$$

The principle of the calculation of the contributions was described in APPENDIX B.

For each orientation, two randomly generated real numbers between 0 and 1, r_ϕ and r_{ϕ_1} , are required. The corresponding angles Φ^γ and ϕ_1^γ are defined by the system generalized from the unidimensional case :

$$r_\phi = \frac{\int_0^{\Phi^\gamma} f(g) \sin\Phi \, d\Phi}{\int_0^{90^\circ} f(g) \sin\Phi \, d\Phi} \quad (C-2) \quad \text{and} \quad r_{\phi_1} = \frac{\int_0^{\phi_1^\gamma} f(g) \, d\phi_1}{\int_0^{90^\circ} f(g) \, d\phi_1} \quad (C-3)$$

This is illustrated in the case of Φ^γ :

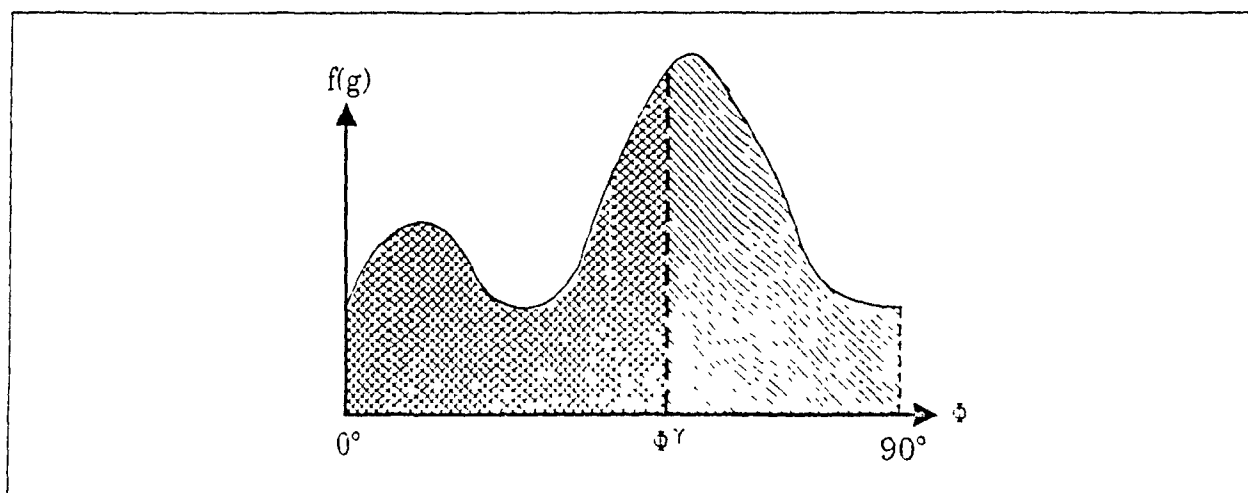


Figure C-1 : $\phi_1^\gamma = \text{constant}$ cut of section "i" of an ODF.

The hatched region under the curve represents the integral between 0 and 90° , whereas the cross-hatched area matches the definition of Φ^γ given in equation (C-2).

The resolution of this system is carried out iteratively :

- a- estimate one of the two angles, for example $\phi^r \in [0, 90^\circ]$,
- b- solve (C-3) for ϕ_1^r with the updated value of ϕ^r ,
- c- solve (C-2) for ϕ^r with the new value of ϕ_1^r , and go to step -b

Steps -b- and -c- have to be performed successively, until $|\Delta\phi_1^r|$ and $|\Delta\phi^r|$ become less than a tolerance ϵ which must be in agreement with the number of grains to be generated.

Problems may arise if $f(g) < 0$ in some areas of the ODF section

- if $\int_0^{90^\circ} f(g).dg > 0$, there is no major difficulty, except that one has to decide whether the negative areas should be taken into account in the integral or simply skipped as "zero" regions. If taken into account, uniqueness can no longer be assured. Although, in this case, the negative regions reduce the value of the integral, the procedure will still not "stop" in such regions :

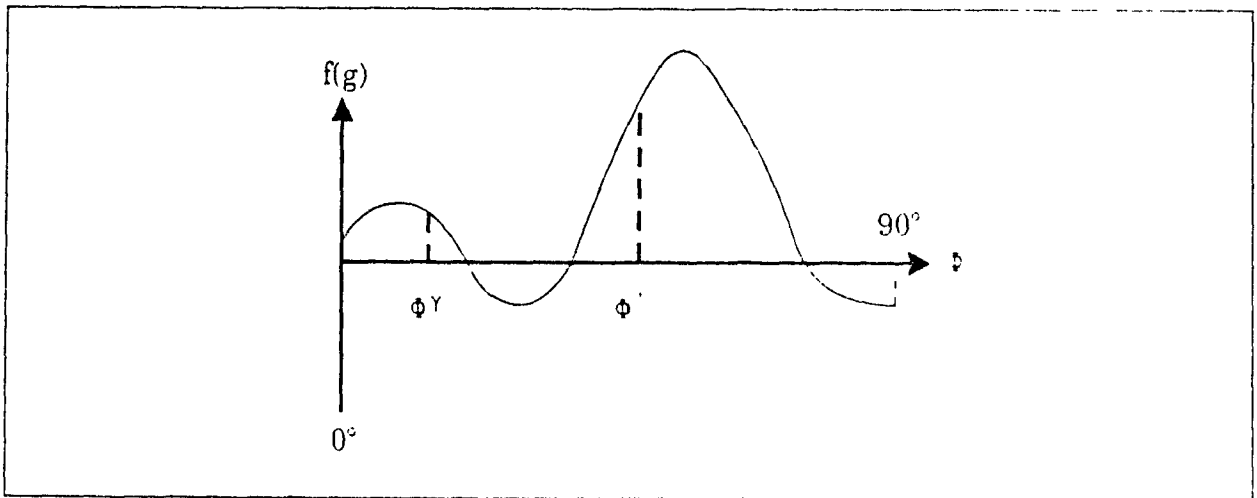


Figure C-2 : Illustration of the non-uniqueness of the solution if negative areas arise.

- if $\int_0^{90^\circ} f(g).dg < 0$, it definitely results from a poor choice of the guessed value of the fixed angle. Another one should thus be chosen and the procedure restarted. Indeed, it cannot result from a previous step in the calculation, otherwise, the procedure would have stopped in a negative region, which is impossible.

APPENDIX D

CALCULATION OF THE SYMMETRIC GENERALIZED
SPHERICAL HARMONIC FUNCTIONS

The aim of this appendix is to propose a procedure for the calculation of the symmetric harmonics in the case of cubic-orthorhombic and cubic-cubic systems.

D-1/ For cubic-orthorhombic systems, the symmetric harmonic functions $\dot{T}_l^{\mu\nu}$ may be obtained as follows:

$$\dot{T}_l^{\mu\nu}(g) = \varepsilon_n \sqrt{2\pi} \sum_{m=0}^{l/4} \dot{B}_l^{4m\mu} S_l^{4m\nu}(g) \quad \text{with} \quad \begin{cases} \varepsilon_n = \sqrt{2} & \text{if } n \neq 0 \\ \varepsilon_0 = 0 \end{cases} \quad (\text{D-1})$$

where n is defined by $n = 2(\nu - 1)$

a/ The symmetric $\dot{B}_l^{4m\mu}$ coefficients have been defined and tabulated by Bunge[-1] and will be considered here as pure mathematical quantities.

b/ The S_l^{mn} functions, for an orientation $g = (\phi_1, \phi, \phi_2)$, are defined by:

$$S_l^{mn}(g) = \left\{ \sum_{s=0(2)}^l a_l^{mns} \cos(s\Phi) \right\} \cos(m\phi_2) \cos(n\phi_1) - \left\{ \sum_{s=1(2)}^l a_l^{mns} \cos(s\Phi) \right\} \sin(m\phi_2) \sin(n\phi_1) \quad (\text{D-2})$$

Only the S_l^{mn} functions with $m+n$ even are required, and their a_l^{mns} coefficients are given by:

$$a_l^{l^{mn}0} = a_l^{mn0}$$

$$a_l^{l^{mn}s} = 2a_l^{mns} \quad \text{for } s \neq 0$$

The calculation of the a_l^{mns} can be performed with the following formulae:

$$a_l^{mns} = Q_l^{ms} Q_l^{n} \quad \text{with} \quad Q_l^{mn} = i^{m+n} P_l^{mn}(0) \quad (\text{D-3})$$

$$P_l^{mn}(0) = c_{lmn} \times \frac{(-1)^{l-m} i^{n-m}}{2^l} \times \frac{\sqrt{(l-n)! (l+n)!}}{\sqrt{(l-m)! (l+m)!}} \quad (\text{D-4})$$

where the c_{lmn} coefficients are defined by

$$c_{lmn} = \sum_{i=0}^{l-n} (-1)^{l-n-i} \binom{l-n-i}{l+m} \binom{l-n-i}{l-n} \quad \text{with } i \leq l-m \quad \text{and} \quad l-n-i \leq l-m \quad (\text{D-5})$$

which for $m \geq n$ transforms into

$$c_{lmn} = \sum_{j=0}^{l-m} (-1)^j \binom{l-j}{l-m} \binom{l-n-j}{l+m} \quad (D-6)$$

The coefficients with $m < n$ are found with the aid of the relation derived from the equality of the Legendre polynomials P_l^{m-1} and P_l^{n-1} .

$$c_{lmn} = c_{lnm} \cdot \frac{(l-m)!(l+m)!}{(l-n)!(l+n)!} \quad (D-7)$$

Finally, the a_l^{mn} coefficients may be obtained from

$$a_l^{mn} = \frac{(-1)^{n-m}}{2^{2l}} \cdot \frac{\sqrt{(l-n)!(l+n)!}}{\sqrt{(l-m)!(l+m)!}} \cdot c_{lmn} \cdot c_{lnm} \quad (D-8)$$

D-2/ For cubic-cubic systems, the symmetric harmonic functions may be defined by

$$\ddot{T}_l^{\mu_2 \mu_1}(g) = 2\pi \sum_{m=0}^{l/4} \ddot{B}_l^{4m \mu_1} \sum_{m'=0}^{l/4} \ddot{B}_l^{4m' \mu_2} S_l^{4m+4m'}(g)$$

and thus are related to the cubic-orthorhombic functions by

$$\ddot{T}_l^{\mu_2 \mu_1}(g) = \sqrt{2\pi} \sum_{m=0}^{l/4} \frac{1}{\varepsilon_{4m}} \ddot{B}_l^{4m \mu_1} \ddot{T}_l^{\mu_2 4m}(g)$$

with

$$\ddot{T}_l^{\mu_2 4m}(g) = \varepsilon_{4m} \sqrt{2\pi} \sum_{m'=0}^{l/4} \ddot{B}_l^{4m' \mu_2} S_l^{4m+4m'}(g)$$

APPENDIX E

THE COUNTERPARTS OF
POLE FIGURES AND INVERSE POLE FIGURES
FOR MISORIENTATION DISTRIBUTION FUNCTIONS

Given the $W_l^{\mu_2\mu_1}$ of the MODF, the orientation density of one phase (1) in the reference frame of another phase (2) is desired.

The intensity of h_2/h_1 is given by :

$$A(h_2, h_1) = \frac{1}{2\pi} \int_0^{2\pi} W(\Delta g) d\psi = \frac{1}{2\pi} \sum_{l, \mu_1, \mu_2} W_l^{\mu_2\mu_1} \int_0^{2\pi} \ddot{T}_l^{\mu_2\mu_1}(\Delta g) d\psi$$

with

$$\int_{h_2 // h_1} \ddot{T}_l^{\mu_2\mu_1}(g) d\phi_2 = \frac{8\pi^2}{2l+1} \dot{k}_l^{\mu_1}(h_1) \dot{k}_l^{\mu_2}(h_2)$$

where the k_l^μ functions are the so-called symmetric surface harmonics.

Hence,

$$A(h_2, h_1) = 4\pi \sum_{l, \mu_1, \mu_2} \frac{W_l^{\mu_2\mu_1}}{2l+1} \dot{k}_l^{\mu_1}(h_1) \dot{k}_l^{\mu_2}(h_2)$$

The surface harmonics can be calculated, for $h = (\beta, \phi) \in [0^\circ, 90^\circ]^2$, as follows

$$\dot{k}_l^\mu(h) = \sum_{m=0(4)}^l \dot{B}_l^{mu} \cos(m\beta) \left(\sum_{s=0(2)}^l a_l^{ms} \cos(s\phi) \right)$$

E-1 Equivalent pole figure : the product orientation h_2 is kept equal to h_1

$$P_{h_1}(h_1) = \sum_l \sum_{\mu_1} \left[\frac{4\pi}{2l+1} \sum_{\mu_2} W_l^{\mu_2\mu_1} \dot{k}_l^{\mu_2}(h_1) \right] \dot{k}_l^{\mu_1}(h_1)$$

E-2' Equivalent inverse pole figure : the parent orientation h_1 is kept equal to h_1

$$R_{h_1}(h_2) = \sum_l \sum_{\mu_2} \left[\frac{4\pi}{2l+1} \sum_{\mu_1} W_l^{\mu_2\mu_1} \dot{k}_l^{\mu_1}(h_1) \right] \dot{k}_l^{\mu_2}(h_2)$$